

REPORT DOCUMENTATION PAGE					Form Approved OMB No. 0704-0188	
<p>The public reporting burden for this collection of information is estimated to average 1 hour per response, including the time for reviewing instructions, searching existing data sources, gathering and maintaining the data needed, and completing and reviewing the collection of information. Send comments regarding this burden estimate or any other aspect of this collection of information, including suggestions for reducing the burden, to the Department of Defense, Executive Service Directorate (0704-0188). Respondents should be aware that notwithstanding any other provision of law, no person shall be subject to any penalty for failing to comply with a collection of information if it does not display a currently valid OMB control number.</p>						
<b>PLEASE DO NOT RETURN YOUR FORM TO THE ABOVE ORGANIZATION.</b>						
1. REPORT DATE (DD-MM-YYYY) 22-04-2008		2. REPORT TYPE Final		3. DATES COVERED (From - To) 1/1/05-12/31/07		
4. TITLE AND SUBTITLE STUDIES OF REAL ROUGHNESS EFFECTS FOR IMPROVED MODELING AND CONTROL OF PRACTICAL WALL-BOUNDED TURBULENT FLOWS			5a. CONTRACT NUMBER			
			5b. GRANT NUMBER FA9550-05-1-0043			
			5c. PROGRAM ELEMENT NUMBER			
6. AUTHOR(S) Christensen, Kenneth T. (PI)  Wu, Yanhua (Graduate Student)			5d. PROJECT NUMBER			
			5e. TASK NUMBER			
			5f. WORK UNIT NUMBER			
7. PERFORMING ORGANIZATION NAME(S) AND ADDRESS(ES) University of Illinois at Urbana-Champaign Urbana, IL 61801				8. PERFORMING ORGANIZATION REPORT NUMBER		
9. SPONSORING/MONITORING AGENCY NAME(S) AND ADDRESS(ES) Air Force Office of Scientific Research 875 N Randolph St Arlington, VA 22201  <i>Rhett Jeffries /MA</i>				10. SPONSOR/MONITOR'S ACRONYM(S) AFOSR		
				11. SPONSOR/MONITOR'S REPORT NUMBER(S)		
12. DISTRIBUTION/AVAILABILITY STATEMENT <i>Approved for public release, distribution unlimited</i>				AFRL-SR-AR-TR-08-0234		
13. SUPPLEMENTARY NOTES						
14. ABSTRACT The present effort investigates the effects of practical roughness replicated from a turbine blade damaged by deposition of foreign materials on statistical and structural characteristics of wall turbulence. Two-dimensional particle image velocimetry (PIV) measurements are performed in the streamwise-wall-normal plane of turbulent boundary layers at momentum Reynolds numbers of 8000 and 13000. The surface conditions include a smooth wall and two highly-irregular rough walls. These rough surfaces have the same roughness topography but differ in spatial scaling. The validity of Townsend's wall similarity hypothesis in the presence of practical roughness is assessed and the impact of this roughness on the spatial structure of the flow is investigated. In addition, stereoscopic PIV measurements are made in streamwise-spanwise planes of smooth- and rough-wall turbulent boundary layers both within and at the outer edge of the roughness sublayer. This data is used to explore the impact of dominant topographical features on the near-wall flow as well as the influence of practical roughness on the spatial organization of the flow. Understanding such effects provides a stepping stone toward efficient modeling and control of practical flows in the presence of roughness.						
15. SUBJECT TERMS						
16. SECURITY CLASSIFICATION OF: a. REPORT    b. ABSTRACT    c. THIS PAGE U              U              U			17. LIMITATION OF ABSTRACT U	18. NUMBER OF PAGES 182	19a. NAME OF RESPONSIBLE PERSON Kenneth Christensen 19b. TELEPHONE NUMBER (Include area code) 217-333-0966	

# STUDIES OF REAL ROUGHNESS EFFECTS FOR IMPROVED MODELING AND CONTROL OF PRACTICAL WALL-BOUNDED TURBULENT FLOWS

AFOSR Grant FA9550-05-1-0043

## Final Report

Kenneth T. Christensen (PI) and Yanhua Wu (Graduate Student)  
*Mechanical Science and Engineering Department*  
*University of Illinois at Urbana-Champaign*

## 1 Introduction

### 1.1 Motivation

Most practical wall-bounded turbulent flows of interest, like flows over turbine blades, through heat exchangers, and over aircraft and ship hulls, are influenced by surface-roughness effects. In some applications, surface defects can be small on an absolute scale but can still be aerodynamically important if they are large relative to the viscous length scale of the turbulence (at high Reynolds number ( $Re$ ), for example). In many other cases, however, the surface conditions in practical wall-bounded flows can degrade over time, from hydraulically smooth prior to deployment to significantly roughened over time due to harsh operating conditions. Examples of such conditions include cumulative damage to turbine blades (Bons, 2002), cumulative algae/barnacle buildup on the surfaces of submarines and ships (Karlsson, 1980) and surface erosion observed on the blades of windmills operating near the sea. In most cases surface roughness significantly increases the wall shear stress and can augment heat and mass transfer at the wall, resulting in an increase in the thermal loading of a system. This latter effect can severely reduce the lifetime of vital parts of many practical engineering systems (like turbine blades). *Therefore, a clear understanding of the impact of surface roughness on wall-bounded turbulent flow is imperative for successful modeling and control of these flows to improve both the efficiency and lifetime of a variety of vital engineering systems.*

Rough-wall turbulence has received intense research attention over the last several decades. The review articles of Raupach *et al.* (1991) and Jimenez (2004), for example, provide thorough summaries of the knowledge gleaned from this research. Unfortunately, nearly all of these studies involved the use of only one roughness scale (sand grain, ordered arrays of elements, wire mesh, etc.) to study the impact of non-ideal surface conditions on wall-bounded turbulence (such idealized roughness conditions will be hereon referred to as “simulated roughness”). However, in the case of turbine blades, surface defects are attributable to multiple damage mechanisms, like deposition of foreign materials, pitting and spallation, that render the surface conditions highly non-uniform (Bons, 2002). As such, a single roughness type and scale cannot be expected to be a sufficient representation of real roughness. *Therefore, successful modeling and control of practical engineering flows, both before operation and throughout the lifetime of a flow system, requires documentation of the influence of roughened surfaces, particularly highly-irregular roughness, on the underlying character of the flow.* The present effort is meant to contribute in this regard.

## 1.2 Background

### 1.2.1 Classical rough-wall boundary layer theory

One of the most well-known effects of surface roughness on wall turbulence is to shift the logarithmic region of the mean velocity profile downwards by an amount of  $\Delta U^+$ , the roughness function, and to shift the origin of the mean profile by some distance  $y_o^*$ . The superscript “+” denotes normalization by the friction velocity,  $u_\tau \equiv \sqrt{\tau_w/\rho}$  and the kinematic viscosity of the fluid,  $\nu$  ( $\tau_w$  is the wall shear stress and  $\rho$  is the fluid density). Therefore, the mean velocity profile in the overlap region can be expressed as

$$U^+ = \frac{1}{\kappa} \ln(y - y_o)^+ + A - \Delta U^+, \quad (1)$$

where  $\kappa$  and  $A$  are the von Karman and integration constants, respectively. Note that upper-case variables will represent mean quantities while primed quantities,  $(\cdot)'$ , will represent fluctuations about the mean throughout. By assuming a universal log-region velocity defect of

$$U_e^+ - U^+ = f(\delta^* U_1 / u_\tau), \quad (2)$$

where  $U_e$  is the freestream velocity and  $\delta^*$  is the displacement thickness, Hama (1954) found that the roughness function is directly related to the local skin-friction coefficient,  $c_f \equiv \tau_w / (\frac{1}{2} \rho U_e^2)$ , over smooth and rough walls as

$$\Delta U^+ = \left( \sqrt{\frac{2}{c_f}} \right)_{\text{smooth}} - \left( \sqrt{\frac{2}{c_f}} \right)_{\text{rough}}. \quad (3)$$

However, the notion of a universal velocity defect law for arbitrary roughness has been questioned by several recent studies (Shafi & Antonia, 1997; Krogstad & Antonia, 1999; Keirsbulck *et al.*, 2002; Tachie *et al.*, 2000, 2003; Poggi *et al.*, 2003; Bhaganagar *et al.*, 2004).

A fundamentally-important issue in rough-wall turbulence is accurate determination of the wall shear stress (or equivalently the friction velocity,  $u_\tau$ ). Direct measurement of  $\tau_w$  over rough surfaces is quite difficult and can be very inaccurate, so various indirect measures of  $u_\tau$  from the measured mean velocity or Reynolds shear stress profiles have been proposed in the literature. These methods include the modified “Clauser chart” method, the velocity profile matching method by Krogstad *et al.* (1992) and the constant stress method. The modified Clauser chart method involves fitting the measured mean velocity profile in the logarithmic layer to Eq. (1) which yields estimates of  $u_\tau$ ,  $y_o$  and  $\Delta U^+$ . In contrast, the profile matching method of Krogstad *et al.* (1992) fits the measured mean velocity profile to both the log law [Eq.. (1)] as well as a wake function near the boundary-layer edge as a means of inferring  $u_\tau$ ,  $y_o$  and  $\Delta U^+$ . Alternatively, one can assess  $u_\tau$  independently from the measured Reynolds shear stress,  $\langle u'v' \rangle$ , profiles. This method relies upon the existence of nearly constant  $\langle u'v' \rangle$  at the outer edge of the log layer. If one considers the mean momentum equation for a turbulent boundary layer given by

$$U^+ \frac{\partial U^+}{\partial x^+} + V^+ \frac{\partial U^+}{\partial y^+} + \frac{\partial \langle u'^+ v'^+ \rangle}{\partial y^+} = \frac{\partial^2 U^+}{\partial y^{+2}}, \quad (4)$$

and invokes standard boundary-layer approximations, one observes that the first two terms on the left-hand-side of Eq. (4) are small compared to the Reynolds stress and viscous terms in the

---

<sup>\*</sup>Throughout this report,  $x$ ,  $y$  and  $z$  will refer to the streamwise, wall-normal and spanwise directions, respectively, while  $u$ ,  $v$  and  $w$  will represent the velocity components in these directions.

near-wall region. Therefore, close to the wall the mean momentum equation reduces to a balance between the net turbulent and viscous forces as

$$\frac{\partial \langle u'^+ v'^+ \rangle}{\partial y^+} = \frac{\partial^2 U^+}{\partial y^{+2}}. \quad (5)$$

Applying the boundary condition  $\partial U^+ / \partial y^+|_{y=0} = 1$ , the above equation can be integrated with respect to  $y$  to obtain

$$-\langle u'^+ v'^+ \rangle + \frac{\partial U^+}{\partial y^+} = 1, \quad (6)$$

or in dimensional form

$$u_\tau^2 = \nu \frac{\partial U}{\partial y} - \langle u' v' \rangle. \quad (7)$$

In the log layer and beyond, the viscous stress [first term on the right-hand-side of Eq. (7)] is now negligible compared to turbulent stress (second term), meaning one can use the measured Reynolds shear stress to estimate  $u_\tau$ . Smalley *et al.* (2001) observed that over most surfaces at relatively high  $Re$ , a plateau of Reynolds stress exists at  $y/\delta \approx 0.2$ . This method has been extensively used in rough-wall boundary layer studies (Mulhearn & Finnigan, 1978; Raupach *et al.*, 1980; Raupach, 1981; Raupach *et al.*, 1986; Weber, 1999, for example). Once  $u_\tau$  is assessed in this manner,  $y_0$  and  $\Delta U^+$  can be determined by fitting the measured mean velocity profile in the log layer to Eq. (1).

Nikuradse (1933) performed the first in-depth studies of rough-wall flow by uniformly gluing sand grains to the inner surface of a circular pipe. The grains were carefully filtered to maximize the size uniformity of the sand grains. Nikuradse (1933) found that the mean velocity profile in the log layer was given by

$$U^+ = \frac{1}{\kappa} \ln(y/k_s) + 8.5, \quad (8)$$

where  $k_s$  is termed the equivalent sand-grain roughness height (in the case of Nikuradse's experiments, it simply represents the mean size of the sand grains). Comparing Eqs. (8) and (1), the sand-grain size,  $k_s$ , can be directly related to the roughness function,  $\Delta U^+$ , as

$$\Delta U^+ = \frac{1}{\kappa} \ln(k_s^+) + A - 8.5. \quad (9)$$

This relationship between  $\Delta U^+$  and  $k_s$  is important because it allows one to relate the effects of non-sand-grain roughness with roughness height  $k$  to the original experiments of Nikuradse (1933) through an *equivalent* sand grain height  $k_s$ . That is,  $k_s$  is the equivalent sand-grain height that yields the same  $\Delta U^+$  as a non-sand-grain roughness with height  $k$ .

If  $k_s$  is proportional to  $k$  (as is the case for most rough surfaces), then the roughness of interest is termed “ $k$ -type”. In this context, the roughness function can be expressed as a function of the roughness Reynolds number,  $k^+ \equiv k u_\tau / \nu$ , as

$$\Delta U^+ = \frac{1}{\kappa} \ln(k^+) + C, \quad (10)$$

where  $C$  is a roughness-dependent constant. If, however,  $k_s$  is not proportional to  $k$  but rather to the outer length scale of the flow (like the pipe diameter  $d$  or the boundary-layer thickness  $\delta$ ), the roughness is termed “ $d$ -type”. In such cases,  $\Delta U^+$  can be expressed as

$$\Delta U^+ = \frac{1}{\kappa} \ln(d^+) + G, \quad (11)$$

where the additive constant  $G$  depends on the character of the roughness. The distinction between “ $k$ -type” and “ $d$ -type” roughness was first made by Perry *et al.* (1969). Finally, while  $k^+$  (or  $k_s^+$ )

represents a measure of the roughness height relative to the viscous length scale, the blockage ratio,  $\delta/k$  (where  $\delta$  is the outer length scale of the flow), represents a measure of the direct effects of surface roughness on the log and outer layers of the flow as proposed by Jimenez (2004).

Finally, flow over a given surface is generally classified into three regimes with regard to roughness effects: hydraulically smooth, transitionally rough and fully rough. It is generally accepted that a surface is hydrodynamically smooth if  $k_s^+ < 4 - 5$ . In such cases, the roughness is entirely submerged in the viscous sublayer and the roughness function effectively vanishes. However, Bradshaw (2000) recently argued that the drag on the surfaces of sparse roughness elements is actually proportional to  $k^2$ , meaning that a “critical roughness height” is not likely to exist. The flow is termed transitionally rough in the range  $5 < k_s^+ < 60 - 70$ . In this flow regime, the roughness function is found to be strongly dependent on the roughness character. Finally, for  $k_s^+ > 70$ , the flow regime is referred to as fully rough and the roughness function is assumed to be universal. In this regime, the drag on the roughness elements is dominant compared with viscous contribution to the skin friction.

### 1.2.2 Wall similarity

As noted earlier, there is intense debate regarding the existence of a universal velocity defect law over arbitrary roughness. The possible existence of such a universal law is certainly consistent with the Reynolds-number similarity hypothesis offered by Townsend (1976) which proposes that turbulence far from the wall is unaffected by the surface conditions at high  $Re$ . In the context of rough-wall turbulence, Raupach *et al.* (1991) summarized this hypothesis, also referred to as wall similarity, as

*“Outside the roughness (or viscous) sublayer, the turbulent motions in a boundary layer at high  $Re$  are independent of the wall roughness and the viscosity, except for the role of the wall in setting the velocity scale  $u_\tau$ , the height  $Z = z - d$  and the boundary-layer thickness  $\delta$ .”*

The roughness sublayer is defined as a layer that is dynamically influenced by length scales associated with the roughness elements and occupies 3–5 roughness heights from the wall. Alternatively, since  $u_\tau \equiv \sqrt{\tau_w/\rho}$ , the wall-similarity hypothesis equivalently states that the roughness sets the drag at the surface and the turbulence above the wall adjusts itself such that it remains universal when scaled appropriately by  $u_\tau$ .

The validity of wall similarity over arbitrary roughness is still an open question. Some studies support this hypothesis while others directly question its validity. These studies have been performed in various facilities (including wind or water tunnels, open channel flumes and turbulent channels) and have considered a wide range of roughness types and scales in terms of both  $k^+$  and  $\delta/k$ . A summary of these studies is given in tables 1 and 2 which detail the flow parameters of studies that support and violate wall similarity, respectively. It should be noted that Jimenez (2004) proposed  $\delta/k > 40$  as a requirement for wall similarity to be valid. Motivation for defining a threshold for wall similarity based on  $\delta/k$  comes from the fact that this ratio represents a measure of the scale separation between the outer length scale of the flow and the characteristic length scale of the roughness. That is, the larger the value of  $\delta/k$  the wider the physical separation between the roughness sublayer and the outer-layer turbulence. Note that there still exists some debate regarding whether the geometric scale of the roughness,  $k$ , or the equivalent sandgrain scale,  $k_s$ , is more representative of the extent of the roughness sublayer. In this regard, Flack *et al.* (2005) suggests that  $\delta/k_s > 40$  is a more suitable threshold than  $\delta/k > 40$  for the existence of wall similarity.

Table 1: Past studies that observe wall-similarity.

Studies	Flow	Roughness	$k^+$	$k_s^+$	$\delta/k$	$\delta/k_s$
Raupach (1981)	BL	Cylinder	337–427	—	19–129	—
Ligrani & Moffat (1986)	BL	Spheres	22–63	—	—	—
Bandyopadhyay & Watson (1988)	BL	2D grooves	15–18	—	60	—
Flack <i>et al.</i> (2005)	BL	Sandpaper	134	100	46.2	62.5
		Woven mesh	64	138	97.2	45.5
Schultz & Flack (2003)	BL	Sandpaper	7.6–32	7–126	32.5–120	175–232
Schultz & Flack (2005)	BL	Spheres	35–182	—	30–34	—
Grass (1971)	BL	Sand	21	21	24	24
		Pebbles	85	—	6.5	—
Krogstad <i>et al.</i> (2005)	TC	2D grooves	13.6–20.4	63–121	30	5–6
Bakken <i>et al.</i> (2005)	TC	2D grooves	20–200	60–1560	30	6–10
		Woven mesh	15–187	30–617	33	9–15
Allen <i>et al.</i> (2007)	TP	honed surface	0.06–14.8	0.17–44.4	51500	17000

BL: Boundary Layer; TC: Turbulent Channel; TP: Turbulent Pipe

### Studies that support wall-similarity

Grass (1971) performed roughness studies in an open water channel at  $Re = DU_b/\nu = 7000$ , where  $D$  is the channel depth and  $U_b$  bulk (average) velocity. The surfaces considered included marine plywood (hydraulically smooth), sandgrain (transitionally rough;  $k^+ = 21$ ,  $D/k = 24$ ) and pebbles (fully rough;  $k^+ = 85$ ,  $D/k = 6.5$ ). Grass (1971) found that the streamwise and wall-normal turbulence intensities,  $\sigma_u$  and  $\sigma_v$ , are independent of roughness conditions when scaled by  $u_\tau$  for  $y/D > 0.2$ . However, immediately adjacent to the bed,  $\sigma_u$  decreased and  $\sigma_v$  increased with increasing roughness height. Grass (1971) also observed extremely violent entrainment over the rough surfaces with ejected fluid rising almost vertically from between the interstices of the roughness elements. Raupach (1981) studied the effect of cylindrical roughness elements on the Reynolds stress in turbulent boundary layers at  $Re_\theta \equiv U_e\theta/\nu = 10,000 – 15,000$ , where  $\theta$  is the momentum thickness of the boundary layer. The cylinders were arranged in either square or diamond arrays with  $k^+ = 337 – 427$  and  $\delta/k = 19 – 125$ . It was observed that the second and third moments of the velocity fluctuations were universal for  $y > 0.15\delta$ . Additionally, quadrant analysis revealed that the fractional difference between stress contributions by sweeps and ejections,  $\Delta_0 = S_{4,0} – S_{2,0}$ , is independent of surface roughness for  $y > 0.2\delta$ . Raupach (1981) determined the friction velocity using the constant stress method.

Ligrani & Moffat (1986) studied structural characteristics of both transitionally and fully rough turbulent boundary layers over uniform spherical roughness elements over the range  $6300 < Re_\theta < 19000$  ( $k^+ = 22 – 63$ ). It was observed that  $u_\tau$  is the universal normalizing parameter in the outer layer for  $\sigma_u^2$  and  $\bar{q}^2$ , the turbulent kinetic energy, in the fully rough regime. However, the free-stream velocity was found to be more appropriate for collapse of  $\sigma_w^2$  and  $\sigma_v^2$  when  $k^+ > 34$ . The local skin friction coefficients were determined from the Reynolds shear stress profiles and mean velocities in the near-wall region. Bandyopadhyay & Watson (1988) investigated turbulent boundary layers over both  $k$ - and  $d$ -type two-dimensional transversely grooved rough surfaces at  $Re_\theta = 2100 – 2900$ . It was observed that the ratio between the Reynolds shear stress and the turbulent kinetic energy is nearly constant between  $0.1 < y/\delta < 0.8$  for all surfaces. The modified Clauser chart method was used to obtain  $u_\tau$  for flow over the rough walls.

Schultz & Flack (2003) performed measurements in a water tunnel for flow over sanded surfaces for  $Re_\theta = 3000 - 16000$ . They found that the mean velocity profiles collapsed well in defect form for all surface conditions. In addition, the Reynolds normal and shear stress profiles normalized by  $u_\tau$  showed good agreement within their experimental uncertainties in the overlap and outer layers. The skin-friction coefficients for the rough-wall experiments were determined from the modified Clauser chart method and verified by the total stress method. Flack *et al.* (2005) pursued a follow-up investigation in which they studied turbulent boundary layers over sandgrain and woven mesh at  $Re_\theta = 14120$ . They chose the roughness characteristics of both surfaces to simultaneously satisfy  $k_s^+ > 100$  (fully rough) and  $\delta/k_s > 40$  (presumably satisfying wall similarity). Reynolds stress and quadrant analysis results over the rough walls collapsed on the smooth-wall results for  $y > 3k_s$ . Furthermore, differences of velocity triple products and higher moment turbulence statistics between rough and smooth walls were only observed for  $y < 5k_s$ . In this context, this effort showed that  $k_s$  may be a more appropriate measure of the relative roughness height in the context of wall similarity.

Finally, Krogstad *et al.* (2005) investigated fully-developed turbulent channel flow wherein the top and bottom walls were roughened by transverse square rods at  $Re_\tau \equiv u_\tau \delta / \nu = 600$ . Wall similarity was observed in the Reynolds stresses, stress ratios and the anisotropy tensor outside the roughness sublayer ( $y > 5k$ ) and the authors argued that wall similarity is highly dependent on the flow of interest. Finally, Bakken *et al.* (2005) studied turbulent channel flows over both two-dimensional (2D) rods and three-dimensional (3D) mesh for  $Re_\tau = 360 - 6000$ . Reynolds stresses and third-order moments were found to be unaffected by the surface conditions for  $y > 5k$ . Satisfactory collapse with  $Re_\tau$  was also demonstrated outside the roughness sublayer when  $u_\tau$  was used for normalization.

#### Studies that do not observe wall similarity

Krogstad *et al.* (1992) studied the outer-layer effects of wire-mesh roughness in a turbulent boundary layer at  $Re_\theta = 12800$  with  $k^+ = 143$  and  $\delta/k = 48$ . The wake strength of the rough-wall outer layer was found to be larger than for flow over a smooth wall. In addition, a significant increase in the wall-normal turbulence intensity together with a moderate increase in the Reynolds shear stress was observed over the roughness compared with flow over a smooth wall. In contrast, the longitudinal turbulence intensities for both surfaces were essentially the same. However, quadrant analysis revealed that Reynolds shear stress contributions from  $Q2$  and  $Q4$  events were enhanced by the roughness. It should be noted that Krogstad *et al.* (1992) proposed a new method for evaluating  $u_\tau$  from the mean velocity that involves curve-fitting the wake portion of the profile. In a follow-up study, Krogstad & Antonia (1999) investigated the effects of two types of roughness, woven mesh and lateral rods, on a turbulent boundary layer for  $Re_\theta = 4800 - 13000$ . The two rough surfaces were designed to yield the same roughness function,  $\Delta U^+$ . It was observed that the roughness effects on the Reynolds stresses were not confined to the wall region. In addition, the turbulent energy production and diffusion were found to be significantly different between the two roughness conditions.

Shafi & Antonia (1997) studied the spanwise and wall-normal vorticity fluctuations and their constituent velocity derivative fluctuations in a turbulent boundary layer over a wire mesh surface at  $Re_\theta = 8000$  with  $k^+ = 54$  and  $\delta/k = 60$ . It was observed that over most of the outer layer, the normalized magnitudes of the velocity derivative variances differed significantly from those over a smooth wall. Furthermore, the vorticity variances were found to be slightly larger than those over a smooth wall. Shafi & Antonia (1997) used the velocity profile matching method of Krogstad *et al.* (1992) to determine  $u_\tau$ .

Table 2: Studies that do not observe wall similarity.

Studies	Flow	Roughness Type	$k^+$	$k_s^+$	$\delta/k$	$\delta/k_s$
Keirsbulck <i>et al.</i> (2002)	BL	2D grooves	150	530	26.3	7.5
Krogstad & Antonia (1999)	BL	Woven mesh	143	458	48	15
		2D grooves	143	458	47	8
Krogstad <i>et al.</i> (1992)	BL	Woven mesh	143	458	48	15
Shafi & Antonia (1997)	BL	Woven mesh	54	—	58.4	—
Tachie <i>et al.</i> (2003)	BL	Sand	33	33	31	31
		Mesh	17	—	63	—
Tachie <i>et al.</i> (2000)	BL	Sand	25–35	25–35	21–29	21–29
		Mesh	17–25	—	67–75	—
Bhaganagar <i>et al.</i> (2004)	TC	Egg carton	5.4–21.6	10–48	18.5–74	8–40

BL: Boundary Layer; TC: Turbulent Channel; TP: Turbulent

Tachie *et al.* (2000) investigated the effect of roughness on the structure of turbulent boundary layers in open channels for  $Re_\theta = 1400 - 4000$ . The roughness studied included a perforated surface, sandgrain and woven mesh with  $k^+ = 17 - 35$ . They found that the wake parameter varied significantly with the type of surface roughness. Additionally, the roughness increased the turbulence levels in the outer region of the boundary layer. More recently, Tachie *et al.* (2003) made measurements in a open channel over both sandgrain and woven mesh for  $Re_\theta = 1900 - 2600$  and  $k^+ = 17 - 33$ . The surface roughness was observed to increase the wake parameter and to enhance the turbulence intensities, Reynolds shear stress and triple correlations over most of the boundary layer. However, the stress anisotropy was found to be decreased by roughness. It should be noted that both studies utilized the velocity profile matching method of Krogstad *et al.* (1992) to determine  $u_\tau$ .

Keirsbulck *et al.* (2002) studied the structure of a turbulent boundary layer over fully rough  $k$ -type two-dimensional square bars at  $Re_\theta = 8500$ . Similar to the studies of Tachie *et al.* (2000), it was observed that the magnitude of the wake strength is increased by the roughness. In the near-wall region, the contribution to the Reynolds shear stress fraction and the diffusion factors were found to depend on the wall roughness conditions. In addition, the wall-normal velocity component appeared to be more sensitive to the roughness effects. As with the previous studies,  $u_\tau$  was determined using the velocity profile matching method described in Krogstad *et al.* (1992).

Finally, Bhaganagar *et al.* (2004) performed a direct numerical simulation (DNS) of turbulent channel flow between a smooth wall and a wall covered with regular three-dimensional “egg carton” roughness elements at  $Re_\tau = 400$  at  $k^+ = 5.4, 10.8$  and  $21.6$ . It was observed that when normalized by the local  $u_\tau$ , the  $u$  and  $w$  fluctuations were smaller while the  $v$  fluctuation was higher in the inner layer for the rough-wall side. However, all three velocity fluctuations were a smaller fraction of  $u_\tau$  on the rough-wall side in the outer layer. On the other hand, the vorticity fluctuations were not significantly altered by roughness in the outer layer.

Based on the evidence discussed above and summarized in Tables 1 and 2, for efforts questioning wall similarity based on studies of zero-pressure-gradient boundary layers each had low  $\delta/k_s$  values ( $< 15$ ). As noted by Flack *et al.* (2005), these extremely low  $\delta/k_s$  values can be interpreted as relatively weak scale separation between the outer layer of the flow and the roughness which is directly counter to the essence of the wall similarity hypothesis. In channel flows, where the flow is constrained by opposing boundaries, the above-cited studies indicate that wall similarity will only exist if both surfaces are rough.

### 1.2.3 Impact of roughness on turbulence structure

While the previous section indicates the possibility of similarity in the outer-layer statistics of rough-wall turbulence to its smooth-wall counterpart, this similarity does not imply that a structural similarity between these flows also exists. This section is dedicated to reviewing previous studies regarding the impact of roughness on the structural foundation of wall turbulence. However, as a basis for this discussion, the body of knowledge regarding the underlying structure of smooth-wall turbulence is summarized first.

#### Structure of smooth-wall turbulence

The results of many recent experimental and computational studies suggest that smooth-wall turbulence is populated by hairpin vortices that tend to streamwise-align into larger-scale coherent groups termed vortex packets both in the near-wall region as well as the outer layer. The phrase “hairpin vortex” is used herein to describe both symmetric and asymmetric hairpin-, lambda- and arch-like structures that are composed of either one or two streamwise-oriented legs connected to a spanwise-oriented head whose rotation is of the same sense as the mean shear. These structures are qualitatively consistent with the horseshoe vortex first proposed by Theodorsen (1952).

At low  $Re$ , Smith (1984) reported the existence of hairpin vortices and suggested an organized alignment of these structures in the streamwise direction. Smith *et al.* (1991) later showed that hairpin vortices can regenerate from an existing vortex. Similar organization and regeneration was noted by Zhou *et al.* (1999) who studied the evolution of an initial hairpin-like structure in the mean turbulent field of a low- $Re$  channel via direct numerical simulation (DNS). Given sufficient strength of the initial structure, multiple hairpin vortices were spawned both upstream and downstream of the initial structure, creating a coherent train of vortices. The legs of vortices residing in the log layer were commonly observed to extend below  $y^+ \equiv y/y_* = 60$  ( $y_*$  is the viscous length scale), consistent with the near-wall quasi-streamwise vortex observations of Brooke & Hanratty (1992) and Schoppa & Hussain (2000), among others. Zhou *et al.* (1999) also observed a preference for asymmetric hairpins, with one leg often stronger than the other. The stereoscopic visualizations of Delo *et al.* (2004) complement these efforts by providing three-dimensional views of this organization at low  $Re$ . Their results highlight the contorted nature of the vortices that agglomerate to form larger-scale structures and further support the coupling between ejections of low-speed fluid away from the wall and the passage of large-scale motions.

Head & Bandyopadhyay (1981) observed ramp-like patterns at the outermost edge of a turbulent boundary layer at higher  $Re$  and proposed these patterns to be the imprint of groups of hairpin vortices inclined away from the wall. More recent particle-image velocimetry (PIV) measurements at moderate  $Re$  in a turbulent boundary layer by Adrian *et al.* (2000) provide evidence that hairpin structures occur throughout the outer layer and streamwise-align to create larger-scale vortex packets. The PIV data permitted visualization of this organization in the streamwise-wall-normal plane within the interior of the boundary layer, showing that packets occur throughout the outer region in a hierarchy of scales. This scale hierarchy is consistent with the mechanisms proposed by Perry & Chong (1982), and Tomkins & Adrian (2003) provide direct evidence of spanwise scale growth via merging on an eddy-by-eddy basis up to  $y^+ = 100$  and propose scenarios by which this scale growth might manifest itself for  $y^+ > 100$ . In addition, the efforts of Liu *et al.* (2001) and Ganapathisubramani *et al.* (2003) underscore the important role these large-scale motions play in log-layer transport processes.

When sliced in the streamwise-wall-normal plane, the heads of hairpin vortices appear as spanwise vortex cores with  $\omega_z < 0$ , where  $\omega_z$  is the fluctuating spanwise vorticity (Spanwise vortices for which  $\omega_z < 0$  are hereafter termed ‘prograde’ since their rotation is in the same sense as the

mean shear). The streamwise-aligned heads of hairpins within a packet form an interface slightly inclined away from the wall, beneath which there exists a large-scale region of streamwise momentum deficit collectively induced by the vortices. Of particular importance, this collective induction generates large-scale ejections of low-speed fluid away from the wall which contribute significantly to the Reynolds shear stress. Recent work by Wu & Christensen (2006a) found that the largest populations of prograde spanwise vortices, most of which bear spatial signatures consistent with hairpin heads, occur in the region  $y < 0.3\delta$ . However, significant numbers of retrograde spanwise vortices, positive  $\omega_z$  cores, were also observed, with their largest populations noted at the outer edge of the log layer. Observations of retrograde spanwise vortices have been reported by Falco (1977), Falco (1983) and Falco (1991), among others, and their occurrence spatially-coincident to prograde spanwise vortices in the outer layer of wall turbulence is often interpreted as the imprint of ring-like structures. More recently, Klewicki & Hirschi (2004) reported observations of hairpin vortices and retrograde structures clustered in the neighborhood of intense near-wall shear layers, with the influence of retrograde structures increasing with Reynolds number. Finally, Natrajan *et al.* (2007) performed a detailed investigation of the spatial signatures of outer-layer retrograde spanwise vortices, particularly their propensity to occur spatially-coincident with prograde cores, and reported that such patterns are also consistent with slicing through omega-shaped hairpin structures. It should be noted that the existence of ring-like vortices is not inconsistent with the hairpin-vortex model as the origin of ring-like structures in wall turbulence has been related to the pinch-off and reconnection of the legs of existing hairpin structures (Moin *et al.*, 1986; Smith *et al.*, 1991; Bake *et al.*, 2002, for example).

When sliced in the streamwise–spanwise plane within the log layer, hairpin packets appear as elongated regions of streamwise momentum deficit (low momentum regions) bounded on either side by wall-normal vortex cores roughly aligned in the streamwise direction. Tomkins & Adrian (2003) and Ganapathisubramani *et al.* (2003) interpreted these wall-normal vortex cores as slices through the inclined legs/arches of the hairpin structures and reported that many of these cores occur in isolation. This observation is counter to the expectation of spanwise-separated vortex pairs when slicing through symmetric hairpin structures, supporting previous observations of a preference toward asymmetric structures (Zhou *et al.*, 1999). Most recently, Hutchins & Marusic (2007) found that these log-layer low-momentum regions often identified in  $\delta$ -scale PIV realizations actually extend significantly longer ( $10 - 20\delta$ ) in the streamwise direction and often meander significantly in the spanwise direction of the flow. Previous studies have shown scales of this streamwise extent to be quite energetic (can contain half of the turbulent kinetic energy) and accountable for a majority of the Reynolds shear stress within the logarithmic region (Kim & Adrian, 1999; Guala *et al.*, 2006).

#### Roughness effects in the near-wall region

The effects of roughness on the structure of the near-wall region (i.e., the roughness sublayer) has been studied extensively both experimentally and computationally. Perry *et al.* (1969) used flow visualization to discover that the eddy structures are qualitatively different for flow over “*k*-type” versus “*d*-type” grooves. For “*d*-type” roughness, since the groove elements were approximately square, a stable eddy was maintained inside the grooves and shedding from the elements was found to be negligible. However, for “*k*-type” roughness the eddies were observed to re-attach before encountering the next element, resulting in the shedding of eddies above the roughness. The structures generated in this manner had length scales proportional to the roughness height “*k*” and were found to blend into the outer flow farther away from the roughness. Subsequent flow visualization studies of individual grooves by Liou *et al.* (1990) and Djenidi *et al.* (1994) provide additional evidence supporting these observations.

The rough-wall study of Grass (1971) in a free-surface channel flow using hydrogen bubbles clearly identified the differences of near-wall ejection and inrush (sweep) events between smooth and rough walls (sand and rounded pebbles). While both ejection and inrush events were commonly observed under both smooth and rough conditions, the former were found to be extremely violent over rough walls. Furthermore, the long streamwise vortices which were readily apparent close to the smooth wall were much less apparent in the case of roughness.

Bandyopadhyay & Watson (1988) presented different models of vortices for flow over two- and three-dimensional roughness, particularly with respect to the effect of the spanwise aspect ratio of the roughness on turbulent boundary layers. The authors argued that in the near-wall region of flows over a smooth wall and 2D roughness, the shear stress is transported outward and this effect can be attributed to the presence of hairpin vortices alone. In contrast, for flows over 3D roughness, the shear stress is often transported inward toward the wall—an effect that cannot be explained by hairpin vortices alone. As such, the authors postulate the presence of additional necklace vortices that remain parallel to the surface and straddle over the roughness elements as the driving mechanism behind this outward transport of shear stress.

As a follow-up to their earlier rough-wall studies, Grass *et al.* (1993) employed three-dimensional hydrogen bubble visualization to measure three-dimensional velocity fields in the vicinity of  $k$ -type spanwise stripes in open channel flow. The 3D vortex lines computed from the velocity information revealed the vortical structures over this rough wall to be horseshoe-like, consistent with smooth-wall boundary layers. These horseshoe vortices were found to exist between the wall and the flow surface and they contributed significantly to the Reynolds shear stress. These observations provides experimental support for the structural model of Bandyopadhyay & Watson (1988) for 2D roughness.

Grass *et al.* (1993) performed a second experiment for flow over closely-packed spheres with surface conditions ranging from smooth to fully rough. Flow visualizations indicated that the rough-wall flow was able to re-order itself in relatively close wall-normal proximity to the roughness elements. In particular, in the immediate vicinity of the roughness, the motion of the hydrogen bubbles indicated highly disturbed flow induced by the roughness, in stark contrast to the well-ordered near-wall streaks commonly observed for smooth-wall flow. However, slightly further above this roughness-dominated region, the visualization traces indicated the reappearance of coherent streaks with a spanwise spacing that scaled with the characteristic roughness height ( $k$ ).

Pearson *et al.* (1998) studied the effect of a short strip of sandpaper on the structure of a low-Re turbulent boundary layer. Flow visualization revealed that the streaks generated by quasi-streamwise vortices were broken when the flow encountered the roughness strip but reappeared following passage over the strip. In addition, the streamwise extent of the two-point streamwise velocity correlation coefficient,  $\rho_{uu}$ , decreased significantly over the roughness strip while its spanwise extent increased. Although the overall shape of  $\rho_{uv}$  was unaffected compared to smooth-wall flow, its streamwise extent was also decreased by the short strip of roughness.

Djenidi *et al.* (1999) studied the near-wall structure of a turbulent boundary layer over  $d$ -type transverse square cavities using laser-induced fluorescence (LIF) in a streamwise–spanwise plane positioned  $6y_*$  above the roughness crests at  $Re_\theta = 1100$ . Low-speed streaks similar to smooth-wall flow were observed over this rough surface. In addition, three other characteristic events were also observed in the vicinity of the surface at a fixed spanwise position: outflows from the cavities, inflows into the cavities, and skimming of the overlying flow over the cavities. Interestingly, the streaks did not appear to be disturbed by the outflows, likely because the outflow was either not strong enough or the length scale of outflow was significantly smaller than that of the streaks. Further investigation led the authors to conclude that the outflows were actually triggered by the pressure fluctuations generated by quasi-streamwise vortices. Additionally, the outflows were

found to alternate with inflows along the span of the cavities, which could be explained by the alternating low-speed and high-speed streaks formed by quasi-streamwise vortices. Finally, this study postulated that the mechanism for sustaining turbulence over *d*-type roughness is closely related to vorticity generation in a manner similar to smooth-wall flow.

Ligrani *et al.* (2001) used flow visualization to study the structure of channel flow with dimples on the bottom wall at Reynolds numbers (based on channel height,  $H$ ) from 600 to 11,000 for various ratios of channel height to dimple diameter  $H/D$ . They found that a primary vortex pair was shed periodically from the center region of each dimple followed by inflow into the dimple cavity. It was also found that with decreasing  $H/D$ , the strength of the primary vortex pair increased and two additional secondary vortex pairs, formed near the edge of the dimples, became stronger and larger. These primary and secondary vortex pairs were found to be closely related to enhancement of Reynolds normal stresses.

Nakagawa & Hanratty (2003) studied the flow patterns of turbulent channel flow with a wavy bottom wall whose equivalent sand roughness height ranged from 7 to 104. The flow was visualized by injecting dye or a surfactant-polymer mixture at the trough and crest of the wavy wall. It was observed that the dye injected at the top of the crest in a fully rough flow dissipated rapidly, indicative of intense turbulent motions. In contrast, the dye injected at the crest for intermediate roughness formed a recirculation region whose position varied in time. Finally, the dye injected from the crest in the hydraulically smooth flow did not show any recirculation region. With respect to polymer injection, fully-rough flow was capable of expelling polymer a large distance away from the wall due to ejections originating in the trough regions.

The effects of roughness on the near-wall structure of turbulence has also been studied extensively via computations. Orlandi *et al.* (2003) performed a direct numerical simulation (DNS) of turbulent channel flow with wall velocity disturbances and observed a reduction in drag when a non-zero streamwise velocity fluctuation,  $u'$ , is applied. In contrast, channel flow with a non-zero spanwise velocity fluctuation,  $w'$ , was found to be similar to undisturbed channel flow. Of particular interest, the authors found that applying a non-zero wall-normal velocity fluctuation,  $v'$ , yielded structural changes similar to those observed over a rough surface. For example, at  $y^+=15$ , the two-point velocity correlations indicated that the streamwise length of the streaks was reduced for both  $v'$  and  $w'$  disturbances. In the spanwise direction, velocity correlations with  $v'$  perturbation were found to lack well-defined minima as in the undisturbed case, indicating that the high- and low-speed streaks were less discernable in the vicinity of the roughness. Contours of streamwise velocity in the streamwise–spanwise plane confirmed these inferences.

Cui *et al.* (2003) provided a detailed description of the instantaneous turbulent structure of channel flow with one wall roughened with *k*-type rib roughness using large-eddy simulation (LES) at a Reynolds number (based on the bulk velocity and half-channel height) of 10,000 and  $k_s^+ = 1891$ . Frequent spanwise motions were observed in front of the base of the ribs due to the blockage effect of the roughness. Just above the crest of the ribs, the streamwise velocity was higher and there were few spanwise motions although weak separation zones were still observed beyond the cavities between the ribs. At  $y/H = 0.25$ , reversed flow vanished but stronger flow fields were still found to be concentrated above the ribs. Above the channel's center, the velocities correlated little with the rib positions. In the streamwise–wall-normal plane, multiple separation regions of differing size and strength were observed both in front of and behind the ribs. Inflows into the cavities and outflows that brought low-momentum fluid into the outer region were found to be generated by the circulation created by the above-mentioned separation regions. In the spanwise–wall-normal planes, strong quasi-streamwise vortices were noted directly above the roughness crests.

The structure of turbulent channel flow over regular three-dimensional roughness elements ("egg-carton") on one wall was investigated by Bhaganagar *et al.* (2004) by DNS at  $Re_\tau=400$  and

$k_s^+=48$ . When the separation in the spanwise direction was normalized by the channel half height, streamwise and wall-normal velocity correlation coefficients ( $\rho_{uu}$  and  $\rho_{vv}$ ) computed in streamwise-spanwise planes positioned at  $y^+ = 30$  and 80 showed little difference. This result indicated that neither the average streak spacing nor the diameter of the streamwise vortices was affected by this particular surface roughness in outer units. However, when the separation distance was normalized in inner units, the rough-wall correlations at  $y^+ = 30$  revealed that the streak spacing increased to  $140y_*$  (compared to  $100y_*$  for smooth-wall flow) and the average diameter of the streamwise vortices increase to  $45y_*$  (compared to  $30y_*$  for smooth-wall flow). The streamwise extents of these structures were also studied using  $\rho_{uu}$  and  $\rho_{vv}$  in the streamwise direction. The length of the streaks was found to be decreased by the roughness in outer units but remained relatively unchanged in inner units. Contours of streamwise velocity at  $y^+=5$  supported these observations. Finally, the authors surmised that the self-sustaining mechanism of near-wall turbulence for the rough-wall case is still due to the linear coupling term between the wall-normal velocity and wall-normal vorticity as is true in smooth-wall flow.

Ashrafiyan *et al.* (2004) also performed a DNS of rough-wall turbulent channel flow, but at  $Re_\tau=400$  with both walls roughened by  $k$ -type 2D square rods (the flow was transitionally rough with  $k^+ = 13.6$ ). This simulation revealed elongated low-speed streaks similar to those in smooth-wall channel flows at  $y^+ = 20$ . Three-dimensional vortical structures were extracted from the background turbulence and were found to be more complex in the near-wall region compared to the quasi-streamwise vortices commonly observed in smooth-wall flow. In particular, incoherent spanwise vortices were observed to be shed from the crests of the rods, generating a highly three-dimensional flow in the vicinity of the roughness elements. Nevertheless, low-speed streaks still persisted in the presence of this highly-perturbed environment.

Finally, Sen *et al.* (2007) applied snapshot POD to a DNS of channel flow with 3D egg-carton roughness elements at  $Re_\tau = 180$ . Their one-dimensional analysis revealed a slower convergence of the POD energy for rough-wall flow due to a larger range of dynamically-important length scales. In addition, they used the first few POD modes to reconstruct the Reynolds stresses and found that the first 10 modes were sufficient for capturing both the location and the amplitude of the peak of the root-mean-square (RMS) streamwise velocity. Two-dimensional POD results in the wall-normal–spanwise plane revealed a decreased spanwise length scale for the first mode but a increased spanwise length for the second mode in the rough-wall flow when compared with the smooth-wall flow. A similar trend was also noted for the first two POD modes in the streamwise–wall-normal plane.

### Roughness effects in the outer layer

While a good deal of effort has been put forth studying the effect of roughness in the immediate vicinity of the surface, its impact on the outer-layer structure has also been evaluated. Bessm & Stevens (1984) studied the inclination angle of large-scale structures in a turbulent boundary layer over a  $k$ -type grooved surface via measurements of the cross-correlation between the wall shear stress and streamwise velocity for  $0.05 < y/\delta < 0.75$ . An inclination angle of approximately  $20^\circ$  was observed which is consistent with the results of Brown & Thomas (1977) and Head & Bandyopadhyay (1981) for smooth-wall turbulence. This angle is also consistent with the inclined interfaces of large-scale hairpin vortex packets observed in smooth-wall turbulence (Adrian *et al.*, 2000; Christensen & Adrian, 2001, among others).

The outer-layer structural consistency between smooth- and rough-wall flow observed by Bessm & Stevens (1984) is in accordance with the many aforementioned studies that support the proposition of outer-layer similarity in the turbulence statistics for rough-wall turbulence. In support

of this similarity, many other studies have observed little difference in the spatial velocity correlations of smooth- and rough-wall flow outside the roughness sublayer. Nakagawa & Hanratty (2001) reported two-point streamwise velocity correlation coefficients computed from ensembles of instantaneous velocity fields acquired by particle image velocimetry (PIV) in channel flow with a wavy bottom wall ( $\delta/k \approx 60$ ) and found that neither their length scale nor their inclination angle were altered in the presence of the wavy surface. Sabot *et al.* (1977) studied pipe flow roughened with spanwise fences ( $\delta/k = 15$ ) and found the streamwise integral length scales of the streamwise and wall-normal velocities to change little from smooth-wall pipe flow. More recently, Volino *et al.* (2007) concluded that the outer-layer structure for flow over a fully-rough woven mesh ( $\delta/k = 71$ ) is similar to that observed in smooth-wall flow by comparing velocity spectra and two-point correlations in both flows. Similar structural consistencies in the outer layer were also observed in a recent direct numerical simulation (DNS) of channel flow with disturbed walls by Flores *et al.* (2007).

The strongest challenge to the possibility of similarity in the outer-layer structure of rough-wall turbulence comes from Krogstad & Antonia (1994). This effort involved the use of X-wire probes to measure streamwise and wall-normal velocity components in a turbulent boundary layer over wire mesh ( $\delta/k \approx 50$ ,  $\delta/k_s \approx 15$ ,  $k^+ = 92$ ,  $k_s^+ = 331$ ). Using this data, Krogstad & Antonia (1994) found that the inclination angle of  $\rho_{uu}$  increased considerably to  $38^\circ$  for flow over the mesh surface. In addition, they reported a decrease in the streamwise extent of velocity and vorticity spatial correlations compared to flow over a smooth wall but found little difference in the spanwise extent of these correlations. It should be noted that Nakagawa & Hanratty (2001) postulated that such effects may not be physical but rather artifacts associated with the use of a convection velocity to infer spatial information from temporal hot-wire data. In addition, Flack *et al.* (2005) indicated that the rough-wall flow of Krogstad & Antonia (1994) may not satisfy the criteria necessary for the existence of outer-layer similarity ( $\delta/k \approx 50 > 40$  but  $\delta/k_s \approx 15 < 40$ ).

Finally, Gunther & von Rohr (2003) performed POD of the velocity field measured by PIV in a developed flow between a sinusoidal bottom wall and a flat top wall at Reynolds numbers (based on bulk velocity and half-height of the channel) of 3800 and 7300. They found that the dominant eigenfunctions have a characteristic spanwise scale of about 1.5 times the wall wavelength,  $\Lambda$ . Smaller structures obtained from the POD analysis were observed at locations with maximum Reynolds shear stress. In a follow-up study, Kruse *et al.* (2003) studied the dynamics of these large-scale structures with a spanwise scale of  $1.5\Lambda$ . The meandering motion of these large-scale structures was followed over 6 seconds as they convected downstream approximately  $65\Lambda$ . These structures provided a mechanism of momentum and scalar transport between the wavy-wall and the bulk flow. The streamwise extent of the large coherent structures was found to be significantly larger than the streamwise domains of typical LES and DNS simulations.

To summarize, it appears that roughness has a significant impact on the near-wall structure of the flow, but that this influence is quite specific to the roughness under consideration. In particular, streaks are still observed in the vicinity of rough walls, although their streamwise and spanwise extents can be modified considerably compared to smooth-wall flow. With respect to the outer layer, some studies indicate substantial similarity between smooth- and rough-wall flow primarily via studies of spatial correlations, although there is still some evidence that subtle differences may exist. However, the exact impact of roughness on outer-layer vortex organization in the form of hairpin vortex packets has received considerably less attention even though such structures play a pivotal role in momentum transport in the outer layer.

#### 1.2.4 Studies of turbulent flow over irregular roughness

It should be noted that the vast majority of the literature summarized above dealt with highly idealized roughness topographies (simulated roughness), like sandgrain,  $k$ - or  $d$ -type transverse bars, wire mesh, etc. These surfaces are typically characterized by a single roughness scale. However, most practical rough surfaces are both irregular in shape and random in roughness element distribution like marine biofouled surfaces or the surface of gas turbine blades which can be roughened by pitting/erosion, spallation and/or deposition of foreign materials. It is not at all clear whether idealized roughness studies can predict the behavior of more practical roughness topographies. Differences between real and simulated roughness have been known for several decades, most notably the obvious differences between Nikuradse's results for sand grain roughness and Colebrook's correlation for friction factor based on "industrial" or real roughness in the transitionally rough regime. There are very few detailed studies of real roughness and they are briefly summarized here.

Acharya *et al.* (1986) studied the influence of four rough surfaces on a turbulent boundary layer. The four surfaces included a stochastically rough surface representative of a newly-finished turbomachinery blading, a variant of this surface with different roughness parameters, a sand-cast surface and a mesh surface. Roughness functions revealed that the turbulent flows over these surfaces fall largely in the transitionally rough regime. The velocity defect profiles at different measurement positions in the streamwise direction over the sand-cast surface showed a larger scatter in the outer region as compared to flow over the other rough surfaces studied. Measurements of Reynolds stresses along the streamwise direction over each rough surface revealed good agreement supporting outer-layer similarity, although cross comparison between different surfaces was not provided. It was shown that the wall shear stress over roughness is a function of both  $Re_\theta$  and surface roughness type. A universal skin-friction correlation was attempted using classical rough-wall boundary theories (including a universal velocity defect law, log-law, and expression for  $k$ -type roughness function) but the derived correlation appeared to depend strongly on the surface conditions.

Bons *et al.* (2001) studied the surface characteristics of a number of in-service land-based turbine blades and vanes. Turbine-blade roughness accumulates over time and is due to a number of different damage mechanisms, including deposition of foreign materials, pitting/erosion, and thermal barrier coating (TBC) spallation. It was observed that these different roughness-generating mechanisms create very distinct roughness signatures. Bons *et al.* (2001) concluded that it is not likely that a single roughness scale, like cones, spheres and cylinders, etc., will effectively represent the wide range of roughness scales observed in real roughness. In a follow-up study, Bons (2002) used scaled replicas of turbine-blade roughness in a turbulent boundary layer to investigate the effects of highly-irregular roughness on heat transfer and skin friction coefficients. Two of the six rough surfaces studied had  $k^+ < 1$ , indicating that they should behave as hydraulically smooth. However, the skin friction coefficients for these two surfaces were found to be larger than the smooth-wall case. The other four rough surfaces had roughness heights that were several times the boundary layer momentum thickness so that they were more like bluff bodies. This work revealed that historical correlations for heat transfer and skin friction severely underestimated the influence of real roughness in the transitionally rough regime.

Subramanian *et al.* (2004) extended the work of Bons (2002) by considering the turbulent statistics over a short strip of turbine-blade roughness in the turbulent boundary layer. Their approach did not follow the conventional rough-wall boundary layer theory by using  $u_\tau$  as the characteristic velocity scale of the flow. Instead, the authors proposed a pressure-gradient velocity scale to capture the pressure effects induced by roughness on the inner-layer properties. Skin friction velocity was argued not to be a meaningful velocity scale since strong roughness may diminish the viscous effects. However, this argument may not be soundly grounded since skin friction velocity

is actually derived from wall shear stress and wall shear stress exists with larger magnitude in the presence of strong roughness even though the viscous contribution is negligible. Further, the boundary layer certainly had not achieved self-similarity due to the short length of the roughness and thus whether the pressure gradient velocity defined in this study is an appropriate velocity scale in the equilibrium rough-wall boundary layer is still in question.

Finally, Allen *et al.* (2007) studied turbulent pipe flow in the presence of a honed surface akin to the “industrial”-type roughness used by Colebrook (1939) in the formulation of the widely-used Moody chart. However, their friction-factor results displayed strong deviation from the Colebrook relationship and instead mimicked the friction-factor trends of Nikuradse’s sand-grain experiments. Allen *et al.* (2007) also presented smooth- and rough-wall mean velocity defect profiles, streamwise turbulence intensity profiles and streamwise velocity spectra that collapsed in the outer layer in accordance with Townsend’s wall similarity hypothesis. These outer-layer similarity observations represent the first of their kind for a more practical surface topology but for extremely large separation between the roughness and outer length scales ( $\delta/k \sim 51000$ ;  $\delta/k_s \sim 17000$ ).

### 1.3 Present effort

The present effort investigates the effects of highly-irregular roughness replicated from a turbine blade damaged by deposition of foreign materials on the statistical and structural characteristics of wall turbulence. Understanding such influences is pivotal for devising efficient and effective modeling and control strategies for technologically relevant flows that suffer from such effects. Two-dimensional particle image velocimetry (PIV) measurements are performed in the streamwise-wall-normal plane of turbulent boundary layers at  $Re_\theta \approx 8000$  and  $13000$ . The surface conditions include a smooth-wall baseline and two highly-irregular rough walls. These two rough surfaces have the same roughness topography but differ in spatial scaling (one is scaled by a factor of two in all three spatial dimensions compared to the other). The validity of Townsend’s wall similarity hypothesis in the presence of practical roughness is assessed and the impact of this roughness on the spatial structure of the flow is investigated. In addition, stereoscopic PIV measurements are made in streamwise-spanwise planes of smooth- and rough-wall turbulent boundary layers both within and at the outer edge of the roughness sublayer at the  $Re_\theta$  noted above. This data is used to explore the impact of dominant topographical features on the near-wall flow as well as the influence of practical roughness on the spatial organization of the flow within the roughness sublayer and in the log layer. *Understanding such effects provides a stepping stone toward efficient modeling and control of practical wall-bounded flows in the presence of highly-irregular roughness, particularly in assessing the usefulness of models and control strategies devised from studies of canonical, smooth-wall turbulence.*

Preliminary experiments involving a short streamwise fetch of turbine-blade roughness in channel flow are summarized in section 2<sup>†</sup>. The remaining sections are then devoted to the wind-tunnel experiments described briefly above that form the vast majority of this effort. The flow facility, characteristics of the rough-wall topography and details of the PIV measurements undertaken are described in section 3. Section 4 assesses the possibility of outer-layer similarity in the turbulence statistics for flow over highly-irregular roughness<sup>‡</sup> while section 5 describes the impact of dominant topographical features of the roughness on the near-wall flow<sup>§</sup>. Finally, section 6 provides an in-depth comparison between the structural characteristics of flow over the highly-irregular roughness under consideration and smooth-wall turbulence both below and within the log layer<sup>¶</sup>.

---

<sup>†</sup>Appeared in *AIAA J.* **44** (12), 3098-3106.

<sup>‡</sup>Appeared in *Phys. Fluids* **19** (8), 085108.

<sup>§</sup>Portions appeared in AIAA Paper 2007-3995. To be submitted for journal publication soon.

<sup>¶</sup>Portions appeared in AIAA Paper 2008-0648. To be submitted for journal publication soon.

## 2 Preliminary experiments involving a short fetch of roughness

This section describes preliminary particle image velocimetry (PIV) measurements made in turbulent channel flow with a smooth surface and with a short streamwise fetch ( $\sim 10h$ , where  $h$  is the channel half-height) of roughness replicated from a turbine blade damaged by spallation. These initial experiments were performed in order to fine-tune the quality of the optical data acquired by PIV in the presence of highly-irregular surface conditions and to observe the flow transition from smooth- to rough-wall flow. Both of these factors required consideration before beginning the main wind-tunnel measurements.

### 2.1 Introduction

It is well known that an abrupt transition from smooth-to-rough surface conditions in a wall-bounded flow promotes the formation of an internal roughness layer that grows in thickness downstream (Smits & Wood, 1985). In such situations, the turbulence intensities and Reynolds shear stress are unaffected except within the internal layer where they can be altered significantly by the surface roughness (Antonia & Luxton, 1971; Andreopoulos & Wood, 1982, among others). Such abrupt transitions occur frequently in actual engineering systems where the surface conditions can vary significantly in the dominant flow direction. Many studies have been performed in the presence of rather idealized roughness conditions, like sandgrain, ordered arrays of elements and woven mesh. However, roughness encountered in most practical engineering applications is quite distinct from these idealized roughness models. The surface conditions in such flows can degrade over time, from hydraulically smooth prior to deployment to significantly roughened over time due to harsh operating conditions, like damage imparted to turbine blades (Bons *et al.*, 2001; Bons, 2002) or cumulative algae/barnacle buildup on the surfaces of submarines and ships (Karlsson, 1980), for example. In the case of damaged turbine blades, surface roughness is attributable to deposition of foreign materials, pitting, and spallation, rendering the surface conditions highly non-uniform. As such, a single roughness type and scale cannot be expected to be a sufficient representation of real roughness. In particular, Bons (2002) used scaled replicas of turbine-blade roughness in turbulent boundary layer studies and found that classical rough-wall scalings for skin friction derived from simulated roughness do not hold for some real roughness conditions. Therefore, it is not clear whether studying the influence of idealized roughness conditions on wall-bounded turbulence will be sufficient for successfully modeling and controlling flows of practical engineering interest in which the surface conditions are less than ideal.

Quadrant analysis, first introduced over thirty years ago (Wallace *et al.*, 1972; Lu & Willmarth, 1973), allows one to investigate the strongest Reynolds-stress-producing events in turbulent flows. This method decomposes the mean Reynolds shear stress,  $\langle uv \rangle(y)$ , outside of a hyperbolic hole region of size  $H$  into four distinct Reynolds-stress-producing events based on the quadrant in the  $u - v$  plane,  $Q$ , in which they reside. These events include outward interactions ( $Q_1$ :  $u > 0$ ,  $v > 0$ ), ejections ( $Q_2$ :  $u < 0$ ,  $v > 0$ ), inward interactions ( $Q_3$ :  $u < 0$ ,  $v < 0$ ) and sweeps ( $Q_4$ ;  $u > 0$ ,  $v < 0$ ). This decomposition methodology has been used extensively to study the Reynolds-stress-producing events in turbulent boundary layers as well as turbulent channel and pipe flows. In the wall region of a smooth-wall turbulent channel flow, Wallace *et al.* (1972) found that ejections and sweeps represented the dominant Reynolds-stress-producing events, with each contributing nearly 70% to the total Reynolds stress at  $y^+ \simeq 15$  while inward and outward interactions each yielded 20% contributions. Their results also indicated that below  $y^+ \simeq 15$  the sweeps and outward interactions were more dominant while outside this region ejections and inward interactions became more important contributors. By comparing the joint probability density distributions of the streamwise ( $u$ ) and wall-normal ( $v$ ) fluctuating velocities with the Reynolds-

stress-contribution distributions, Wallace & Brodkey (1977) concluded that most of the Reynolds stress is generated by the large, energetic motions. Teitel & Antonia (1990) applied quadrant analysis to investigate the interaction region of a turbulent channel flow and their results indicated that ejections originating on one side of the centerline can often reach the opposing wall. Finally, Sabot & Comte-Bellot (1976) studied the intermittent coherent structures in the core region of a smooth-wall turbulent pipe flow and determined that ejections dominated the wall region.

Quadrant analysis has also been used to assess differences between the Reynolds-stress-producing events in smooth- and rough-wall flows. Grass (1971) investigated intermittent ejections and sweeps in rough-wall boundary layers using hydrogen bubble visualization and found that the entrainment of low momentum fluid trapped between the roughness elements was much more violent than the entrainment of smooth-wall viscous sublayer fluid. Raupach (1981) observed that sweeps accounted for most of the turbulent stress near rough surfaces and that the relative magnitude of the sweep component increased both with surface roughness and with proximity to the surface. Similarly, Krogstad *et al.* (1992) observed that contributions from sweeps were significantly greater over rough surfaces (wire mesh) than over smooth surfaces, particularly in the near-wall region. They also found that strong ejections and sweeps occurred almost twice as frequently in the presence of surface roughness. More recently, Demare *et al.* (1999) observed that ejections accounted for 80% of the total Reynolds stress for flow over a smooth wall but only 60–65% in the presence of a rough wall composed of two-dimensional square bars. Further, recent direct numerical simulations (DNS) and experiments by Krogstad *et al.* (2005) in a channel flow roughened on both walls with square bars showed little influence of roughness on the Reynolds stress outside the roughness sublayer ( $y > 5k$ ), particularly in the ratio of ejection to sweep contributions for intermediate roughness heights. This behavior is consistent with the experiments of Flack *et al.* (2005) for flow over sandpaper and wire mesh where the ratio of ejections to sweeps was found to be insensitive to surface roughness in the outer layer. In contrast, the experiments of Nakagawa & Hanratty (2001) over wavy walls in channel flow indicate that this ratio is strongly influenced by surface roughness well outside the roughness sublayer for roughness heights beyond the intermediate regime. However, it should be noted that all of these studies involved long streamwise fetches of roughness (exceeding fifty outer length scales in all cited cases) for which the internal roughness layer grew sufficiently to occupy the entire wall-normal domain of the flow (streamwise fetches smaller than that required to achieve such behavior are necessarily classified as “short”).

The present effort assesses the Reynolds-stress enhancement associated with a short streamwise fetch of highly-irregular surface roughness replicated from a damaged turbine blade using quadrant analysis. Both the impact of highly-irregular surface conditions on wall turbulence as well as the character of rough-wall flow over short fetches of roughness have received little attention in the literature despite their vital importance in many practical engineering flows. These issues are therefore the focus of this work.

## 2.2 Experiment

The channel-flow facility used in the present effort has a development length of  $216h$  (where  $h = 25.4$  mm is the half-height of the channel) and an aspect ratio of 10.125:1, yielding two-dimensional flow along the channel’s spanwise centerline. The working fluid of the channel is air and the flow is suitably conditioned upstream of the channel entrance by a series of screens, honeycomb and a contraction. The flow is then tripped with 36-grit sandpaper, ensuring fully-developed conditions at the test section [The flow quality of this channel has been well documented in past turbulence studies (Christensen, 2001; Christensen & Adrian, 2001)]. Static pressure taps are mounted along the length of the channel’s development section to evaluate the wall shear stress,  $\tau_w$ . Density and viscosity are assessed from measurements of the atmospheric pressure and fluid temperature and

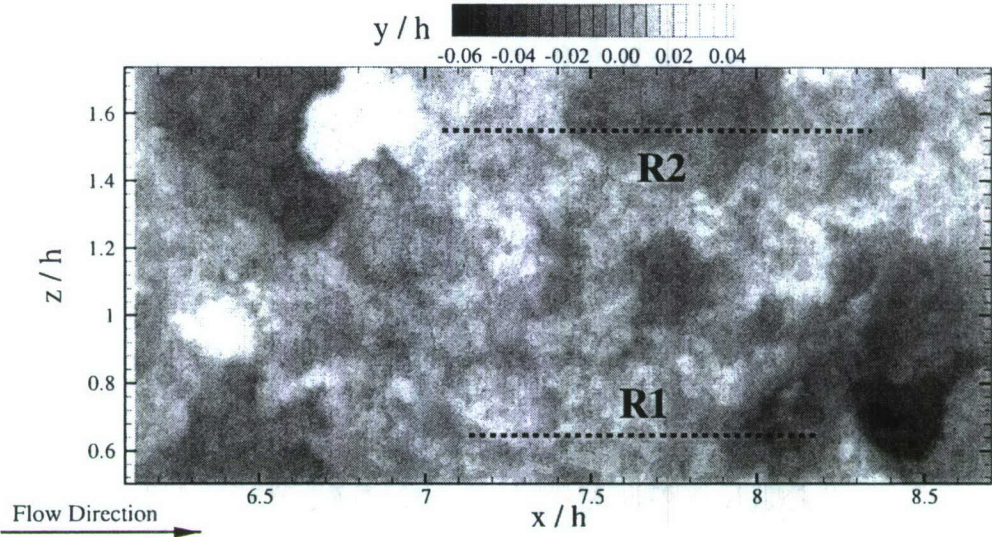


Figure 1: Contour plot of the surface topology of the replicated turbine-blade roughness. The abscissa indicates the position relative to the leading edge of the roughness panel and the dashed lines demarcate the streamwise–wall-normal planes where PIV measurements are made.

are then used to determine the smooth-wall friction velocity,  $u_\tau \equiv (\tau_w/\rho)^{1/2}$ , and the viscous length scale,  $y_* \equiv \nu/u_\tau$ .

The roughness studied herein is quite distinct from other roughness conditions presented in the literature, some of which are cited in the introduction. The present effort focuses on roughness replicated from a surface scan of a damaged turbine blade [denoted surface 3 in Bons (2002)]. The surface imperfections often encountered on these blades are attributable to deposition of foreign material, pitting, and spallation, all of which render the surface conditions highly non-uniform. Therefore, a single roughness type and scale, such as those extensively cited in the literature, cannot be expected to be a sufficient representation of this form of “real” roughness. This particular scan was chosen from the six scans discussed in Bons (2002) because it embodies both large- and small-scale topological features. Figure 1 presents a contour plot of the surface topology at the downstream end of the roughness insert, illustrating the highly non-uniform surface conditions. A file containing the topological data is input into a three-dimensional printer with  $80\text{ }\mu\text{m}$  resolution which constructs a physical replica of the roughness layer by layer. A smooth leading edge of length  $0.75h$  transitions the flow from the smooth- to rough-wall conditions and the surface topology is periodically-extended in both the streamwise and spanwise directions to fill the entire insert area, consistent with the replications of Bons (2002). The average peak-to-valley roughness height, often used as an estimate of  $k$  (Bons, 2002), is  $1.35\text{ mm}$ , yielding  $h/k = 18.8$ .

A new test section was designed and constructed allowing a roughness insert to be placed flush along the bottom wall of the channel. The surface roughness is first mounted on an cast aluminum plate which then rests upon three screws within the test section that allow one to adjust the mean elevation of the roughness to be coincident with the upstream smooth wall. The insert is  $10h$  long in the streamwise direction but spans the entire width of the channel. *As such, these measurements represent the influence of a short fetch of highly-irregular roughness on the character of fully-developed turbulent channel flow.* Further, while the roughness insert impedes optical access from below, such access is still achieved with glass windows embedded in the top and

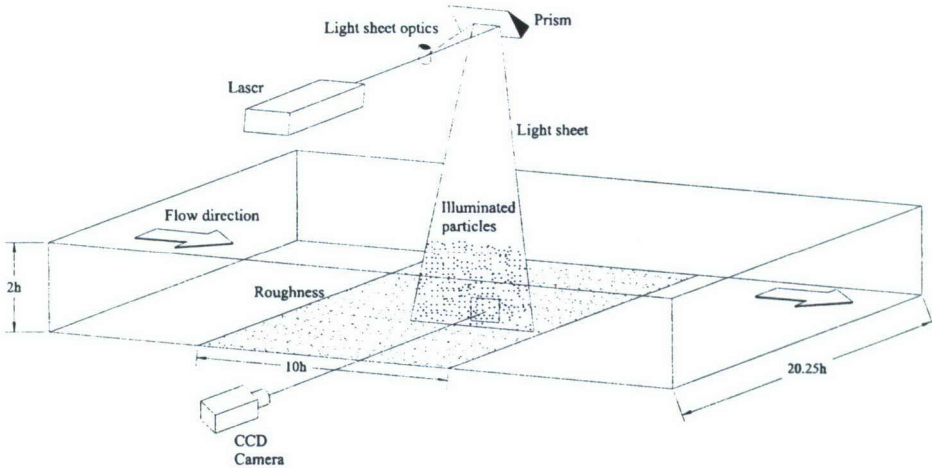


Figure 2: Schematic of experimental setup.

side walls of the channel (above and on both sides of the roughness insert, respectively). Smooth-wall measurements are achieved with an anodized cast aluminum plate inserted in place of the roughness panel. Figure 2 presents a schematic of the experimental arrangement.

Particle-image velocimetry (PIV) is used to measure two-dimensional velocity ( $\tilde{u}, \tilde{v}$ ) fields over an  $h \times h$  field of view in the streamwise–wall-normal plane along the channel’s spanwise center for smooth-wall conditions (SM) and two spanwise separated rough-wall positions (R1 and R2), the latter of which are illustrated in figure 1. These two spanwise positions were chosen to assess how distinct local surface features exert their influence upon the flow. Position R1 occurs over relatively small-scale roughness while position R2 is just downstream of a step in surface height from a large-scale, deep depression to a plateau. The air flow in the channel is seeded with  $1\text{ }\mu\text{m}$  olive-oil droplets, a dual-cavity Nd:Yag laser is used for illumination and the scattered light from the particles is imaged with an 8-bit  $1\text{k} \times 1\text{k}$  cross-correlation CCD camera. The pairs of PIV images are interrogated using two-frame cross-correlation methods with first-interrogation windows of size  $18 \times 18$  pixels (streamwise  $\times$  wall-normal) at 50% overlap to satisfy Nyquist’s criterion. These parameters yield vector grid spacings of  $\Delta = 18.9y_*^{SM}, 19.8y_*^{SM}$  and  $21.0y_*^{SM}$  in both the streamwise and wall-normal directions for cases SM, R1 and R2, respectively. A larger second window of  $24 \times 22$  pixels is chosen to minimize bias errors associated with loss of particle pairs and the second window is offset in the mean flow direction by the bulk displacement of the flow in order to further increase the fidelity of the correlation. The resulting vector fields are then validated using standard deviation and magnitude difference comparisons to remove any erroneous velocity vectors. On average, 97–99% of the velocity vectors in any given velocity realization are found to be valid, minimizing the need for interpolation of holes. Finally, each velocity field is low-pass filtered with a narrow Gaussian filter to remove noise associated with frequencies larger than the sampling frequency of the interrogation.

The measurements are performed at the same friction Reynolds number ( $\text{Re}_\tau \equiv u_\tau h/\nu$ ) based on the upstream smooth-wall flow conditions of approximately 1830. The roughness Reynolds number based on the viscous length scale of the upstream smooth-wall conditions,  $k^+ = k/y_*^{SM}$ , is 97 which is close to the fully-rough regime. This value of  $k^+$  is in fact a lower bound on the actual value of  $k^+$  because  $y_*$  over the roughness is expected to be smaller than  $y_*^{SM}$  since the wall

Experiment	$\text{Re}_\tau$	$u_\tau^{SM}$ (m/s)	$y_*^{SM}$ ( $\mu\text{m}$ )	$\Delta^+$	$k^+ = k/y_*^{SM}$	$h/k$
SM	1832	1.12	13.9	18.9	—	—
R1	1828	1.12	13.9	19.8	97	18.8
R2	1815	1.12	14.0	21.0	96	18.8

Table 3: Summary of flow parameters for all experiments.

shear stress, and hence  $u_\tau$ , would be enhanced by the roughness. However, an accurate measure of the wall shear stress over the roughness was not available and so the smooth-wall values are used as a baseline. Several thousand PIV realizations are acquired at each condition, ensuring proper convergence of single- and multi-point statistics. Table 3 summarizes the experimental parameters.

Prasad *et al.* (1992) showed that the random error associated with determining particle displacements in PIV is approximately 5% of the particle-image diameter. In the present study, the mean particle-image diameter is approximately 2 pixels, yielding a random error of 0.1 pixels. Therefore, since the time delay between the PIV images for a given experiment (13  $\mu\text{s}$  for cases SM and R1 and 14  $\mu\text{s}$  for case R2) is chosen to yield a bulk displacement of 10–12 pixels, this random error is less than 1% of the full-scale velocity. Furthermore, these random errors do not affect statistics of the velocity since they average to zero for a suitably large ensembles like those considered herein. One must also consider two sources of bias error that can appear in PIV measurements. Bias due to loss of image pairs is minimized in the present study since a larger second interrogation window and a bulk window offset are utilized during interrogation of the PIV images. Bias errors due to the peak-locking effect are also minimized in the present experiment since the particle-image diameters exceed 2 pixels (Westerweel, 1997; Christensen *et al.*, 2004). We therefore estimate the bias errors in our PIV measurements at 1% of the full-scale velocity (The reader is directed to Westerweel (1997), Christensen & Adrian (2002) and Christensen *et al.* (2004) for a more comprehensive discussion of PIV measurement errors).

## 2.3 Results and Discussion

### 2.3.1 Reynolds stress profiles

Figure 3 presents profiles of the Reynolds stress over smooth and rough walls as a function of wall-normal position. These profiles are computed from velocity ensembles exceeding 3500 statistically-independent realizations per condition. The lines in figure 3 represent ensemble- and streamwise-averaged profiles for the three cases while the symbols represent the ensemble-averaged profiles for case R2 at the upstream ( $x = 7h$ ) and downstream ( $x = 8h$ ) ends of the PIV field of view (to be discussed below). The wall-normal origin for the rough-wall cases is taken to be the mean elevation of the roughness, which is consistent with the streamwise–spanwise plane at which the wall shear stress appears to act, and the upstream smooth-wall friction velocity,  $u_\tau^{SM}$ , is used to normalize the Reynolds shear stress since an accurate measure of the local shear stress over the roughness was not available. As such, any collapse of the roughness profiles with the smooth-wall data does not imply outer-layer similarity but simply the existence of smooth-wall outer-layer conditions. The mean Reynolds stress profile from a direct numerical simulation (DNS) of smooth-wall turbulent channel flow at  $\text{Re}_\tau = 550$  is included in figure 3 and comparison with the smooth-wall PIV measurements indicates that the measurements slightly under-predict the mean Reynolds stress close to the wall. This under-prediction has been observed previously in PIV studies of smooth-wall channel flow (Christensen, 2001; Liu *et al.*, 1994) and is due to the spatial averaging associated with the coarser grid spacings of the PIV measurement ( $\sim 19y_*$  for the present cases) relative to the much finer grid

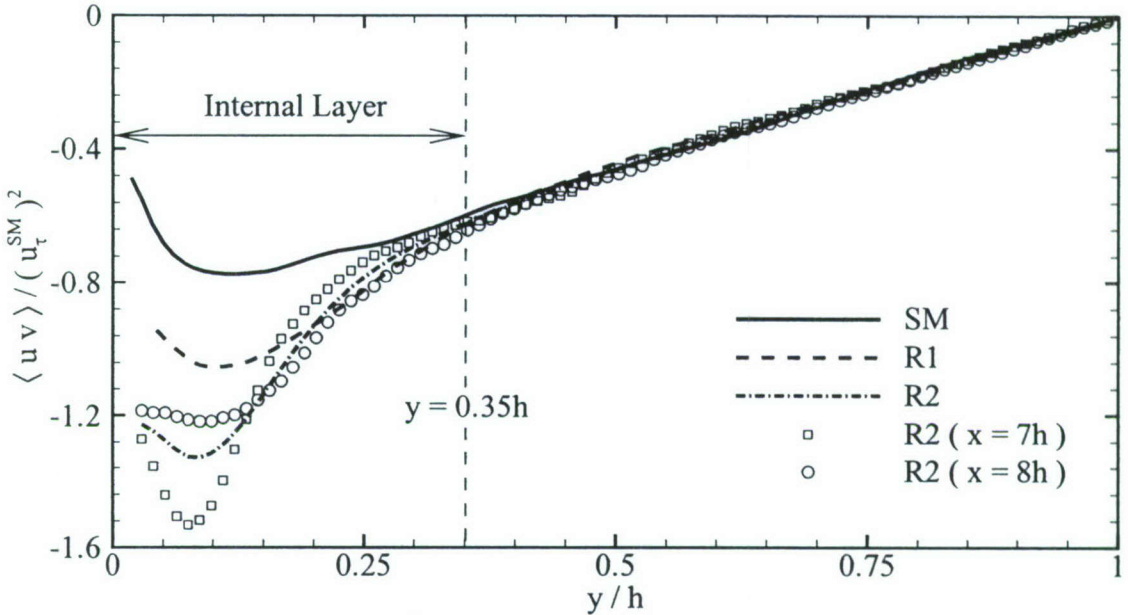


Figure 3: Mean Reynolds stress as a function of wall-normal position.

spacings achievable in DNS (A few  $y_*$  close to the wall).

When the smooth-wall profile is compared to the R1 and R2 profiles it is clear that an internal roughness layer has formed given the significant enhancement of the mean Reynolds stress in the presence of the replicated turbine-blade roughness. However, the internal roughness layer only protrudes to  $y = 0.35h$ , not even halfway to the centerline of the channel, even after nearly eight outer length scales of development downstream. It should be noted that the roughness results well-exceed the linear total stress profile expected in fully-developed, smooth-wall turbulent channel flow because they are normalized with the smooth-wall friction velocity (since independent measures of  $u_\tau$  for the rough-wall cases were not available). Therefore, the fact that the rough-wall profiles exceed the smooth-wall Reynolds-stress and linear total-stress profiles implies that the surface roughness has dramatically increased the local wall shear stress, yielding a commensurate increase in the rough-wall  $u_\tau$  compared to  $u_\tau^{SM}$ .

The R2 profiles highlight the strong influence that the local roughness topology can have on the flow. Recalling that the R2 measurements occur just downstream of a distinct step from a deep pocket to a plateau (near  $x = 6.75h$  in figure 1), the Reynolds stress at  $x = 7h$  for case R2 ( $\square$  symbols) is significantly enhanced compared to the smooth-wall results, case R1 (relatively fine-scale roughness) and even the R2 profile further downstream at  $x = 8h$  ( $\circ$  symbols). Examination of the ensemble-averaged Reynolds stress for the R2 case (figure 4) indicates that this abrupt step in surface roughness generates a thin, elongated region of intense Reynolds stress near  $x = 7h$ , with heightened levels of  $\langle uv \rangle$  extending at least  $1.25h$  downstream of the step. This region of enhanced Reynolds stress is most-likely associated with the wake generated by the abrupt, large-scale step in surface roughness noted earlier. This behavior is consistent with what has been observed in studies of arrays of discrete roughness elements where each element generates a wake that contributes significantly to the local flow behavior (Tomkins, 2001). As such, dramatic local changes in the surface topology generate flow modifications that can persist for some appreciable

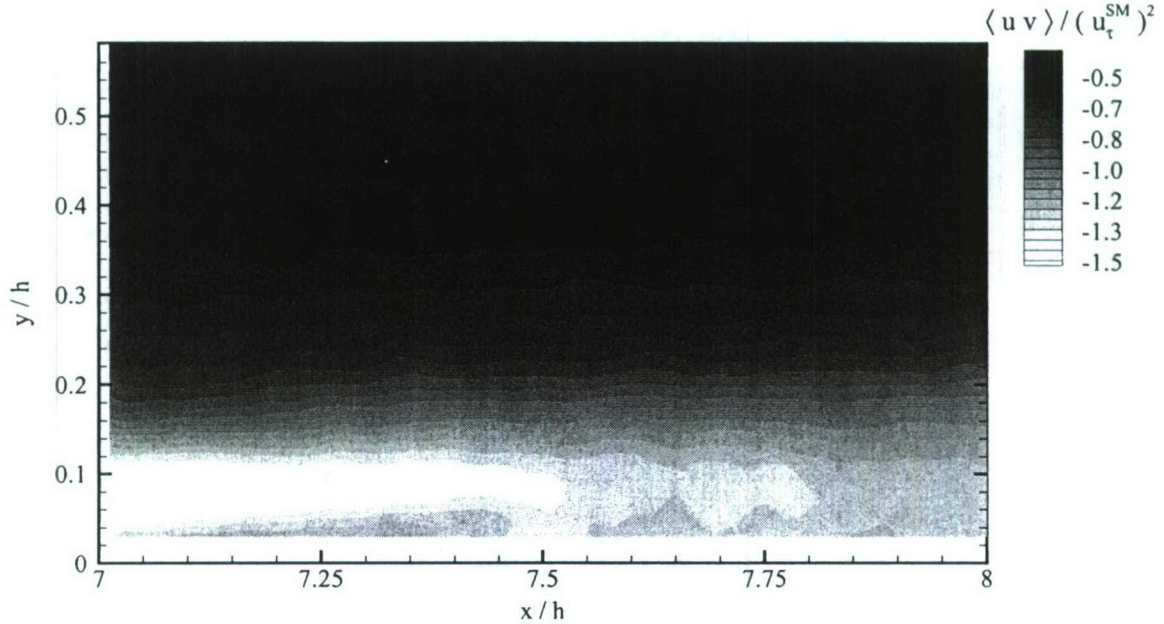


Figure 4: Ensemble-averaged Reynolds stress for case R2.

distance downstream. In contrast, these flow modifications do not appear to alter the wall-normal growth of the internal layer since all the roughness profiles collapse onto the smooth-wall result near  $y = 0.35h$ .

Figure 5 presents probability density functions (pdf's) of  $uv$  at  $y = 0.1h$ ,  $0.2h$ ,  $0.5h$  and  $h$  normalized by the absolute value of the maximum Reynolds stress from the smooth-wall case:  $|\langle uv \rangle|_{max}^{SM}$ . This value is chosen as a universal normalization so that the relative enhancement of the Reynolds-stress-producing events by the surface roughness can be directly observed. As expected, the pdf's are notably skewed toward negative values for  $y = 0.1h$ ,  $0.2h$ ,  $0.5h$  in both the smooth- and rough-wall cases, consistent with the mean Reynolds stress profiles shown in figure 3. In contrast, symmetry in the  $uv$  pdf's is noted at the centerline of the channel where the total mean Reynolds stress is zero. In addition, it is observed that a vast majority of the Reynolds-stress-producing events are quite small in magnitude, whereas only a small number of  $uv$  events yield extremely large instantaneous Reynolds shear stress in both the smooth- and rough-wall cases.

Figure 5(a) indicates that the surface roughness generates a larger number of significant negative  $uv$  events at  $y = 0.1h$  (within the log layer) compared to the smooth-wall case. This behavior is most notable for case R2 where the largest enhancement of the mean Reynolds stress was observed. In contrast, the number of significant positive  $uv$  events increases only slightly in the presence of surface roughness. Further, the roughness has little effect on both the negative and positive  $uv$  events with relatively small magnitude ( $uv < 4|\langle uv \rangle|_{max}^{SM}$ ). At  $y = 0.2h$  [figure 5(b)], the enhancement of  $uv$  by the surface roughness is weaker than at  $y = 0.1h$  but still notable in the negative tails of the pdf's. Outside the internal layer at  $y = 0.5h$  [figure 5(c)], the pdf's collapse irrespective of surface condition which is consistent with the collapse of the mean total Reynolds stress profiles in this wall-normal region (figure 3). The pdf's become symmetric at the centerline [figure 5(d)], although  $uv$  events several times larger than  $|\langle uv \rangle|_{max}^{SM}$  can still exist. This latter observation is quite consistent with the results of Sabot & Comte-Bellot (1976) for turbulent pipe

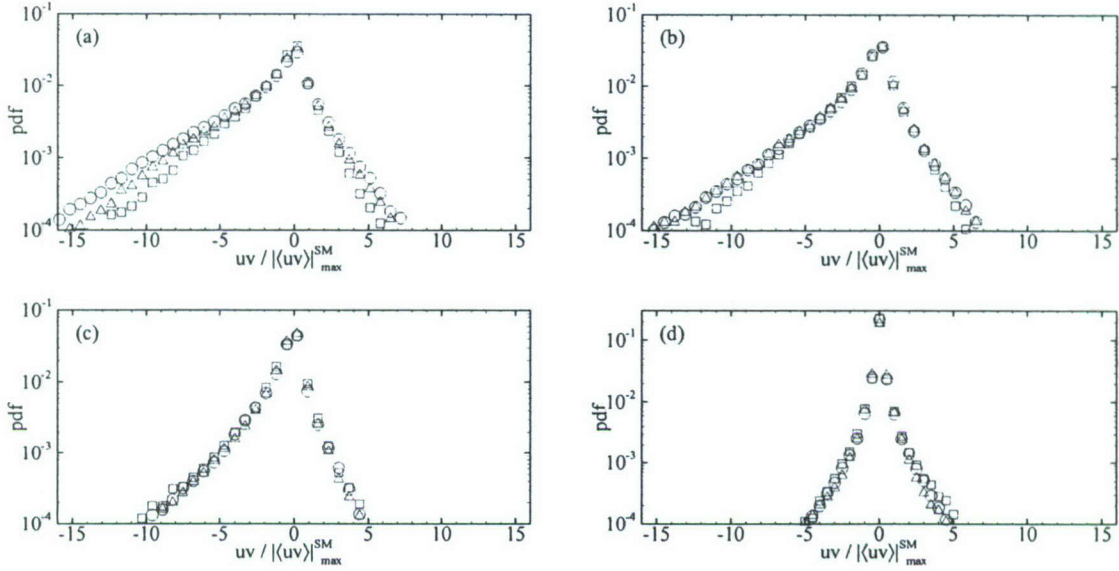


Figure 5: Probability density functions of  $uv$  normalized by  $|\langle uv \rangle|_{max}^{SM}$  at (a)  $y = 0.1h$ , (b)  $y = 0.2h$ , (c)  $y = 0.5h$  and (d)  $y = h$ .  $\square$ : SM;  $\triangle$ : R1;  $\circ$ : R2. Every fourth point is shown for clarity.

flow. Taken together, these results suggest that the surface roughness studied herein only alters the tails of the  $uv$  pdf's through the generation of significant instantaneous positive and negative  $uv$  events, more so the latter than the former, while having little influence on  $uv$  events of smaller magnitude.

The pdf's of  $uv$  for four wall-normal locations are presented in figure 6(a–c) for the SM, R1 and R2 cases, respectively. It is interesting to note that the pdf's of positive  $uv$  events remain relatively unchanged from the log layer ( $y = 0.1h$ ) to the centerline in the smooth-wall case [figure 6(a)], indicating that the turbulent motions responsible for such contributions maintain their intensities across the outer layer. The same cannot be said of the negative  $uv$  events in the smooth-wall case as the negative tails of the  $uv$  pdf's show a distinct wall-normal dependence. Similar wall-normal behavior is noted in both roughness cases (figure 6(b) for R1 and figure 6(c) for R2), although the negative and positive  $uv$  tails show notable enhancement within the internal roughness layer.

### 2.3.2 Quadrant analysis

The results presented in figures 3–6 indicate that the surface roughness replicated from a damaged turbine blade yields a net increase in the mean Reynolds stress through the generation of significant, yet highly intermittent, instantaneous negative  $uv$  events. However, it is not known whether these negative  $uv$  events are associated with an increased number of ejections, sweeps or both. Likewise, the surface roughness also appears to generate an increased number of significant positive  $uv$  events, albeit a much smaller number than the negative  $uv$  events, yet it is not clear if this is associated with an increased incidence of outward interactions, inward interactions or both. Therefore, quadrant analysis is used to identify the dominant contributors to the Reynolds-stress enhancement noted in the presence of surface roughness.

Following Wallace *et al.* (1972) and Lu & Willmarth (1973), the mean Reynolds stress at each wall-normal position can be decomposed into contributions from four quadrants ( $Q = 1 - 4$ ),

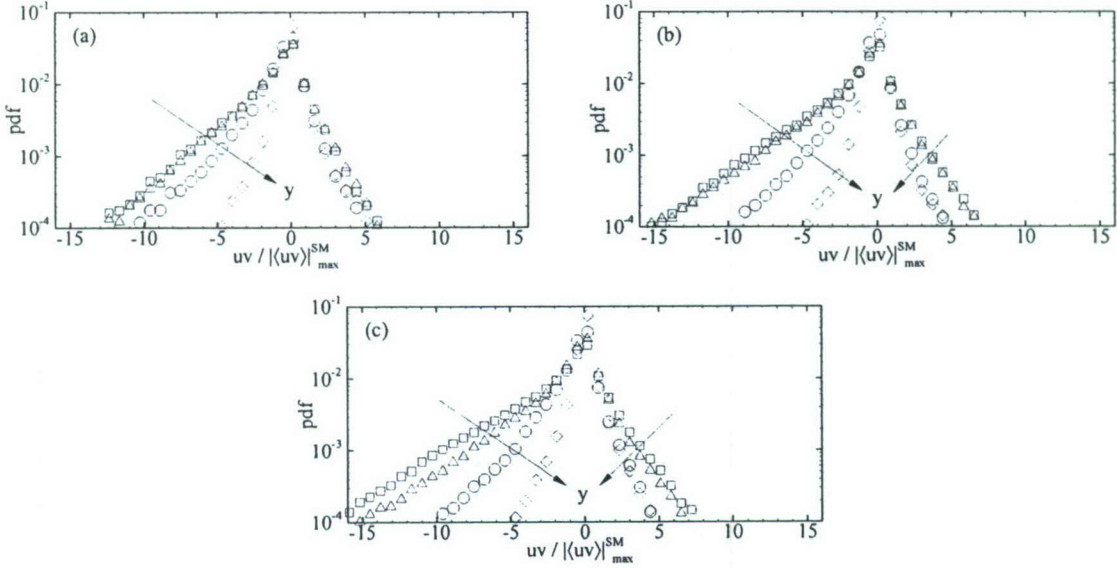


Figure 6: Probability density functions of  $uv$  normalized by  $|\langle uv \rangle|_{max}^{SM}$  for (a) SM, (b) R1 and (c) R2 at various wall-normal locations.  $\square$ :  $y = 0.1h$ ;  $\triangle$ :  $y = 0.2h$ ;  $\circ$ :  $y = 0.5h$ ;  $\diamond$ :  $y = h$ . Every fourth point is shown for clarity.

excluding a hyperbolic hole of size  $H$ , as

$$\langle uv \rangle_Q(y) = \frac{1}{M} \sum_{j=1}^M u(x_j, y)v(x_j, y)I_Q(x_j, y), \quad (12)$$

where  $I_Q$  is the indicator function defined as

$$I_Q(x_j, y) = \begin{cases} 1 & \text{when } |u(x_j, y)v(x_j, y)|_Q \geq H|\langle uv \rangle|_{max}^{SM}, \\ 0 & \text{otherwise} \end{cases}, \quad (13)$$

and  $M$  is the total number of vectors at each wall-normal position. Hence, the summation in equation (12) represents an ensemble average amongst statistically-independent realizations and a line average in the streamwise direction for fixed wall-normal location. As noted earlier, a universal threshold  $|\langle uv \rangle|_{max}^{SM}$  is used to define  $I_Q$  so that the enhancement of Reynolds-stress-producing events due to the surface roughness can be clearly identified relative to the smooth-wall case. In addition, a non-zero hole size,  $H$ , is used to exclude  $uv$  events of small magnitude in order to determine the relative contributions of the significant  $uv$  events identified in the previous section.

Quadrant analysis yields three quantities of interest in assessing the overall contributions of ejections, sweeps and inward/outward interactions to the mean Reynolds stress:

1. The Reynolds stress contributed by each quadrant for a given  $H$ :  $\langle uv \rangle_Q(y)$ ;
2. The stress fraction associated with each quadrant event for a given  $H$ :

$$S_Q(y) = \frac{\langle uv \rangle_Q(y)}{\langle uv \rangle(y)}; \quad (14)$$

3. The space fraction occupied by each quadrant for a given  $H$ :

$$N_Q(y) = \frac{\sum I_Q(y)}{M}. \quad (15)$$

Three hole sizes,  $H = 0$ ,  $2$ , and  $5$ , are studied and represent contributions to the total mean Reynolds stress from all, only moderate-to-strong events and only strong events, respectively. However, only the results for  $H = 0$  and  $H = 5$  will be presented herein as the  $H = 2$  trends are qualitatively similar to those at  $H = 5$ . Further, the wall-normal trends of these quantities are only presented within the internal layer ( $y \leq 0.35h$ ) where the surface roughness exerts its influence.

Figure 7 presents the Reynolds stress contributions,  $\langle uv \rangle_Q$ , from ejections, sweeps and inward/outward interactions corresponding to  $H = 0$  for the smooth and rough cases as a function of wall-normal position. The case  $H = 0$  implies that

$$\sum_{Q=1}^4 \langle uv \rangle_Q(y) = \langle uv \rangle(y), \quad (16)$$

meaning that all contributions to the mean Reynolds stress, intense and weak, are included in this quadrant decomposition. Surface roughness significantly enhances the Reynolds-stress contributions of ejections and sweeps while increasing the contributions from the inward/outward interactions only slightly. The R2 case displays the largest increase in ejection and sweep contributions, consistent with the observations noted earlier. In addition, ejections and sweeps appear to contribute equally to the mean Reynolds stress for  $y < 0.1h$ ; however, for  $y > 0.1h$ , the contributions from ejections begin to outweigh those from sweeps. As with the total Reynolds stress profiles presented in figure 3, the contributions presented in figure 7 are normalized by the smooth-wall friction velocity since measurements of the wall shear stress over the roughness were not available.

While the absolute contributions of Reynolds-stress-producing events, particularly ejections and sweeps, are altered in the presence of surface roughness, the stress fractions for  $H = 0$  show little dependence on surface roughness (figure 8). In particular, ejections account for roughly 60–70% of the mean Reynolds stress while sweeps account for approximately 60% in the region  $y \leq 0.35h$  in both the smooth- and rough-wall cases. The inward and outward interactions generate stress fractions with magnitudes more than three times smaller than those of the ejections and sweeps over the same wall-normal extent. Finally, surface roughness appears to have little influence on the space fractions of the ejections, sweeps and inward/outward interactions as the smooth- and rough-wall results collapse in the region  $y \leq 0.35h$  (figure 9). Ejections and sweeps are found to occupy a significant fraction of space in this wall-normal region, accounting for nearly 70% of the events for  $H = 0$  irrespective of surface condition with the remaining 30% associated with inward and outward interactions.

Figure 10 presents the Reynolds stress contributions from ejections, sweeps and inward/outward interactions corresponding to  $H = 5$  for the smooth and rough cases. The use of  $H = 5$  ensures that only the most intense Reynolds-stress-producing events are considered in the quadrant decomposition. For  $H = 5$ , the contributions from both outward and inward interactions are essentially zero for both the smooth- and rough-wall cases. In contrast, both ejections and sweeps show clear dependence on the surface conditions as both the R1 and R2 cases yield a significant enhancement of the smooth-wall contributions of such events, most notably in the case of R2. The contributions from ejections are found to be slightly larger than those of sweeps except close to the wall where sweeps contribute slightly more to the overall Reynolds stress compared to ejections. These wall-normal trends are consistent with the recent turbulent-boundary-layer results of Flack *et al.* (2005) over long streamwise fetches of sandpaper and wire mesh.

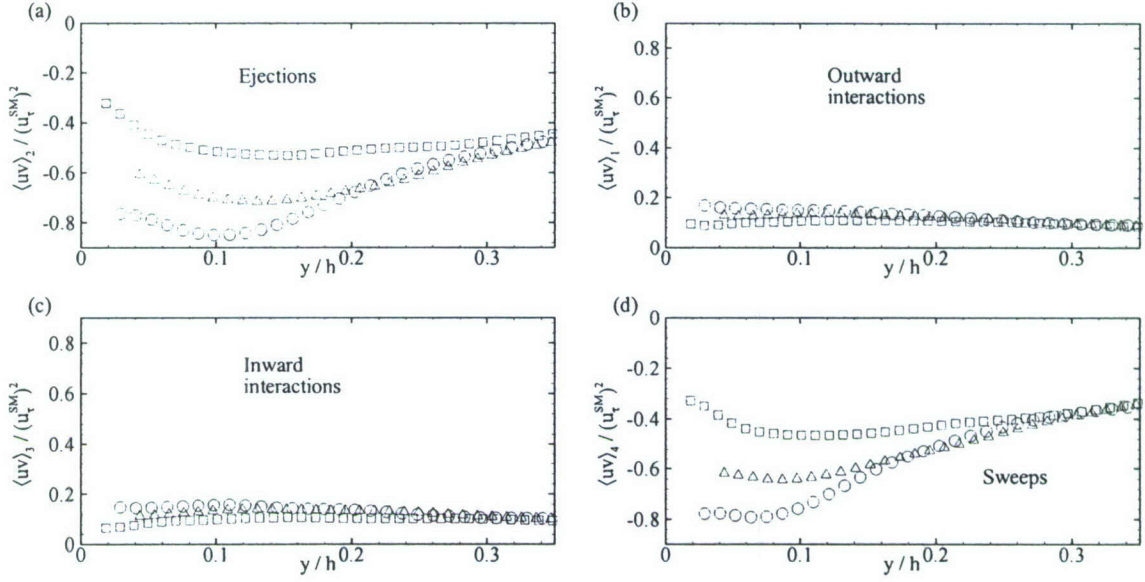


Figure 7: Contributions of each quadrant to the mean Reynolds stress,  $\langle uv \rangle_Q$ , as a function of wall-normal position for  $H = 0$ . (a) Ejections; (b) Outward interactions; (c) Inward interactions; (d) Sweeps.  $\square$ : SM;  $\triangle$ : R1;  $\circ$ : R2.

The dependence of the Reynolds stress contributions on surface condition for  $H = 5$  is also notable in the stress fractions presented in figure 11. The R1 and R2 cases are found to yield ejection stress fractions significantly larger than the smooth-wall case for  $y < 0.35h$  while the same rough-wall cases yield enhanced sweep stress fractions for  $y < 0.2h$ . Therefore, while the stress fractions for  $H = 0$  display little sensitivity to the surface conditions, the stress fractions associated with the most intense  $uv$  events display significant dependence on the surface topology. Further, the stress fractions associated with inward/outward interactions are found to be nearly zero for  $H = 5$ , meaning that the most intense Reynolds-stress-producing events are almost always ejections or sweeps, irrespective of surface condition.

While ejections and sweeps account for the most intense  $uv$  events, they occupy very little physical space (figure 12). In particular, while intense ejections and sweeps together account for as much as 70–80% of the mean Reynolds stress (most notably in case R2), these events occupy only a small fraction of space, with the space fraction increasing slightly in the presence of roughness. This slight increase of  $N_Q$  in the presence of surface roughness is consistent with the pdf's of  $uv$  presented in figure 5 which illustrate that surface roughness generates a larger number of significant ejection and sweep events. Most notably, the R2 case generates the largest space fraction for both ejections and sweeps, 3–6%, attributable to the generation of many more intense  $uv$  events compared to the smooth-wall case and even the R1 case. Therefore, while the overall ( $H = 0$ ) stress and space fractions are unaffected by the surface conditions, the stress and space fractions of the most intense  $uv$  events are strongly correlated with the surface topology as evidenced by the notable differences between the smooth-wall, R1 and R2 cases for  $H = 5$ .

Finally, the relative contributions of ejections and sweeps as a function of wall-normal position can be quantified by the ratio

$$\alpha(y) = \frac{\langle uv \rangle_2(y)}{\langle uv \rangle_4(y)}, \quad (17)$$

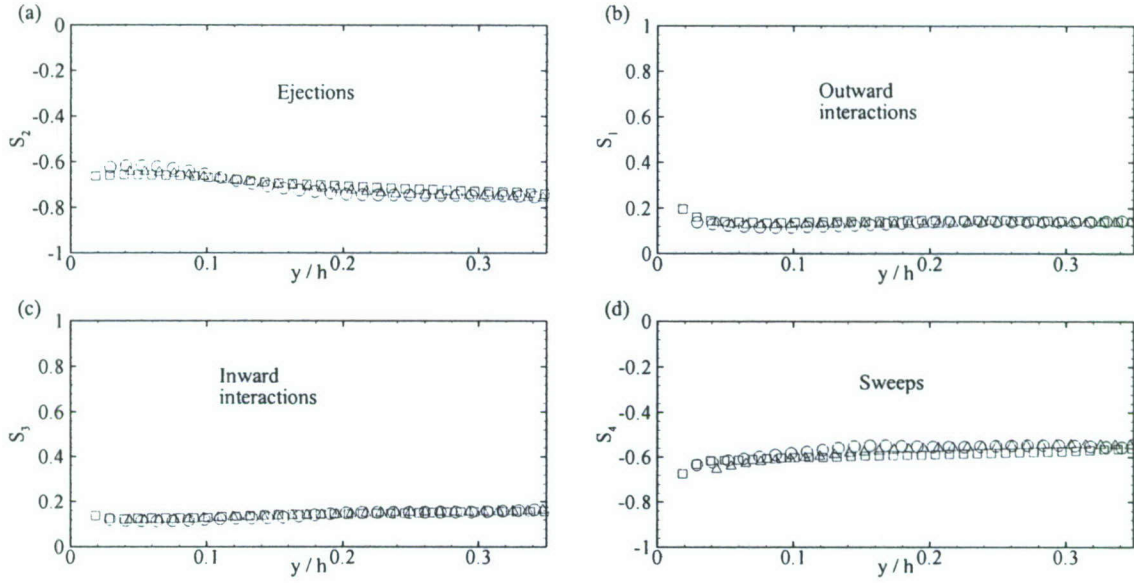


Figure 8: Stress fractions contributed by each quadrant,  $S_Q$ , as a function of wall-normal position for  $H = 0$ . (a) Ejections; (b) Outward interactions; (c) Inward interactions; (d) Sweeps.  $\square$ : SM;  $\triangle$ : R1;  $\circ$ : R2.

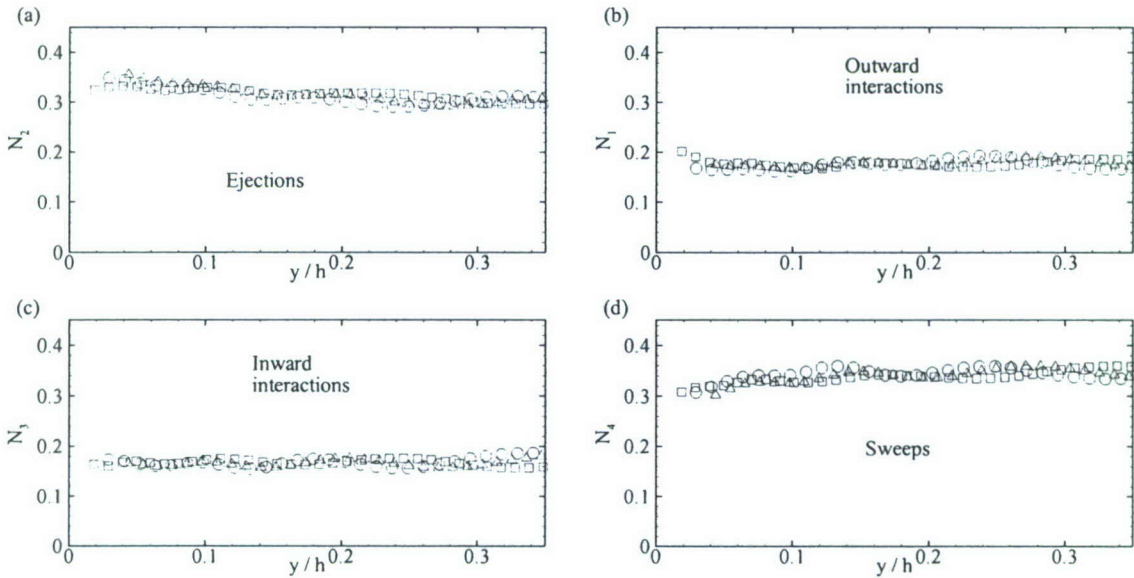


Figure 9: Space fractions occupied by each quadrant,  $N_Q$ , as a function of wall-normal position for  $H = 0$ . (a) Ejections; (b) Outward interactions; (c) Inward interactions; (d) Sweeps.  $\square$ : SM;  $\triangle$ : R1;  $\circ$ : R2.

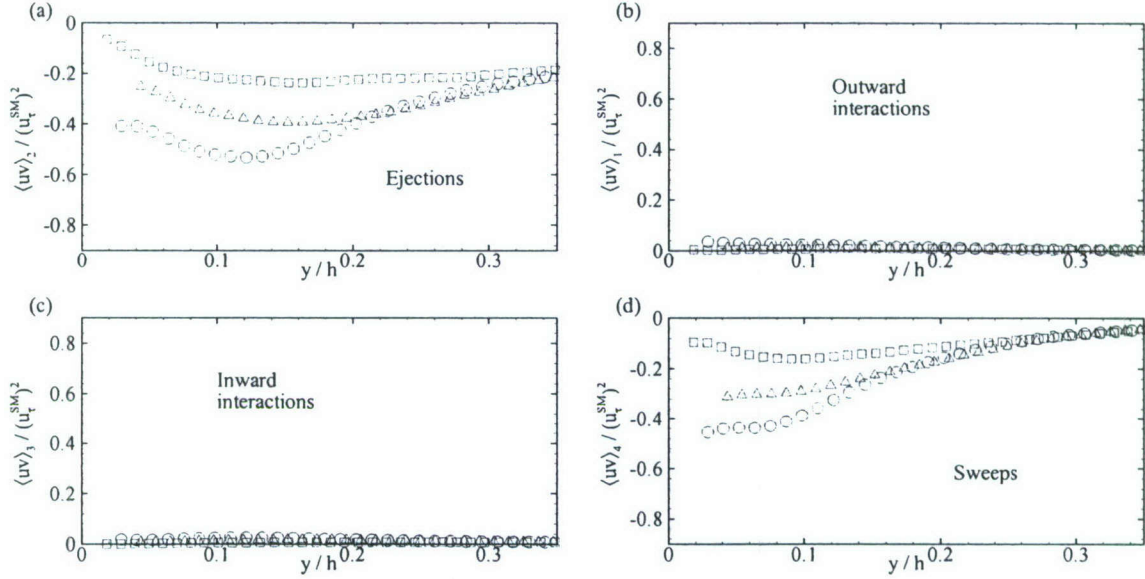


Figure 10: Contributions of each quadrant to the mean Reynolds stress,  $\langle uv \rangle_Q$ , as a function of wall-normal position for  $H = 5$ . (a) Ejections; (b) Outward interactions; (c) Inward interactions; (d) Sweeps.  $\square$ : SM;  $\triangle$ : R1;  $\bigcirc$ : R2.

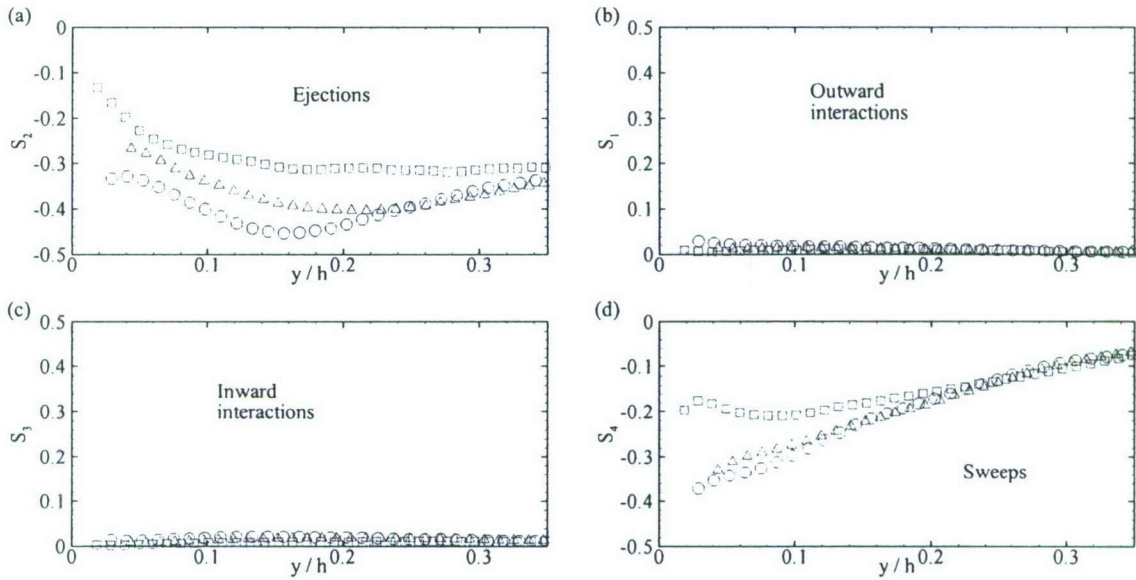


Figure 11: Stress fractions contributed by each quadrant,  $S_Q$ , as a function of wall-normal position for  $H = 5$ . (a) Ejections; (b) Outward interactions; (c) Inward interactions; (d) Sweeps.  $\square$ : SM;  $\triangle$ : R1;  $\bigcirc$ : R2.

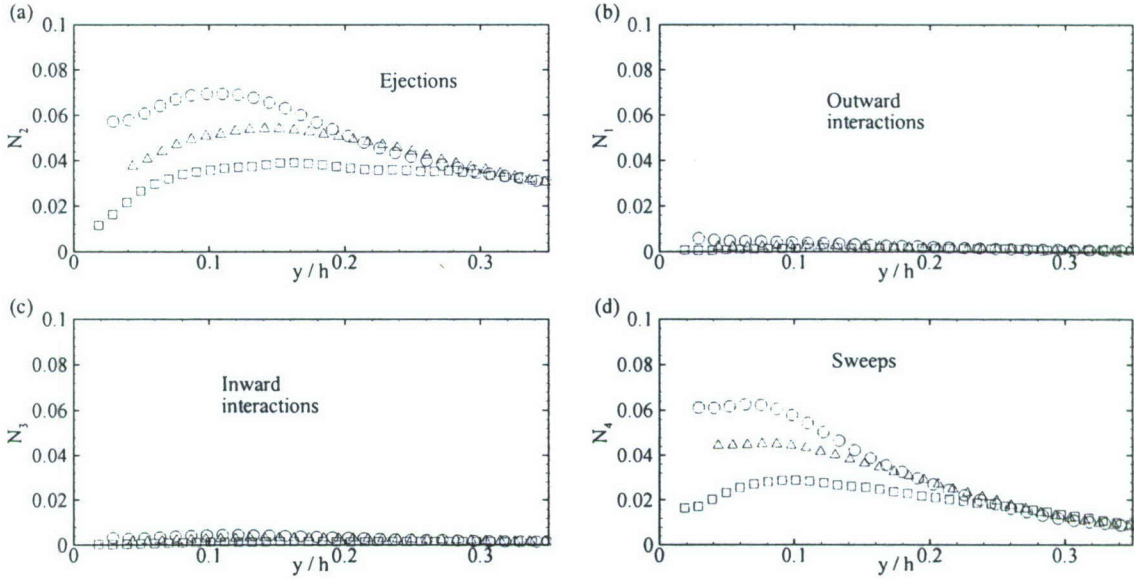


Figure 12: Space fractions occupied by each quadrant,  $N_Q$ , as a function of wall-normal position for  $H = 5$ . (a) Ejections; (b) Outward interactions; (c) Inward interactions; (d) Sweeps.  $\square$ : SM;  $\triangle$ : R1;  $\circ$ : R2.

where  $\alpha > 1$  and  $\alpha < 1$  represent stronger/weaker contributions to the mean Reynolds stress from ejections as compared to sweeps. For  $H = 0$  [figure 13(a)],  $\alpha$  slowly increases from one near the wall to nearly 1.4 at the edge of the internal layer ( $y = 0.35h$ ). In addition,  $\alpha$  displays no dependence on surface condition as the smooth- and rough-wall results collapse for  $H = 0$ , consistent with the collapse of the stress and space fractions for  $H = 0$  (figures 8 and 9). Figure 13(b) presents  $\alpha$  as a function of wall-normal position for  $H = 5$ . These results suggest that intense ejections dominate over intense sweep events in all regions except the very near-wall region where  $\alpha$  is near one and are consistent with the observations of Flack *et al.* (2005) over much simpler roughness surfaces (sandpaper and wire mesh). In addition, the smooth-wall values of  $\alpha$  are observed to be slightly larger for  $y < 0.1h$ , which is consistent with the dependence of the  $H = 5$  stress and space fractions of ejections and sweeps on the surface conditions. This behavior is also consistent with the roughness-sublayer observations of Flack *et al.* (2005). However, for  $y > 0.1h$ , this ratio increases slightly in the presence of roughness, indicating a slightly larger contribution from ejections than sweeps at the outer edge of the log layer.

## 2.4 Summary

The dominant Reynolds-stress-producing events in smooth-wall turbulence and turbulence over a short strip of roughness replicated from a damaged turbine blade are found to show significant dependence on the surface conditions. In particular, the mean Reynolds stress is found to increase dramatically, particularly in regions where the surface topology contains large-scale defects. This increase is most-likely associated with an enhancement in the overall wall shear stress in the presence of the roughness. Probability density functions of  $uv$  indicate that, while positive  $uv$  events are relatively unaffected by the presence of surface roughness, the number of intense negative  $uv$  events increases dramatically over the roughness. This increased occurrence of intense negative  $uv$

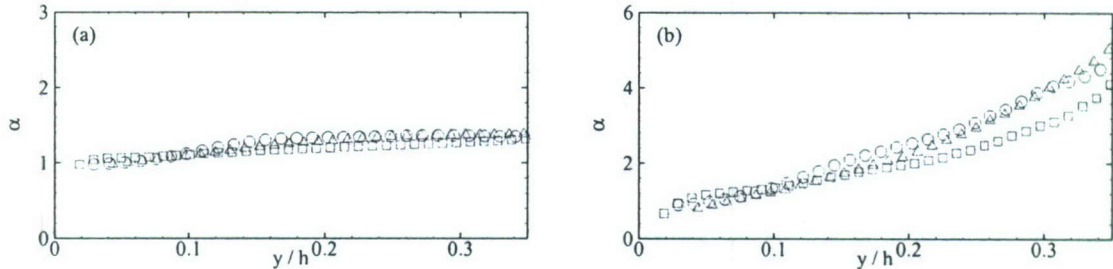


Figure 13: Ratio of ejection to sweep contributions,  $\alpha$ , as a function of wall-normal position for (a)  $H = 0$  and (b)  $H = 5$ .  $\square$ : SM;  $\triangle$ : R1;  $\bigcirc$ : R2.

events, coupled with the insensitivity of positive  $uv$  events to surface roughness, clearly accounts for the dramatic increase in the mean Reynolds stress within the internal layer. Further, the local topology plays a crucial role in the enhancement of the mean Reynolds stress as large-scale surface defects are found to generate significant, but localized, Reynolds-stress-producing events. This latter observation is consistent with the behavior often noted in studies of discrete roughness elements where the wake of each element significantly alters the local flow character (Tomkins, 2001).

Quadrant analysis reveals that surface roughness significantly increases the overall contributions of ejections and sweeps to the mean Reynolds stress compared to the smooth-wall case. In contrast, the inward and outward interaction contributions remain relatively unchanged in the presence of surface roughness. For  $H = 0$ , the stress and space fractions of ejections, sweeps and inward/outward interactions are found to be insensitive to the surface topology. This behavior is consistent with the pdf's of  $uv$  events which showed clear insensitivity to the surface conditions for weak negative and positive  $uv$  events. In contrast, the most intense  $uv$  events generate stress and space fractions that show strong dependence on the surface topology, indicating that the increase in the mean Reynolds stress is directly attributable to the generation of extremely intense, yet highly intermittent, ejections and sweeps.

Finally, the fact that the  $H = 0$  stress/space fractions and  $\alpha$  display little sensitivity to the surface topology indicates that the flow over the replicated turbine-blade roughness and smooth-wall turbulence may indeed be similar in the spirit of outer-layer similarity. If this is indeed the case, then the intense  $uv$  events, which display significant dependence on surface topology, may play a role in defining the enhanced wall shear stress over the roughness. Further, given that many of the trends noted herein are consistent with other studies over idealized roughness (sandgrain, discrete elements, etc.), such studies may in fact be sufficient for describing the influence of highly-irregular surface conditions on the flow. An accurate measure of the wall shear stress over the rough surface would be needed to confirm these conjectures and such a measure was unfortunately not available in the present experiments. Finally, the present short-fetch observations cannot be regarded as *quantitatively* representative of flow over much longer fetches of highly-irregular surface roughness. However, the *qualitative* consistency between the present observations and the aforementioned studies of idealized roughness over long fetches in the fully-rough regime ( $k^+ > 90 - 100$ ; high  $Re_\tau$ ) suggests that the present results may at least retain *qualitative* consistency with fully-rough flow over longer streamwise fetches of highly-irregular roughness. Direct assessment of this possibility is required.

### 3 Wind-tunnel experiments

This section summarizes all aspects of the wind-tunnel experiments undertaken, including a description of the flow facility, a detailed discussion of the roughness under consideration as well as all details pertaining to the particle image velocimetry (PIV) measurements that form the foundation of this experimental effort.

#### 3.1 Flow facility

The flow facility employed in this study is an existing low-turbulence, open circuit, Eiffel-type wind tunnel. The characteristics and quality of this facility are well-documented in many past studies of smooth-wall turbulence (Meinhart, 1994; Meinhart & Adrian, 1995; Adrian *et al.*, 2000; Tomkins, 2001; Tomkins & Adrian, 2003; Wu & Christensen, 2006a; Natrajan *et al.*, 2007, among others). In short, air is drawn into the tunnel via an elliptical inlet and the flow is conditioned prior to entering the test section with a series of screens and honeycomb to maximize uniformity and minimize turbulence levels. This conditioning yields a relatively low free-stream turbulence intensity of approximately 0.16% (Meinhart, 1994). The flow rate of the air is controlled through the fan speed by adjusting the frequency input of the control box. The facility was originally designed to allow boundary layers to develop over a 6096 mm-long by 914 mm-wide hydraulically-smooth flat plate that has an elliptically-shaped leading edge and is mounted 100 mm above the bottom surface of the 457 mm-tall test section. This plate is formed by two equal-length sections joined together at the streamwise center of the test section and each section has a 610 mm-wide by 2048 mm-long float glass window smoothly embedded, facilitating optical access from below. In addition, float glass windows are smoothly embedded in the side walls of the test section, providing optical access from the sides as well. As reported in Adrian *et al.* (2000), the test section of this facility was designed so that the side-wall boundary layers were less than 9% of the total width of the test section, ensuring two-dimensionality of the flow in the central 80% of the test-section width. Finally, the elevation of the test-section ceiling is adjustable, allowing precise control of the mean streamwise pressure gradient. Static pressure taps are mounted along the streamwise length of the flat plate at 0.3 m intervals for precise documentation of the streamwise pressure gradient. In order to ensure spanwise uniform transition as well as to stabilize the streamwise location of transition, flow over the flat plate is normally tripped with a 4.7 mm-diameter cylindrical rod placed downstream of the leading edge (the precise streamwise location of the trip varies with Reynolds number). A more thorough description of this facility can be found in Meinhart (1994).

Finally, while this tunnel was originally designed to allow laser illumination directly through the float glass windows embedded within the flat plate, the addition of opaque roughness in this study renders this illumination scheme impossible. Therefore, one aluminum section of the wind tunnel's ceiling was replaced by a transparent mylar sheet. A comparison of measurements of the flow before and after this modification reveal no discernable effect of the mylar sheet on the flow within the boundary layer.

#### 3.2 Rough surface

The surface studied herein is one of the surfaces characterized in Bons *et al.* (2001) [surface 4] and a digitized version of this topography was generously provided to our group by Prof. J. Bons of Ohio State University. The roughness of this particular surface is attributable to deposition of foreign materials. It should be noted that the original profilometry measurements of this damaged turbine-blade surface by Bons *et al.* (2001) yielded roughness heights on the order of tens to hundreds of microns. Therefore, in order to generate both transitionally- and fully-rough conditions for the

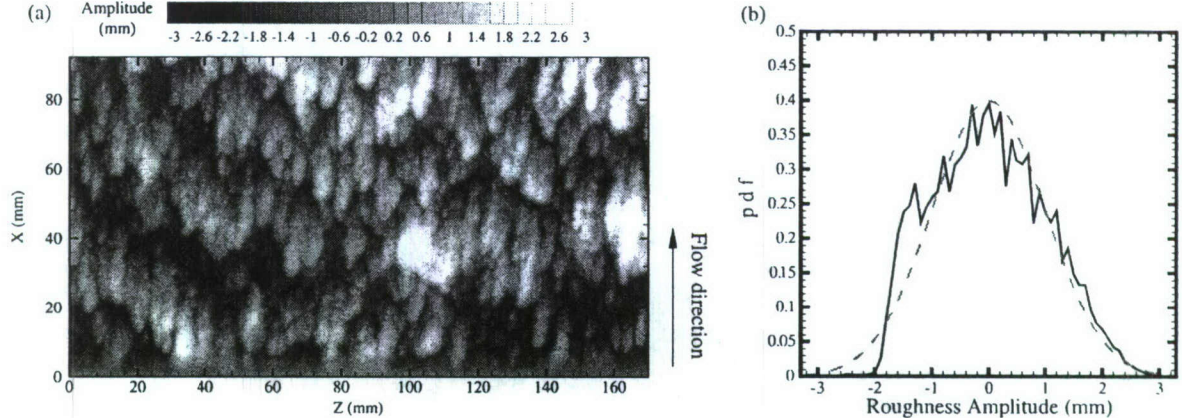


Figure 14: (a) Contour plot of a portion of the surface topology for the RF1 case. (b) Probability density function (pdf) of the roughness amplitude about the mean elevation for the RF1 case (—) contrasted with a Gaussian distribution with an equivalent RMS (---).

relatively thick boundary layers generated by the flow facility employed ( $\delta \sim 100$  mm) at the  $Re_\theta$  considered herein, the original profilometry information was scaled up in all three dimensions to yield two different topographical conditions: one rough-wall condition with  $k = 4.2$  mm (hereafter referred to as the RF1 case) and an additional rough surface with  $k = 2.1$  mm denoted the RF2 case (Following Bons (2002), the characteristic roughness height,  $k$ , is taken to be the average peak-to-valley roughness height of the surface.). The root-mean-square (RMS) roughness heights,  $k_{rms}$ , for the RF1 and RF2 surfaces are 1.0 mm and 0.50 mm, respectively, while the skewness and flatness of both topographies are 0.19 and 2.35, respectively. Therefore, while the underlying topographical features of RF1 and RF2 are identical in character, the RF2 case is scaled down in all three dimensions by a factor of two relative to the RF1 case. Given that the boundary layers under consideration have thicknesses of approximately 100 mm, the RF1 condition gives  $\delta/k \approx 25$  while the RF2 condition gives  $\delta/k \approx 50$ —below and above the threshold of  $\delta/k = 40$  proposed by Jimenez (2004) for the validity of the wall similarity hypothesis (The boundary-layer thickness,  $\delta$ , is taken as the wall-normal position where the mean streamwise velocity equals 99% of the free-stream velocity for all cases). Figure 14(a) presents a contour plot of the RF1 scaling. The dominant topographical features of this surface, attributable to deposition of foreign materials, are elliptical in shape and are generally aligned in the streamwise direction. However, a broad range of topographical scales is also clearly evident in this surface. Figure 14(b) presents the probability density function (pdf) of the roughness amplitude about the mean elevation for the RF1 case contrasted with a Gaussian distribution with an equivalent RMS. This pdf highlights the broad range of topographical fluctuations that exist about the mean elevation but, as the aforementioned flatness value of 2.35 suggests, the pdf of the roughness amplitude is not strictly Gaussian.

The final digitized topographies for each case were fed to a three-dimensional powder-deposition printer with  $80\ \mu\text{m}$  resolution that is housed in the Imaging Technology Group Lab (ITGL) at the Beckman Institute. This printer builds replicas of the topography layer-by-layer with a maximum spatial footprint of  $254\ \text{mm} \times 304.8\ \text{mm}$ . Figure 15(a) presents a contour plot of surface topography for the RF1 roughness panel while figure 15(b) presents a zoomed-in view of the RF1 topography coincident with the streamwise–spanwise field of view of the stereo PIV measurements (as described below) wherein the surface features with heights above the mean elevation are accentuated. Several distinct roughness protrusions are clearly notable in figure 15(b) and are labeled A–G for later

comparison with the PIV data.

In order to achieve a self-similar boundary layer one must have a sufficient streamwise length of roughness prior to the measurement location [ $\sim 15 - 20\delta$ ] (Antonia & Luxton, 1971). The boundary layers in question have thickness of  $\delta \approx 100$  mm, so we have chosen to cover the downstream 3 m of the flat plate in the wind tunnel with roughness to achieve self similarity at the measurement location. To accommodate these roughness panels, the upstream half of the flat plate was raised relative to the downstream half such that the mean elevation of the roughness is coincident with the upstream smooth wall. Further, since the original spatial footprint of the digitized topography is certainly not sufficient to fill this large of an area, the topography was mirrored in both the streamwise and spanwise directions to achieve an appropriate streamwise fetch of roughness. Therefore, in order to properly cover the full downstream half of the flat plate in the wind tunnel with roughness, 80 individual roughness panels were generated for each case (RF1 and RF2). These panels were then mounted to cast aluminum plates which were laid along the downstream half of the wind tunnel. The leading row of roughness panels for both the RF1 and RF2 surfaces were manufactured with an additional 25.4 mm-long (in the streamwise direction) smooth region with a thickness equal to the mean elevation of the roughness. This extra smooth strip facilitated proper alignment of the rough surfaces with the upstream smooth plate and also provided a relatively clean transition from smooth to rough conditions.

### 3.3 Streamwise–wall-normal ( $x - y$ ) measurements

Two-dimensional PIV measurements were performed in the streamwise–wall-normal plane over smooth, RF1 and RF2 surface conditions. All flows were seeded with nominally  $1\text{ }\mu\text{m}$  olive oil droplets generated with a Laskin nozzle. These seed particles were illuminated over a pre-defined field of view with overlapping laser light sheets generated by a pair of BigSky Nd:YAG lasers with a maximum energy of 190 mJ per pulse at a wavelength of 532 nm with a pulse width of 5 ns. The laser light sheets were generated by passing the laser beams through a combination of cylindrical and spherical lenses. A high-energy mirror of 50.8 mm diameter was used to direct the light sheets normal to the flow boundary and their thickness in the field of view was approximately 0.5 mm. A high resolution  $4\text{k} \times 2.8\text{k}$  12-bit frame-straddle CCD camera from TSI Inc. in concert with a 105 mm lens was employed to record pairs of time-delayed images of the particles. The *Insight 3G* software (TSI, Inc.) was used to perform all image acquisition. A schematic of the experimental setup for the streamwise–wall-normal measurements is presented in figure 16. The measurements over both smooth and rough walls were performed at the spanwise center of the wind tunnel and 5.55 m downstream of the leading edge of the flat plate (in the case of the rough walls, this is equivalently 2.5 m downstream of the leading edge of the roughness where the boundary layer has approached self-similarity). The roughness in the vicinity of the measurement location was painted black to reduce reflections of laser light and the boundary layer was tripped upstream of the roughness with a cylindrical rod to ensure that the flow had achieved a turbulent state prior to encountering the roughness. Despite a significant reduction in the laser light reflections from the surface, a not insignificant level of reflection remained unsuppressed which rendered measurements in the region  $y < 0.08\delta$  and  $y < 0.05\delta$  unachievable for the RF1 and RF2 cases, respectively. Measurements were performed at two different Reynolds numbers per surface condition: at a lower free-stream velocity of  $U_e \approx 10$  m/s (yielding  $\text{Re}_\theta = \theta U_e / \nu \approx 8000$ ) and at a higher free-stream velocity of  $U_e \approx 17$  m/s (yielding  $\text{Re}_\theta \approx 13000$ ). The relevant flow parameters are presented in Table 4.

The pairs of PIV images were interrogated using two-frame cross-correlation methods with a discrete window offset specified *a priori*. The interrogation was carried out within the *Insight 3G* software (TSI, Inc.). An iterative, two-pass interrogation scheme was employed to improve the

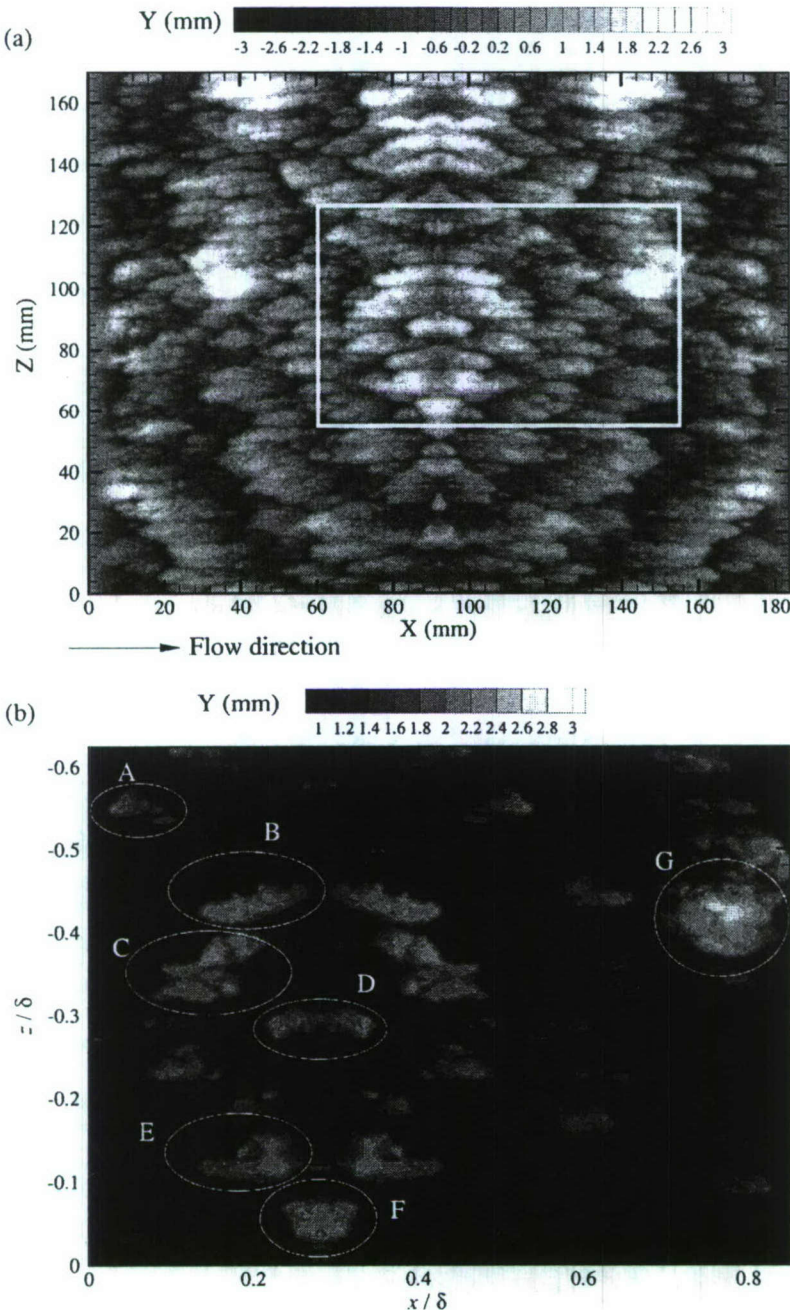


Figure 15: (a) Surface contours of a portion of the roughness topography plotted as fluctuations about the mean roughness height and oriented such that flow is from left to right. The stereo PIV measurement domain is highlighted with the white rectangle. (b) Surface contours of the roughness above the mean height coincident with the stereo PIV field measurement domain.

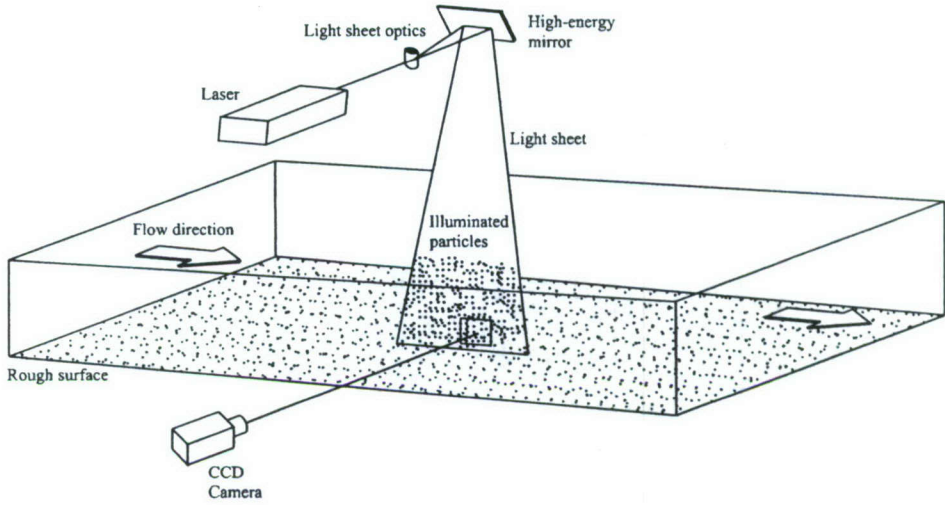


Figure 16: Experimental setup for the PIV measurements in the streamwise-wall-normal plane.

Table 4: Flow parameters for boundary layers at two different Reynolds numbers in the presence of smooth, RF1 and RF2 surface conditions.

Parameters	Low Re Case			High Re Case		
	Smooth	RF1	RF2	Smooth	RF1	RF2
$Re_\theta = \theta U_e / \nu$	8178	9000	8332	11943	14781	13685
$Re_\delta = \delta U_e / \nu$	72547	73891	71808	106160	122627	118315
$\delta^+ = \delta / \nu$	2477	3338	2855	3467	5531	4764
$U_e$ (m/s)	10.3	10.0	9.9	16.2	16.9	16.8
$\delta$ (mm)	110	113.3	112.9	104	112	109.8
$\theta$ (mm)	12.4	13.8	13.1	11.7	13.5	12.7
$\delta^*$ (mm)	16.2	19	17.3	15.1	18.6	16.9
$H$ ( $\delta^*/\theta$ )	1.31	1.38	1.32	1.29	1.38	1.33
$u_\tau$ (m/s)	0.35	0.45	0.39	0.53	0.76	0.68
$y^*$ ( $\mu m$ )	44.4	33.9	39.5	30.0	20.3	23.1
$\Delta U^+$	—	7.1	3.5	—	8.2	4.9
$k^+$	—	124	53	—	207	91
$k_s^+$	—	74	17	—	115	29
$\delta/k$	—	27	54	—	27	52
$\delta/k_s$	—	45	170	—	48	162

resolution and accuracy of the vector fields. The size of the interrogation windows was chosen to maintain consistency in the grid spacings between the smooth and rough-wall data when scaled in inner units (by  $u_\tau$  and  $\nu$ ) to ensure that the same range of spatial scales was resolved for all surface conditions at a given Reynolds number. The grid spacing in the low Reynolds number case is  $\Delta x^+ = \Delta y^+ = \Delta^+ \approx 11$  and the grid spacing in the high Reynolds number case is  $\Delta x^+ = \Delta y^+ = \Delta^+ \approx 18$ . Twenty-five hundred statistically-independent realizations were acquired for the smooth-wall cases and five thousand for the rough-wall cases (See Wu (2008) for further details regarding interrogation procedure).

The raw velocity vector fields were validated using the *Cleanvec* software (Meinhart, 1994; Soloff, 1998) to remove invalid vectors. Objective statistical tests, including standard deviation and magnitude difference comparisons, were employed to identify and remove erroneous velocity vectors. On average, 95-97% of the velocity vectors were found to be valid, minimizing the need for interpolation of holes. Finally, each velocity field was low-pass filtered with a narrow Gaussian filter to remove noise associated with frequencies larger than the sampling frequency of the interrogation (See Wu (2008) for further details regarding validation procedure).

With respect to uncertainty, there are both random and bias errors associated with PIV measurements. The random errors primarily arise from estimation of the peak location in the correlation plane. Prasad *et al.* (1992) showed that this error is approximately 5% of the particle-image diameter. In the present measurements, the mean particle image diameter is approximately 2–3 pixels, yielding a random error of about 0.1 pixels. Therefore, because the time delay between the PIV images for a given experiment is chosen to yield a bulk displacement of 10–12 pixels, this random error is less than 1% of the full-scale velocity. However, these random errors have minimal effect on the statistics of the velocity since a large number of realizations are obtained in the current experiments (2500 realizations for the smooth-wall case and 5000 for the rough-wall cases). There are two sources of bias error that can appear in PIV measurements. One source of bias error comes from velocity gradients present within the interrogation window where particles moving faster are more likely to leave the interrogation region from one time to the next (Keane & Adrian, 1992). This bias due to loss of image pairs is minimized in the present study since a larger second interrogation window and a bulk window offset are utilized during interrogation of the PIV images. This error is further reduced through the use of an iterative interrogation methodology. The other common source of bias error in PIV is the peak-locking effect due to under-sampling of the particle images (Adrian, 1995; Westerweel, 1997; Christensen, 2004). This bias error is also reduced in the present experiments because the particle-image diameters exceed 2 pixels (Westerweel, 1997). We therefore estimate the bias errors in our PIV measurements at 1% of the full-scale velocity.

Once the PIV velocity fields have been validated, many of the flow quantities in table 4 can be computed. The boundary-layer thickness,  $\delta$ , is defined as the wall-normal location where the mean streamwise velocity,  $U$ , reaches 99% of the free-stream velocity,  $U_e$ . The momentum thickness,  $\theta$ , is computed as

$$\theta = \delta \int_0^1 \frac{U}{U_e} \left(1 - \frac{U}{U_e}\right) d\left(\frac{y}{\delta}\right), \quad (18)$$

using the mean streamwise velocity profile evaluated from the PIV ensembles for a particular flow case. In a similar manner, the displacement thickness,  $\delta^*$ , is computed as

$$\delta^* = \delta \int_0^1 \left(1 - \frac{U}{U_e}\right) d\left(\frac{y}{\delta}\right). \quad (19)$$

As mentioned in section 1, the friction velocity,  $u_\tau$ , is an important, yet difficult, quantity to assess in rough-wall flows. In the present effort,  $u_\tau$  is determined from the measured Reynolds shear stress,  $\langle u'v' \rangle$ , profiles computed from the PIV ensemble of each flow case. This method relies

upon the existence of nearly constant  $\langle u'v' \rangle$  at the outer edge of the log layer. If one considers the mean momentum equation for a turbulent boundary layer, given by

$$U^+ \frac{\partial U^+}{\partial x^+} + V^+ \frac{\partial U^+}{\partial y^+} + \frac{\partial \langle u'^+ v'^+ \rangle}{\partial y^+} = \frac{\partial^2 U^+}{\partial y^{+2}}, \quad (20)$$

and invokes standard boundary-layer approximations, one observes that the first two terms on the left-hand-side of Eq. (20) are small compared to the Reynolds stress and viscous terms in the near-wall region. Therefore, close to the wall the mean momentum equation reduces to a balance between the net turbulent and viscous forces as

$$\frac{\partial \langle u'^+ v'^+ \rangle}{\partial y^+} \cong \frac{\partial^2 U^+}{\partial y^{+2}}. \quad (21)$$

Using the boundary condition  $\partial U^+ / \partial y^+|_{y=0} = 1$ , the above equation can be integrated with respect to  $y$  to obtain

$$u_\tau^2 \cong \nu \frac{\partial U}{\partial y} - \langle u'v' \rangle. \quad (22)$$

In the log layer and beyond, the first term on the right-hand-side of Eq. (22) is negligibly small, meaning one can use the measured Reynolds shear stress to estimate  $u_\tau$ . This methodology is employed herein for both the smooth- and rough-wall cases.

Once  $u_\tau$  is assessed from the measured  $\langle u'v' \rangle$  profiles, the zero-plane displacement,  $y_o$ , and roughness function,  $\Delta U^+$ , are assessed using the Clauser chart method by fitting the measured mean velocity profile in the log layer to the standard log law given by Eq. (1). This curve-fitting process was performed using the curve-fit toolbox in the latest version of MATLAB (7.1). It should be noted that the efficacy of the total stress method for determining  $u_\tau$  was validated by performing a Clauser chart assessment of  $u_\tau$  for the smooth-wall cases which yielded values within 5% of those obtained with the total stress method.

### 3.4 Streamwise–spanwise ( $x - z$ ) measurements

In addition to the 2D, streamwise–wall-normal PIV measurements described above, stereoscopic PIV experiments were performed in select streamwise–spanwise planes over the smooth and RF1 surfaces. Stereo PIV utilizes an additional camera to provide two distinct perspectives of the particle motion which, after proper calibration of the imaging arrangement, yields a measure of all three velocity components, in-plane velocities  $u$  and  $w$  and out-of-plane velocity  $v$ , on a measurement plane defined by the laser light sheet. The principle of stereo PIV is described in detail by Prasad (2000) so only a brief description of the angular displacement stereo PIV arrangement adopted for the current experiments is provided.

As illustrated in Figure 17, stereo PIV utilizes two CCD cameras positioned along different off-axis directions to obtain distinct simultaneous displacements of the particles illuminated by the laser light sheet. These distinct views of the particle motion can be combined to infer both in-plane and out-of-plane velocity components on the measurement plane. For the angular displacement system, the two cameras' axes are rotated at an angle  $\theta$  with respect to the system axis. In order to ensure uniform image focus in both cameras across the entire field of view, the Scheimpflug condition (Altenhofen, 1952), wherein the object plane, lens plane and image plane intersect at a common line, must be satisfied. This arrangement is presented in figure 17. The PIV image pairs acquired by each camera are interrogated and validated independently using standard 2D PIV interrogation procedures. The particle displacements obtained from each camera are then reconstructed into three-component velocity fields using a three-dimensional calibration of the imaging system. First

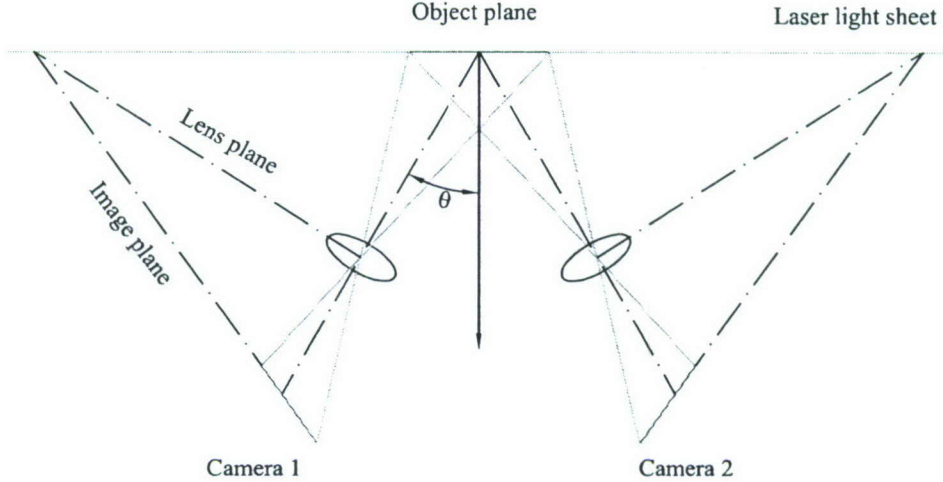


Figure 17: Angular displacement configuration of a stereoscopic PIV system.

proposed by Soloff *et al.* (1997), this robust 3D calibration method does not require knowledge of the system geometry, rendering the calibration much simpler than ray-tracing methods. In addition, the method of Soloff *et al.* (1997) is advantageous because it will account for, and therefore correct, optical distortions that might exist along the viewing path of the imaging system.

Following the analysis of Soloff *et al.* (1997), the relationship between positions of particles in the image plane of each camera,  $\mathbf{X}$ , and their positions in the object plane,  $\mathbf{x}$ , can be written as

$$\mathbf{X} = F(\mathbf{x}), \quad (23)$$

where  $F$  is termed the mapping function. This mapping function is approximated by a polynomial of a given order for both the in-plane coordinates ( $x$  and  $z$ ) and the out-of-plane coordinate ( $y$ ). The particle displacement in the image plane can then be expressed as

$$\Delta\mathbf{X} = F(\mathbf{x} + \Delta\mathbf{x}) - F(\mathbf{x}), \quad (24)$$

and can be approximated as

$$\Delta\mathbf{X} \approx \nabla F(\mathbf{x})\Delta\mathbf{x}, \quad (25)$$

where

$$(\nabla F)_{ij} = \frac{\partial F_i}{\partial x_j} = F_{i,j}, \quad (26)$$

is the gradient of the mapping function  $F$ , and  $i=1,2$  and  $j=1,2,3$ . The displacements measured by the two cameras can be consolidated as

$$\begin{bmatrix} \Delta X_1^{(1)} \\ \Delta X_2^{(1)} \\ \Delta X_1^{(2)} \\ \Delta X_2^{(2)} \end{bmatrix} = \begin{bmatrix} F_{1,1}^{(1)} & F_{1,2}^{(1)} & F_{1,3}^{(1)} \\ F_{2,1}^{(1)} & F_{2,2}^{(1)} & F_{2,3}^{(1)} \\ F_{1,1}^{(2)} & F_{1,2}^{(2)} & F_{1,3}^{(2)} \\ F_{2,1}^{(2)} & F_{2,2}^{(2)} & F_{2,3}^{(2)} \end{bmatrix} \begin{bmatrix} \Delta x_1 \\ \Delta x_2 \\ \Delta x_3 \end{bmatrix}, \quad (27)$$

where the superscripts (1) and (2) refer to the two cameras employed. Equation (27) can then be solved using a least-squares approach.

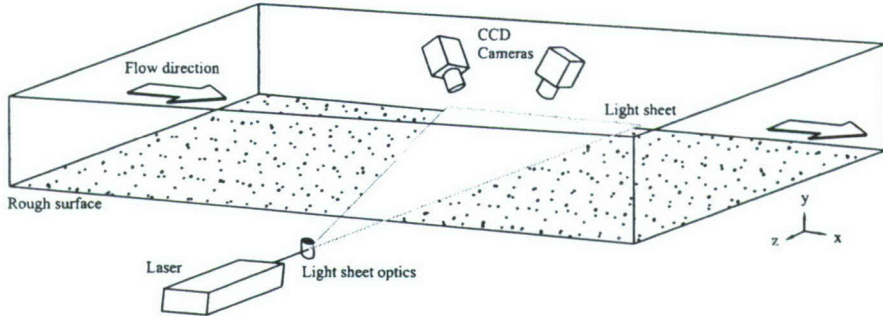


Figure 18: Experimental setup for the PIV measurements in select streamwise–spanwise planes.

Before discussing the detailed calibration procedure required for determination of  $F$ , the general experimental setup is described. The same seeding, illumination and imaging equipment described for the aforementioned 2D PIV experiments was employed for the stereo PIV experiments with the addition of a second identical CCD camera. The light sheet (of thickness 0.5 mm) was formed using the same lens arrangement as the 2D cases and two high-energy mirrors with diameters 25.4 mm and 50.8 mm were employed to direct the light sheet parallel to the flow boundary. Two rotation stages were used to control the yaw and roll of the 50.8 mm-diameter mirror to guarantee a wall-parallel light sheet. In addition, the vertical position of the 50.8 mm mirror was adjustable with two high-precision lab jacks in order to facilitate measurements at various wall-normal locations. Since the roughness under consideration was opaque, the field of view defined by the light sheet was imaged through the previously-described transparent mylar sheet in the ceiling of the tunnel. To facilitate such an arrangement, an optical bench was mounted to the upper framing of the wind tunnel, upon which the cameras were carefully arranged in an angular manner and focused on an identical field of view within the measurement plane defined by the laser light sheet. The cameras were rotated at angles of  $\pm 15^\circ$  with respect to the wall-normal ( $y$ ) axis. The Scheimpflug condition was satisfied by rotating the CCD mount of the camera to ensure uniform image focus in both cameras across the entire field of view. A schematic of the experimental setup for the streamwise–spanwise measurements is presented in figure 18.

As described by Soloff *et al.* (1997), Prasad (2000) and Ganapathisubramani *et al.* (2002), a stereo PIV system can be calibrated with a target containing distinct markings spaced in an ordered manner in all three spatial directions. The present effort employed a dual-plane (1-mm separation) target of white dots spaced at 10 mm intervals over a 20 cm  $\times$  20 cm region. This target, provided by TSI, Inc., is illustrated in figure 19. The target must be placed coincident with the plane defined by the laser light sheet. Once in place, images of this target were acquired by both cameras and a mapping function was constructed that relates positions in the image plane to corresponding locations in the object plane. A third-order polynomial was used for the in-plane ( $x$  and  $z$ ) coordinates, while a first-order polynomial was employed for the out-of-plane ( $y$ ) coordinate. This mapping function was then optimized using the self-calibration scheme proposed by Wieneke (2005) to reduce registration errors generated by inherent misalignment between the laser sheet and the calibration target. The final mapping function was then used to reconstruct the three-dimensional velocity vectors on the measurement plane of interest. All of these calibration and reconstruction operations were performed within the TSI *Insight 3G* software package along with the original acquisition, interrogation and validation of the individual image pairs from each camera. Complete and detailed calibration procedures of the stereo PIV measurements are described in the manuals of the *Insight 3G* software and strictly followed for the current experiments (See Wu (2008)

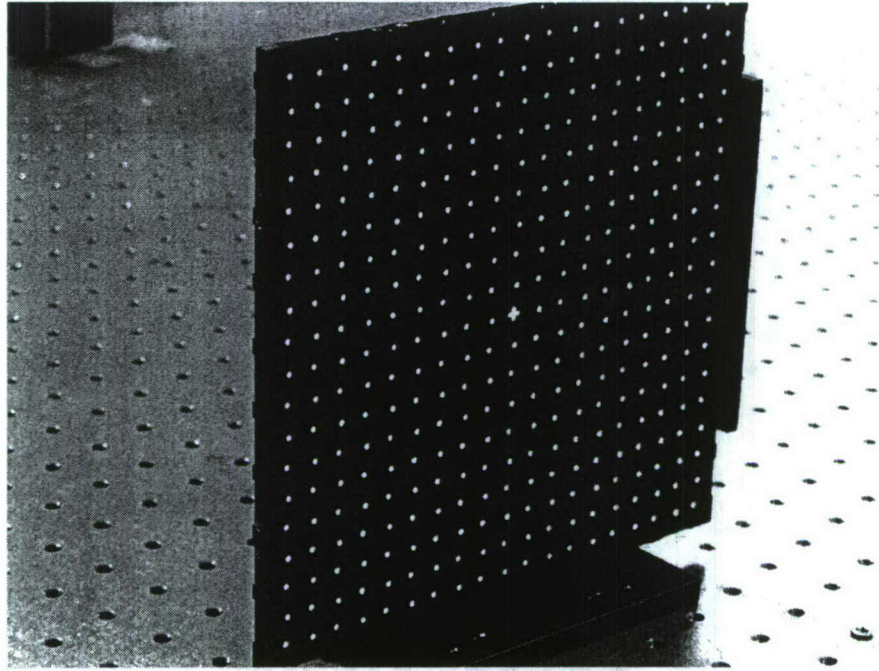


Figure 19: Calibration target employed for the stereo PIV measurements in the streamwise-spanwise plane.

for further details regarding stereo calibration procedure).

Stereo PIV measurements were made in two distinct wall-parallel planes over the RF1 surface: one within ( $y = 0.065\delta = 1.7k = 3k_s$ ) and the other at the outer edge ( $y = 0.15\delta = 4k = 7.3k_s$ ) of the roughness sublayer. Stereo PIV measurements were also made for smooth-wall flows at the same wall-normal positions,  $y = 0.065\delta$  and  $y = 0.15\delta$ . Data was acquired at  $\text{Re}_\theta \approx 8000$  and 13000 for both smooth and RF1 surfaces to match the flow conditions of the 2D PIV measurements in the wall-normal ( $x - y$ ) plane. To maximize this consistency, the input frequency of the wind-tunnel blower was fine-tuned until the mean streamwise velocities from the wall-parallel experiments (computed by both ensemble and area averaging) were within 1% of those in the wall-normal plane experiments. Such consistency is necessary since many of the flow parameters listed in table 4 are not computable from wall-parallel data and must therefore be inferred from the wall-normal plane experiments.

The pairs of PIV images for each camera were interrogated in a manner similar to that employed for the aforementioned 2D PIV experiments. The size of the interrogations windows was chosen to maintain consistency of velocity grid spacing in inner units between smooth- and rough-wall data. The grid spacing in the low Reynolds number case is  $\Delta x^+ = \Delta z^+ \approx 11$  and the grid spacing in the high Reynolds number case is  $\Delta x^+ = \Delta z^+ \approx 18$ . The interrogated velocity vector fields obtained from each camera were then validated as previously described, but within the *Insight 3G* software, to remove invalid measurements before being combined into 3D velocity fields using the mapping function generated from the calibration of the imaging system. Twenty-five hundred statistically-independent realizations were acquired for the smooth-wall cases while five thousand were acquired for the rough-wall cases (See Wu (2008) for further details regarding interrogation procedure).

For an angular stereo PIV configuration with perfect registration, the in-plane errors for  $u$  and  $w$  velocity components are reduced by a factor of  $\frac{1}{\sqrt{2}}$  compared to the uncertainty of approximately

0.1 pixels for a single camera arrangement (Prasad, 2000). However, the error for the out-of-plane velocity component,  $v$ , is  $\frac{1}{\tan\theta}$  times the in-plane error (Zang & Prasad, 1997; Lawson & Wu, 1997; Prasad, 2000), where  $\theta = 15^\circ$  in the present case. The experimental calibration procedures of Soloff *et al.* (1997) showed that the error associated with the out-of-plane velocity component could be a magnitude higher than the error of the in-plane velocity components. However, the self-calibration scheme developed by Wieneke (2005) to correct the registration errors yields final displacements with uncertainties less than that introduced from the basic PIV correlation algorithm. Therefore, we estimate the random and bias errors associated with the present stereo PIV velocity measurements to be similar to the 2D uncertainties of 1% of the full-scale velocity.

Finally, validation of the present stereoscopic PIV methodology was achieved by comparing the turbulence statistics computed from the stereoscopic PIV measurements in the wall-parallel measurement plane at both wall-normal positions,  $y = 0.065\delta$  and  $0.15\delta$ , under smooth-wall conditions with the turbulence statistics garnered from the aforementioned two-dimensional PIV measurements in the streamwise-wall-normal plane over a smooth wall at equivalent  $Re_\theta$ . Table 5 presents such a comparison for the inner-scaled mean velocity,  $U^+$ , as well as the inner-scaled Reynolds normal and shear stresses  $\langle u'^2 \rangle^+$ ,  $\langle v'^2 \rangle^+$  and  $-\langle u'v' \rangle^+$ . It is seen that the relative differences are all within 5%, validating the efficacy of the stereoscopic calibration and reconstruction methodology employed herein. It should be noted that Tomkins (2001) performed a similar comparison of turbulence statistics computed from both wall-normal and wall-parallel PIV measurements (although both were 2D) at fixed  $y$  and a similar level of consistency was reported.

Table 5: Comparison of turbulence statistics computed from the smooth-wall stereoscopic PIV measurements in the streamwise–spanwise plane at both  $y = 0.065\delta$  and  $y = 0.15\delta$  with the smooth-wall statistics at the same wall-normal locations from the two-dimensional PIV measurements in the streamwise–wall-normal plane. The last column presents the relative differences between the various statistics.

		$y = 0.065\delta$		
Experiments	Statistics	2D PIV	Stereo PIV	Relative Difference
$\text{Re}_\theta \approx 8000$	$U^+$	18.34	18.43	0.5%
	$\langle u'^2 \rangle^+$	4.84	4.88	0.8%
	$\langle v'^2 \rangle^+$	1.14	1.19	4.4%
	$-\langle u'v' \rangle^+$	0.99	0.96	3.0%
$\text{Re}_\theta \approx 13000$	$U^+$	19.70	19.64	0.3%
	$\langle u'^2 \rangle^+$	5.02	5.08	1.2%
	$\langle v'^2 \rangle^+$	1.15	1.17	1.7%
	$-\langle u'v' \rangle^+$	0.98	0.96	2.0%
		$y = 0.15\delta$		
Experiments	Statistics	2D PIV	Stereo PIV	Relative Difference
$\text{Re}_\theta \approx 8000$	$U^+$	20.41	20.24	0.8%
	$\langle u'^2 \rangle^+$	4.41	4.24	3.9%
	$\langle v'^2 \rangle^+$	1.30	1.25	3.8%
	$-\langle u'v' \rangle^+$	1.00	0.96	4.0%
$\text{Re}_\theta \approx 13000$	$U^+$	21.74	21.80	0.3%
	$\langle u'^2 \rangle^+$	4.41	4.46	1.1%
	$\langle v'^2 \rangle^+$	1.30	1.31	0.8%
	$-\langle u'v' \rangle^+$	1.00	0.99	1.0%

## 4 Outer-layer similarity in turbulence statistics

### 4.1 Background

It is generally accepted that within the roughness sublayer,  $\sim 3 - 5k$  away from the wall, turbulence is strongly affected by surface conditions. However, conflicting evidence exists as to whether roughness effects penetrate *beyond* the roughness sublayer and into the outer layer of the flow. Townsend (1976) first hypothesized that at high Reynolds numbers, the turbulent motions in the outer layer are independent of surface conditions and viscosity except for their role in setting the wall shear stress (and hence the friction velocity,  $u_\tau = [\tau_w/\rho]^{1/2}$ ) and the boundary-layer thickness,  $\delta$ . With respect to rough-wall flows, this hypothesis implies that if the characteristic height of the roughness,  $k$ , is sufficiently small compared to  $\delta$  then the direct impact of roughness is confined within the viscously-dominated roughness sublayer. Under such conditions, the turbulence in the outer layer is only indirectly influenced by roughness through its role in determining  $u_\tau$  and  $\delta$  (Raupach *et al.*, 1991). Since this wall similarity hypothesis was first proposed, many studies have indeed observed the various single-point statistics of smooth- and rough-wall flows, including the mean velocity deficit as well as profiles of the Reynolds normal and shear stresses, to behave similarly outside the roughness sublayer when appropriately scaled by  $u_\tau$ . In particular, wall similarity has been observed for turbulent flow over a variety of roughness topographies, including cylindrical roughness (Raupach, 1981), sand grain (Flack *et al.*, 2005), mesh (Flack *et al.*, 2005; Perry & Li, 1990), spheres (Ligrani & Moffat, 1986) and two-dimensional grooves (Bandyopadhyay & Watson, 1988). However, it should be noted that all of these topographies are *idealized* in the sense that they are characterized by a dominant topographical scale arranged in an ordered manner. Further, these studies span a broad range in both  $Re$ , inner-scaled roughness height ( $k^+ \equiv k/y_*$ ) and scale separation ( $\delta/k$ ), although it is generally accepted that the roughness sublayer and the outer region of the flow must be sufficiently separated for wall similarity to exist, implying  $\delta \gg k$ . However, despite the fact that  $k$  is a physically-meaningful measure of the characteristic roughness height, rough-wall flows are generally classified as hydraulically smooth ( $k_s^+ < 5$ ), transitionally rough ( $5 < k_s^+ \lesssim 70$ ) and fully rough ( $k_s^+ \gtrsim 70$ ) via an equivalent sand-grain height,  $k_s$ , that relates arbitrary roughness topographies to the sand-grain experiments of Nikuradse (1933) through the roughness function,  $\Delta U^+$ . As such,  $k_s$  is not a representative geometric scale for a given roughness topography (unless the roughness is sand grain) but simply relates the bulk impact of an arbitrary roughness on the mean flow to sand grain of height  $k_s$ . Table 1 summarizes the salient details of many of the aforementioned studies that observe wall similarity. Interestingly, the common feature between these studies is actually not a threshold on  $k^+$  or  $k_s^+$  as similarity is observed for both transitionally- and fully-rough flows. Instead, the common thread amongst these efforts is a substantial separation between the roughness scale and the outer length scale of the flow via large  $\delta/k$  or  $\delta/k_s$ . It should be noted that Jimenez (2004) proposed a criterion for the existence of wall similarity based on the physical roughness height  $k$  ( $\delta/k \geq 40$ ) while Flack *et al.* (2005) recently proposed a threshold based on  $k_s$  ( $\delta/k_s \geq 40$ ).

Despite significant evidence supporting the validity of Townsend's wall similarity hypothesis in the presence of many different idealized roughness topographies, other studies have indicated substantial modification of the outer layer in the presence of roughness. In particular, Krogstad *et al.* (1992) observed strong outer-layer effects imposed by woven mesh, including modifications of the mean velocity profile and the Reynolds stresses. Numerous other recent studies over different idealized rough surfaces also indicate that wall similarity may not be a universal characteristic of rough-wall turbulence (Shafi & Antonia, 1997; Krogstad & Antonia, 1999; Keirsbulck *et al.*, 2002). The pertinent details of these studies are summarized in table 2 and the most obvious common feature amongst them appears to be rather weak separation between the roughness and

outer length scales. In particular, while a number of these studies have relatively large  $\delta/k$  values, nearly all of them have relatively small values of  $\delta/k_s$ . Therefore, considering this trend, in concert with the trend noted in the studies supporting outer-layer similarity, it appears that substantial separation between the roughness sublayer and the outer flow in the form of large  $\delta/k_s$  represents the appropriate condition for the existence of wall similarity. Interestingly,  $\delta/k$  does not appear to play as strong of a role in this regard despite  $k$  being a more representative measure of the actual wall-normal extent of the specific topography under consideration.

While the many studies mentioned above consider the validity of wall similarity in the presence of sand grain,  $k$ - or  $d$ -type transverse bars, wire mesh and ordered arrays of elements, these surfaces must be considered highly idealized since they typically contain a single roughness scale arranged in an ordered manner. Unfortunately, the roughness encountered in a variety of technologically-relevant applications, like the surfaces of damaged turbine blades and the surfaces of ships and submarines, can be highly irregular and contain a broad range of topographical scales. Unfortunately, few studies have considered the validity of wall similarity in the presence of such surfaces. For example, Allen *et al.* (2007) studied turbulent pipe flow in the presence of a honed surface akin to the industrial-type roughness used by Colebrook (1939) in the formulation of the widely used Moody chart. However, their friction-factor results displayed strong deviation from the Colebrook relationship and instead mimicked the friction-factor trends of Nikuradses sand-grain experiments. Allen *et al.* (2007) also presented smooth- and rough-wall mean velocity defect profiles, streamwise turbulence intensity profiles and streamwise velocity spectra that collapsed in the outer layer in accordance with Townsend's wall similarity hypothesis. Their outer-layer similarity observation represented the first of its kind for a more practical surface topology but for extremely large separation between the roughness and outer length scales ( $\delta/k \sim 51000$ ;  $\delta/k_s \sim 17000$ ).

A crucial and lingering question in rough-wall turbulence is whether wall similarity can be expected in the presence of non-ideal surface topographies that are highly irregular at more moderate  $\delta/k$  and/or  $\delta/k_s$  [i.e. closer to the thresholds proposed by Jimenez (2004) and Flack *et al.* (2005)]. Such behavior is characteristic of many practical flow systems wherein the surface conditions degrade significantly over time. If such similarity is observed in the presence of such surfaces, then outer-layer modeling of many practical rough-wall flows could be greatly simplified. To this end, the present effort assesses the validity of Townsend's wall similarity hypothesis in the presence of the highly-irregular surface topography introduced in section 3 using the PIV measurements in the streamwise-wall-normal plane for smooth, RF1 and RF2 surface conditions.

## 4.2 Mean velocity profiles

The inner-scaled mean velocity profiles at  $Re \approx 13000$  are presented in figure 20(a) for the smooth- and rough-wall cases [Statistics at  $Re_\theta \approx 8000$  are omitted throughout for brevity but can be found in Wu (2008)]. The mean velocity profiles are computed by ensemble-averaging the velocity fields for a given case followed by line-averaging in the streamwise direction in a manner similar to other recent PIV studies of rough-wall turbulence (Nakagawa & Hanratty, 2001; Bijillon *et al.*, 2006). As expected, the presence of roughness shifts the logarithmic region of the mean velocity profiles downward by an  $Re$ -dependent  $\Delta U^+$  and enhances the friction velocity relative to the smooth-wall baseline for RF1 and RF2, respectively. Given  $\Delta U^+ = 8.2$  at  $Re_\theta = 14781$  and  $\Delta U^+ = 7.1$  at  $Re_\theta = 9000$  for RF1, in concert with Eq. (9), the equivalent sand-grain height,  $k_s^+$ , is found to be 115 (2.5 mm) at  $Re_\theta = 14781$  and 74 (2.35 mm) at  $Re_\theta = 9000$ . These  $k_s^+$  values place the RF1 case within the fully-rough regime at both  $Re_\theta$  based on accepted historical classifications. The existence of fully-rough flow under the present RF1 conditions can be verified by ensuring that the skin friction coefficient,  $c_f \equiv 2\tau_w/\rho U_e^2$ , has approached a constant value, independent of  $Re_\theta$  [and hence viscosity since  $c_f$  must only depend on the character of the roughness in the fully-rough

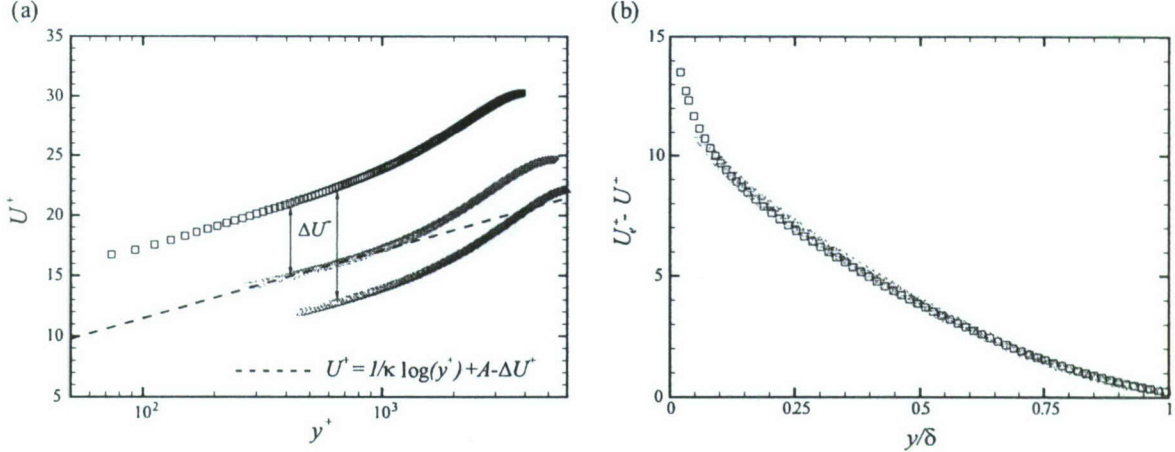


Figure 20: Mean velocity profiles over smooth and rough surfaces at  $Re_\theta \approx 13000$ . (a) Inner scaling; (b) Velocity defect scaling. Not all data points shown for clarity.  $\square$ : Smooth,  $\triangle$ : RF1,  $\nabla$ : RF2.

regime(Schlichting, 1979)]. Alternatively, one can evaluate the onset of fully-rough flow by verifying that the inner-scaled free-stream velocity,  $U_e^+$ , has approached a constant value, independent of  $Re_\theta$ , since  $C_f = 2(U_e^+)^{-2}$ . Current measurements at  $Re_\theta = 9000$  give  $U_e^+ = 22.1$  and  $U_e^+ = 22.2$  is obtained at  $Re_\theta = 14781$ . This consistency in  $U_e^+$  supports the notion that the present RF1 case is fully rough. For the RF2 case,  $\Delta U^+ = 4.9$  gives  $k_s^+ = 29$  at  $Re_\theta = 13685$  while  $\Delta U^+ = 3.5$  yields  $k_s^+ = 17$  at  $Re_\theta = 8332$ . Comparing  $U_e^+ = 24.8$  for the RF2 case at  $Re_\theta = 13685$  with  $U_e^+ = 25.2$  at  $Re_\theta = 8332$  indicates that the RF2 flow is still in transition toward a fully-rough state. It should be noted, however, that both RF1 and RF2 satisfy  $\delta/k_s > 40$  despite the fact that  $\delta/k < 40$  for RF1. Recall that most studies supporting wall similarity (table 1) exhibit large  $\delta/k_s$  values and Flack *et al.* (2005) proposed  $\delta/k_s \geq 40$  as a threshold for wall similarity to exist. In contrast, most studies that do not observe outer-layer similarity suffer from low  $\delta/k_s$  values despite having large values of  $\delta/k$ . As such, the present roughness cases allow evaluation of the Flack *et al.* (2005) threshold of  $\delta/k_s \geq 40$  as well as that of Jimenez (2004) ( $\delta/k \geq 40$ ) for the case of more practical surface roughness.

Figure 20(b) presents the mean velocity profiles for the smooth and rough cases in velocity defect form ( $U_e^+ - U^+$  versus  $y/\delta$ ). Excellent agreement is noted between the two rough-wall velocity defect profiles and the smooth-wall baseline in the overlap and outer layers. This agreement indicates that roughness effects on the mean velocity are confined to the inner layers of the rough-wall flows, supporting the existence of outer-layer similarity. Similar collapse of smooth- and rough-wall mean velocity profiles in defect scaling was also noted recently by Connelly *et al.* (2006) for turbulent boundary layers in the presence of sand grain and wire mesh as well as by Allen *et al.* (2007) for honed surfaces in turbulent pipe flow.

### 4.3 Reynolds stresses

Profiles of the streamwise Reynolds stress,  $\langle u'^2 \rangle$ , in physical units as a function wall-normal position are presented in figure 21(a) for the smooth, RF1 and RF2 cases at  $Re_\theta \approx 13000$ . It is clear that roughness significantly augments  $\langle u'^2 \rangle$  compared to the smooth-wall baseline. In particular, surface RF1 generates a more substantial enhancement of  $\langle u'^2 \rangle$  compared to the RF2 case since its characteristic roughness height is twice that of RF2. A similar enhancement due to roughness is also noted in profiles of the wall-normal Reynolds stress,  $\langle v'^2 \rangle$ , in physical units [figure 22(a)].

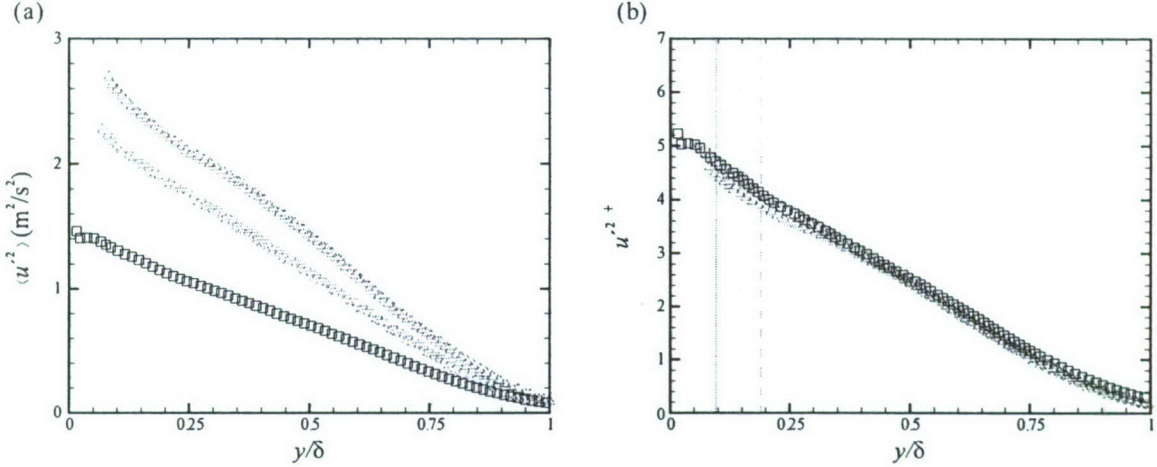


Figure 21: Streamwise Reynolds stress,  $\langle u'^2 \rangle$ , as a function of wall-normal position over smooth and rough surfaces at  $\text{Re}_\theta \approx 13000$ . (a) Physical units ( $\text{m}^2/\text{s}^2$ ); (b) Normalized by  $u_\tau^2$ . Not all data points shown for clarity. Dashed and solid lines in (b) denote the  $5k/\delta$  positions for RF1 and RF2, respectively.  $\square$ : Smooth,  $\triangle$ : RF1,  $\nabla$ : RF2.

When the physical-scale profiles of  $\langle u'^2 \rangle$  and  $\langle v'^2 \rangle$  are normalized by their respective  $u_\tau^2$  values [figure 21(b) for  $\langle u'^2 \rangle$  and figure 22(b)  $\langle v'^2 \rangle$ ], excellent collapse is achieved throughout the outer region from the upper extent of the roughness sublayer (demarcated by the vertical lines at the  $5k/\delta$  positions for the RF1 and RF2 cases) to the boundary-layer edge. This collapse is consistent with the notion of outer-layer similarity wherein the surface conditions set the drag at the boundary (which equivalently sets  $u_\tau$ ) and the turbulence away from the wall adjusts itself to this drag in a universal manner. Similar collapse of rough-wall inner-scaled profiles of  $\langle u'^2 \rangle$  and  $\langle v'^2 \rangle$  with smooth-wall data was recently reported by Flack *et al.* (2005) for flow over sand grain and wire mesh and by Schultz & Flack (2005) for flow over close-packed spheres, with all rough-wall conditions satisfying  $\delta/k_s > 40$ . In addition, Allen *et al.* (2007) noted similar collapse of  $\langle u'^2 \rangle^+$  in the outer layer for smooth- and rough-wall (honed surface) turbulent pipe flow for  $\delta/k_s \sim 17000$ .

Figure 23(a) present profiles of Reynolds shear stress,  $-\langle u'v' \rangle$ , in physical units for the smooth and rough cases at  $\text{Re}_\theta \approx 13000$ . As with the Reynolds normal stresses, the RF1 case yields the greatest enhancement of the turbulent shear stress relative to both the smooth-wall baseline and the RF2 case. In particular, RF1 enhances the peak Reynolds shear stress by a factor of two relative to the smooth-wall case at  $\text{Re}_\theta \approx 13000$ . When normalized by  $u_\tau^2$  [figure 23(b)], excellent collapse of the rough-wall profiles on the smooth-wall baseline is achieved outside of the roughness sublayer ( $y > 5k$ ). This collapse of the mean Reynolds shear stress profiles on  $u_\tau^2$  is again consistent with the notion of outer-layer similarity.

Finally, these Reynolds normal and shear stress profiles indicate that the accepted measure for the outer edge of the roughness sublayer from studies of idealized roughness ( $\sim 3 - 5k$ ) appears to hold well for the roughness studied herein. It should be noted that Flack *et al.* (2005) proposed  $\sim 5k_s$  as a more consistent measure for the outer extent of the roughness sublayer. However, a lack of data below  $5k_s$  in the present experiments does not allow for a detailed evaluation of this possibility for these rough-wall conditions.

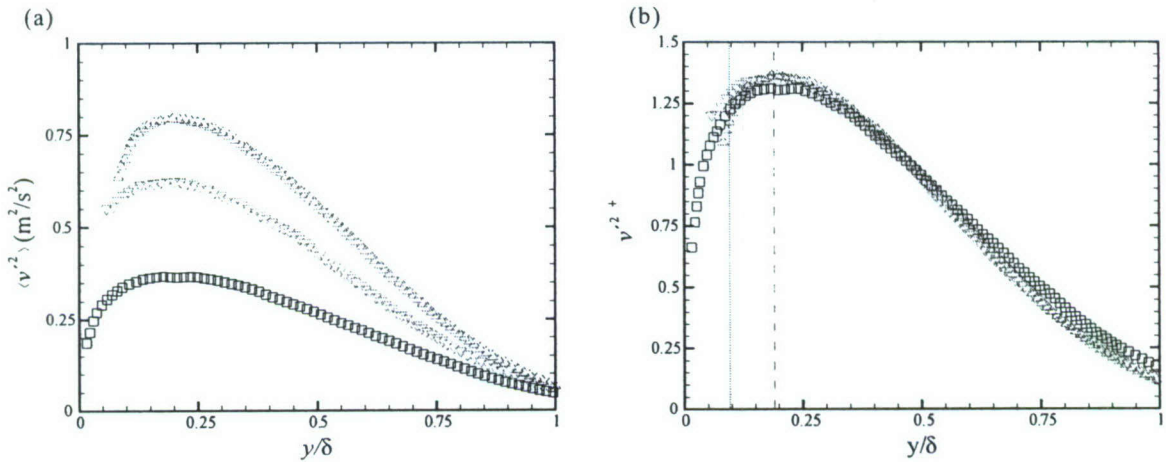


Figure 22: As figure 21, but for wall-normal Reynolds normal stress at  $\text{Re}_\theta \approx 13000$ ,  $\langle v'^2 \rangle$ .

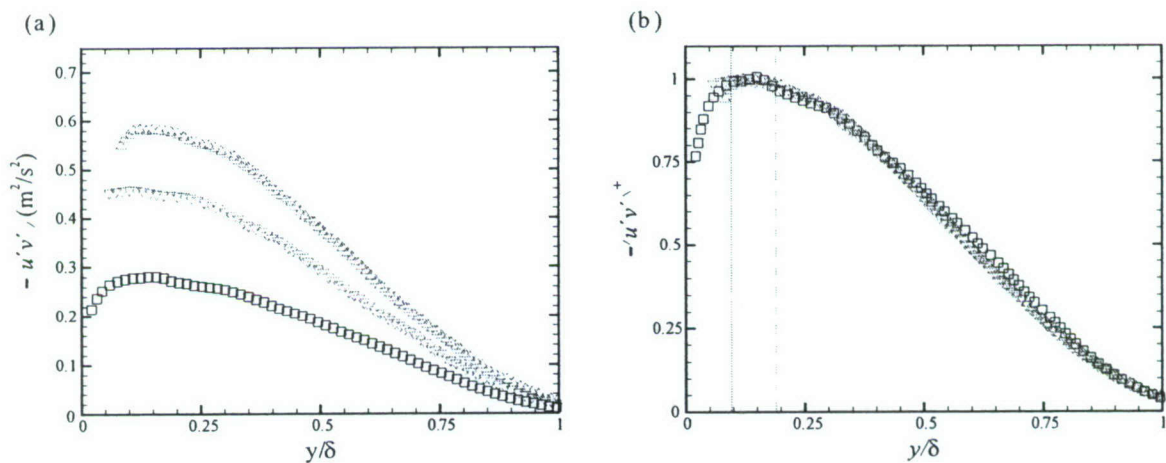


Figure 23: As figure 21, but for Reynolds shear stress at  $\text{Re}_\theta \approx 13000$ ,  $-\langle u'v' \rangle$ .

#### 4.4 Quadrant analysis

While the profiles of  $\langle u'v' \rangle$  show similarity in the outer region when scaled by  $u_\tau^2$ , this collapse need not require that the distributions of the instantaneous  $u'v'$  events contributing to these average profiles be identical between the smooth- and rough-wall cases. To explore such issues, we first consider probability density functions (pdf's) of  $u'v'$  in physical units as presented in figures 24(a)–(c) for the smooth and rough cases at  $y = 0.1\delta$ ,  $0.25\delta$ , and  $0.5\delta$ , respectively, at  $Re_\theta \approx 13000$ . As expected, the pdf's are notably skewed toward negative values in both the smooth- and rough-wall cases, indicative of the dominant contributions of ejection and sweep events to the overall Reynolds stress profiles. Of particular interest is the noted enhancement of both negative and positive  $u'v'$  events in the presence of roughness, particularly in the case of RF1. This enhancement is noted both within the roughness sublayer at  $y = 0.1\delta$  as well as outside the roughness sublayer at  $y = 0.25\delta$  and  $0.5\delta$ . Similar enhancement of Reynolds-stress-producing events was noted by Wu & Christensen (2006b) in fully-developed turbulent channel flow encountering a short streamwise fetch of highly-irregular roughness replicated from a turbine blade damaged by spallation.

When the instantaneous  $u'v'$  events contributing to the pdf's are normalized by  $u_\tau^2$ , excellent collapse of the pdf's is observed irrespective of surface condition and this collapse improves as one moves farther away from the roughness sublayer [figures 24(d)–(f)]. Therefore, while the mean Reynolds shear stress profiles display clear outer-layer similarity when scaled by  $u_\tau^2$ , the collapse of these  $u'v'$  pdf's on  $u_\tau^2$  provides strong support for outer-layer similarity in the Reynolds-stress-producing events that contribute to the overall mean profiles.

One can further evaluate the perceived similarity in the Reynolds-stress-producing events by discriminating between the various quadrant events that contribute to the overall mean Reynolds shear stress profiles. For example, the negative tails of the pdf's embody contributions from both ejections ( $Q2$ ) and sweeps ( $Q4$ ) while the positive tails contain contributions from both outward ( $Q1$ ) and inward ( $Q3$ ) interactions. To explore possible modifications of these individual quadrant events in the presence of roughness, quadrant analysis, as first proposed by Lu & Willmarth (1973), is applied to the smooth and rough cases. In quadrant analysis, the mean Reynolds shear stress at each wall-normal position is decomposed into contributions from the four quadrants of the  $u' - v'$  plane excluding a hyperbolic hole of size  $H$  as

$$\langle u'v' \rangle_Q(y; H) = \frac{1}{M} \sum_{j=1}^M u(x_j, y)v(x_j, y)I_Q(x_j, y; H), \quad (28)$$

where  $M$  is the total number of velocity vectors at each wall-normal position and  $I_Q$  is an indicator function defined as

$$I_Q(x_j, y; H) = \begin{cases} 1, & \text{when } |u'(x_j, y)v'(x_j, y)|_Q \geq H\sigma_u(y)\sigma_v(y) \\ 0, & \text{otherwise,} \end{cases} \quad (29)$$

where  $\sigma_u \equiv \langle u'^2 \rangle^{1/2}$  and  $\sigma_v \equiv \langle v'^2 \rangle^{1/2}$  are root-mean-square streamwise and wall-normal velocities, respectively. The value  $H$  represents a threshold on the strength of the Reynolds-stress-producing events considered in the analysis, with  $H = 0$  allowing all  $u'v'$  events to be included in the decomposition and increasing values of  $H$  allowing inclusion of only increasingly intense Reynolds-stress-producing events.

The contributions from events of all four quadrants to the Reynolds shear stress,  $\langle u'v' \rangle_Q$  ( $Q = 1 - 4$ ), with  $H = 0$  are presented in figures 25(a) and 25(b) at  $Re_\theta \approx 13000$  for smooth and rough cases. The smooth-wall results are consistent with past studies of smooth-wall turbulence:  $Q2$  (ejection) and  $Q4$  (sweep) events contribute heavily to the mean Reynolds shear stress compared to  $Q1$  (outward interaction) and  $Q3$  (inward interaction) events. When the rough-wall contributions

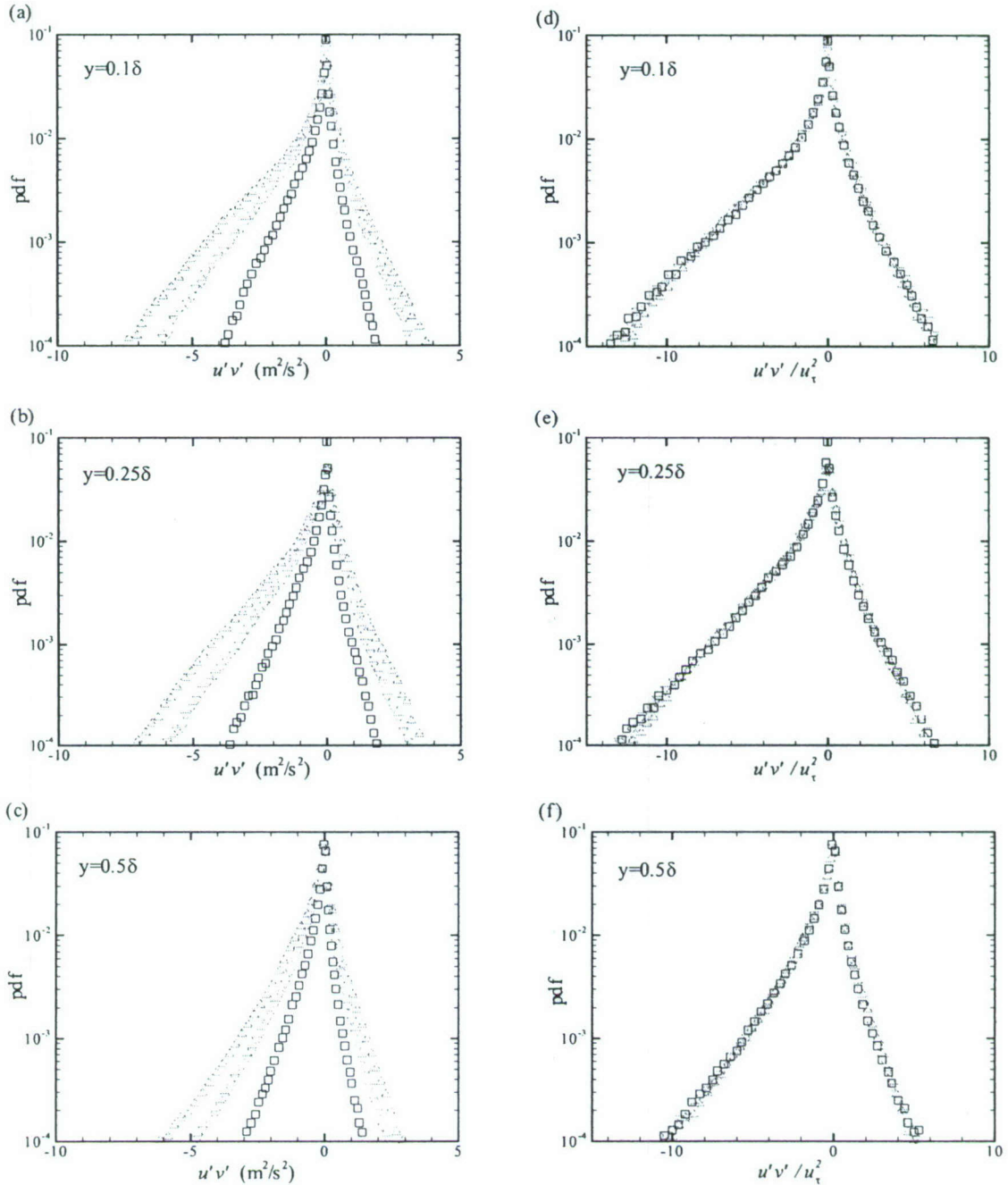


Figure 24: Probability density functions of instantaneous  $u'v'$  events (a,b,c) in physical units ( $\text{m}^2/\text{s}^2$ ) at  $y = 0.1\delta$ ,  $0.25\delta$  and  $0.5\delta$ , respectively and (d,e,f) normalized by  $u_\tau^2$  at  $y = 0.1\delta$ ,  $0.25\delta$  and  $0.5\delta$ , respectively at  $\text{Re}_\theta \approx 13000$ . Not all data points shown for clarity.  $\square$ : Smooth,  $\triangle$ : RF1,  $\nabla$ : RF2.

are compared to the smooth-wall baseline, excellent collapse is observed outside the roughness sublayer ( $y > 5k$ ) for all four quadrant events when appropriately scaled by  $u_\tau^2$ , consistent with the outer-layer similarity observed in the mean Reynolds shear stress. This outer-layer collapse is

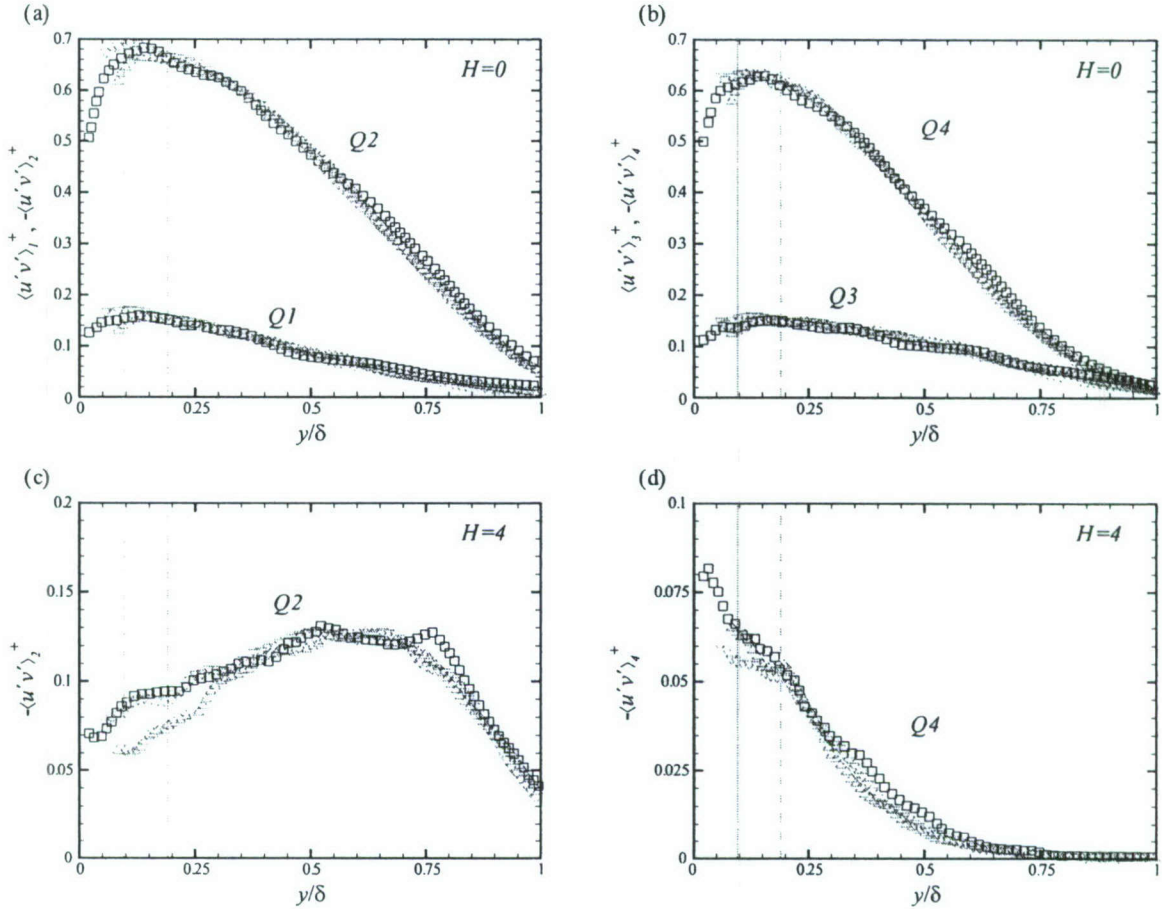


Figure 25: Quadrant contributions to the mean Reynolds shear stress,  $\langle u'v' \rangle_Q^+$ , as a function of wall-normal position for (a,b)  $H = 0$  and (c,d)  $H = 4$  at  $\text{Re}_\theta \approx 13000$ . Lines as in figure 21 and not all data points shown for clarity.  $\square$ : Smooth,  $\triangle$ : RF1,  $\nabla$ : RF2.

also consistent with the quadrant-analysis results of Flack *et al.* (2005) for flow over sand grain and wire mesh topologies. In contrast, Krogstad *et al.* (1992) observed that the contributions from  $Q2$  and  $Q4$  events were enhanced by wire-mesh roughness across most of the outer layer compared to smooth-wall turbulence. It should be noted that the roughness considered in Krogstad *et al.* (1992) was quite strong as evidenced by a relatively weak scale separation of  $\delta/k_s = 15$ .

Figures 25(c) and 25(d) present the  $Q2$  and  $Q4$  contributions, respectively, to the mean Reynolds shear stress for  $H = 4$ . The value  $H = 4$  indicates that only the most intense  $u'v'$  events are included (The contributions from  $Q1$  and  $Q3$  events are nearly zero for  $H = 4$  and are therefore not presented). As with the  $H = 0$  case, reasonable agreement between the smooth and rough cases is observed outside the roughness sublayer ( $y > 5k$ ). These profiles have slightly wider scatter than the  $H = 0$  profiles simply because there are much fewer  $u'v'$  events that satisfy the intense threshold of  $H = 4$ . This scatter is most apparent in the  $Q2$  contributions to the mean Reynolds shear stress for  $H = 4$ , although the variations relative to the smooth-wall baseline are within the estimated uncertainty for this statistic ( $\sim 10 - 15\%$  due the relatively small sample size). Therefore, outer-layer similarity appears to hold for even the most intense Reynolds-stress-producing events. Similar collapse outside the roughness sublayer (with comparable scatter) was also observed by Flack *et al.*

(2005) for  $H = 4$  quadrant contributions in the presence of sand grain and wire mesh.

The collapse observed in the mean Reynolds shear stress profile, the pdf's of the instantaneous Reynolds-stress-producing events and the quadrant contributions to the mean Reynolds shear stress provide significant evidence that the Reynolds-stress-producing events over smooth and rough walls are similar. One question still remains, however, related to the fraction of space in the flow occupied by these Reynolds-stress-producing events for smooth- and rough-wall turbulence. One can define a space fraction,  $N_Q(y; H)$ , for a given  $H$  as

$$N_Q(y; H) = \frac{\sum I_Q(y; H)}{M}, \quad (30)$$

where  $I_Q$  is given by equation (29) and  $M$  is the total number of sample points at a given wall-normal location. Figures 26(a) and 26(b) present the space fractions for  $Q1 - Q4$  events for  $H = 0$  at  $\text{Re}_\theta \approx 13000$ . The smooth- and rough-wall space fractions display strong consistency in the outer layer, indicating that a similar fraction of space in the flow is occupied by the various quadrant events despite markedly different surface conditions. Similar collapse is noted in the space fractions for the most intense Reynolds-stress-producing events ( $H = 4$ ) as presented in figures 26(c) and 26(d) for  $Q2$  and  $Q4$  events, respectively (the space fractions for  $Q1$  and  $Q3$  events are nearly zero for  $H = 4$  and are therefore not presented).

Finally, the ratio of the contributions from  $Q2$  events to contributions from  $Q4$  events,

$$\alpha(y; H) = \frac{\langle u'v' \rangle_2(y; H)}{\langle u'v' \rangle_4(y; H)}, \quad (31)$$

quantifies the relative importance of these events at a given wall-normal position for a specified hole size,  $H$ . Figures 27(a) and 27(b) present  $\alpha$  for the smooth and rough cases at both  $\text{Re}$  for  $H = 0$  and  $H = 4$ , respectively. For  $H = 0$ ,  $\alpha$  collapses across the outer layer except very near  $y = \delta$  where extremely small differences in the Reynolds shear stress contributions are magnified. Values of  $\alpha$  from the wire-mesh studies of Krogstad *et al.* (1992) are included for comparison and consistency is noted with the present results. For  $H = 4$ , the profiles of  $\alpha$  show good collapse in classic semi-log form. The  $\alpha$  results of Flack *et al.* (2005) and Krogstad *et al.* (1992) are also included for comparison and agree well with the present results except very close to the wall. It should be noted that while Krogstad *et al.* (1992) observed noted modifications in the individual Reynolds-stress contributions of ejection and sweep events, these modifications still yielded  $\alpha$  profiles that were consistent between smooth- and rough-wall flows except very close to the wall where substantial differences were noted.

#### 4.5 Two-point velocity correlation coefficients

The single-point statistics presented above show strong similarity between the smooth- and rough-wall cases in the outer layer, consistent with many past studies of idealized roughness topologies (see table 1). However, a question still remains as to whether the *spatial structure* of these flows are similar in the outer layer as well. In particular, understanding modifications of the spatial character of the flow by roughness is important as many turbulence models (large-eddy simulation (LES) subgrid-scale models, for example) and control strategies rely heavily on details of the flow's spatial structure. As outlined in chapter 1, past studies of wall turbulence indicate that the two-point autocorrelation coefficients of streamwise and wall-normal velocity in the  $x - y$  plane,  $\rho_{uu}$  and  $\rho_{vv}$ , given by

$$\rho_{uu}(r_x, y; y_{\text{ref}}) = \frac{\langle u'(x, y_{\text{ref}})u'(x + r_x, y) \rangle}{\sigma_u(y_{\text{ref}})\sigma_u(y)}, \quad (32)$$

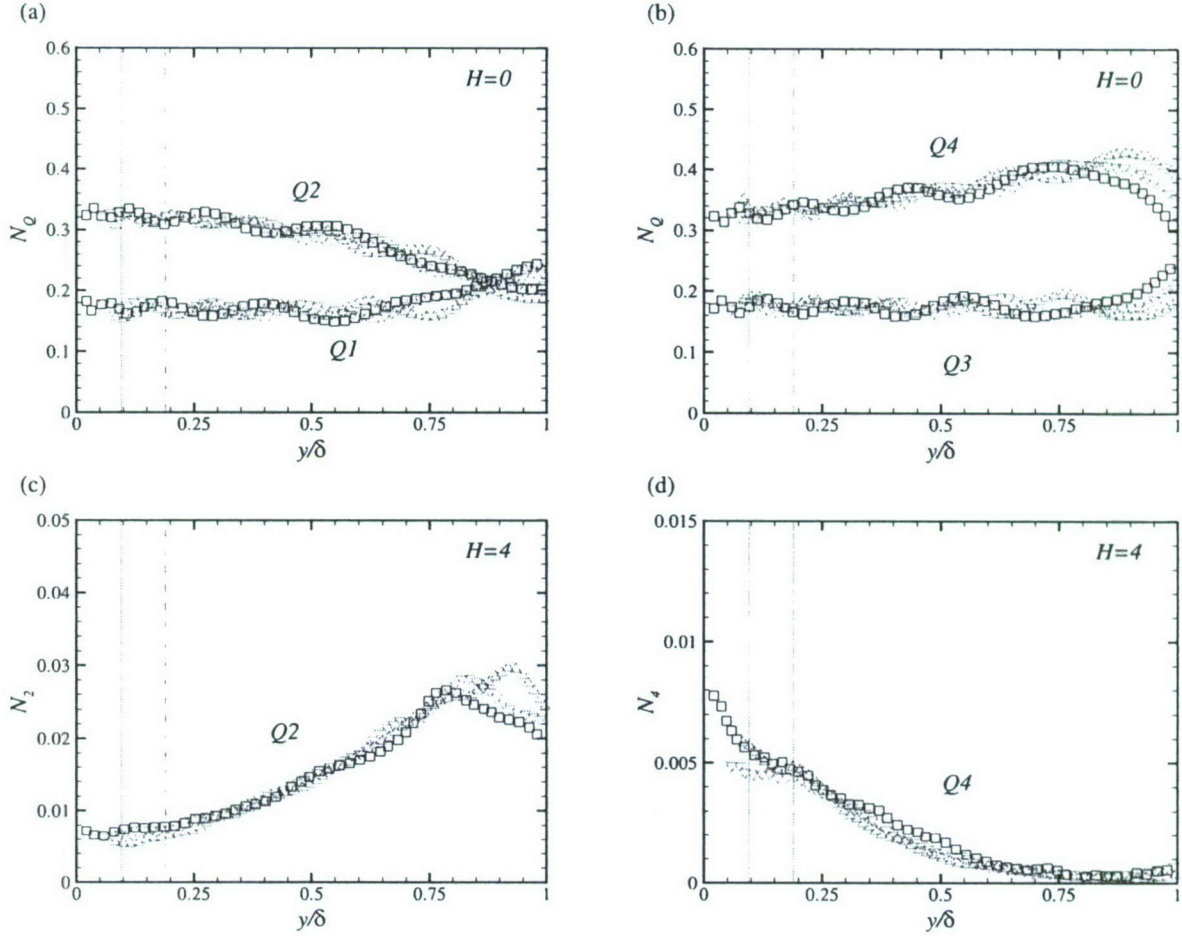


Figure 26: Space fractions,  $N_Q$ , as a function of wall-normal position for (a,b)  $H = 0$  and (c,d)  $H = 4$  at  $\text{Re}_\theta \approx 13000$ . Lines as in figure 21 and not all data points shown for clarity.  $\square$ : Smooth,  $\triangle$ : RF1,  $\nabla$ : RF2.

and

$$\rho_{vv}(r_x, y; y_{\text{ref}}) = \frac{\langle v'(x, y_{\text{ref}}) v'(x + r_x, y) \rangle}{\sigma_v(y_{\text{ref}}) \sigma_v(y)}, \quad (33)$$

mimic the average spatial characteristics of the underlying flow structure. In equations (32) and (33),  $r_x$  is the spatial separation in the streamwise direction,  $y_{\text{ref}}$  is the fixed wall-normal position at which the correlation maps are calculated and  $\sigma_u$  and  $\sigma_v$  are the root-mean-square streamwise and wall-normal velocities, respectively. In particular, Christensen *et al.* (2004) showed that the spatial characteristics of  $\rho_{uu}$  in the  $(r_x, y)$  plane mimic those of large-scale hairpin vortex packets both in streamwise extent and inclination angle. In addition, this effort also revealed a clear consistency between the spatial extent of  $\rho_{vv}$  and the individual spanwise vortices. Therefore, modifications of  $\rho_{uu}$  and/or  $\rho_{vv}$  by roughness would be indicative of possible modifications of the underlying spatial structure of the flow.

While a vast majority of the rough-wall literature has focused on the impact of roughness on the single-point statistics, a few of these efforts have also assessed the impact of idealized roughness on the average spatial character of the flow, typically via two-point autocorrelations of velocity. Krogstad & Antonia (1994) observed a significant reduction in the streamwise extents of  $\rho_{uu}$  and  $\rho_{vv}$

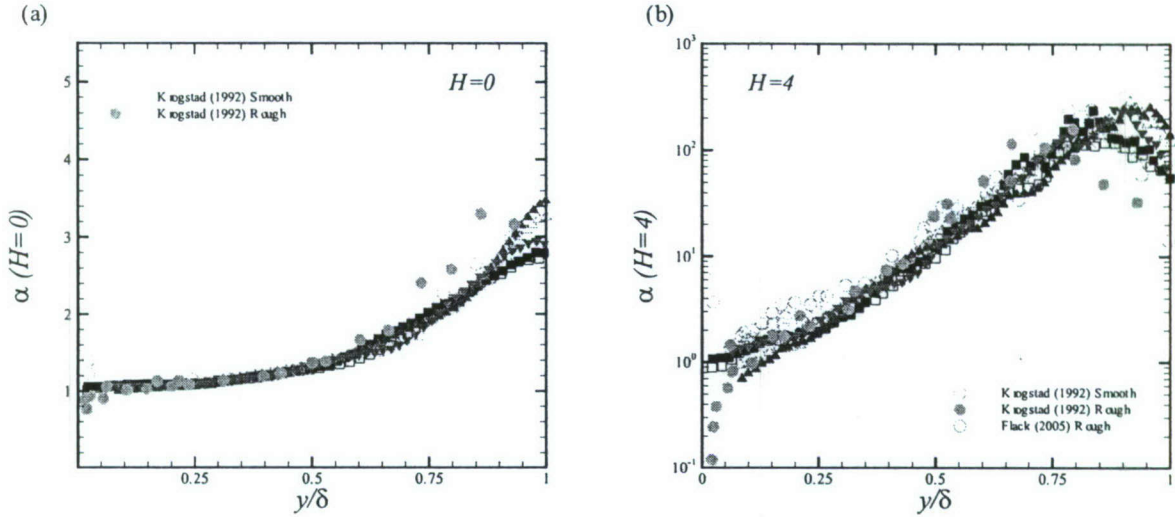


Figure 27: Ratio of Reynolds-shear-stress contributions from  $Q_2$  and  $Q_4$  events,  $\alpha$ , as a function of wall-normal position for (a)  $H = 0$  and (b)  $H = 4$ . Lines as in figure 21 and not all data points shown for clarity.  $\square$ : Smooth at  $Re_\theta \approx 13000$ ,  $\triangle$ : RF1 at  $Re_\theta \approx 13000$ ,  $\nabla$ : RF2 at  $Re_\theta \approx 13000$ ,  $\blacksquare$ : Smooth at  $Re_\theta \approx 8000$ ,  $\blacktriangle$ : RF1 at  $Re_\theta \approx 8000$ ,  $\blacktriangledown$ : RF2 at  $Re_\theta \approx 8000$ .

both within the roughness sublayer and in the outer layer (as inferred from time series of velocity acquired by cross-wire probes) in the presence of woven mesh with  $k_s^+ = 331$  and  $\delta/k_s = 15$ . This effort also reported a drastic increase in the inclination angle of  $\rho_{uu}$  in the  $(r_x, y)$  plane under rough-wall conditions. In contrast, the recent PIV measurements of fully-rough flow over a wavy surface by Nakagawa & Hanratty (2001) indicate a strong similarity in the streamwise extent and inclination angle of  $\rho_{uu}$  as well as the spatial extent of  $\rho_{vv}$  in the outer layer when compared to similar features in smooth-wall turbulence. Nakagawa & Hanratty (2001) hypothesize that the stark differences between their observations and those of Krogstad & Antonia (1994) may be partially attributable to the assumption of a constant convection velocity by Krogstad & Antonia (1994) in the application of Taylor's hypothesis to infer spatial variations of the autocorrelations from time-series data. Finally, Allen *et al.* (2007) reported strong outer-layer similarity in streamwise velocity spectra for smooth- and rough-wall (honed surface) turbulent pipe flow for  $\delta/k_s \sim 17000$ , indicating a negligible impact of roughness on the outer-layer structure under these conditions.

The characteristic streamwise extents of  $\rho_{uu}$  and  $\rho_{vv}$  can be assessed by plotting their one-dimensional profiles for fixed wall-normal position (i.e.  $y = y_{\text{ref}}$ ). Figure 28(a-f) presents one-dimensional profiles of  $\rho_{uu}$  at  $y/\delta = 0.086, 0.1, 0.15, 0.25, 0.4$  and  $0.5$ , respectively, as a function of  $r_x/\delta$  for the smooth and rough cases at  $Re_\theta \approx 13000$ . The wall-normal location  $y = 0.086\delta$  is chosen for comparison because it is the closest position to the surface for which data is available in the  $x - y$  plane measurements for all three surface conditions. Also note that the first three wall-normal locations are within the roughness sublayer defined by  $y < 5k$  for the RF1 case while the first two wall-normal positions are inside the roughness sublayer for the RF2 case. Near the wall, subtle differences exist between the smooth-wall baseline and the rough-wall cases. In particular,  $\rho_{uu}$  is enhanced slightly at moderate  $r_x$  for the RF2 case but diminished slightly for the RF1 case relative to the smooth-wall baseline. Therefore, the characteristic streamwise length scale of  $\rho_{uu}$ , representative of the streamwise extent of outer-layer vortex organization, is enhanced slightly by RF2 but diminished by RF1 relative to the smooth-wall baseline. Recall that the most obvious distinction between RF1 and RF2 is the factor of two difference in the characteristic roughness

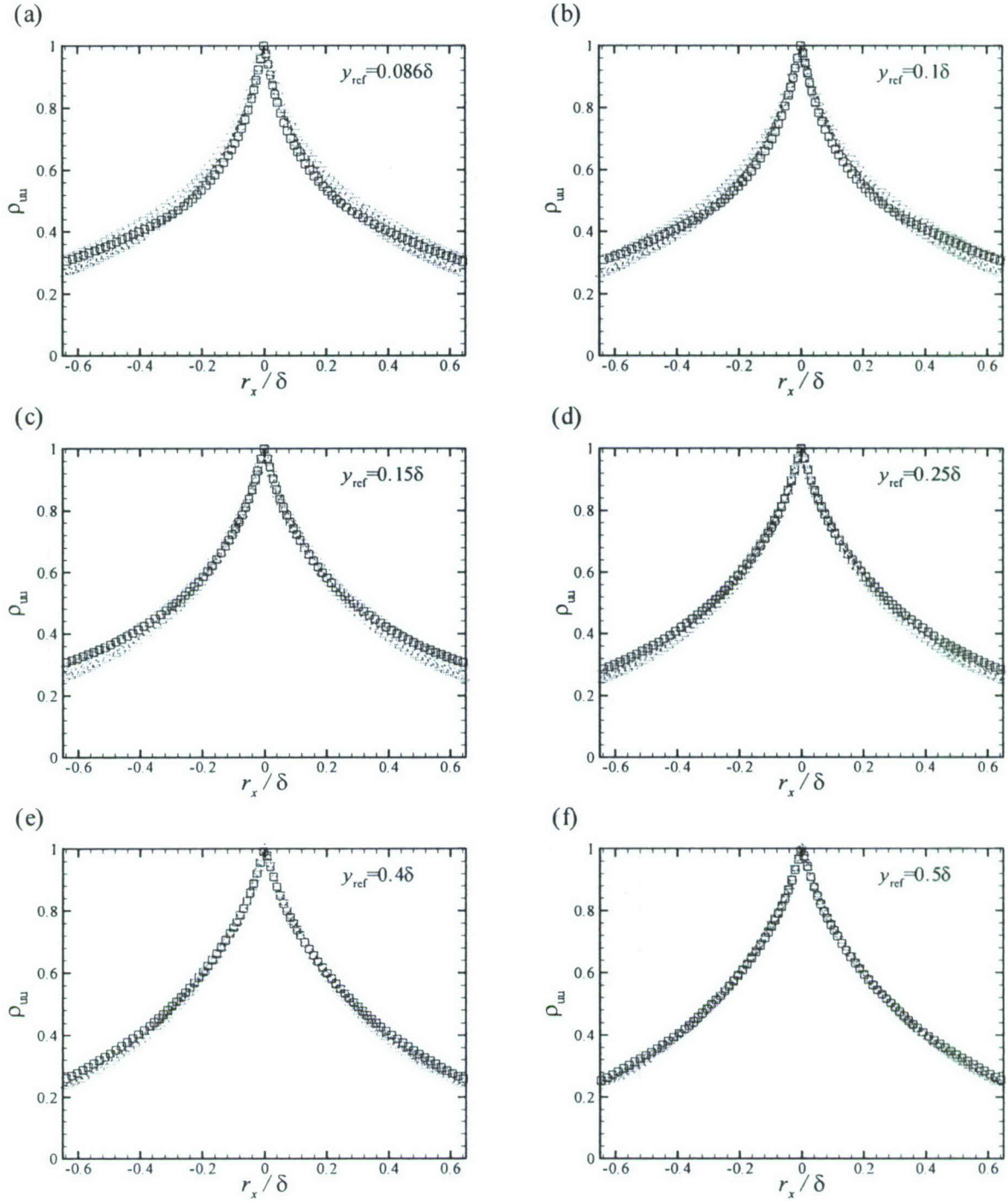


Figure 28: Streamwise velocity autocorrelation coefficients,  $\rho_{uu}$ , at (a)  $y = 0.086\delta$ , (b)  $y = 0.1\delta$ , (c)  $y = 0.15\delta$ , (d)  $y = 0.25\delta$ , (e)  $y = 0.4\delta$ , and (f)  $y = 0.5\delta$  at  $\text{Re}_\theta \approx 13000$ . Not all data points shown for clarity.  $\square$ : Smooth,  $\triangle$ : RF1,  $\nabla$ : RF2.

height,  $k$ , which places RF1 in the fully-rough regime and RF2 in the transitionally-rough regime. However, this factor of two scaling of RF1 relative to RF2 is not only reflected in  $k$  but also in the characteristic *spacing* of the dominant topographical features of the roughness in the streamwise and spanwise directions. As such, the opposing impacts of RF1 and RF2 on  $\rho_{uu}$  in the roughness sublayer may be attributable to one or both of these differences. From a structural viewpoint, these slight differences in  $\rho_{uu}$  within the roughness sublayer may be tied to a roughness-induced modification of the hairpin vortex regeneration mechanism thought to drive the formation and sustainment of coherent vortex packets (Zhou *et al.*, 1996, 1997).

Nevertheless, these roughness effects diminish significantly as the outer layer is approached, with RF2 displaying similarity with the smooth case for  $y > 0.1\delta$  and RF1 showing similarity for  $y > 0.25\delta$ . This outer-layer similarity in  $\rho_{uu}$  is quite consistent with the observations of Nakagawa & Hanratty (2001) for fully-rough flow over a wavy surface but certainly inconsistent with the drastic reduction in the streamwise extent of  $\rho_{uu}$  observed by Krogstad & Antonia (1994) for fully-rough flow over wire mesh. While Nakagawa & Hanratty (2001) attributed these differences to the use of time-series data to infer the character of spatial correlations, these differences may also be due to the weak scale separation ( $\delta/k_s = 15$ ) in the Krogstad & Antonia (1994) experiments.

Figure 29 presents  $\rho_{vv}$  at  $y/\delta = 0.086, 0.1, 0.15, 0.25, 0.4$  and  $0.5$ , respectively, for the smooth and rough cases at  $Re_\theta \approx 13000$ . While roughness has a relatively subtle influence on  $\rho_{uu}$ , it has a much more dramatic impact on  $\rho_{vv}$ . In particular, roughness increases the characteristic width of  $\rho_{vv}$  close to the wall for both roughness cases. In the context of the underlying spatial structure, roughness appears to increase the spatial extent over which the spanwise vortex cores (believed to be the imprint of hairpin heads) exert their influence. This roughness effect diminishes as one moves away from the wall, with excellent collapse occurring for  $y \geq 0.25\delta$ . It should be noted that while  $\rho_{uu}$  collapsed outside the roughness sublayer for the RF2 case ( $y > 0.1\delta$ ), collapse between the RF2 and smooth cases for  $\rho_{vv}$  is not noted until  $y = 0.25\delta$ . Finally, while RF1 and RF2 yield opposing effects on  $\rho_{uu}$ , they produce a nearly identical enhancement of  $\rho_{vv}$  for moderate  $r_x$  despite a factor of two difference in their characteristic roughness scales. This noted enhancement of the streamwise extent of  $\rho_{vv}$  within the roughness sublayer is counter to the reduction in the spatial extent of  $\rho_{vv}$  reported by Krogstad & Antonia (1994) for flow over wire mesh (both within and outside the roughness sublayer) while the outer-layer similarity in  $\rho_{vv}$  reported herein is consistent with the outer-layer similarity reported by Nakagawa & Hanratty (2001) for flow over a wavy surface.

Finally, figures 30 and 31 present one-dimensional profiles of cross-correlation coefficients of streamwise and wall-normal velocities,  $\rho_{uv}$  and  $\rho_{vu}$ , respectively, at  $Re_\theta \approx 13000$  for both smooth and rough surfaces. These cross-correlations are given by

$$\rho_{uv}(r_x, y; y_{ref}) = \frac{\langle u'(x, y_{ref})v'(x + r_x, y) \rangle}{\sigma_u(y_{ref})\sigma_v(y)}, \quad (34)$$

and

$$\rho_{vu}(r_x, y; y_{ref}) = \frac{\langle v'(x, y_{ref})u'(x + r_x, y) \rangle}{\sigma_v(y_{ref})\sigma_u(y)}, \quad (35)$$

It is seen that within the roughness sublayer, the streamwise extents of  $\rho_{uv}$  and  $\rho_{vu}$  are significantly increased in the presence of roughness, with RF1 and RF2 yielding similar enhancements. Further away from the wall, similarity in the cross correlations is observed, consistent with the similarity noted in the autocorrelations outside the roughness sublayer.

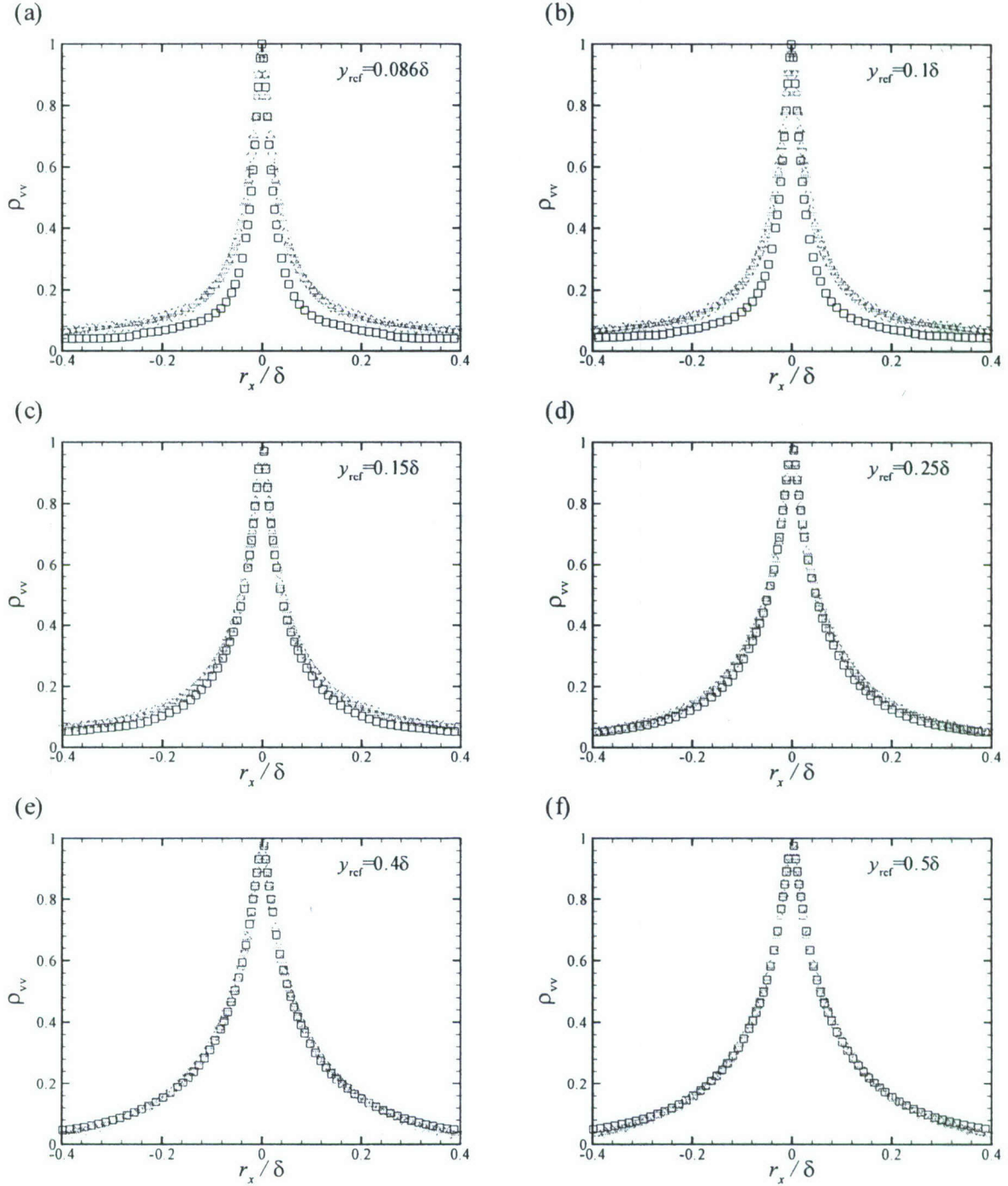


Figure 29: As figure 28 but for wall-normal velocity autocorrelation coefficients,  $\rho_{vv}$ , at  $Re_\theta \approx 13000$ .

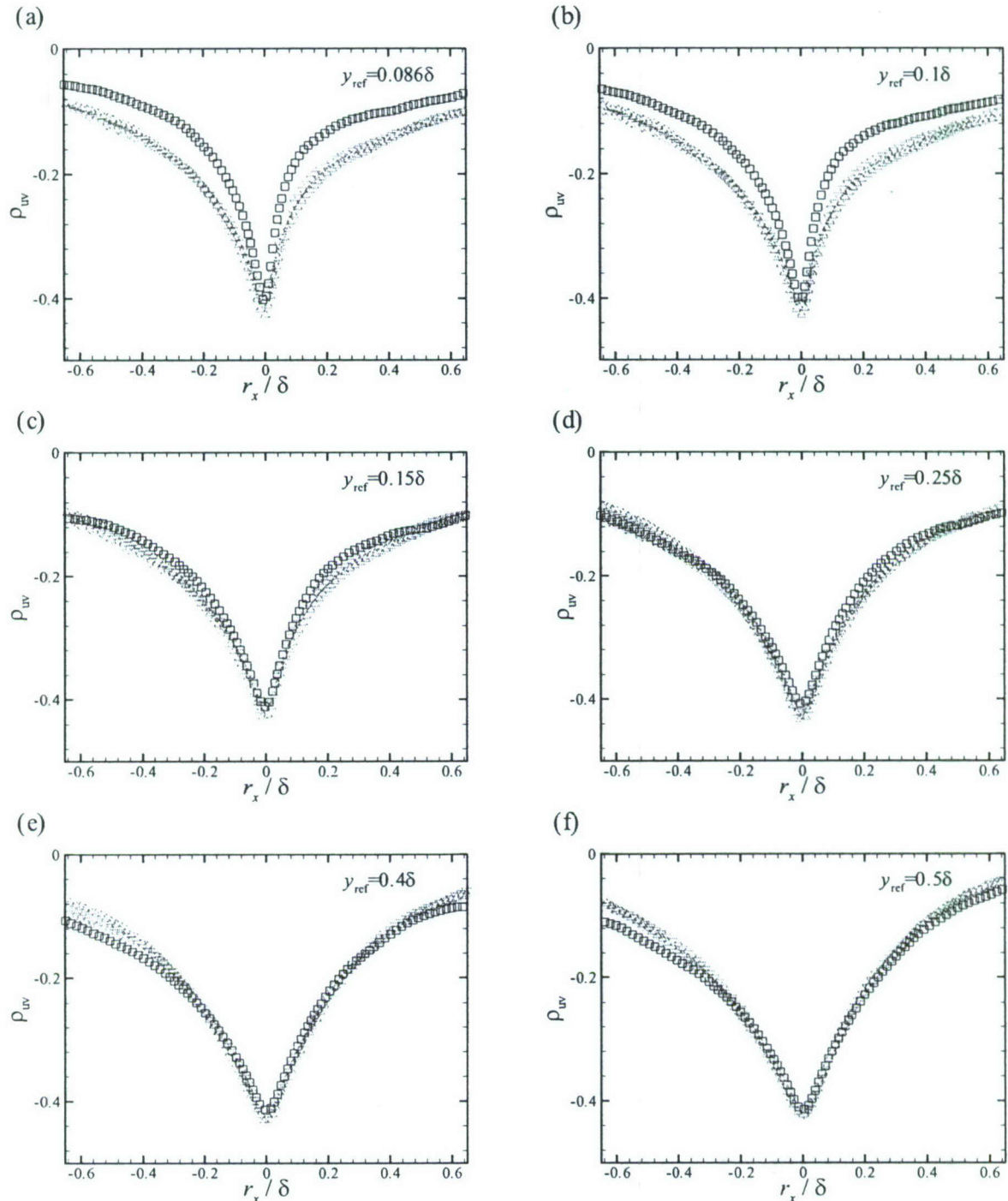


Figure 30: As figure 28 but for velocity cross-correlation coefficients,  $\rho_{uv}$ , at  $\text{Re}_\theta \approx 13000$ .

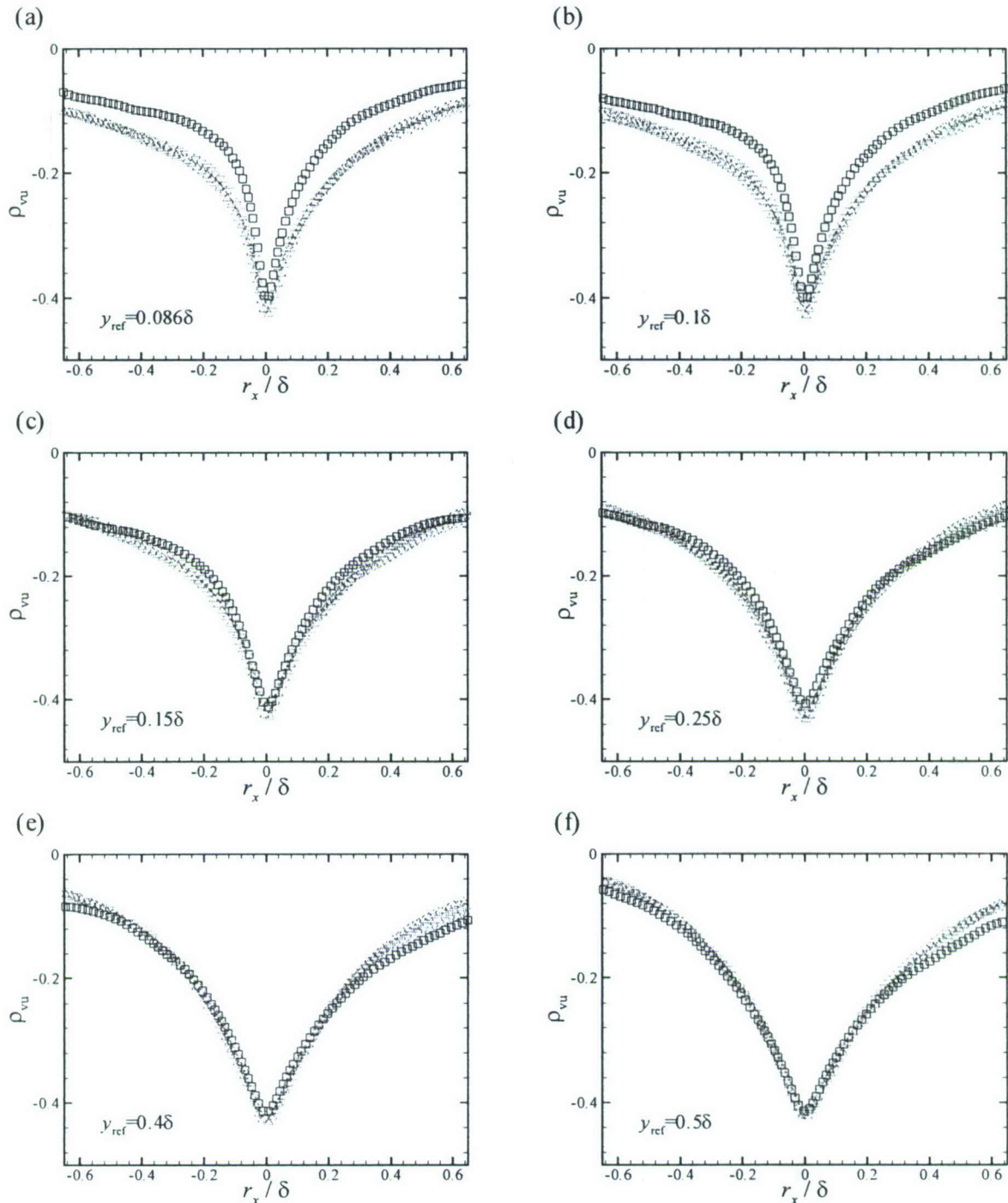


Figure 31: As figure 28 but for velocity cross-correlation coefficients,  $\rho_{vu}$ , at  $\text{Re}_\theta \approx 13000$ .

## 4.6 Summary

High-resolution PIV measurements are performed in the streamwise-wall-normal plane of a zero-pressure-gradient turbulent boundary layer over both smooth and rough walls at  $Re_\theta \approx 8000$  and 13000. Of particular interest is the fact that the roughness studied herein is quite distinct from the idealized topographies normally studied in the laboratory (sand grain, wire mesh, etc.) in that it is highly irregular and contains a broad range of topographical scales. Inner-scaled mean velocity profiles over the rough surfaces display the expected downward shift of the log region by the roughness function  $\Delta U^+$ . In addition, the mean velocity profiles are found to collapse in velocity defect scaling irrespective of surface condition. This collapse supports the existence of outer-layer similarity in the presence of the roughness studied herein.

The Reynolds normal and shear stresses are found to be significantly enhanced by the roughness in an absolute sense, particularly for the RF1 case. However, excellent collapse of these stress profiles is noted outside the roughness sublayer when scaled by  $u_r^2$ , supporting the notion of wall similarity. Similar collapse is noted when quadrant analysis is used to assess the contributions from various Reynolds-stress-producing events to the overall mean Reynolds shear stress. These observations of outer-layer similarity in the Reynolds stresses represent the first of their kind for a highly-irregular surface topography at moderate  $\delta/k_s$  that is representative of what one might encounter in a technologically relevant flow.

Two-point autocorrelations of streamwise and wall-normal velocity fluctuations indicate a modification of the underlying spatial structure of the flow within the roughness sublayer, particularly a noted enhancement in the streamwise extent of  $\rho_{vv}$  for both rough-wall cases. It is also observed that the degree of this enhancement depends on Reynolds number, with the lower-Re rough-wall flows generating subtler deviations from smooth-wall flow. In addition, at  $Re_\theta \approx 13000$ , the effects of the two roughness conditions on  $\rho_{uu}$  in the roughness sublayer are counter to one-another, with RF2 yielding a slight enhancement in the streamwise extent of  $\rho_{uu}$  relative to the smooth-wall baseline as compared to a slight reduction produced by RF1. On the other hand, the lower-Reynolds-number case indicates little effect of the RF2 surface on  $\rho_{uu}$ . Despite the above noted differences in the roughness sublayer, similarity is noted in both  $\rho_{uu}$  and  $\rho_{vv}$  when the smooth- and rough-wall cases are compared in the outer layer, consistent with the observations of Nakagawa & Hanratty (2001) for flow over a wavy surface as well as the similarity noted in streamwise velocity spectra for smooth- and rough-wall turbulent pipe flow by Allen *et al.* (2007). Therefore, while the underlying structure of the turbulence appears modified slightly in the roughness sublayer, the length scales of the outer-layer structure appear minimally affected in the presence of the roughness topography presented herein. Further, the streamwise extents of the cross-correlation coefficients of streamwise and wall-normal velocities,  $\rho_{uv}$  and  $\rho_{vu}$ , are only influenced by roughness within the roughness sublayer, as collapse is noted in the outer layer at both  $Re$ .

Finally, the present results suggest that the classical measure of  $\sim 3 - 5k$  for the outer extent of the roughness sublayer as determined from idealized roughness studies holds well for the more practical roughness topography studied herein. Unfortunately, while it was recently proposed by Flack *et al.* (2005) that  $\sim 5k_s$  may be a more consistent measure of the roughness sublayer's outer boundary, a lack of data below  $5k_s$  in the present effort does not allow a proper evaluation of this proposition. Finally, it should be noted that wall similarity is noted in both the RF1 and RF2 cases, despite the fact that  $\delta/k = 28 < 40$  for RF1. In terms of  $\delta/k_s$ , both RF1 and RF2 satisfy the threshold of  $\delta/k_s > 40$  proposed by Flack *et al.* (2005) for the existence of wall similarity. Therefore, the present results lend further support to the importance of  $\delta/k_s$ , rather than  $\delta/k$ , in assessing whether wall similarity should be expected in a rough-wall flow.

## 5 Turbulence modifications in the roughness sublayer

### 5.1 Background

As noted earlier, it is well-documented that turbulence is strongly affected in the immediate vicinity of a rough surface. In particular, the wall-normal velocity fluctuations appear to be most sensitive to rough-wall conditions (Raupach, 1981; Bandyopadhyay & Watson, 1988; Krogstad *et al.*, 1992; Krogstad & Antonia, 1999; Keirnsbulck *et al.*, 2002). It has also been extensively reported that these modifications are often highly dependent on the details of the local surface conditions (Raupach, 1981; Bandyopadhyay & Watson, 1988; Raupach *et al.*, 1991; Krogstad & Antonia, 1999; Keirnsbulck *et al.*, 2002; Jimenez, 2004) and that such effects may be attributable to the local generation of additional intense vortical structures in rough-wall flows via shedding from dominant topographical features (Bandyopadhyay & Watson, 1988).

A rather significant body of literature exists documenting vortical structures generated by discrete wall-mounted elements (and isolated wall disturbances, like blowing) in both laminar and turbulent wall-bounded flows. Acarlar & Smith (1987a), for example, observed the periodic shedding of hairpin-like vortices from a wall-mounted hemisphere in an otherwise laminar boundary layer for  $120 < Re_R = \hat{u}R/\nu < 3400$ , where  $\hat{u}$  is the streamwise velocity at the tip of the bump and  $R$  is the height of the bump. The hairpin structures periodically shed from the hemisphere were observed to convect downstream and this train of vortices generated an elongated low-momentum region in the wake of the element. In addition, a stationary “necklace” vortex was observed to form around the perimeter of the element whose legs extended well downstream of the hemisphere. With regard to the influence of isolated roughness elements in a turbulent boundary layer, Castro & Robins (1977) studied the flow around a rather large surface-mounted cube ( $h/\delta = 0.1$ , where  $h$  is the linear dimension of the cube) in both laminar and turbulent boundary layers and found that increased turbulence levels upstream of the cube reduced the size of the wake generated downstream of the element. Savory & Toy (1986) also considered the flow downstream of a large surface-mounted element (hemispheres with  $R/\delta > 0.26$ ) for smooth- and rough-wall upstream flows and reported that if vortices are shed from the hemisphere their influence is certainly limited to the region just downstream of the element. They conjectured that the absence of sustained shedding and large-scale wakes was attributable to strong turbulence levels in the vicinity of the element as well as the three-dimensionality of the flow. Similar lack of consistent shedding from and persistent wakes downstream of large surface-mounted elements immersed in turbulent boundary layers has also been reported in other studies (Schofield & Logan, 1990; Martinuzzi & Tropea, 1993).

Other studies have considered the influence of much smaller discrete roughness elements in the presence of turbulence, particularly their impact within the near-wall region and the possible generation of sustained wakes as an explanation for the increased turbulence levels observed in the roughness sublayer. Bandyopadhyay & Watson (1988), for example, noted significant differences in the vertical flux of the Reynolds shear stress,  $\langle u'v' \rangle$ , for smooth, 2-D (transversely grooved) rough and 3-D rough surfaces. In the case of smooth and 2D rough conditions, it was suggested that the net vertical transport of  $\langle u'v' \rangle$  away from the wall can be accounted for by the existence of hairpin-like vortices that may be shed by the discrete roughness elements in the case of the rough-wall flow. However, the observed transport of  $\langle u'v' \rangle$  toward the wall in the 3D roughness case was interpreted in terms of an additional vortical structure, “necklace” vortices, that straddle the 3D roughness elements near their bases. This latter explanation is quite consistent with the structural observations of Acarlar & Smith (1987a) for laminar flow around an isolated surface-mounted hemisphere. More recently, Tomkins (2001) performed detailed particle image velocimetry (PIV) measurements for flow over ordered arrays of hemispheres. Significant modifications of the

turbulence were observed just downstream of the elements; however, the flow was found to relax toward a state consistent with smooth-wall turbulence rather quickly ( $\sim \delta$ ) downstream of the discrete hemispheres.

This section explores the turbulence heterogeneities generated in the immediate vicinity of dominant topographical features of the RF1 surface within the roughness sublayer using the aforementioned stereo PIV measurements in a streamwise–spanwise plane within the roughness sublayer ( $y = 0.065\delta$ ). The persistence of observed heterogeneities outside the roughness sublayer is also explored with stereo PIV measurements in a streamwise–spanwise plane inside the logarithmic region but at the outer edge of the roughness sublayer ( $y = 0.15\delta$ ). Finally, structural explanations for roughness-induced heterogeneities are considered and the wall-normal extent of these modifications is documented.

## 5.2 Statistical imprints of the roughness

The turbulence statistics presented in section 4 indicate that roughness does indeed alter the quantitative values of the turbulence statistics in the roughness sublayer. Unfortunately, the  $x - y$ -plane data used to assess the validity of outer-layer similarity does not provide sufficient information in the immediate vicinity of the rough surface to effectively study these influences. The aforementioned PIV measurements in select streamwise–spanwise planes within and at the outer edge of the roughness sublayer, however, provide an excellent opportunity to explore these differences in greater detail. These quantitative differences can be further explored by computing various statistics of the flow, including the ensemble-averaged mean velocity fields as well as the ensemble-averaged Reynolds normal and shear stress fields in the measurement plane. These statistics can then be used to answer several questions, including: Do certain roughness features generate consistent low- and/or high-momentum regions? Are the turbulent stresses enhanced by dominant topographical features and if so, then how localized are these modifications? Are there structural explanations for any observed roughness-induced modifications? It should be noted that in the discussion that follows, the smooth-wall statistics are omitted for brevity since, as should be expected, they all appear uniform (within statistical sampling bounds) in the streamwise–spanwise planes of interest. The focus is therefore upon the ensemble-averaged statistics for the rough-wall flow in streamwise–spanwise planes at  $y = 0.065\delta$  (within the roughness sublayer) and  $y = 0.15\delta$  (toward the outer edge of the roughness sublayer).

To facilitate this discussion, the roughness topography spatially coincident with the streamwise–spanwise PIV measurement planes is plotted in figure 32, with figure 32(b) highlighting topographical features that protrude into the flow relative to the mean elevation of the roughness (same as figure 15). Several strong roughness protrusions above the mean elevation exist and are labeled A–G in figure 32(b). Figures 33(a) and 33(b) present the ensemble-averaged streamwise velocity fields,  $\langle u \rangle$ , normalized by the ensemble- and area-averaged streamwise velocity,  $U$ , at  $y = 0.065\delta$  and  $y = 0.15\delta$ , respectively for  $Re_\theta = 14781$  (Throughout,  $\langle \cdot \rangle$  implies an ensemble-averaged quantity that retains its dependence on spatial location). In addition, data for  $Re_\theta \approx 8000$  is not presented for brevity but can be found in Wu (2008.). Weak reductions of the local mean streamwise velocity, less than 10% of  $U$ , are evident in the roughness sublayer [figure 33(a)] and occur at spatial locations coincident with roughness protrusions A–G as identified in figure 32(b). There are, however, no identifiable large-scale imprints of low- or high-momentum regions in the ensemble-averaged streamwise velocity field within the roughness sublayer, indicating that such large-scale flow features are not consistently generated by dominant roughness features. In addition, these roughness-induced heterogeneities in  $\langle u \rangle$  are found to be localized within the roughness sublayer as the mean streamwise velocity field at  $y = 0.15\delta$  appears uniform (within statistical sampling bounds) as shown in figure 33(b).

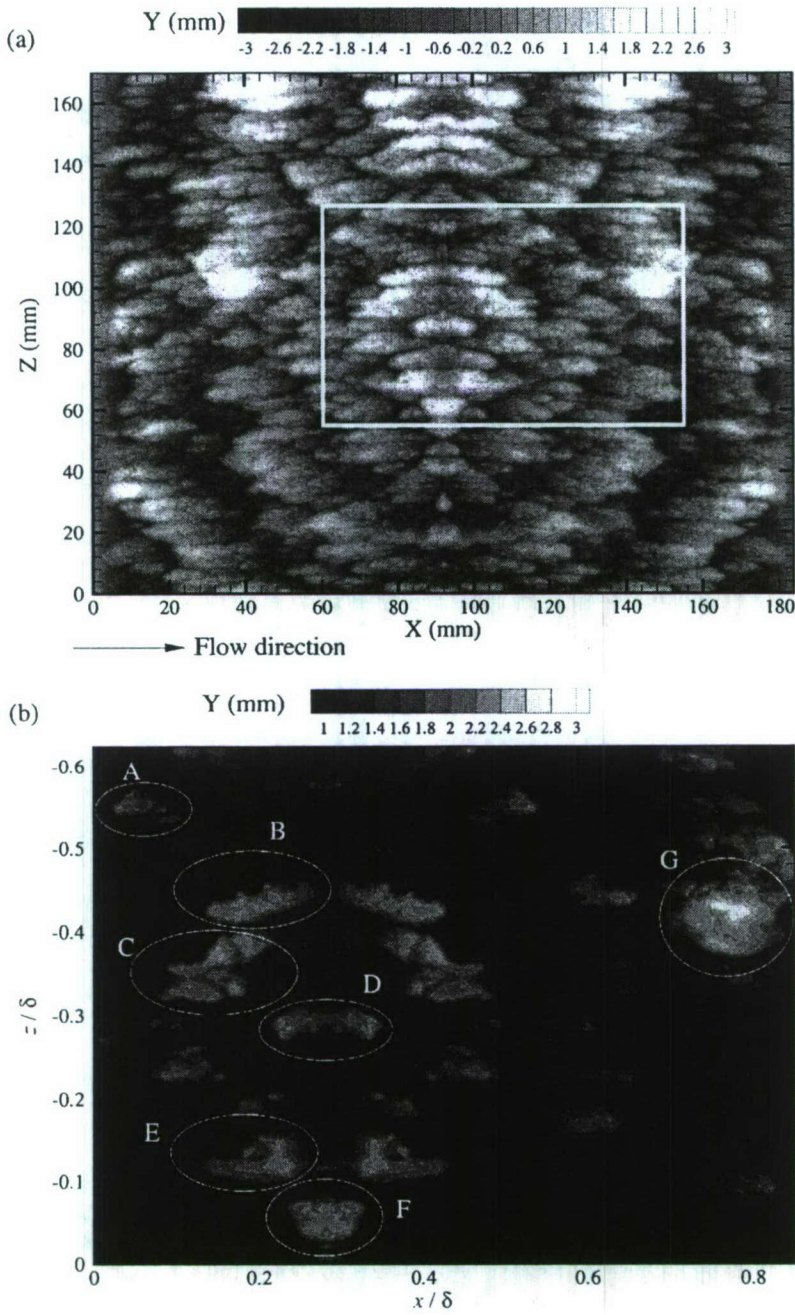


Figure 32: (a) Surface contours of a portion of the roughness topography plotted as fluctuations about the mean roughness height and oriented such that flow is from left to right. The stereo PIV measurement domain is highlighted with the white rectangle. (b) Surface contours of the roughness above the mean height coincident with the stereo PIV field measurement domain.

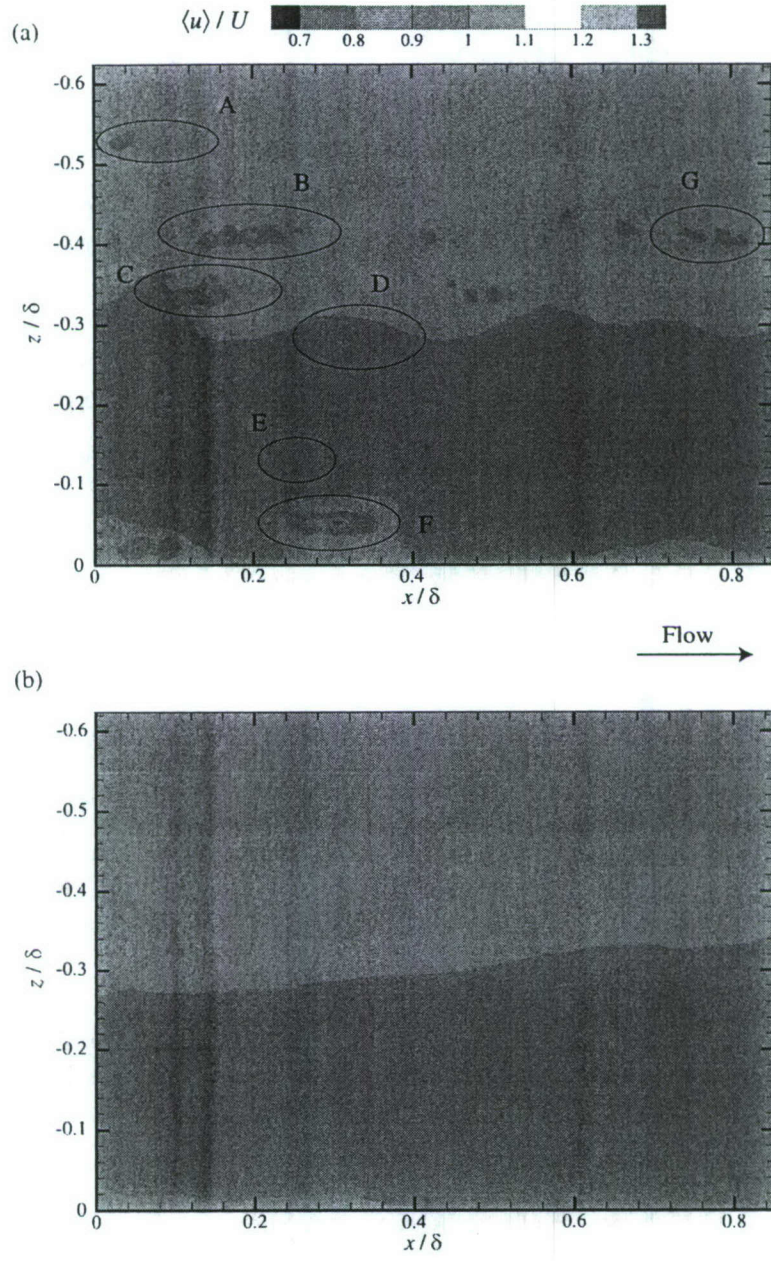


Figure 33: Ensemble-averaged streamwise velocity,  $\langle u \rangle$ , normalized by the ensemble- and area-averaged mean streamwise velocity,  $U$ , in streamwise–spanwise planes at (a)  $y = 0.065\delta$  and (b)  $y = 0.15\delta$  for flow over the RF1 surface at  $\text{Re}_\theta = 14781$ .

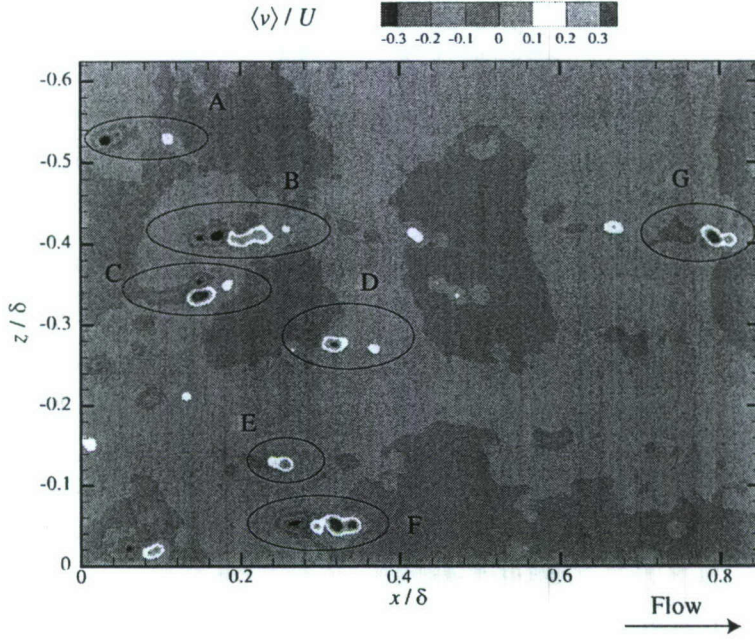


Figure 34: Ensemble-averaged wall-normal velocity,  $\langle v \rangle$ , normalized by the ensemble- and area-averaged mean streamwise velocity,  $U$ , in the streamwise–spanwise plane at  $y = 0.065\delta$  for flow over the RF1 surface at  $\text{Re}_\theta = 14781$ .

Figure 34 presents the normalized ensemble-averaged wall-normal velocity,  $\langle v \rangle/U$ , within the roughness sublayer at  $y = 0.065\delta$  for  $\text{Re}_\theta = 14781$ . Significant roughness-induced heterogeneities in  $\langle v \rangle$ , almost 30% of  $U$  in some cases, are notable within the roughness sublayer but these modifications are again localized around roughness features A–G. As with  $\langle u \rangle$ , there are no discernable imprints of persistent wakes being generated downstream of roughness features A–G in  $\langle v \rangle$ . In addition, near the outer edge of the roughness sublayer, at  $y = 0.15\delta$ , these localized roughness effects are not noted as the mean wall-normal velocity field (not shown for brevity) displays uniformity akin to that of  $\langle u \rangle$  in figure 33(b).

Figure 35(a) presents the streamwise Reynolds normal stress in inner units,  $\langle u'^2 \rangle^+$ , in the streamwise–spanwise plane at  $y = 0.065\delta$  for flow over the rough wall at  $\text{Re}_\theta = 14781$ . In the present analysis, the velocity fluctuations,  $u'_i$ , are computed as

$$u'_i(x, y, z) = u_i(x, y, z) - \langle u_i \rangle(x, y, z), \quad (36)$$

where  $u_i$  is the total instantaneous velocity and  $\langle u_i \rangle$  is the ensemble-averaged velocity as defined earlier. As with the ensemble-averaged mean velocities, localized heterogeneities in  $\langle u'^2 \rangle^+$  are noted throughout the measurement region. In particular, each of these regions represents a slight reduction of  $\langle u'^2 \rangle^+$  relative to the background levels and they occur spatially coincident with roughness features A–G. Further, there is again no evident of persistent wakes being generated by dominant topographical events as elongated regions of modification in  $\langle u'^2 \rangle^+$  are not noted downstream of roughness features A–G. Finally, the heterogeneities in  $\langle u'^2 \rangle$  at  $y = 0.065\delta$  appear confined to the roughness sublayer as a relatively uniform  $\langle u'^2 \rangle^+$  field is observed for flow over the rough wall at  $y = 0.15\delta$  [figure 35(b)].

Figure 36 presents the wall-normal Reynolds normal stress in inner units,  $\langle v'^2 \rangle^+$ , in a streamwise–spanwise plane within the roughness sublayer at  $y = 0.065\delta$  for  $\text{Re}_\theta = 14781$ . In contrast to  $\langle u'^2 \rangle^+$ ,

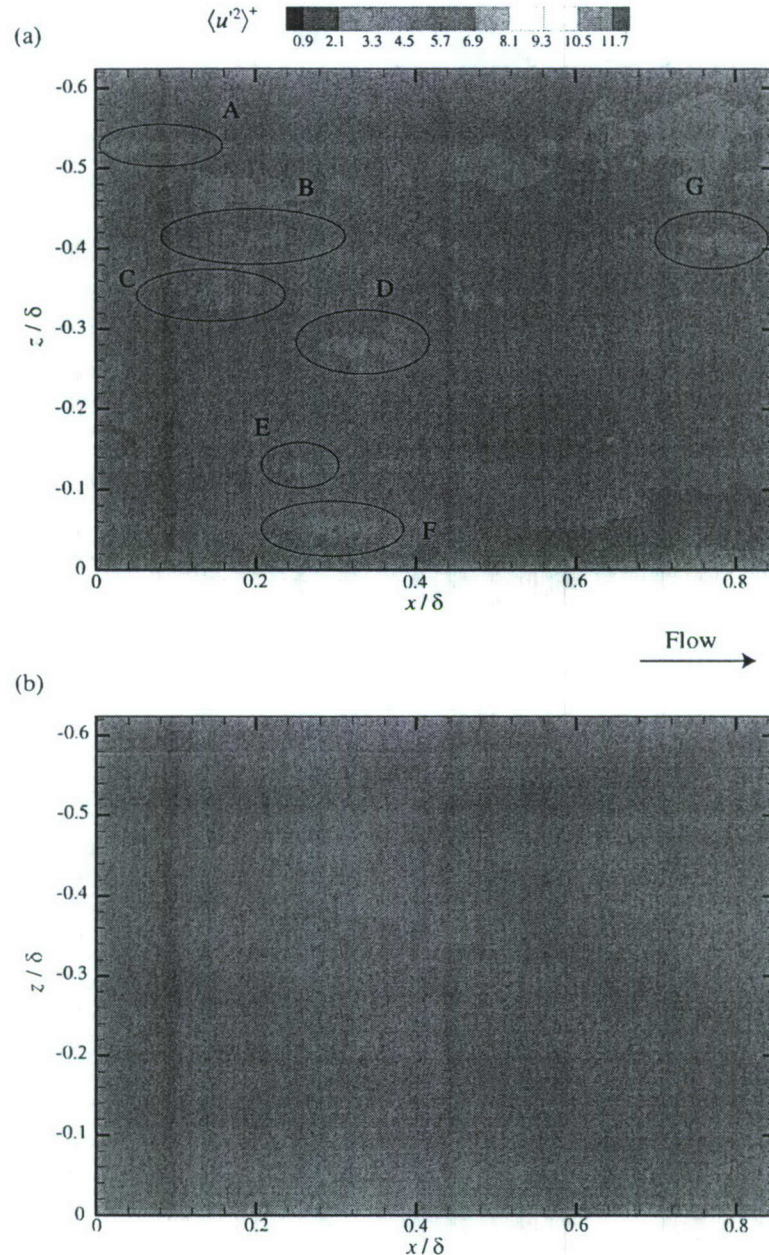


Figure 35: Inner-scaled streamwise Reynolds normal stress,  $\langle u'^2 \rangle^+$ , in streamwise-spanwise planes at (a)  $y = 0.065\delta$  and (b)  $y = 0.15\delta$  for flow over the RF1 surface at  $\text{Re}_\theta = 14781$ .

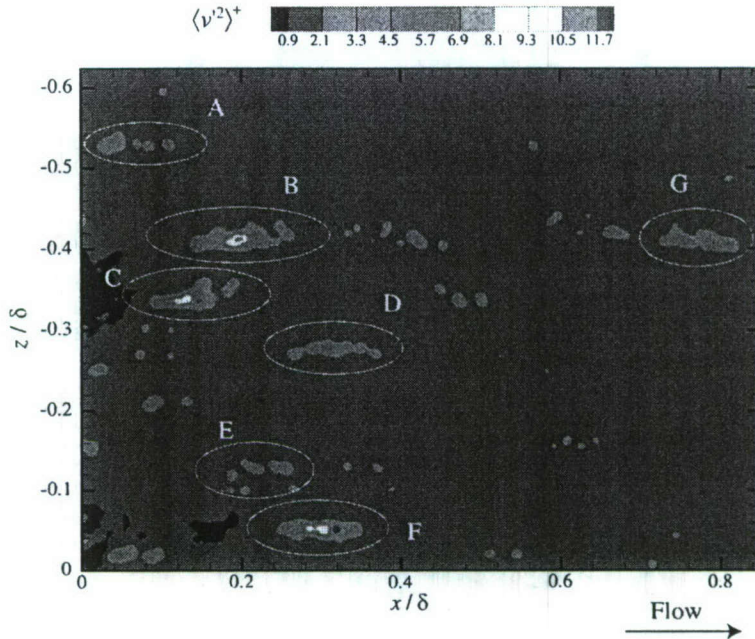


Figure 36: Inner-scaled wall-normal Reynolds normal stress,  $\langle v'^2 \rangle^+$ , in the streamwise–spanwise plane at  $y = 0.065\delta$  for flow over the RF1 surface at  $\text{Re}_\theta = 14781$ .

$\langle v'^2 \rangle^+$  shows rather significant enhancement locally around topographical features A–G compared to the surrounding regions. Despite the intensity of these local heterogeneities in  $\langle v'^2 \rangle^+$  within the roughness sublayer, there is again no evidence of persistent wakes being generated downstream of topographical features A–G and these heterogeneities diminish quickly as one moves further away from the wall as  $\langle v'^2 \rangle^+$  at  $y = 0.15\delta$  (not shown for brevity) displays similar spatial uniformity as  $\langle u'^2 \rangle^+$  at the same wall-normal location [figure 35(b)]. It should be noted that the strong enhancement of the wall-normal velocity fluctuations in the presence of roughness presented herein is quite consistent with similar observations reported in the literature for flow over idealized roughness (Krogstad *et al.*, 1992; Krogstad & Antonia, 1999; Keirbulck *et al.*, 2002).

Figure 37 presents the spanwise Reynolds normal stress in inner units,  $\langle w'^2 \rangle^+$ , in the streamwise–spanwise plane at  $y = 0.065\delta$  for the rough-wall flow at  $\text{Re}_\theta = 14781$ . As was observed for  $\langle u'^2 \rangle^+$ , slight reductions in  $\langle w'^2 \rangle^+$  are noted locally around topographical features A–G. As with the other normal turbulent stresses, these heterogeneities in  $\langle w'^2 \rangle^+$  diminish quickly as one moves further from the surface as  $\langle w'^2 \rangle^+$  displays similar uniformity at  $y = 0.15\delta$  (not shown for brevity) as  $\langle u'^2 \rangle^+$  and  $\langle v'^2 \rangle^+$ .

Finally, figure 38 presents the Reynolds shear stress in inner units,  $-\langle u'v' \rangle^+$ , in a streamwise–spanwise plane within the roughness sublayer at  $y = 0.065\delta$  for  $\text{Re}_\theta = 14781$ . Significant heterogeneities in the Reynolds shear stress are noted locally around topographical features A–G, particularly a strong enhancement of ejection and sweep contributions to  $-\langle u'v' \rangle^+$ . Therefore, while the streamwise velocity fluctuations appear to be slightly muted by the roughness, particularly locally around topographical features A–G, the simultaneous enhancement of the vertical velocity fluctuations at the same spatial locations yields an overall enhancement of  $-\langle u'v' \rangle^+$ . As with the Reynolds normal stresses, there is no evidence supporting the generation of persistent wakes downstream of the dominant topographical features and these strong spatial inhomogeneities in  $-\langle u'v' \rangle^+$  decay

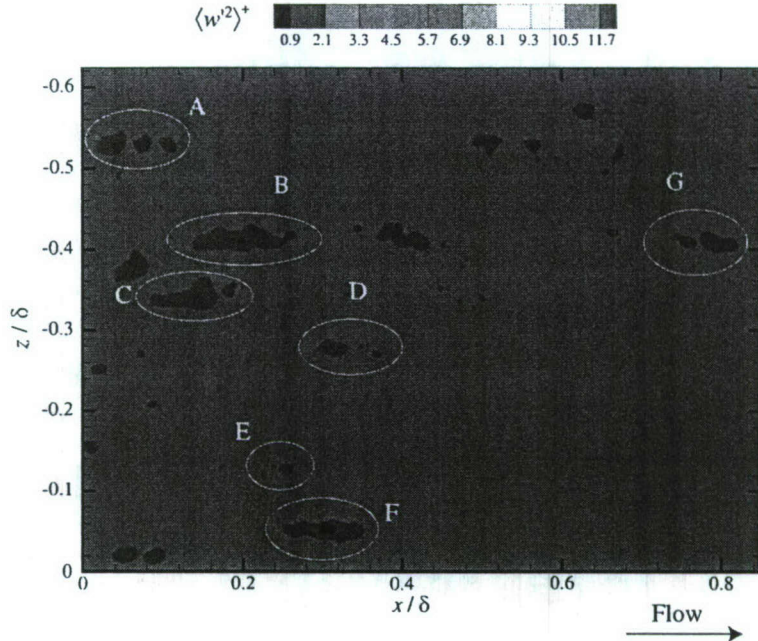


Figure 37: Inner-scaled spanwise Reynolds normal stress,  $\langle w'^2 \rangle^+$ , in the streamwise–spanwise plane at  $y = 0.065\delta$  for flow over the RF1 surface at  $\text{Re}_\theta = 14781$ .

quickly with wall-normal position as  $-(u'v')^+$  at  $y = 0.15\delta$  (not shown for brevity) appears with a uniformity consistent with the Reynolds normal stresses.

### 5.3 Structural imprints of the roughness

All of the aforementioned turbulence statistics indicate isolated, and in some instances substantial, modifications of the underlying turbulence locally around roughness features A–G. As noted earlier, past studies of idealized roughness surmise that enhancement of turbulent velocity fluctuations in the roughness sublayer is likely tied to the localized shedding of vortical structures from roughness elements. It is therefore possible that the localized modifications noted in figures 33–38 may be attributable to vortical structures shed locally by the dominant topographical features present in the highly-irregular rough surface considered herein.

To further explore such a possibility, statistics of the wall-normal (out-of-plane) vorticity,  $\omega_y$ , are computed. Figure 39(a) presents the inner-scaled, ensemble-averaged wall-normal vorticity,  $\Omega_y^+ \equiv \langle \omega_y \rangle^+$ , in the streamwise–spanwise plane at  $y = 0.065\delta$  for  $\text{Re}_\theta = 14781$ . Heterogeneities in  $\Omega_y$  are noted coincident with roughness features A–G. In particular,  $\Omega_y$  displays both a strong local minimum and an intense local maximum slightly separated in the spanwise direction. Such a signature is most notable near features B and F. These roughness-induced heterogeneities diminish rapidly as one moves farther away from the wall as the  $\Omega_y$  fields at  $y = 0.15\delta$  appear quite uniform [figure 39(b)]. Spatially-coincident peaks near roughness features A–G are also evident in the root-mean-square (RMS) of the wall-normal vorticity,  $\langle (\omega_y^+)^2 \rangle^{1/2}$ , presented in figure 40 (The RMS wall-normal vorticity field at  $y = 0.15\delta$  is not shown for brevity but displays similar uniformity as  $\Omega_y$  at the same wall-normal position). These strong, localized heterogeneities in the wall-normal vorticity statistics observed within the roughness sublayer could be the imprint of

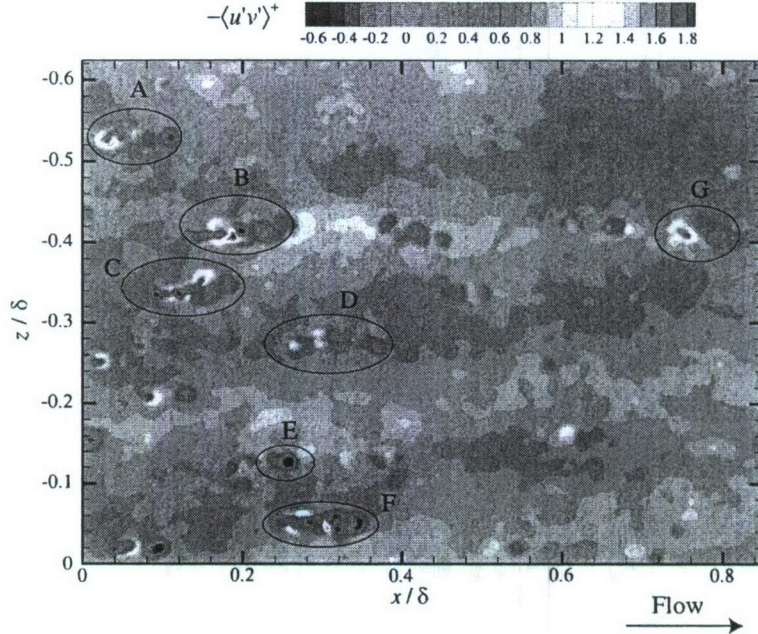


Figure 38: Inner-scaled Reynolds shear stress,  $-\langle u'v' \rangle^+$ , in the streamwise–spanwise plane at  $y = 0.065\delta$  for flow over the RF1 surface at  $\text{Re}_\theta = 14781$ .

vortical structures generated locally by roughness features A–G. However, it should be noted that if persistent wakes were formed downstream of roughness features A–G, then one would expect to observe relatively large-scale regions of non-zero  $\Omega_y$  and/or  $(\langle \omega_y^+ \rangle^2)^{1/2}$  elongated in the streamwise direction downstream of each roughness feature. No such elongated regions are noted in either of the wall-normal vorticity statistics, the absence of which is consistent with the lack of wake signatures in the turbulence statistics within the roughness sublayer.

Nevertheless, given the localized patterns observed in the ensemble-averaged and RMS wall-normal vorticity fields within the roughness sublayer, one could interpret such characteristics as slices through counter-rotating, wall-normal oriented pairs of vortical structures that are generated locally by roughness features A–G. Unfortunately, vorticity cannot serve as an unambiguous identifier of embedded structure, particularly in wall-bounded flows, since it can be biased by strong shearing motions as well. Therefore, the swirling strength ( $\lambda_{ci}$ ), the imaginary portion of the complex eigenvalues of the local velocity gradient tensor, is computed to determine whether the heterogeneities in the ensemble-averaged and RMS wall-normal vorticity fields are indeed attributable to in-plane swirling motions. Swirling strength is Galilean invariant and is superior to vorticity as a vortex identifier, particularly in wall-bounded flows, because it only identifies regions of rotation (Zhou *et al.*, 1999). Figure 41 presents the inner-scaled RMS swirling strength field,  $(\langle \lambda_{ci}^+ \rangle^2)^{1/2}$ , in the streamwise–spanwise plane at  $y = 0.065\delta$  for  $\text{Re}_\theta = 14781$ . Spanwise-separated pairs of concentrated RMS swirling strength are indeed noted spatially-coincident with the concentrated regions of ensemble-averaged and RMS wall-normal vorticity presented earlier, indicating that these spatial imprints are likely due to persistent counter-rotating pairs of in-plane swirling motions generated locally by dominant roughness features. As with all the other turbulence statistics, the RMS swirling strength at  $y = 0.15\delta$  (not shown for brevity) appears spatially uniform, indicating that these structural heterogeneities are only prevalent in the roughness sublayer.

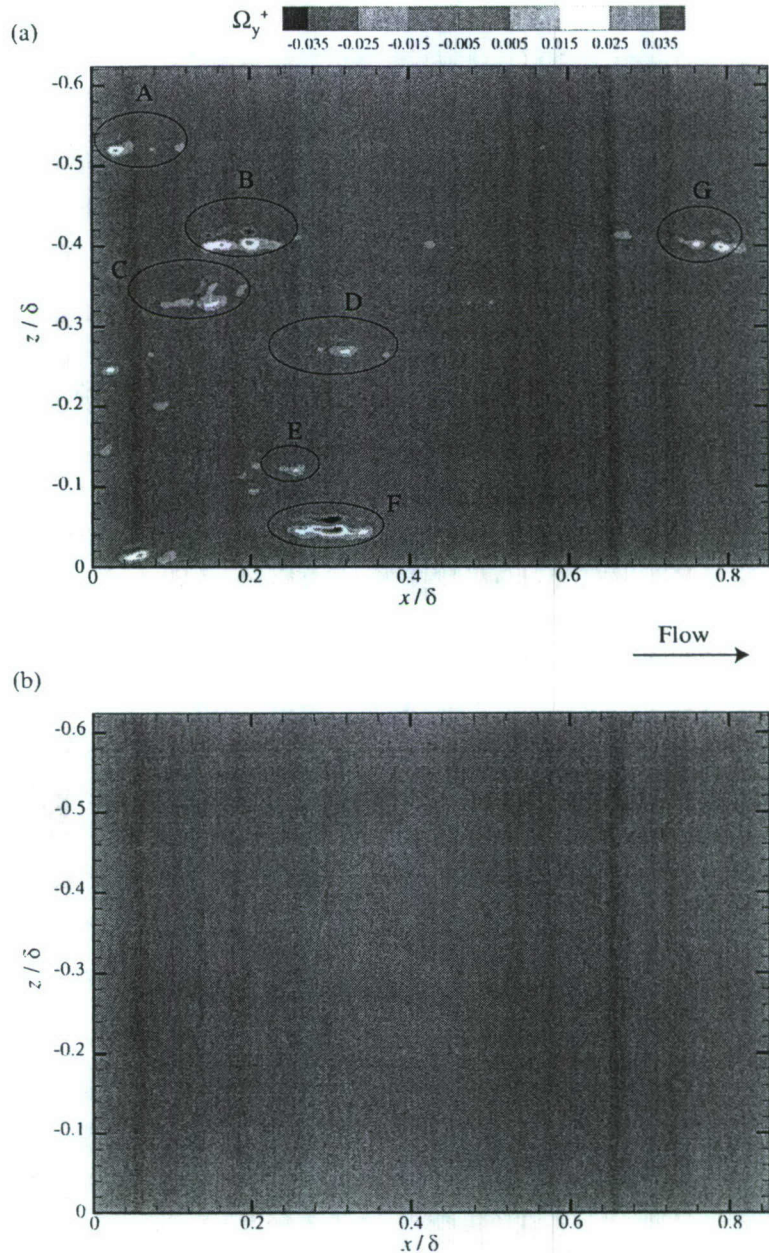


Figure 39: Inner-scaled, ensemble-averaged wall-normal vorticity,  $\Omega_y^+$ , in streamwise–spanwise planes at (a)  $y = 0.065\delta$  and (b)  $y = 0.15\delta$  for flow over the RF1 surface at  $\text{Re}_\theta = 14781$ .

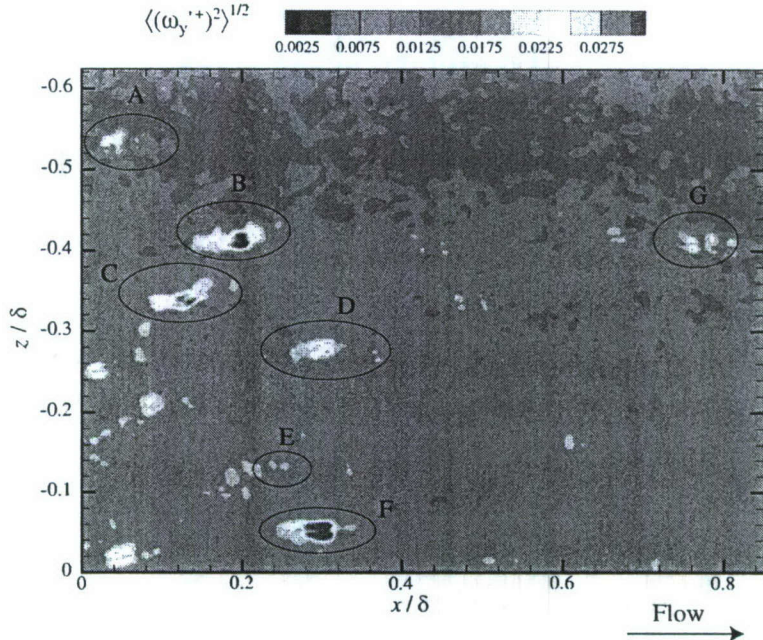


Figure 40: Inner-scaled RMS wall-normal vorticity,  $\langle(\omega_y'^+)^2\rangle^{1/2}$ , in the streamwise–spanwise plane at  $y = 0.065\delta$  for flow over the RF1 surface at  $\text{Re}_\theta = 14781$ .

Finally, the patterns noted in the ensemble-averaged and RMS wall-normal vorticity as well as the RMS swirling strength at  $y = 0.065\delta$  are quite consistent with what one would observe if a hairpin-like vortex (or possibly an inclined ring-like vortex) were sliced in the streamwise–spanwise plane. As noted at the beginning of this chapter, many past studies have observed vortex shedding, both periodic as well as unsteady, from discrete roughness elements in both laminar and turbulent boundary layers. Figure 42(a) illustrates a scenario for the present rough-wall case by which hairpin-like structures could be shed from dominant roughness protrusions and how a streamwise–spanwise measurement plane within the roughness sublayer would cut through such a structure. Indeed, a counter-rotating pair of wall-normal vortices would be observed in the measurement plane downstream of the roughness protrusion as illustrated in figure 42(b) and this pattern is quite consistent with the patterns noted downstream of roughness protrusions in the mean and RMS wall-normal vorticity and RMS swirling strength at  $y = 0.065\delta$ . However, while such structures may be shed locally around these roughness protrusions, coherent “packets” of these structures do not appear to advect downstream as evidenced by the lack of wake signatures in the mean velocity fields and the various turbulence statistics presented above. As such, these structures are likely shed in a highly unsteady manner, though at a consistent spatial location because the counter-rotating pairs persist in the statistics wall-normal vorticity and swirling-strength statistics, but quickly become engulfed into the surrounding turbulence. Such a scenario is supported by past studies that indicate high turbulence levels in the immediate vicinity of roughness elements tend to suppress large-scale wake formation downstream of isolated roughness elements, albeit for idealized roughness elements (Savory & Toy, 1986; Schofield & Logan, 1990; Martinuzzi & Tropea, 1993, for example).

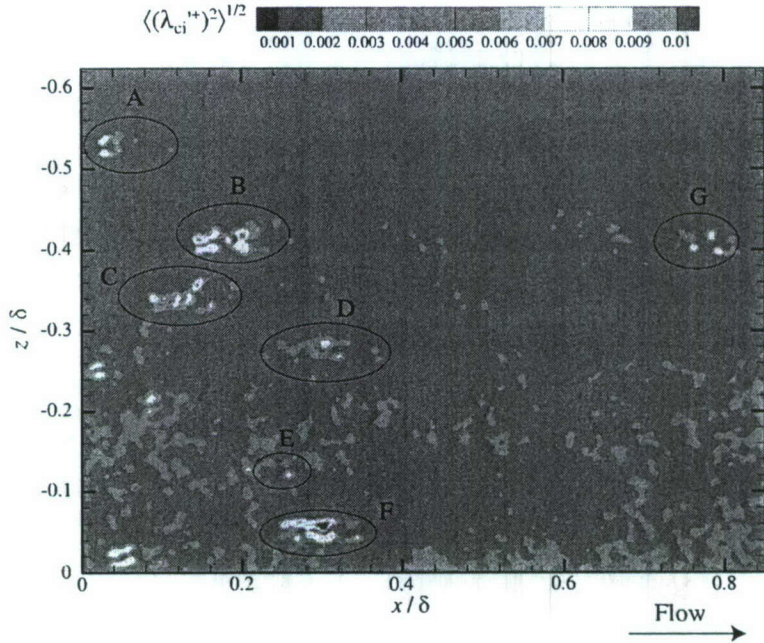


Figure 41: Inner-scaled RMS swirling strength,  $\langle(\lambda_{ci}^{'+})^2\rangle^{1/2}$ , in the streamwise–spanwise plane at  $y = 0.065\delta$  for flow over the RF1 surface at  $Re_\theta = 14781$ .

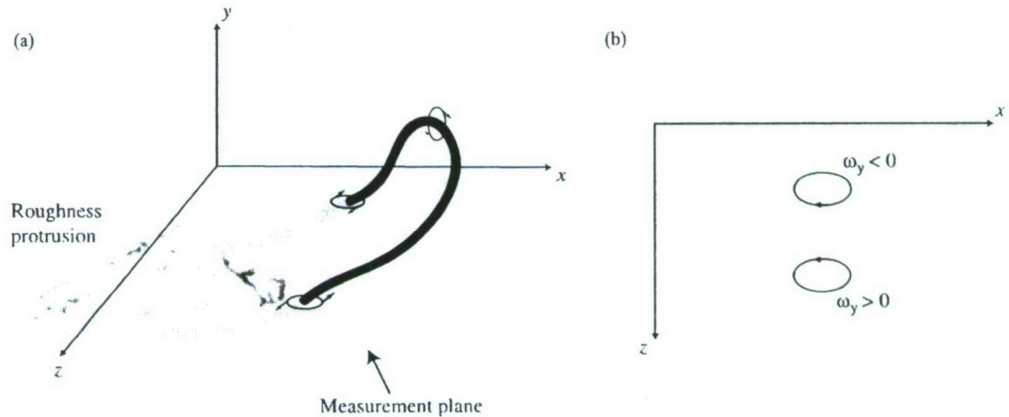


Figure 42: (a) Three-dimensional schematic illustrating the scenario of hairpin-like structures being shed locally from dominant roughness protrusions. (b) Spatial signature one would observe if the hairpin-like structure in (a) were sliced by a streamwise–spanwise measurement plane within the roughness sublayer.

## 5.4 Summary

The stereoscopic PIV measurements in a wall-parallel plane within the roughness sublayer reveal strong turbulence modifications spatially-coincident with dominant roughness features of the highly-irregular topography considered herein. In particular, intense heterogeneities in the wall-normal Reynolds normal stress, the Reynolds shear stress and the mean and RMS wall-normal vorticity are observed locally around intense protrusions of the roughness into the flow. Of interest is that the noted enhancement of the wall-normal velocity fluctuations presented herein is quite consistent with similar observations made for flow over idealized rough surfaces (Krogstad *et al.*, 1992; Krogstad & Antonia, 1999; Keirsbulck *et al.*, 2002). However, persistent wakes downstream of these dominant roughness features are not observed in any of turbulence statistics, indicating that if vortical structures are shed from these features they only influence the flow locally. Further, the roughness-induced heterogeneities are confined within the roughness sublayer as the turbulence statistics computed from stereo PIV measurements in a streamwise–spanwise plane toward the outer edge of the roughness sublayer at  $y = 0.15\delta$  relax toward a spatially homogeneous state. Finally, mean and RMS wall-normal vorticity fields in the roughness sublayer, in concert with statistics and spatial distributions of the swirling strength, indicate that counter-rotating pairs of wall-normal-oriented vortices are locally generated around dominant topographical events. This spatial signature is quite consistent with what one would observe if a hairpin-like or inclined ring-like vortex were sliced in the streamwise–spanwise plane.

Further, the results of this chapter provide an indication that the flow regions that are directly affected by roughness have a dependence on  $Re$ . As such, the thickness of the roughness sublayer should reflect such a dependence. Therefore, although the results in section 4 confirm that using roughness height ( $3 - 5k$ ) to define the extent of roughness sublayer is still appropriate for the current rough surface, a more appropriate representation that embodies  $Re$  may help explain subtle contradictions in the literature regarding the wall-normal extent of the roughness sublayer.

## 6 Structural characteristics of the rough-wall flow

### 6.1 Background

As noted earlier, vortical structures are thought to contribute significantly to momentum transport in smooth-wall turbulence. The various observations reported in the literature in this regard are summarized in detail in section 1. In particular, the outer layer of smooth-wall turbulence appears dominated by coherent trains of hairpin-like structures aligned in the streamwise direction. These hairpin vortex packets collectively induce strong ejections of fluid away from the wall which contribute heavily to the mean Reynolds shear stress,  $\langle u'v' \rangle$ . These large-scale structures, as well as the individual vortices within a packet, leave distinct imprints in instantaneous velocity realizations in both the streamwise-wall-normal and streamwise-spanwise planes as well as in the spatial statistics of the flow. In particular, the spatial velocity correlations mimic many of the spatial characteristics of hairpin vortex packets, from the elongated streamwise extent and inclination of  $\rho_{uu}$  away from the wall which are interpreted as the imprint of vortex packets to the compact coherence of  $\rho_{vv}$  which is more representative of the spatial domain over which individual hairpin-like structures exert their influence (Christensen, 2001, for example).

The impact of roughness on the structure of wall turbulence has also been investigated, although much less so than smooth-wall turbulence. Of particular interest is the fact that conflicting evidence exists regarding the impact of roughness on both the near-wall and outer-layer structure. For example, while Krogstad & Antonia (1994) observed a significant reduction in the streamwise extent as well as a dramatic increase in the inclination angle of  $\rho_{uu}$  for flow over wire mesh, other studies have reported no observable differences in this regard. In particular, Nakagawa & Hanratty (2001) reported strong consistency in both the streamwise length scale and inclination angle of  $\rho_{uu}$  for flow over a wavy surface in turbulent channel flow. More recently, Volino *et al.* (2007) reported a slight reduction in the streamwise extent of  $\rho_{uu}$  but no change in its inclination angle for turbulent flow over wire mesh. It should be noted that all of these studies employed simulated roughness characterizations to study the impact of roughness on the structure of wall turbulence. With regard to more practical roughness characterizations, Allen *et al.* (2007) reported collapse of streamwise velocity spectra in the outer region of turbulent pipe flow roughened in a manner consistent with the “industrial” roughness considered by Colebrook (1939).

Other recent studies of rough-wall turbulence have employed proper orthogonal decomposition (POD) to study the impact of roughness on the spatial character of wall turbulence. Since its introduction to the study of turbulence by Lumley (1967), POD has become one of the most important tools for objectively identifying the dominant spatial features and events in smooth-wall turbulence (Bakewell & Lumley, 1967; Moin & Moser, 1989; Ball *et al.*, 1991; Sirovich *et al.*, 1991; Liu *et al.*, 1994, 2001; Liberzon *et al.*, 2005; Gurka *et al.*, 2006, among others). In POD, a set of orthogonal spatial eigenfunctions, or eigenmodes, are generated based on an ensemble of data. These POD modes form an optimal basis of the flow in the sense that the energy content of the basis converges faster than any other basis set (Berkooz *et al.*, 1993; Holmes *et al.*, 1996). These basis functions can then be used to form low-order models of the flow upon which instantaneous flow realizations can be projected upon to generate low-pass- and high-pass-filtered fields. Several recent studies have attempted to use POD to investigate the large-scale structures in rough-wall turbulence. Gunther & von Rohr (2003) performed POD of the velocity field measured by PIV in a developed turbulent channel flow between a sinusoidal bottom wall and a flat top wall at Reynolds numbers (based on bulk velocity and half-height of the channel) of 3800 and 7300. They found that the dominant eigenfunctions had a characteristic spanwise scale of about 1.5 times the wall wavelength,  $\Lambda$ . Smaller structures obtained from the POD analysis were observed at locations with maximum Reynolds shear stress. The dynamics of these large-scale structures with a spanwise

scale of  $1.5\Lambda$  were explored further by Kruse *et al.* (2003) using POD analysis of the velocity fields measured in the same wavy-wall channel. The meandering motion of these large-scale structures was followed over 6 seconds convecting downstream over a length of about 65 wall wavelengths and it was determined that this meandering provided a mechanism of momentum and scalar transport between the wavy-wall and the bulk flow. Sen *et al.* (2007) applied snapshot POD in a DNS of turbulent channel flow with 3D egg-carton roughness elements at  $Re_\tau = 180$ . Their one-dimensional analysis revealed that the POD energy converged slower for the rough-wall flow than for the smooth-wall flow due to a larger range of dynamically-important spatial scales in the rough-wall flow. They used the first few most energetic POD modes to reconstruct the Reynolds stresses and found that the first ten modes were sufficient for capturing both the location and the amplitude of the peak in the streamwise Reynolds normal stress. Two-dimensional POD results in the wall-normal–spanwise ( $y - z$ ) plane revealed a decreased spanwise length scale for the first (most energetic) POD mode but an increased spanwise length for the second mode in the rough-wall flow when compared with the smooth-wall flow. They also observed that in the streamwise–wall-normal plane, the length scale of the first POD mode was decreased in the presence of roughness.

This section is devoted to a comparison of the underlying structural character of turbulent flow over the RF1 surface with that of smooth-wall turbulence at  $Re_\theta \approx 13000$  [It should be noted that the results presented in this section for  $Re_\theta \approx 13000$  are quite consistent with the trends observed in identical analysis of the  $Re_\theta \approx 8000$  cases. As such, all plots pertaining to the  $Re_\theta \approx 8000$  cases are not shown for brevity but can be found in Wu (2008)]. Representative instantaneous velocity realizations in both the streamwise–wall-normal ( $x - y$ ) and streamwise–spanwise ( $x - z$ ) planes are presented first as a means of identifying the dominant spatial characteristics of flow over both the smooth and RF1 surfaces. The spatial characteristics of velocity and swirling strength correlations are then explored in the  $x - z$  measurement planes as well as the  $x - y$  plane as a means of identifying quantitative modifications imposed by roughness on the underlying spatial structure of the flow compared to smooth-wall turbulence. Finally, conditional averaging and POD are employed to explore these similarities and differences further.

## 6.2 Instantaneous structure

Figure 43(a) presents a representative instantaneous velocity realization acquired in the streamwise–wall-normal ( $x - y$ ) plane of the smooth-wall flow at  $Re_\theta = 11943$  visualized with a constant advection velocity of  $0.77U_e$  removed. Several swirling motions with clockwise rotation are noted in this realization and are referred to as prograde spanwise vortices since they have the same rotational sense as the mean shear. These vortices appear aligned in the streamwise direction and form an interface inclined slightly away from the wall over the field of view beneath which exists a large-scale region of streamwise momentum deficit. This coherent organization of structures is interpreted as a slice through a hairpin vortex packet by the streamwise–wall-normal measurement plane whereby the spanwise prograde vortices represent slices through the heads of the individual hairpin structures (Adrian *et al.*, 2000). In addition, the large-scale region of low momentum fluid enveloped beneath the inclined interface of the packet is attributable to the mutual induction of the vortices within a packet. As a part of this induction, each vortex generates a strong ejection ( $Q2$  event) of low-momentum fluid away from the wall just upstream and below its head and these ejection events are thought to contribute significantly to the production of turbulent shear stress. The strength of these ejection events is quite evident in figure 43(b) which presents instantaneous  $u'v'$  computed from the fluctuating velocity field associated with figure 43(a). Line contours are overlaid on this  $u'v'$  field illustrating the outer boundary of the low-momentum region of this hairpin packet. Intense, negative  $u'v'$  is observed over much of the region below the inclined interface of the packet due to the strong ejections ( $Q2$  events) induced by these vortical structures. Finally, the vortical activity levels

present in this instantaneous realization can be seen in figure 43(c) which presents instantaneous swirling strength ( $\lambda_{ci}$ ) computed from the velocity field in figure 43. The sign of the instantaneous fluctuating spanwise vorticity,  $\omega_z$ , is assigned to  $\lambda_{ci}$  to aid in distinguishing between prograde (negative  $\omega_z$ ; clockwise) and retrograde (positive  $\omega_z$ ; counterclockwise) spanwise vortices. Several negative patches of  $\lambda_{ci}$  line up along the inclined interface outlined by the line contours showing the outer edge of the low-momentum region. These patches are spatially coincident with the swirling motions evident figure 43(a) and are interpreted as the  $\lambda_{ci}$  imprint of the hairpin vortex heads. Although less numerous, there still exist several positive  $\lambda_{ci}$  patches that represent retrograde spanwise vortices. Wu & Christensen (2006a) found that these counterclockwise-rotating retrograde spanwise vortices have their largest populations toward the outer edge of the log layer where they generally occur in close proximity to prograde spanwise vortices. Natrajan *et al.* (2007) found that these spatially-coincident pairs of prograde and retrograde spanwise vortices may be linked to the measurement plane slicing through the shoulders of omega-shaped hairpin-like structures.

Figure 44(a) illustrates a representative instantaneous velocity field in the  $x - y$  plane for flow over the RF1 surface at  $Re_\theta = 14781$  visualized with a constant advection velocity of  $0.72U_e$  removed. The character of this field is quite similar to that in figure 43(a) for smooth-wall flow as several prograde spanwise vortices are observed to align roughly in the streamwise direction, forming an inclined interface beneath which a region of significant streamwise momentum deficit exists. The instantaneous  $u'v'$  field associated with this velocity field [figure 44(b)] shows the generation of intense, negative  $u'v'$  via ejections of low-speed fluid away from the wall beneath the inclined interface of the packet (shown as line contours). Of interest, the size of the spanwise vortices appears to be slightly reduced in the rough-wall case when one compares the instantaneous  $\lambda_{ci}$  field [figure 44(c)] for the rough-wall velocity field in figure 44(a) with that from the smooth-wall realization [figure 43(c)]. Nevertheless, prograde spanwise vortices (negative patches of  $\lambda_{ci}$ ) still appear spatially coincident with the inclined interface of the low-momentum region, indicating that hairpin vortex packets still represent an important structural attribute of flow over the RF1 surface.

While figures 43 and 44 illustrate the imprint of the spatial organization present in flow over both smooth and RF1 surface conditions within the  $x - y$  plane, these structures also leave a definitive imprint within velocity fields acquired in the streamwise–spanwise ( $x - z$ ) plane. Figure 45(a) presents a representative instantaneous fluctuating velocity field in a wall-parallel plane at  $y = 0.065\delta$  for the smooth-wall case at  $Re_\theta = 11943$ . The in-plane velocity components ( $u', w'$ ) are shown as vectors while the out-of-plane velocity component,  $v'$ , is presented via background contours. Two dominant large-scale events are notable in this field: an elongated low-momentum region ( $u' < 0$ ; labeled ‘LMR’) and an elongated high-momentum region ( $u' > 0$ ; labeled ‘HMR’). It should be noted that the wall-normal position of this PIV measurement plane is well within the logarithmic layer so these low- and high-momentum regions are distinct from the near-wall low- and high-speed streaks first observed by Kline *et al.* (1967) in the vicinity of the viscous sublayer. Numerous swirling motions are noted along the boundaries of these elongated regions and intense ejections of fluid away from the wall ( $v' > 0$ ) and sweeps of fluid toward the wall ( $v' < 0$ ) occur spatially-coincident with these low- and high-speed regions. These intense wall-normal velocity fluctuations, in concert with strong streamwise velocity fluctuations, generate intense instantaneous contributions to the Reynolds shear stress,  $\langle u'v' \rangle$ . The spatial footprints of these low- and high-momentum regions can be clearly seen in figure 45(b) which presents contours of instantaneous streamwise velocity,  $u$ , normalized by the ensemble- and area-averaged mean velocity,  $U$ . These elongated regions of relatively constant streamwise momentum extend  $O(\delta)$  in the streamwise direction and are quite consistent with the streamwise–spanwise smooth-wall PIV observations reported by Tomkins & Adrian (2003) and Ganapathisubramani *et al.* (2003). Figure 46(a) presents  $u'v'$

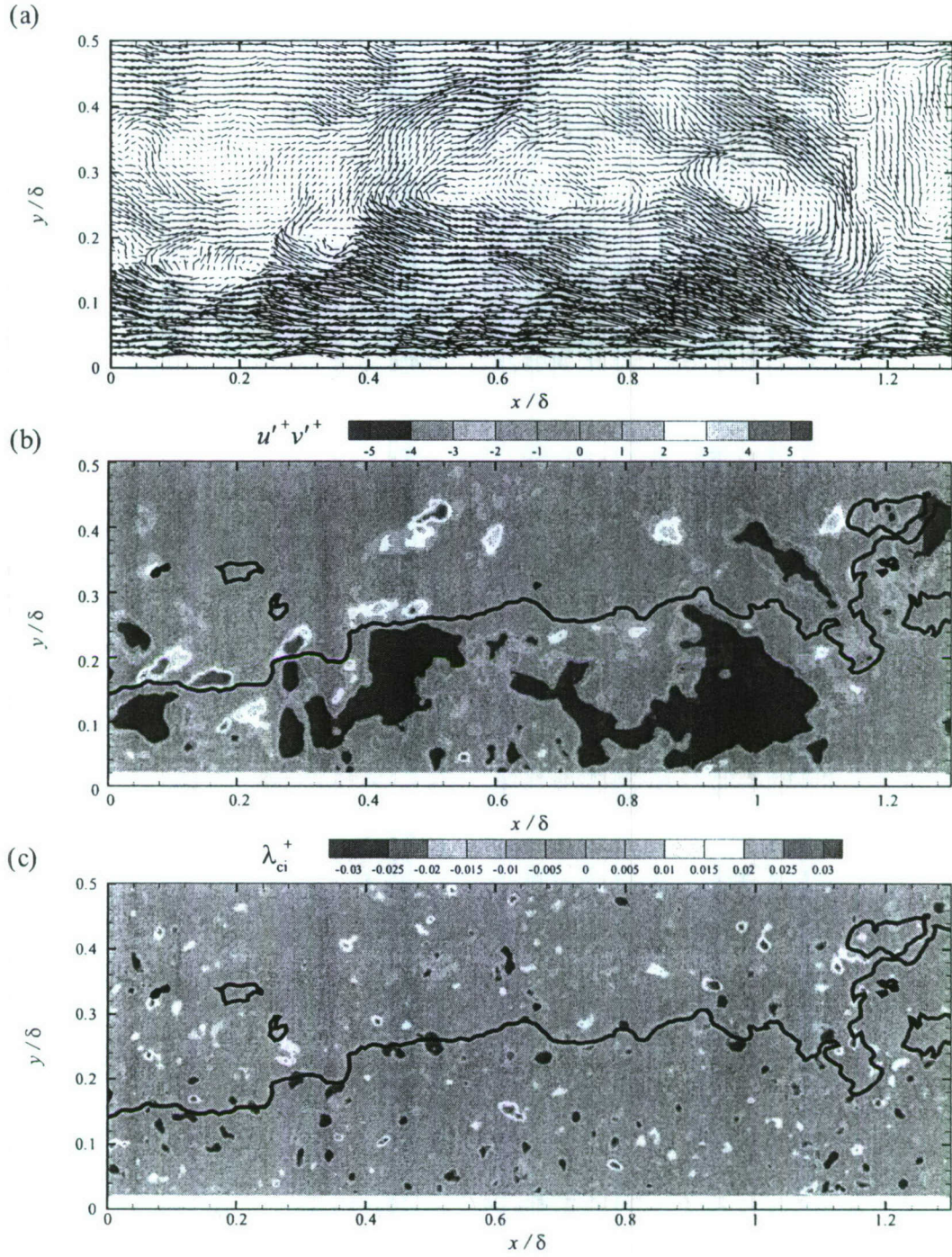


Figure 43: A representative instantaneous velocity realization in the streamwise–wall-normal plane for flow over the RF1 surface at  $\text{Re}_\theta = 11943$ . (a) Galilean decomposition of the in-plane velocities,  $(u, v)$  with a constant streamwise advection velocity of  $0.77U_e$  removed; (b) Instantaneous turbulent shear stress,  $u'v'$ , computed from (a); (c) Instantaneous swirling strength,  $\lambda_{ci}^+$ , computed from (a). Line contours outlining low-momentum interface (with  $0.77U_\infty$  threshold) overlaid in (b) and (c).

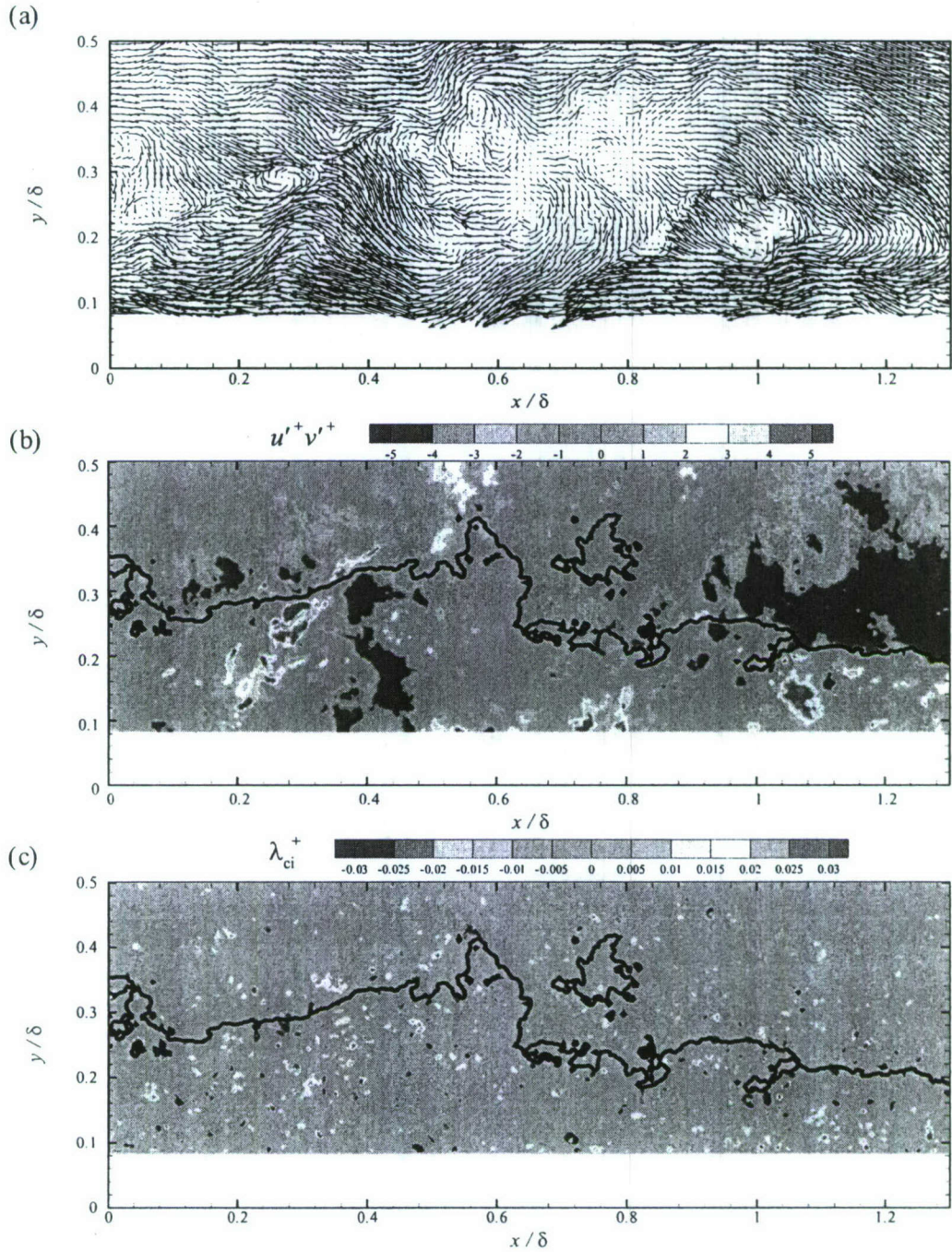


Figure 44: A representative instantaneous velocity realization in the streamwise–wall-normal plane for flow over a smooth wall at  $\text{Re}_\theta = 14781$ . (a) Galilean decomposition of the in-plane velocities,  $(u, v)$  with a constant streamwise advection velocity of  $0.72U_e$  removed; (b) Instantaneous turbulent shear stress,  $u'v'$ , computed from (a); (c) Instantaneous swirling strength,  $\lambda_{ci}$ , computed from (a). Line contours outlining low-momentum interface (with  $0.72U_\infty$  threshold) overlaid in (b) and (c).

contours computed from the instantaneous velocity field of figure 45 with line contours outlining the low- (white) and high-momentum (black) regions. It is clear that the most intense  $u'v'$  events occur *within* these LMR's and HMR's. Further, the wall-normal swirling motions outboard of the LMR's and HMR's can be clearly identified in figure 46(b) which presents contours of  $\lambda_{ci}$  for this velocity realization. In particular, opposing-sign  $\lambda_{ci}$  is noted along the spanwise boundaries of these regions. From a structural viewpoint, the LMR bounded by swirling motions and within which intense  $u'v'$  events are noted is consistent with what one would observe if a streamwise-aligned hairpin vortex packet were sliced in a wall-parallel plane within the log layer. In particular, the LMR itself represents a slice through the region of relatively uniform streamwise momentum deficit generated by the collective induction of the vortices in a packet, the swirling motions bounding the LMR represent slices through the legs/necks of the individual hairpin structures and the intense  $u'v'$  events noted within the LMR are the footprint of Reynolds-stress-producing events induced by the individual vortices in the packet. It should also be noted that these features are quite consistent with the patterns noted in slices of hairpin packets in the streamwise-wall-normal plane (figures 43 and 44). In contrast, the HMR can be interpreted as a region of relatively high-momentum fluid formed outboard of the hairpin packets due to the collective induction of the vortices which draw high-momentum fluid and pump it towards the wall. These sweeps of high-momentum fluid toward the wall also contribute significantly to the overall Reynolds shear stress as is evident in figure 46(a).

Similar qualitative spatial characteristics are noted in figure 47(a) which presents a representative instantaneous velocity realization in a wall-parallel plane at  $y = 0.065\delta = 1.7k$  for flow over the RF1 surface at  $Re_\theta = 14781$ . Low- and high-momentum regions are noted in this realization as well, with their spatial extents highlighted in figure 47(b) (contours of instantaneous streamwise velocity normalized by the ensemble- and area-averaged mean velocity). Of note is the rather significant enhancement of the intermittent  $v'$  events, relative to the smooth-wall example in figure 45(a), that, coupled with strong  $u'$  events, generate ejections and sweeps of fluid away from and toward the surface, respectively, as can be seen in figure 48(a) which presents instantaneous  $u'v'$  for this velocity realization (with line contours demarcating the boundaries of the LMR and HMR). Apart from this clear difference between the smooth- and rough-wall realizations, as well as the slightly smaller wall-normal vortices evident in the rough-wall case compared to the smooth-wall flow [figure 48(b)], the spatial character of this instantaneous velocity field is quite consistent with the smooth-wall field in terms of the occurrence and streamwise extents of the low- and high-momentum regions as well as the existence of swirling motions along their boundaries. Therefore, the qualitative aspects of the spatial structure of the turbulence appears to be consistent between the smooth and rough cases despite this measurement occurring in quite close proximity to significant surface defects in the rough-wall case.

Finally, figure 49 presents a representative velocity realization in the  $x - z$  plane further from the wall ( $y = 0.15\delta$ ) for smooth-wall flow at  $Re_\theta = 11943$  (the  $u'v'$  and  $\lambda_{ci}$  fields are shown in figure 50) while figure 51 presents a representative field for flow over the RF1 surface at the same wall-normal location (the  $u'v'$  and  $\lambda_{ci}$  fields are shown in figure 52). Both of these realizations show strong consistency both in the occurrence of LMR's and HMR's and in the generation of intense, negative  $u'v'$  events within these regions and the occurrence of opposing-sign swirling motions at the spanwise boundaries of these elongated regions. It should be noted that the differences in the intensity of  $v'$  as well as differences in the diameters of the vortex cores between smooth- and rough-wall flow closer to the wall appear to have diminished at this wall-normal location. Similar characteristics are also observed in instantaneous velocity realizations of smooth- and rough-wall flow at  $Re_\theta \approx 8000$  [see Wu (2008)].

The qualitative consistencies between these smooth- and rough-wall instantaneous fields indicate that LMR's and HMR's are robust spatial features of both flows, even very close to the surface where

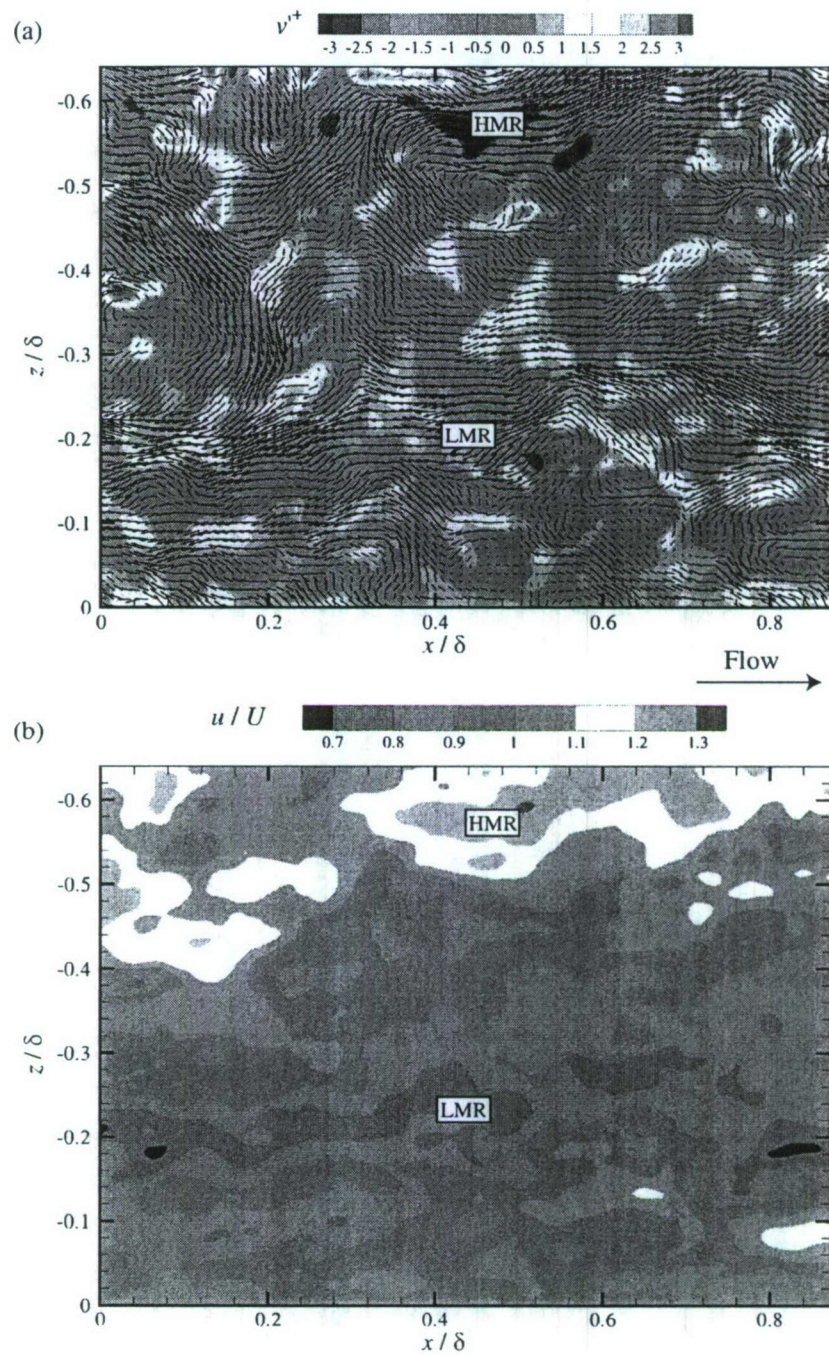


Figure 45: A representative instantaneous velocity realization in the streamwise–spanwise plane at  $y = 0.065\delta$  for flow over a smooth wall at  $\text{Re}_\theta = 11943$ . (a) Fluctuating in-plane velocities ( $u'$ ,  $w'$ ) are presented as vectors and the fluctuating out-of-plane velocity,  $v'$ , is presented as contours. (b) Contours of normalized streamwise velocity,  $u/U$ , where  $U$  represents the ensemble- and area-averaged streamwise velocity.

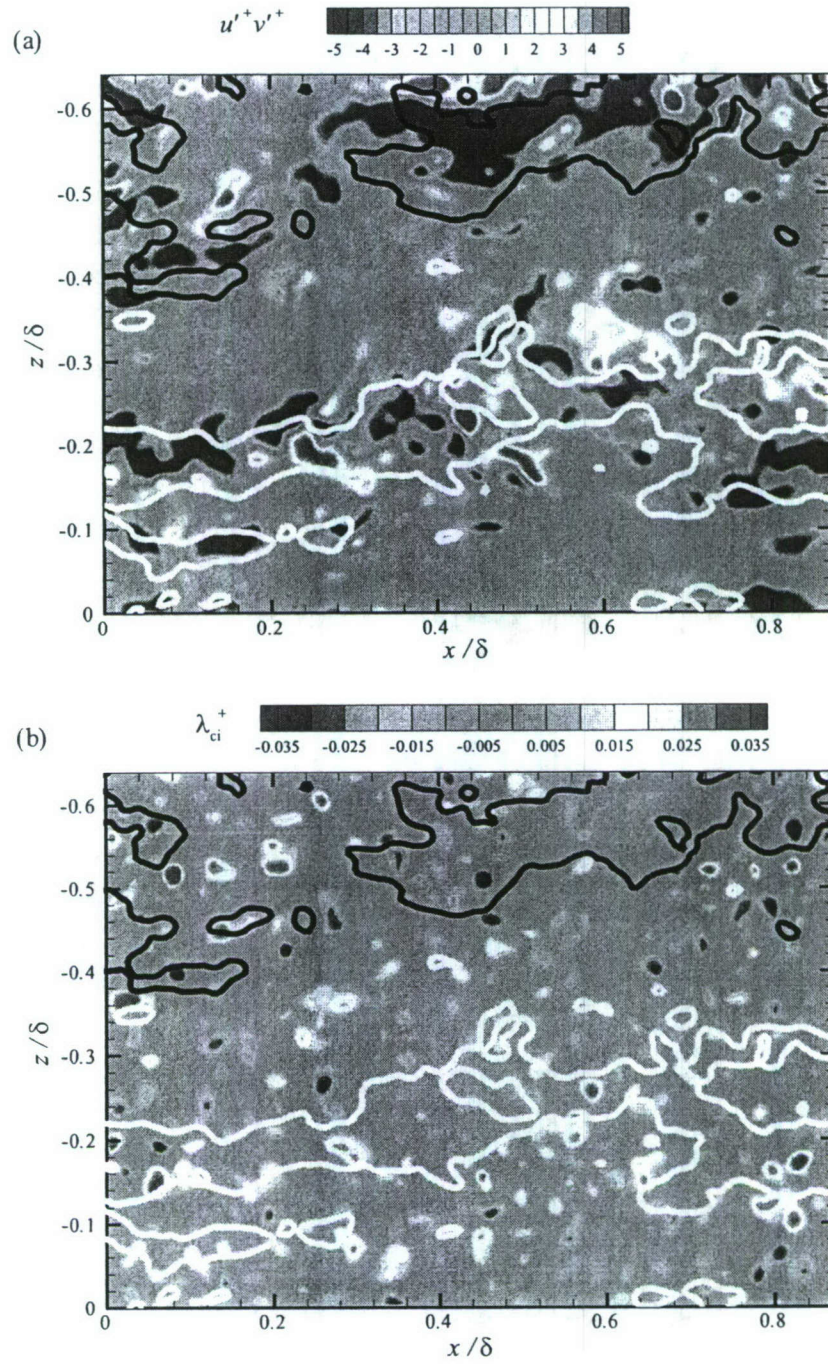


Figure 46: Instantaneous (a) turbulent shear stress,  $u'v'$ , and (b) swirling strength,  $\lambda_{ci}$ , computed from the instantaneous velocity realization presented in figure 45. Line contours of low- (white;  $0.85U$ ) and high-momentum (black;  $1.15U$ ) regions are presented in the background.

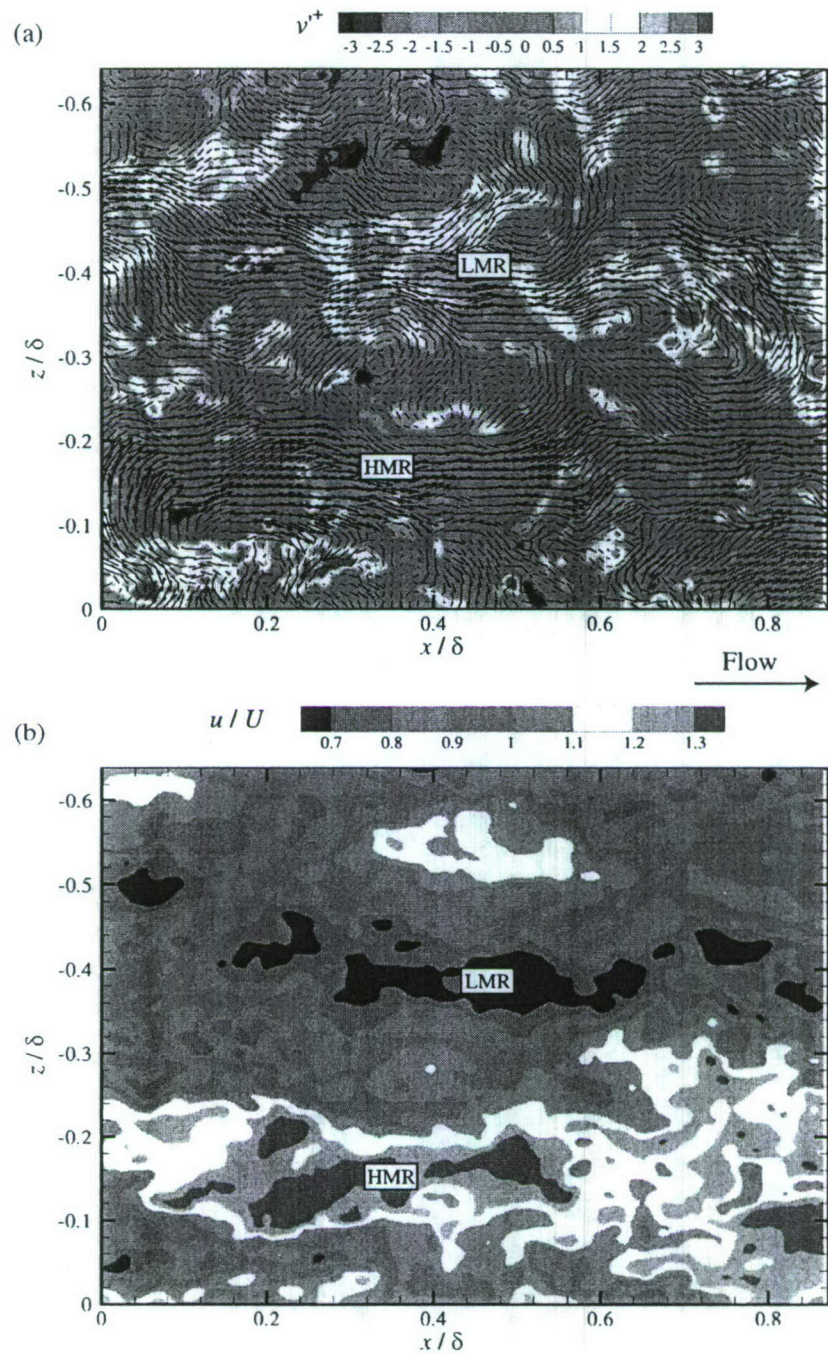


Figure 47: A representative instantaneous velocity realization in the streamwise–spanwise plane at  $y = 0.065\delta = 1.7k$  for flow over the RF1 surface at  $\text{Re}_\theta = 14781$ . (a) Fluctuating in-plane velocities ( $u', w'$ ) are presented as vectors and the fluctuating out-of-plane velocity,  $v'$ , is presented as contours. (b) Contours of normalized streamwise velocity,  $u/U$ , where  $U$  represents the ensemble- and area-averaged streamwise velocity.

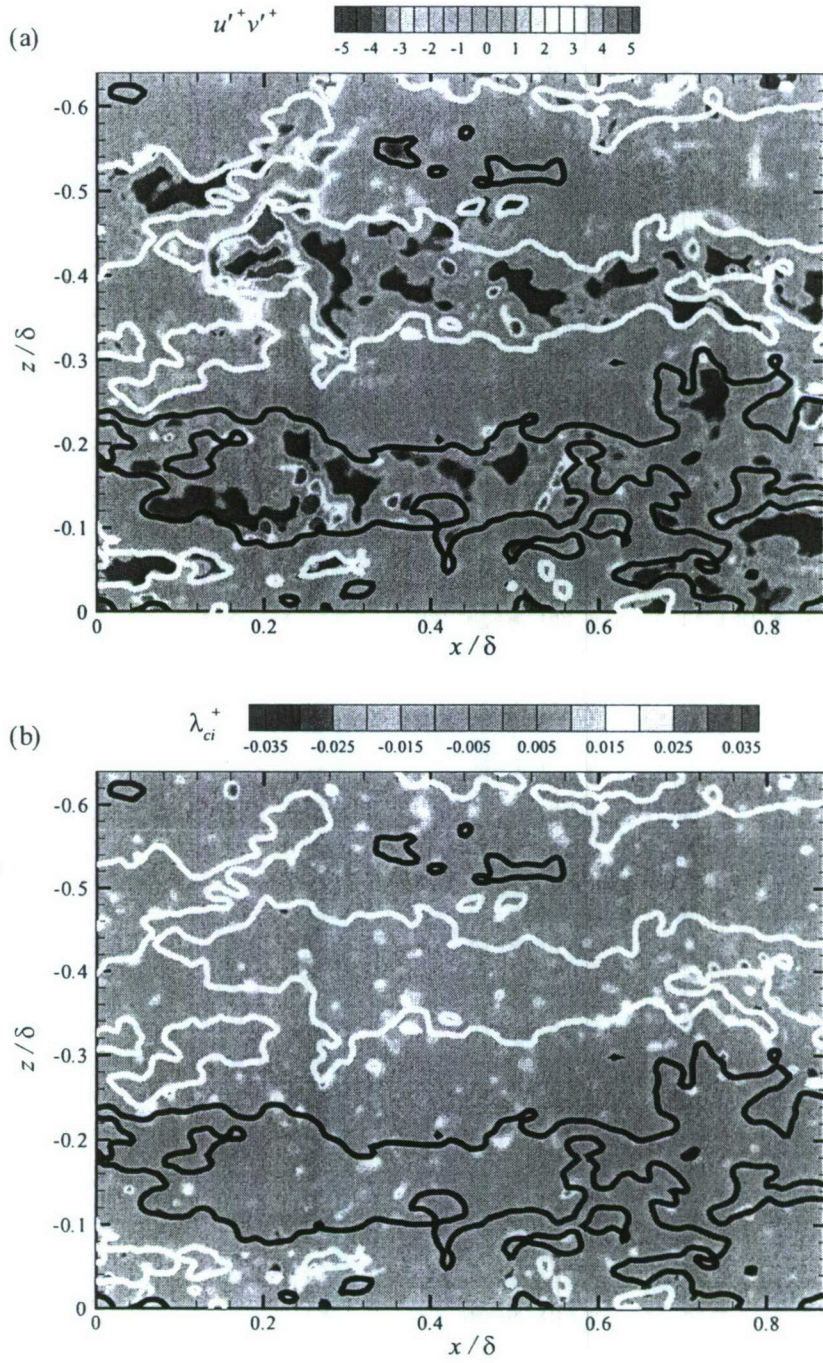


Figure 48: Instantaneous (a) turbulent shear stress,  $u'v'$ , and (b) swirling strength,  $\lambda_{ci}$ , computed from the instantaneous velocity realization presented in figure 47. Line contours of low- (white;  $0.85U$ ) and high-momentum (black;  $1.15U$ ) regions are presented in the background.

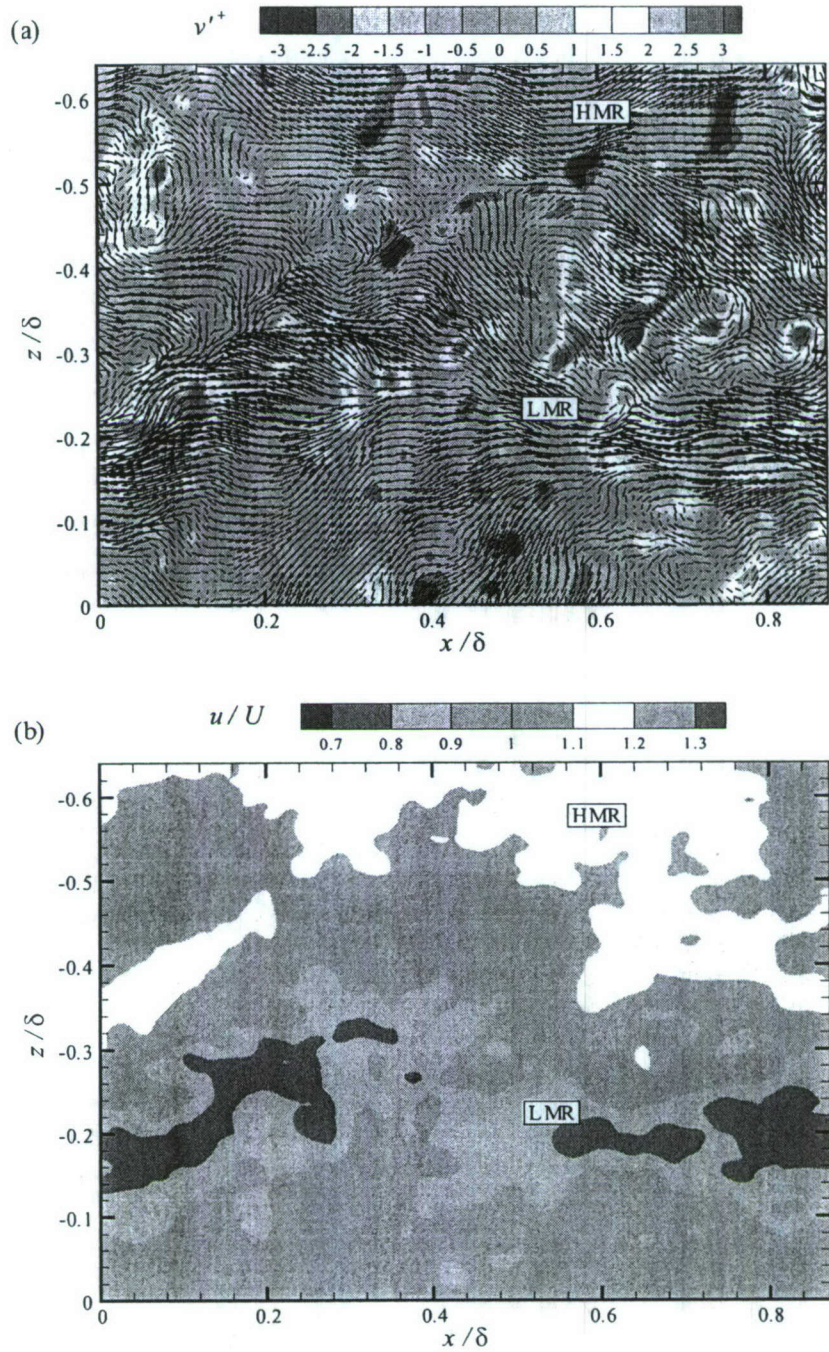


Figure 49: A representative instantaneous velocity realization in the streamwise–spanwise plane at  $y = 0.15\delta$  for flow over a smooth wall at  $\text{Re}_\theta = 11943$ . (a) Fluctuating in-plane velocities ( $u', w'$ ) are presented as vectors and the fluctuating out-of-plane velocity,  $v'$ , is presented as contours. (b) Contours of normalized streamwise velocity,  $u/U$ , where  $U$  represents the ensemble- and area-averaged streamwise velocity.

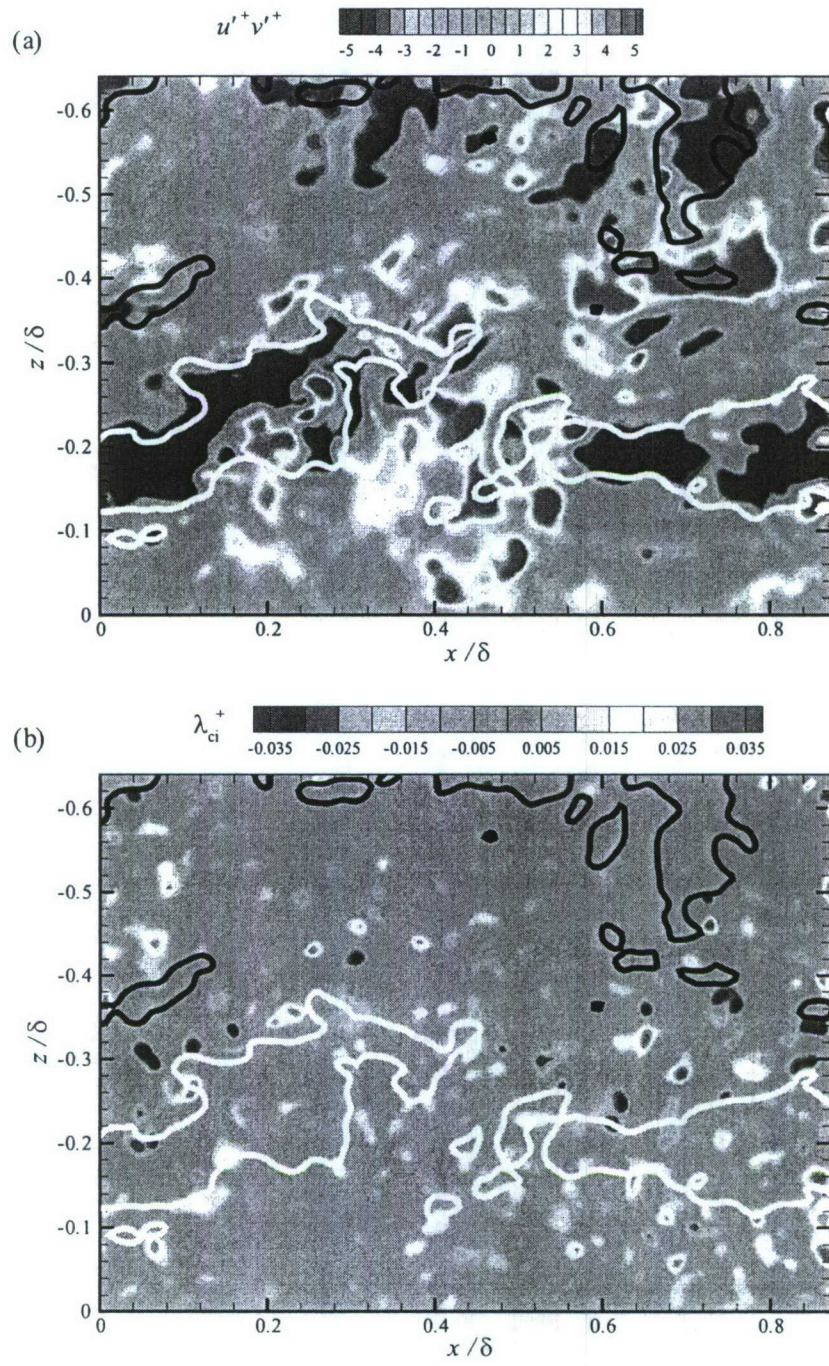


Figure 50: Instantaneous (a) turbulent shear stress,  $u'v'$ , and (b) swirling strength,  $\lambda_{ci}$ , computed from the instantaneous velocity realization presented in figure 49. Line contours of low- (white;  $0.85U$ ) and high-momentum (black;  $1.15U$ ) regions are presented in the background.

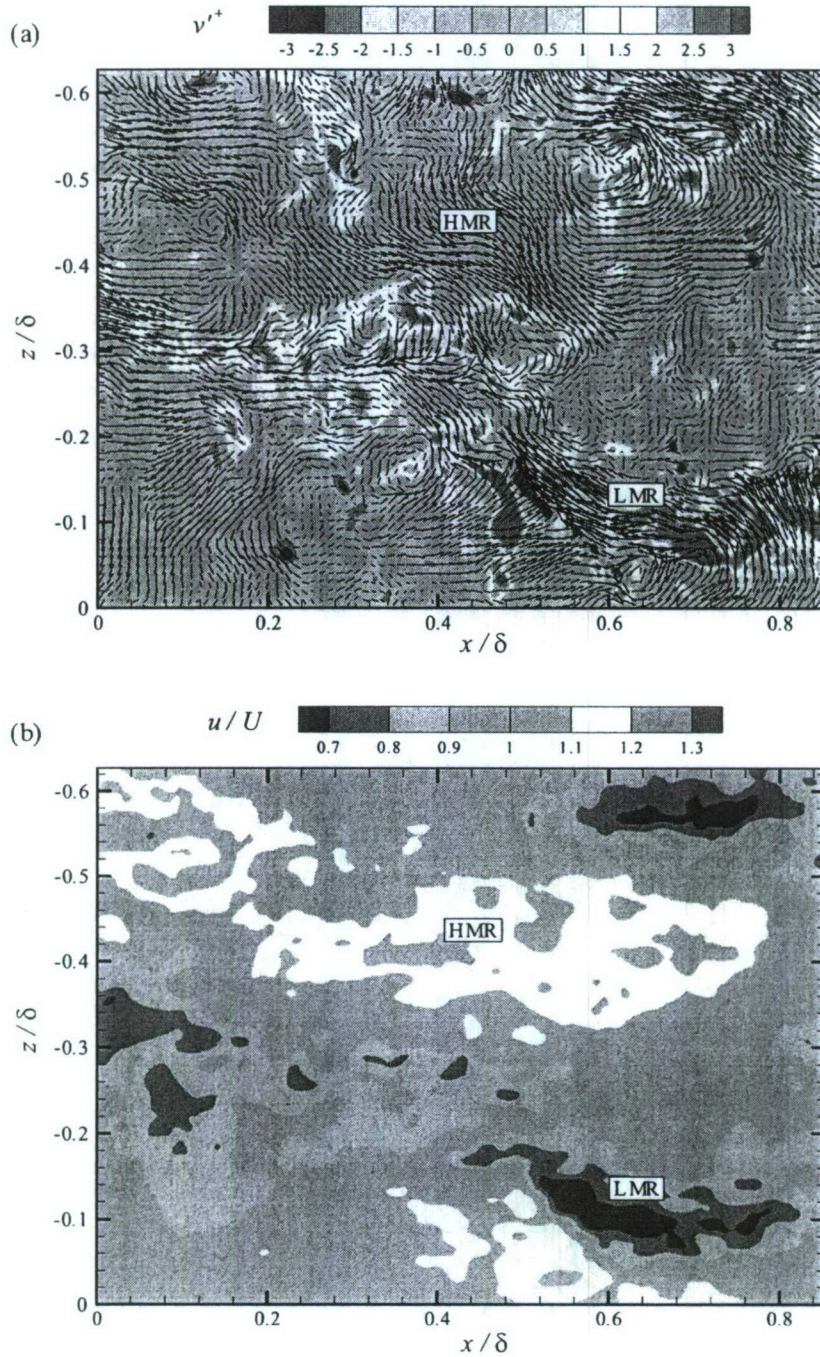


Figure 51: A representative instantaneous velocity realization in the streamwise–spanwise plane at  $y = 0.15\delta = 3.9k$  for flow over the RF1 surface at  $\text{Re}_\theta = 14781$ . (a) Fluctuating in-plane velocities ( $u', w'$ ) are presented as vectors and the fluctuating out-of-plane velocity,  $v'$ , is presented as contours. (b) Contours of normalized streamwise velocity,  $u/U$ , where  $U$  represents the ensemble- and area-averaged streamwise velocity.

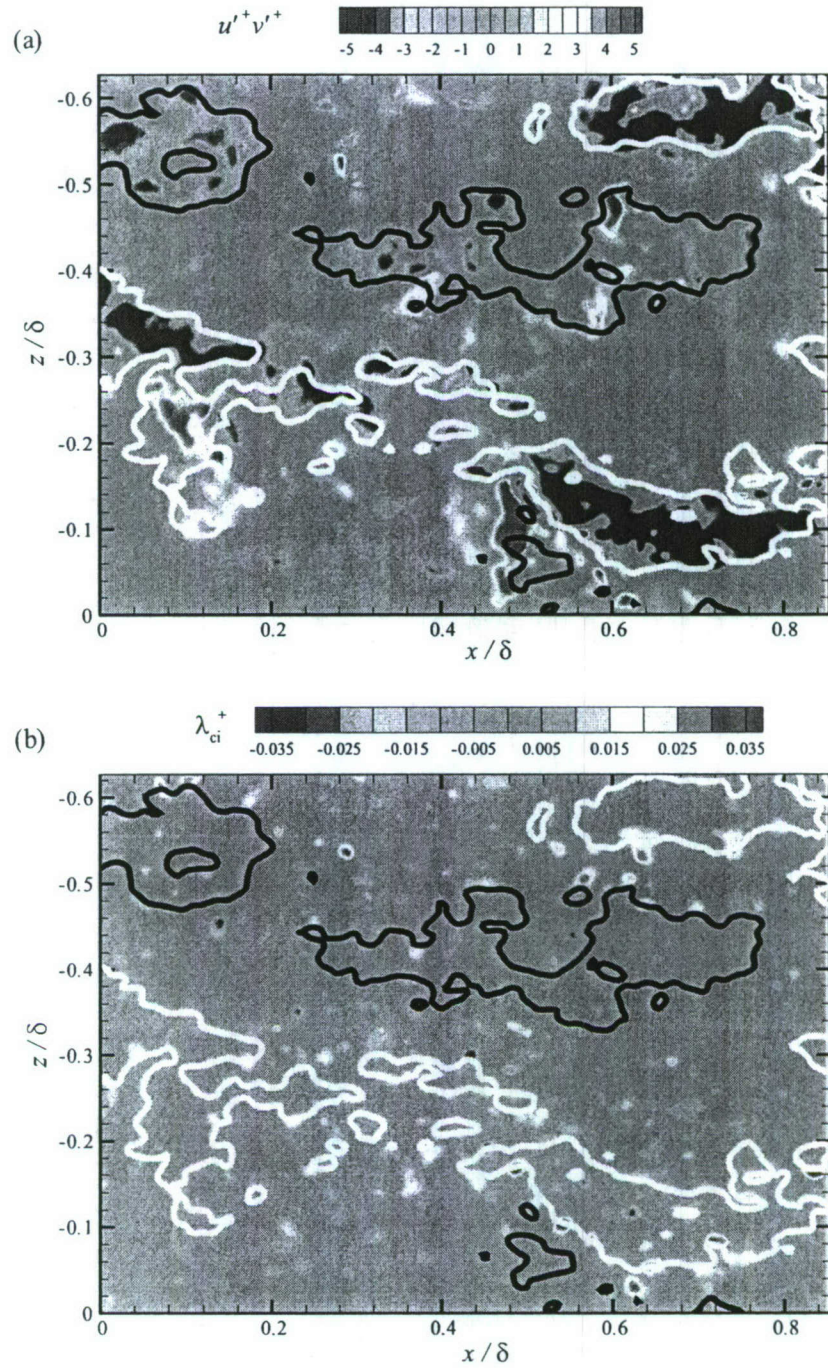


Figure 52: Instantaneous (a) turbulent shear stress,  $u'v'$ , and (b) swirling strength,  $\lambda_{ci}$ , computed from the instantaneous velocity realization presented in figure 51. Line contours of low- (white;  $0.85U$ ) and high-momentum (black;  $1.15U$ ) regions are presented in the background.

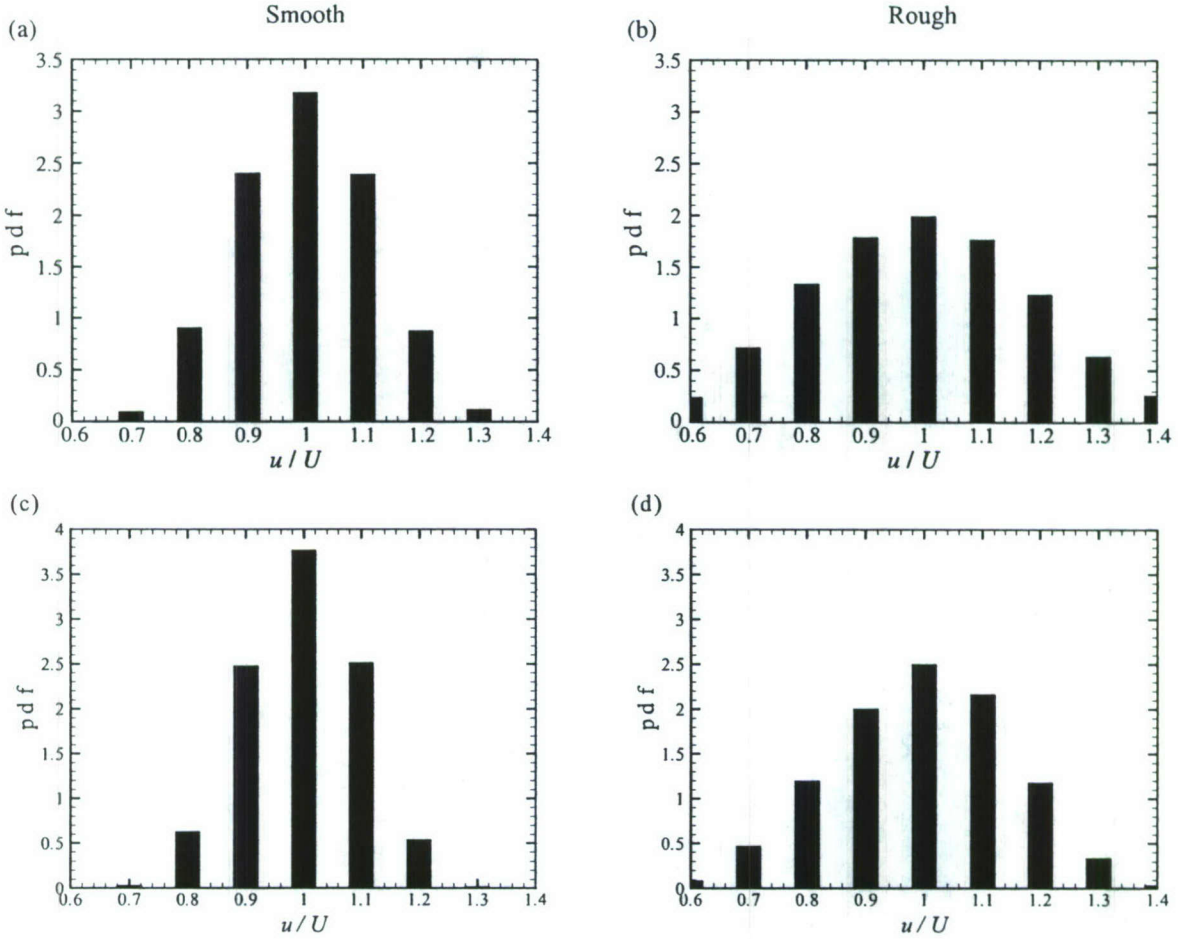


Figure 53: Probability density functions of normalized streamwise velocity,  $u/U$ , in the streamwise-spanwise plane for  $\text{Re}_\theta \approx 13000$  at (a, b)  $y = 0.065\delta$  and (c, d)  $y = 0.15\delta$  for flow over the smooth and RF1 surfaces, respectively.

roughness effects can be intense. Quantitatively, however, in addition to the obvious enhancement of  $v'$  in the presence of roughness, the excursions of the instantaneous streamwise velocity,  $u$ , about the mean,  $U$ , appear to be much stronger in the rough-wall case when figures 45(b) and 47(b) ( $y = 0.065\delta$  fields) as well as figures 49(b) and 51(b) ( $y = 0.15\delta$  fields) are compared. The exact extent of these excursions can be quantified by ensemble-averaged probability density functions (pdf's) of the normalized instantaneous streamwise velocity,  $u/U$ , as presented in figures 53 for the smooth- and rough-wall cases at both  $y = 0.065\delta$  and  $0.15\delta$  for  $\text{Re}_\theta \approx 13000$ . While the excursions of  $u$  about the mean are no more than 20% in the smooth-wall case at  $y = 0.065\delta$ , these excursions can exceed 40% in the RF1 case. At  $y = 0.15\delta$ , these excursions are again less than 20% for the smooth-wall case but still 30% in the rough-wall case.

Given the differences noted in the excursions of  $u$  about  $U$ , it is of interest to compare the contributions of these LMR's to various turbulence quantities of interest ( $\langle u'v' \rangle$ , for example) for flow over the smooth and RF1 surfaces. Low-momentum regions are chosen for this analysis particularly because they are likely attributable to the induction of hairpin vortex packets and the  $u'v'$  events noted within LMR's are attributable to ejections generated by the individual vortices

within packets. To facilitate this analysis, a threshold,  $U_{th}$ , on an LMR is established (some fraction of the ensemble- and area-averaged mean streamwise velocity,  $U$ ) and an indicator function,  $I$ , is assigned at every gridpoint in the  $j^{th}$  velocity realization as

$$I(x_j, z_j; U_{th}) = \begin{cases} 1, & \text{when } u(x_j, z_j) \leq U_{th} \\ 0, & \text{otherwise,} \end{cases} \quad (37)$$

to distinguish between gridpoints that meet the LMR threshold and those that do not (This methodology is identical in spirit to the quadrant analysis method discussed in chapter 3 but with a different physical threshold). The contributions of the LMR's identified with a given threshold  $U_{th}$  to a given quantity of interest,  $S$ , are then assessed as

$$\langle S \rangle(U_{th}) = \frac{1}{M \times P} \sum_{\text{all } x} \sum_{\text{all } z} \sum_{j=1}^M S(x_j, z_j) I(x_j, z_j; U_{th}), \quad (38)$$

where  $M$  is the total number of velocity realizations while  $P$  is the total number of gridpoints within a velocity realization (in both the  $x$  and  $z$  directions) and  $\langle S \rangle$  can be any turbulence quantity of interest (Reynolds normal or shear stresses, turbulent kinetic energy, etc.). In addition, the fraction of space,  $N$ , occupied by the LMR's satisfying the  $U_{th}$  threshold can be evaluated as

$$N(U_{th}) = \frac{\sum I(U_{th})}{M \times P}, \quad (39)$$

where the summation is over all realizations and gridpoints.

The results of this analysis are presented in table 5.1 for smooth- and rough-wall flow at  $Re_\theta \approx 13000$  at both  $y = 0.065\delta$  and  $0.15\delta$ . Contributions to  $\langle u'v' \rangle$ , the Reynolds normal stresses ( $\langle u'^2 \rangle$ ,  $\langle v'^2 \rangle$  and  $\langle w'^2 \rangle$ ) and the turbulent kinetic energy ( $\langle q^2 \rangle$ ) within LMR's for  $U_{th} = 0.9U$ ,  $0.8U$  and  $0.7U$  are tabulated. For  $U_{th} = 0.9U$  (a weak threshold on LMR's since it includes most all possibilities), the contributions of LMR's to  $\langle u'v' \rangle$ ,  $\langle u'^2 \rangle$ ,  $\langle w'^2 \rangle$  and  $\langle q^2 \rangle$  are all quite similar between the smooth- and rough-wall flows (46% versus 50% for  $\langle u'v' \rangle$  at  $y = 0.065\delta$ , for example). However, the fraction of space occupied by LMR's satisfying  $U_{th} = 0.9U$  is 10% higher in the case of flow over the RF1 surface and the percent contribution of these regions to  $\langle v'^2 \rangle$  is doubled in the presence of roughness. Further, while the space fraction (0.2%) and associated contributions to the various turbulence statistics (< 1.5%) for  $U_{th} = 0.7U$  are all minimal for smooth-wall flow at  $y = 0.065\delta$ , they are all an order of magnitude larger for the RF1 case, most notably a space fraction of 5% and a contribution to  $\langle u'v' \rangle$  of 19%. This result highlights the increased importance of LMR's with quite large streamwise momentum deficits in the rough-wall case. The same general trends hold for the contributions of LMR's to the turbulence statistics at  $y = 0.15\delta$  though the differences between the smooth- and rough-wall cases are less. This wall-normal trend is consistent with a weakening influence of roughness as one moves away from the rough surface as was observed in chapters 3 and 4.

### 6.3 Two-point spatial correlation coefficients

As noted previously, spatial correlations involving two- or more points of interest contain a wealth of information regarding the average spatial structure of a flow. In the context of the present work, modifications of the underlying structure of the flow in the presence of roughness can be further explored by directly comparing various spatial correlations of smooth-wall flow to those computed for flow over the RF1 surface. In its most general form, the two-point spatial correlation coefficient between two arbitrary quantities,  $p$  and  $q$ , is defined by

$$\rho_{pq}(\mathbf{x}_o, \mathbf{x}) = \frac{\langle p(\mathbf{x}_o)q(\mathbf{x}) \rangle}{\sigma_p(\mathbf{x}_o)\sigma_q(\mathbf{x})}, \quad (40)$$

Table 6: Contributions of LMR's to the Reynolds stresses and turbulent kinetic energy,  $\langle q^2 \rangle$ , at  $Re_\theta \approx 13000$  for flow over the smooth and RF1 surfaces.

$y = 0.065\delta$							
	$U_{th}$	$-\langle u'v' \rangle$	$\langle u'^2 \rangle$	$\langle v'^2 \rangle$	$\langle w'^2 \rangle$	$\langle q^2 \rangle$	Space Fraction, $N$
Smooth	0.9U	46%	43%	14%	29%	34%	21%
	0.8U	18%	16%	4%	5%	12%	4%
	0.7U	1.3%	1.2%	0.3%	0.1%	0.8%	0.2%
RF1	0.9U	50%	47%	31%	27%	40%	31%
	0.8U	39%	36%	16%	12%	27%	15%
	0.7U	19%	18%	6%	4%	13%	5%

$y = 0.15\delta$							
	$U_{th}$	$-\langle u'v' \rangle$	$\langle u'^2 \rangle$	$\langle v'^2 \rangle$	$\langle w'^2 \rangle$	$\langle q^2 \rangle$	Space Fraction, $N$
Smooth	0.9U	44%	40%	21%	15%	31%	16%
	0.8U	12%	10%	4%	2%	7%	2%
	0.7U	0.4%	0.3%	0.1%	0.02%	0.2%	0.03%
RF1	0.9U	51%	48%	31%	26%	39%	26%
	0.8U	34%	31%	13%	9%	22%	9%
	0.7U	12%	11%	3%	2%	7%	2%

where  $\mathbf{x}_o$  and  $\mathbf{x}$  are the points of interest and  $\sigma_p$  and  $\sigma_q$  are root-mean-square (RMS) values of  $p$  and  $q$ , respectively. This representation can be simplified by noting that the spanwise ( $z$ ) direction of a zero-pressure-gradient turbulent boundary layer is homogeneous and the streamwise ( $x$ ) direction can be considered approximately homogeneous for the fields of view under study since the boundary-layer thickness grows slowly with  $x$ . As a result, the two-point spatial correlation coefficient  $\rho_{pq}$  is only a function of  $(y, y_{ref}, \Delta x, \Delta z)$ , where  $y_{ref}$  is the wall-normal reference location and  $\Delta x$  and  $\Delta z$  are spatial separations in the streamwise and spanwise directions, respectively (Kovasznay *et al.*, 1970; Krogstad & Antonia, 1994; Ganapathisubramani *et al.*, 2005). For velocity measurements residing in a streamwise–spanwise ( $x - z$ ) plane at a wall-normal position  $y$ , the representation for  $\rho_{pq}$  reduces to

$$\rho_{pq}(\Delta x, \Delta z; y) = \frac{\langle p(x_0, z_0; y) q(x_0 + \Delta x, z_0 + \Delta z; y) \rangle}{\sigma_p(y) \sigma_q(y)}. \quad (41)$$

Similarly, for velocity measurements residing in the streamwise–wall-normal ( $x - y$ ) plane,  $\rho_{pq}$  reduces to

$$\rho_{pq}(\Delta x, y; y_{ref}) = \frac{\langle p(x, y_{ref}) q(x + \Delta x, y) \rangle}{\sigma_p(y_{ref}) \sigma_q(y)}. \quad (42)$$

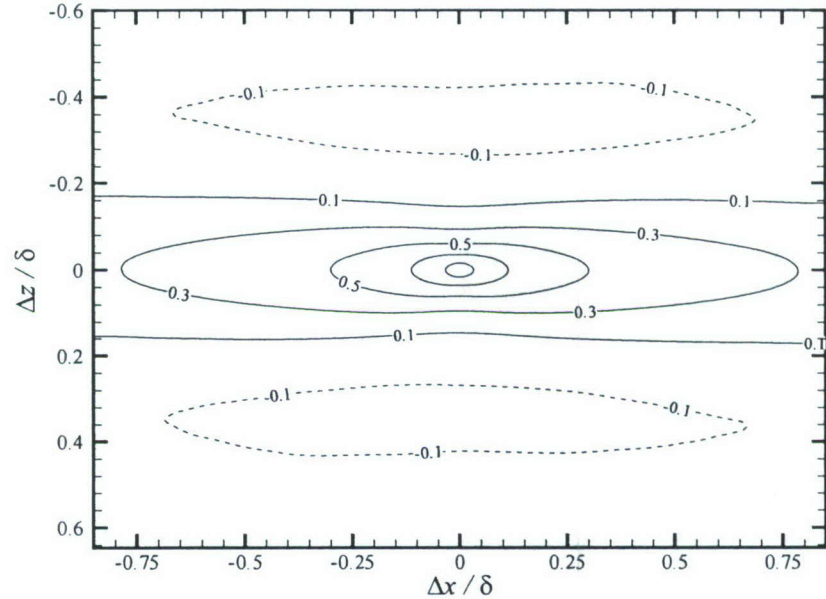
These correlation coefficients are computed using fast Fourier transforms (FFT) in a manner consistent with many recent studies of spatial correlations in wall-bounded turbulent flows (Christensen, 2001; Christensen & Wu, 2005; Ganapathisubramani *et al.*, 2005, among others). The FFT methodology employed was verified by comparing a few representative correlations computed in this manner with results achieved by computing the correlations directly in physical space. The two methods yielded identical results.

### 6.3.1 Streamwise velocity ( $\rho_{uu}$ )

Figure 54 presents  $\rho_{uu}$  in a streamwise–spanwise ( $x - z$ ) plane positioned at  $y = 0.065\delta$  for flow over the smooth and RF1 surfaces at  $Re_\theta \approx 13000$ . Despite the fact that this wall-normal location is within the roughness sublayer, there exists little qualitative difference between  $\rho_{uu}$  over the smooth and rough surfaces as they are both elongated in the streamwise direction and are bounded by weak negative, yet streamwise-elongated, correlations in the spanwise direction. These characteristics are quite consistent with previous observations of  $\rho_{uu}$  over smooth walls and are likely attributable to the streamwise-aligned, spanwise-alternating LMR's and HMR's (Ganapathisubramani *et al.*, 2005; Tomkins & Adrian, 2003). In fact, the streamwise and spanwise extents of  $\rho_{uu}$  are quite consistent with the streamwise and spanwise length scales of the LMR's and HMR's noted in the instantaneous velocity realizations presented in section 6.2 at this wall-normal location for both smooth- and rough-wall flows (figures 43–48). As noted earlier, LMR's are thought to be generated by the collective induction of multiple hairpin-like vortices in hairpin vortex packets while HMR's usually occur outboard of the hairpin packets due to the induction of higher-speed fluid toward the wall by the rotational sense of the hairpins. Consistent with instantaneous evidence, these correlations further support the observation that LMR's and HMR's are dominant flow patterns in the rough-wall flow. However, while strong qualitative consistency exists in  $\rho_{uu}$  for smooth- and rough-wall flow, quantitative differences do exist. For example, the streamwise extent of the  $\rho_{uu} = 0.3$  contour level is approximately  $0.8\delta$  over the smooth wall but only  $0.6\delta$  for flow over the RF1 surface. In contrast, the spanwise extents of  $\rho_{uu}$  are quite similar between the smooth- and rough-wall cases. It should be noted that Krogstad & Antonia (1994) reported a reduction of a factor of two in the streamwise extent of the  $\rho_{uu} = 0.3$  contour level for flow over wire mesh at  $Re_\theta \approx 6000$  but reported no difference in the spanwise extent of  $\rho_{uu}$ .

A quantitative comparison of  $\rho_{uu}$  in smooth- and rough-wall flow at  $y = 0.065\delta$  is shown in figures 55(a) and 55(b) which presents one-dimensional profiles of  $\rho_{uu}$  from figure 54 in the spanwise

(a)



(b)

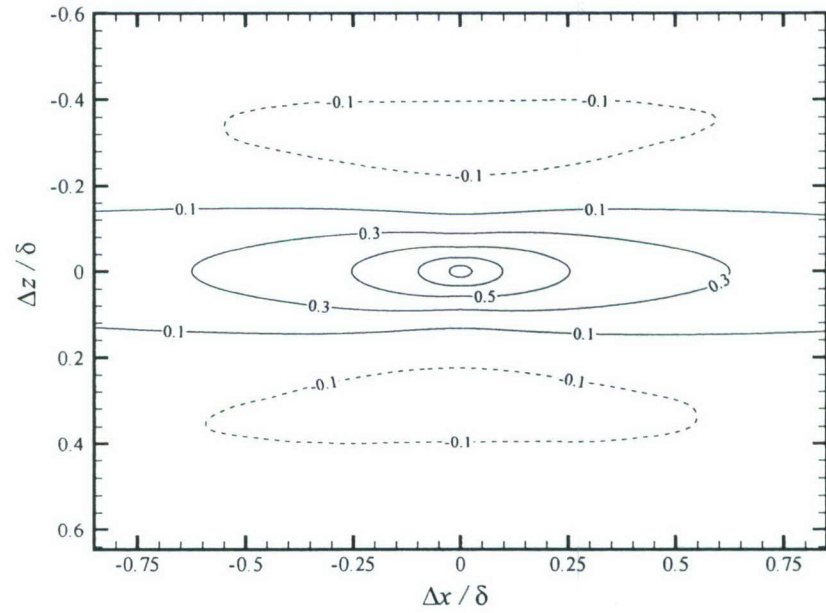


Figure 54: Streamwise velocity correlation coefficients,  $\rho_{uu}$ , in the  $x - z$  plane at  $y = 0.065\delta$  for  $Re_\theta \approx 13000$ . (a) Smooth; (b) RF1. Contour levels are -0.1, 0.1, 0.3, 0.5, 0.7 and 0.9.

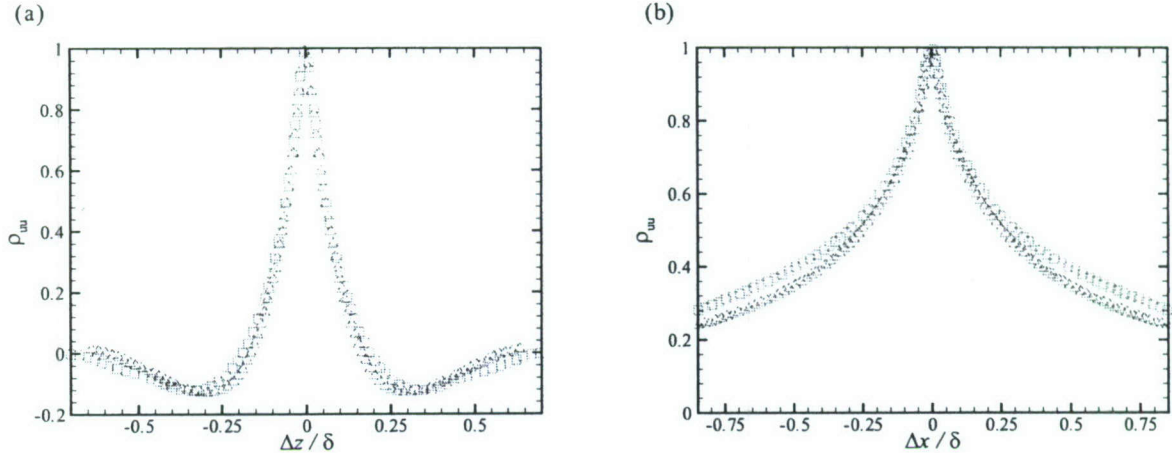


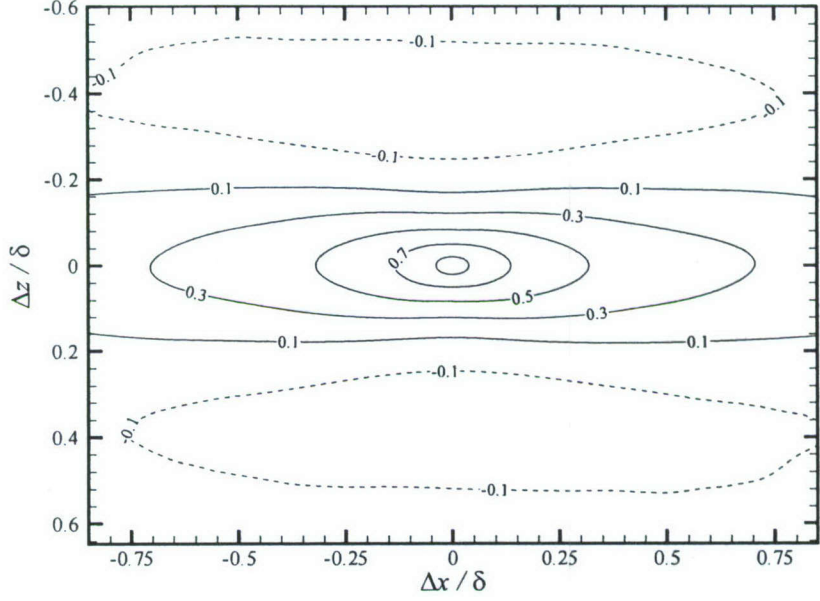
Figure 55: One-dimensional profiles of  $\rho_{uu}$  from figure 54 in the (a) spanwise ( $\Delta x = 0$ ) and (b) streamwise ( $\Delta z = 0$ ) directions at  $y = 0.065\delta$  for  $Re_\theta \approx 13000$ . ■: Smooth; △: RF1.

and streamwise directions, respectively. One-dimensional profiles of  $\rho_{uu}$  in the spanwise direction ( $\Delta x = 0$ ) confirm little effect of roughness on the spanwise extent of  $\rho_{uu}$  at  $y = 0.065\delta$  as the smooth- and rough-wall profiles collapse. In contrast, the streamwise profile of  $\rho_{uu}$  ( $\Delta z = 0$ ) for rough-wall flow is found to be reduced compared to the smooth-wall result, particularly for  $\Delta x > 0.1\delta$ . Since the streamwise extent of  $\rho_{uu}$  is representative of the streamwise length scales of LMR's and HMR's which are thought to be the byproducts of hairpin vortex packets, this reduction in the streamwise extent of  $\rho_{uu}$  may indicate an overall reduction in the streamwise scales of these packets. Such a reduction could manifest itself either via a reduction in the streamwise spacing of consecutive vortices in a packet or possibly through an alteration in the vortex regeneration mechanism thought to be the impetus for this organization (Zhou *et al.*, 1996, 1997, 1999). Alternatively, recalling that LMR's and HMR's have been observed to extend  $5 - 10\delta$  in the streamwise direction while meandering in the spanwise direction Hutchins & Marusic (2007), roughness may enhance this spanwise meandering which would manifest itself as a reduction in the streamwise coherence of  $\rho_{uu}$  along a fixed spanwise position.

Figure 56 presents  $\rho_{uu}$  in an  $x-z$  plane positioned at  $y = 0.15\delta$  for flow over the smooth and RF1 surfaces at  $Re_\theta \approx 13000$ . The qualitative features of  $\rho_{uu}$  at this wall-normal location are consistent with its general character closer to the wall:  $\rho_{uu}$  is elongated in the streamwise direction and the positive correlation region is bounded in the spanwise direction by weaker, yet still elongated, negative correlation regions. Again, these patterns are interpreted as the imprint of spanwise-alternating LMR's and HMR's. However, several things become immediately apparent upon comparing  $\rho_{uu}$  at  $y = 0.065\delta$  and  $y = 0.15\delta$ . First, the spanwise extents of  $\rho_{uu}$  have increased (but are still quite similar between the smooth- and rough-wall cases), consistent with previous observations of spanwise scale growth in wall turbulence (Tomkins & Adrian, 2003; Ganapathisubramani *et al.*, 2005). Second, the rough-wall and smooth-wall streamwise extents are considerably more comparable than at  $y = 0.065\delta$ , although  $\rho_{uu}$  for the RF1 case is still slightly reduced compared to the smooth-wall result.

The character of  $\rho_{uu}$ , particularly differences between smooth- and rough-wall flow, can also be explored in the streamwise-wall-normal plane. Unfortunately, due to intense laser reflections from the surfaces velocity data is not available for evaluation of  $\rho_{uu}$  at  $y = 0.065\delta$  in the  $x-y$  plane. However,  $\rho_{uu}$  can be evaluated and compared at  $y = 0.15\delta$ . Figure 57 illustrates  $\rho_{uu}$  in

(a)



(b)

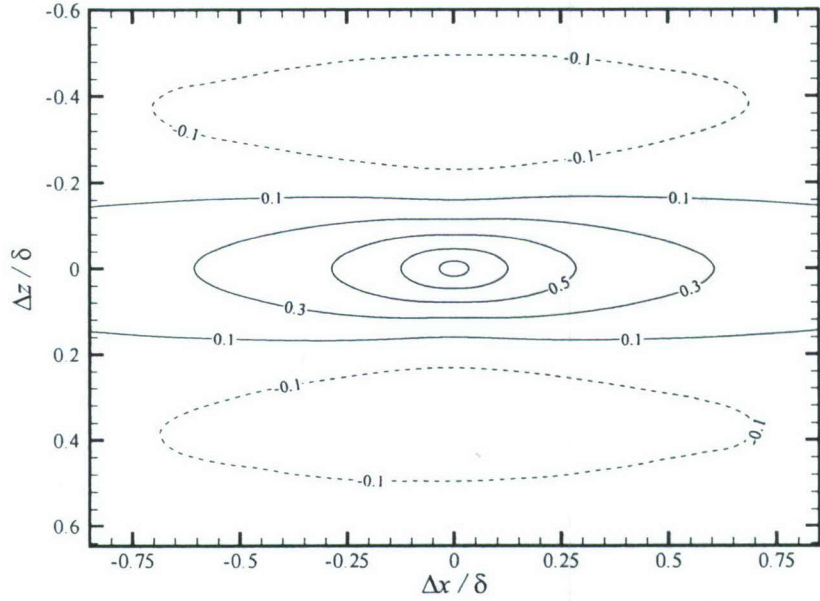


Figure 56: Streamwise velocity correlation coefficients,  $\rho_{uu}$ , in the  $x - z$  plane at  $y = 0.15\delta$  for  $Re_\theta \approx 13000$ . (a) Smooth; (b) RF1. Contour levels are -0.1, 0.1, 0.3, 0.5, 0.7 and 0.9.

the  $x - y$  plane for flow over both smooth and RF1 surfaces at  $y_{\text{ref}} = 0.15\delta$  for  $\text{Re}_\theta \approx 13000$ . As should be expected from the character of  $\rho_{uu}$  in the  $x - z$  planes,  $\rho_{uu}$  is quite elongated in the streamwise direction as well as inclined slightly away from the wall at its downstream end for both smooth- and rough-wall flow. This inclination is quite consistent with the inclination noted in instantaneous snapshots of hairpin vortex packets and is therefore interpreted as a structural imprint of such entities (Christensen & Adrian, 2001; Christensen, 2001; Christensen & Wu, 2005). It should be noted that Krogstad & Antonia (1994) observed a significant increase in the inclination angle of  $\rho_{uu}$  from  $10^\circ$  in smooth-wall flow to  $38^\circ$  for flow over wire mesh. However, the present results indicate a consistency in the inclination angle of  $\rho_{uu}$  for the smooth- and rough-wall cases considered herein.

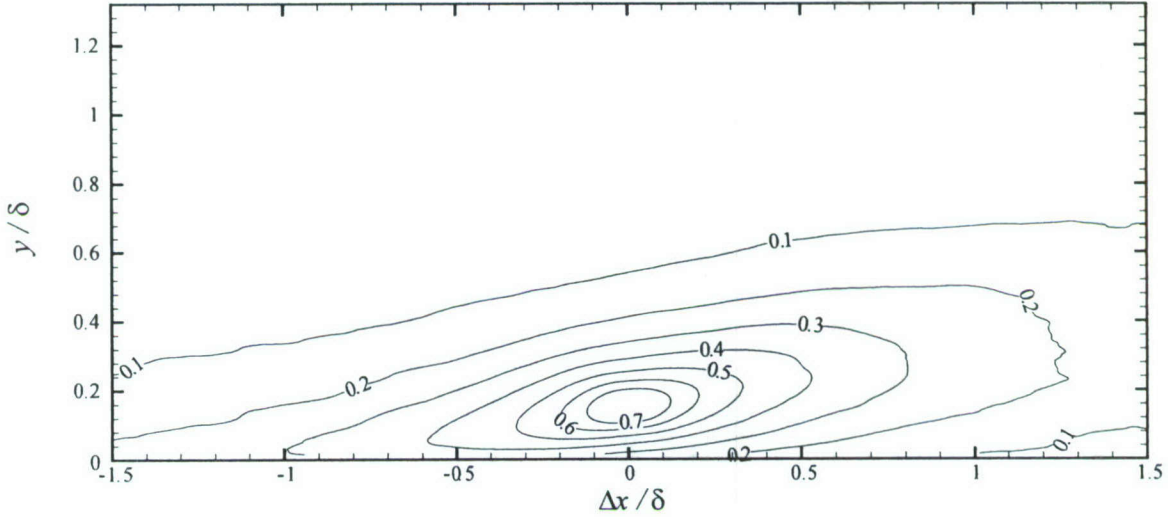
A quantitative comparison of  $\rho_{uu}$  at  $y = 0.15\delta$  for the smooth- and rough-wall cases can be made by plotting one-dimensional profiles of  $\rho_{uu}$  in the spanwise, streamwise and wall-normal directions [figures 58(a), 58(b) and 58(c), respectively]. The comparisons in the spanwise ( $\Delta x = 0$ ) and streamwise ( $\Delta y = 0$ ) directions are achieved using the  $x - z$  plane data while the comparison in the wall-normal direction is accomplished using the  $x - y$  plane data. As the two-dimensional correlations in figure 56 suggest, the RF1 surface has little impact on the spanwise extent of  $\rho_{uu}$  as the smooth- and rough-wall results collapse well. As was the case at  $y = 0.065\delta$ , a slight reduction in the streamwise extent of  $\rho_{uu}$  is still observed at  $y = 0.15\delta$ , although the difference between the smooth and rough cases has reduced with distance from the wall. Finally, the wall-normal extent of  $\rho_{uu}$  appears relatively unaffected by roughness as  $\rho_{uu}$  collapses as a function of  $y$  for  $y_{\text{ref}} = 0.15\delta$  in figure 58(c).

The  $\rho_{uu}$  results in the  $x - y$  plane can also be used to assess its inclination angle for the smooth- and rough-wall cases as a function of wall-normal location. Christensen & Wu (2005) reported the inclination angle of  $\rho_{uu}$  in smooth-wall turbulent channel flow to be approximately  $11^\circ$ , with a weak increase (a few degrees) with wall-normal position but little sensitivity to  $\text{Re}$ . Interestingly, Morris *et al.* (2007) also reported an average inclination angle of  $\rho_{uu}$  of  $11^\circ$  for  $y^+ < 3000$  computed from transitionally-rough atmospheric boundary layer measurements at  $\delta^+ = 600,000$ . The present effort employs the same methodology used by Christensen & Wu (2005) for determining the inclination angle of  $\rho_{uu}$ . In this method, the  $(\Delta x, y)$  spatial location that is farthest away from the reference location  $[(\Delta x, y) = (0, y_{\text{ref}})]$  on a given contour level is extracted. This procedure is applied to five contour levels (0.8, 0.7, 0.6, 0.5 and 0.4) and linear regression is then used to fit these points to a line from which the average inclination angle of  $\rho_{uu}$  is assessed. Figure 59 presents this average angle,  $\beta$ , as a function of  $y$  for the smooth and RF1 cases at  $\text{Re}_\theta \approx 13000$ . While some scatter in the data exists, the inclination angle is found to grow weakly with wall-normal location, from  $8^\circ$  close to the wall to  $13 - 15^\circ$  near  $y = 0.4\delta$ . Of particular importance, the smooth- and rough-wall inclination angles agree extremely well both in magnitude and trend. The quantitative agreement between the inclination angles of smooth- and rough-wall flow is quite consistent with the observations of Nakagawa & Hanratty (2001) for turbulent channel flow in the presence of wavy walls as well as the more recent work by Volino *et al.* (2007) for turbulent flow over wire mesh. However, this similarity is entirely inconsistent with the marked increase in inclination angle in the presence of mesh roughness reported by Krogstad & Antonia (1994).

### 6.3.2 Wall-normal velocity ( $\rho_{vv}$ )

Figure 60 presents two-point correlation coefficients of wall-normal velocity,  $\rho_{vv}$ , in a streamwise-spanwise plane located at  $y = 0.065\delta$  for flow over the smooth and RF1 surfaces. Previous studies have indicated that  $\rho_{vv}$  embodies the influence of the individual hairpin vortices in outer-layer vortex organization in contrast to  $\rho_{uu}$  which has spatial characteristics more consistent with the larger-scale vortex organization itself (Christensen, 2001, for example). Therefore, any modifications of

(a)



(b)

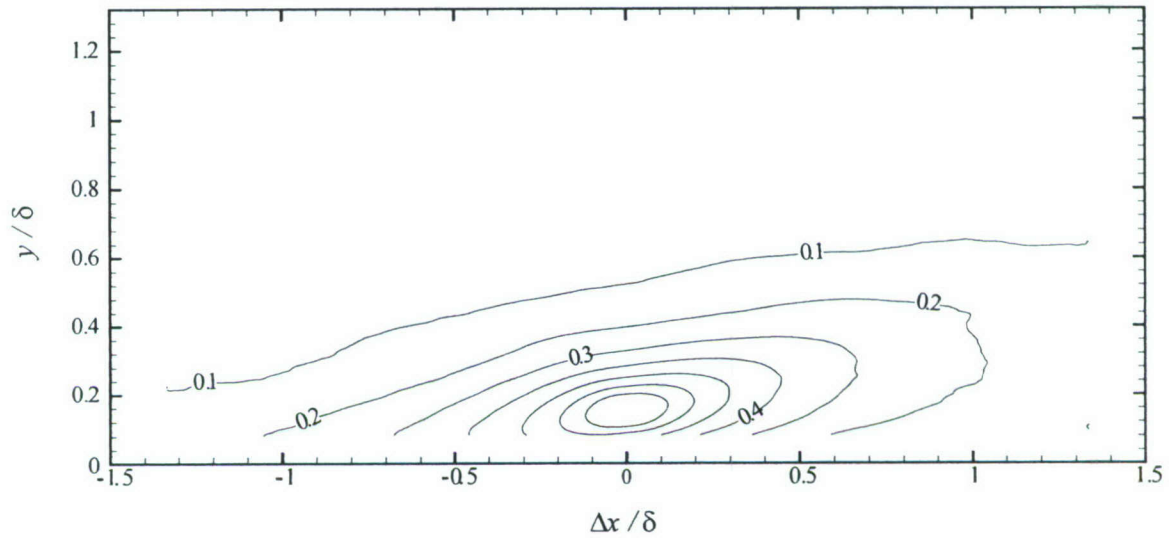


Figure 57: Streamwise velocity correlation coefficients,  $\rho_{uu}$ , in the  $x - y$  plane at  $y_{\text{ref}} = 0.15\delta$  for  $\text{Re}_\theta \approx 13000$ . (a) Smooth; (b) RF1. Contour levels are from 0.1 to 0.7 with interval of 0.1.

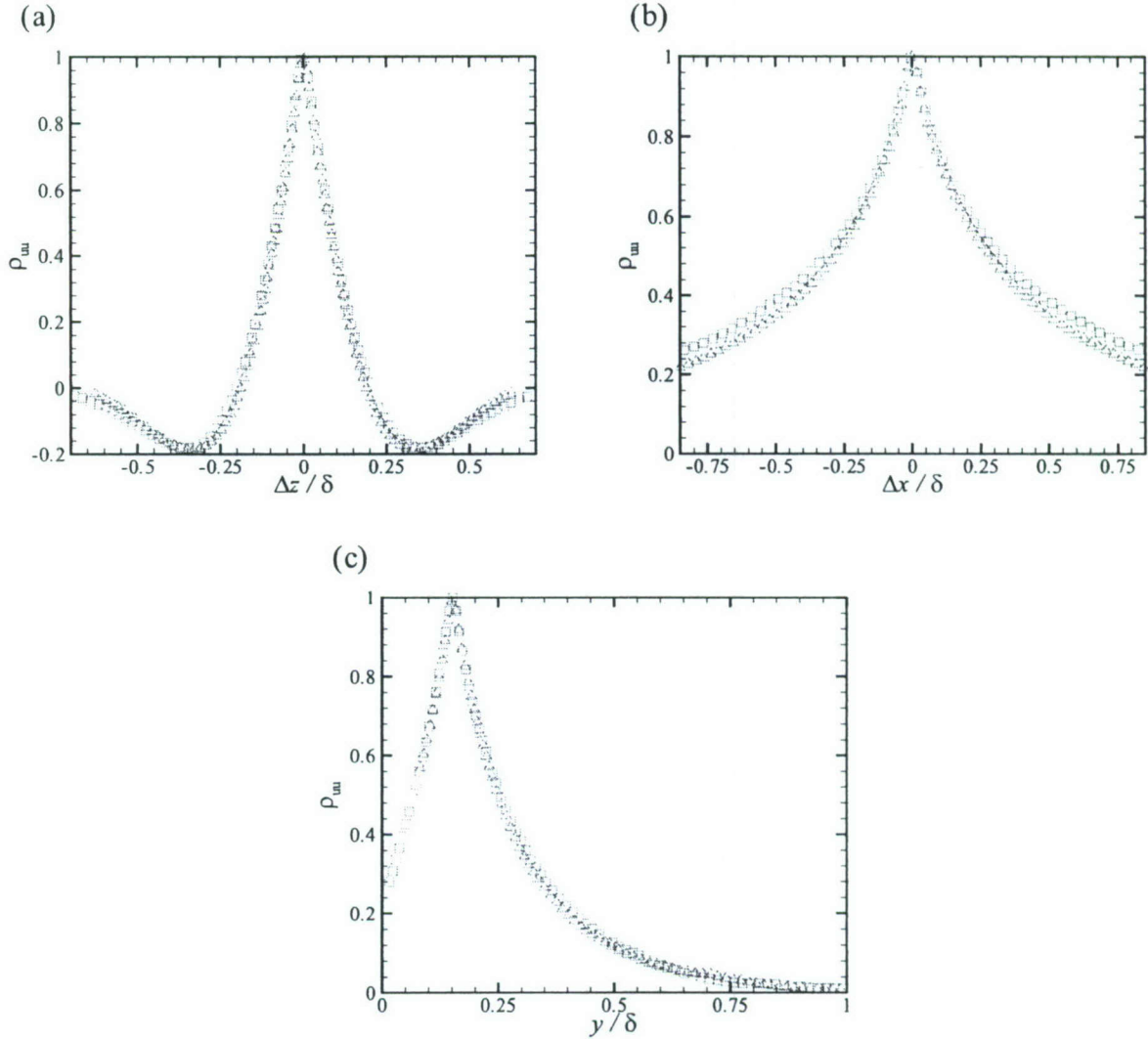


Figure 58: One-dimensional profiles of  $\rho_{uu}$  from figure 56 in the (a) spanwise ( $\Delta x = 0$ ), (b) streamwise ( $\Delta z = 0$ ) and (c) wall-normal ( $\Delta x = 0$ ) directions at  $y = 0.15\delta$  for  $Re_\theta \approx 13000$ .  $\square$ : Smooth;  $\triangle$ : RF1.

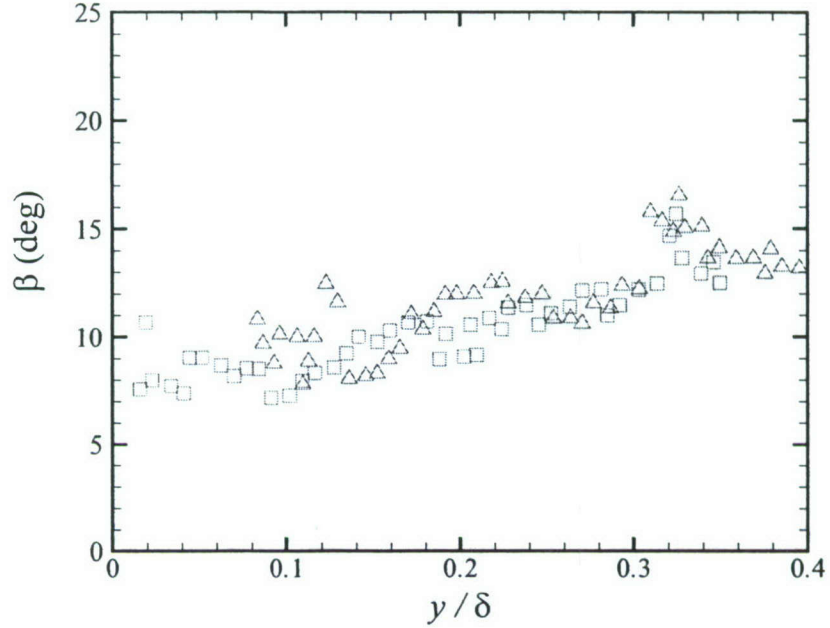


Figure 59: Average inclination angle of  $\rho_{uu}$  as a function of wall-normal position at  $\text{Re}_\theta \approx 13000$ . □: Smooth; △: RF1.

$\rho_{vv}$  in the presence of roughness could represent an alteration of hairpin-like structures themselves. At  $y = 0.065\delta$ ,  $\rho_{vv}$  is elliptical in shape, with an elongated extent in the streamwise direction on the order of  $0.2\text{--}0.3\delta$ . This streamwise length scale is clearly shorter than that of  $\rho_{uu}$  (approximately  $\delta$ ), supporting the observation that  $\rho_{vv}$  embodies imprints of smaller- to intermediate-scale structural features of the flow. Comparison of figure 60(a) [smooth] with figure 60(b) [rough] indicates that while the compact, higher correlation-level contours have streamwise and spanwise extents that are quite consistent between the smooth and rough cases, the streamwise extent of the  $\rho_{vv} = 0.1$  contour level is slightly reduced in the presence of roughness. Further, while there exists a difference in the streamwise extent of this low contour level, the spanwise extent of the  $\rho_{vv} = 0.1$  level appears unaffected by roughness. These more quantitative trends can be seen clearly in figures 61(a) and 61(b) which present one-dimensional profiles of  $\rho_{vv}$  at  $y = 0.065\delta$  in the spanwise and streamwise directions, respectively. While the spanwise profiles collapse extremely well, indicating a relative insensitivity to roughness, the streamwise extent of  $\rho_{vv}$  is slightly reduced in the presence of roughness, particularly for lower correlation levels. These roughness effects should not be surprising given that  $y = 0.065\delta$  is well within the roughness sublayer where roughness-induced modifications are expected to be most obvious. It also should be noted that attempts to scale the streamwise profiles with  $y_*$  rather than  $\delta$  (not shown for brevity) yielded larger disparities between the smooth- and rough-wall profiles.

The slight reduction in the streamwise extent of  $\rho_{vv}$  at  $y = 0.065\delta$  is not observed further from the wall at  $y = 0.15\delta$ . Figure 62 illustrates  $\rho_{vv}$  in the  $x - z$  plane for flow over the smooth and RF1 surfaces at  $y = 0.15\delta$  and the smooth and rough results appear nearly identical in both streamwise and spanwise extents, even at the lower correlation levels where differences were most profound at  $y = 0.065\delta$ . As with  $\rho_{uu}$ , velocity data is not available in the  $x - y$  plane to evaluate the character of  $\rho_{vv}$  at  $y = 0.065\delta$ , though data is available at  $y = 0.15\delta$  [figures 63(a) and 63(b) for the smooth and RF1 cases, respectively]. As was noted in the  $x - z$  plane,  $\rho_{vv}$  is relatively compact in the

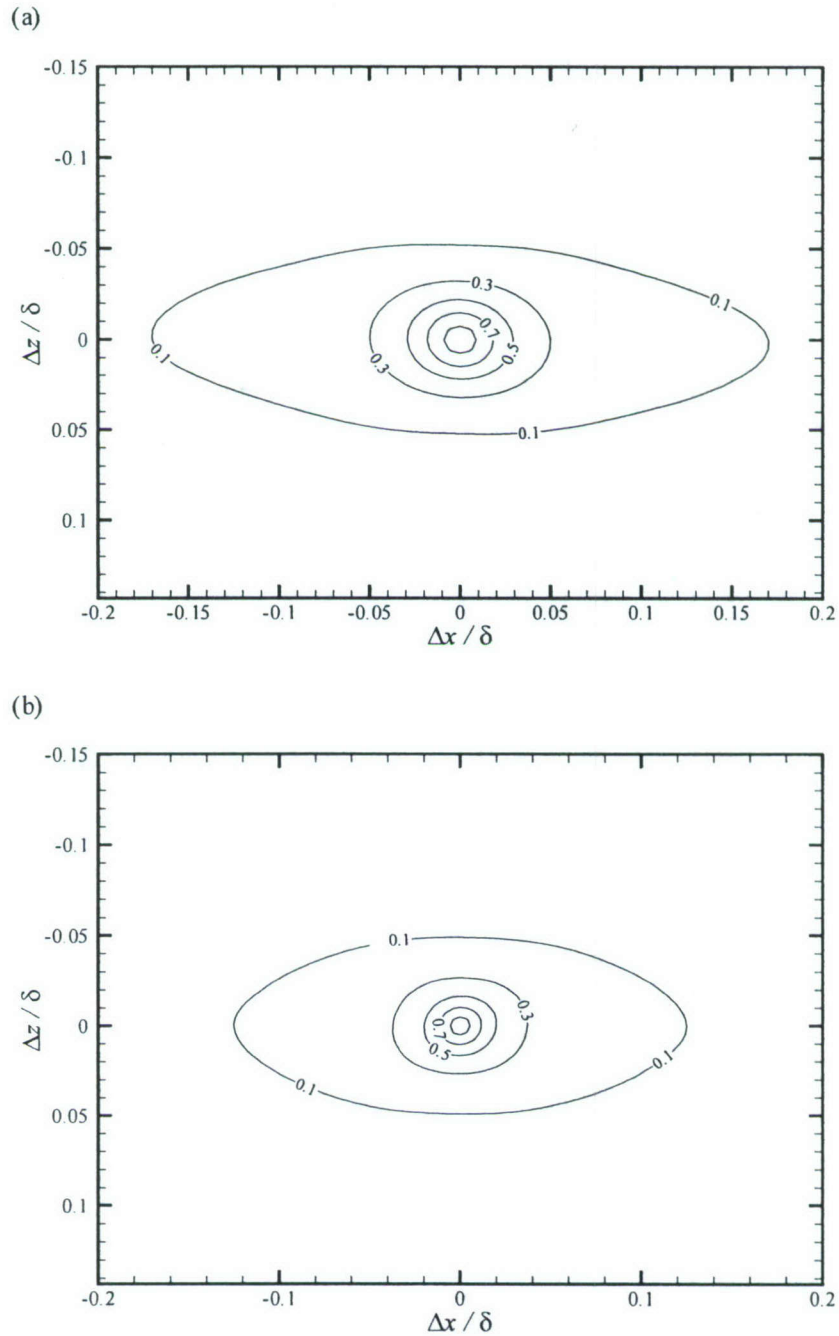


Figure 60: Wall-normal velocity correlation coefficients,  $\rho_{vv}$ , in the  $x - z$  plane at  $y = 0.065\delta$  for  $Re_\theta \approx 13000$ . (a) Smooth; (b) RF1. Contour levels are 0.1, 0.3, 0.5, 0.7 and 0.9.

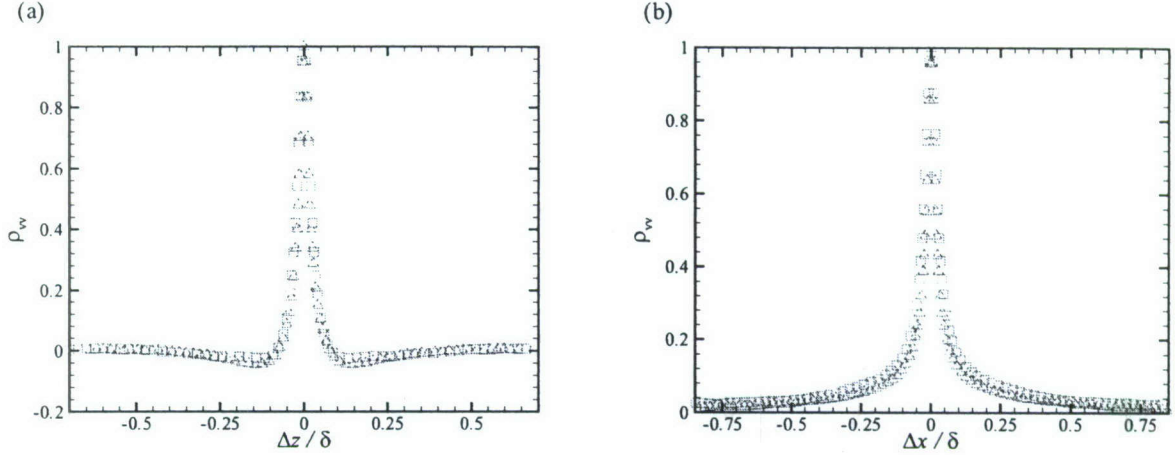


Figure 61: One-dimensional profiles of  $\rho_{vv}$  from figure 60 in the (a) spanwise ( $\Delta x = 0$ ) and (b) streamwise ( $\Delta z = 0$ ) directions at  $y = 0.065\delta$  for  $Re_\theta \approx 13000$ . □: Smooth; △: RF1.

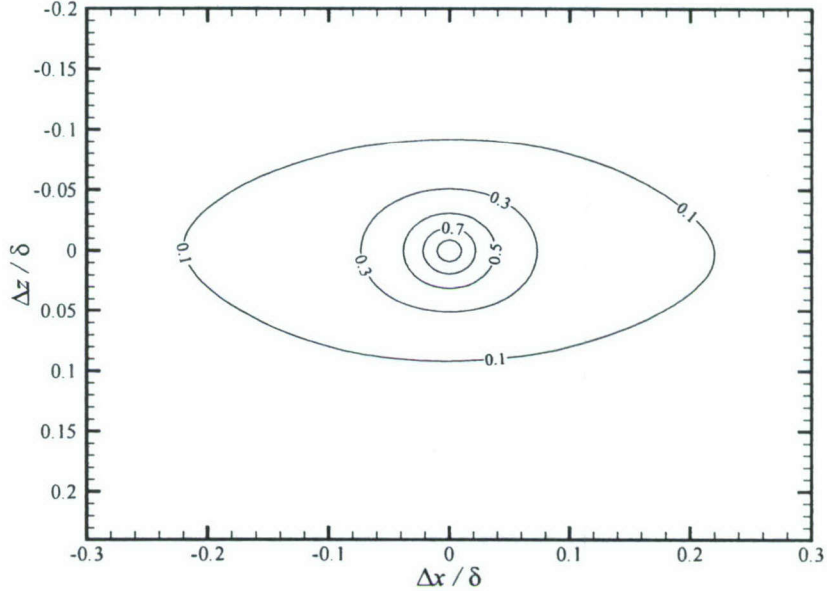
$x - y$  plane, although the  $\rho_{vv} = 0.1$  contour level extends beyond  $0.4\delta$  in the streamwise direction and is slightly inclined away from the wall based on the small bulges present upstream/below and downstream/above the reference location. It has been postulated that these two bulges might reflect the influence of upstream and downstream hairpin vortices within a hairpin vortex packet (Christensen, 2001, for example). Interestingly, both the smooth and rough  $\rho_{vv}$  in the  $x - y$  plane display these bulges, providing another inference that hairpin vortex packets still persist in flow over the rough surface considered herein. Finally, the quantitative consistency in  $\rho_{vv}$  for flow over the smooth and RF1 surfaces at  $y = 0.15\delta$  is clear in figure 64 which presents one-dimensional profiles of  $\rho_{vv}$  in the spanwise, streamwise and wall-normal directions. Excellent collapse is noted in all three cases.

### 6.3.3 Spanwise velocity ( $\rho_{ww}$ )

Two-point correlations of spanwise velocity,  $\rho_{ww}$ , in the  $x - z$  plane at  $y = 0.065\delta$  are presented in figure 65 for flow over the smooth and RF1 surfaces at  $Re_\theta \approx 13000$ . These correlations indicate that  $\rho_{ww}$  is an intermediate-scale correlation: larger than  $\rho_{vv}$  but smaller than  $\rho_{uu}$ . It was noted previously that LMR's and HMR's can meander in the spanwise direction rather than remain perfectly aligned in the streamwise direction (Hutchins & Marusic, 2007) and this phenomenon might be primarily responsible for the coherence of  $\rho_{ww}$ . In any case, the spatial extents of  $\rho_{ww}$  appear minimally affected by roughness at  $y = 0.065\delta$  even though this wall-normal location is well within the roughness sublayer. This quantitative consistency is clearly evident in figures 66(a) and 66(b) which present one-dimensional profiles of  $\rho_{ww}$  in the spanwise and streamwise directions, respectively, for smooth- and rough-wall flow at  $y = 0.065\delta$ . The smooth and rough profiles collapse extremely well in both spatial directions, indicating little or no influence of roughness on the physics associated with the spanwise velocity fluctuations. Note that this consistency is in contrast with that reported by Krogstad & Antonia (1994) who observed a significant decrease in the streamwise length scale of  $\rho_{ww}$  for flow over mesh compared to smooth-wall flow.

A similar consistency is noted in  $\rho_{ww}$  in the  $x - z$  plane at  $y = 0.15\delta$  (figure 67). Of interest,  $\rho_{ww}$  appears to be tending toward an isotropic state with increasing wall-normal position as its streamwise and spanwise extents are approaching similar values as evidenced by its relatively square

(a)



(b)

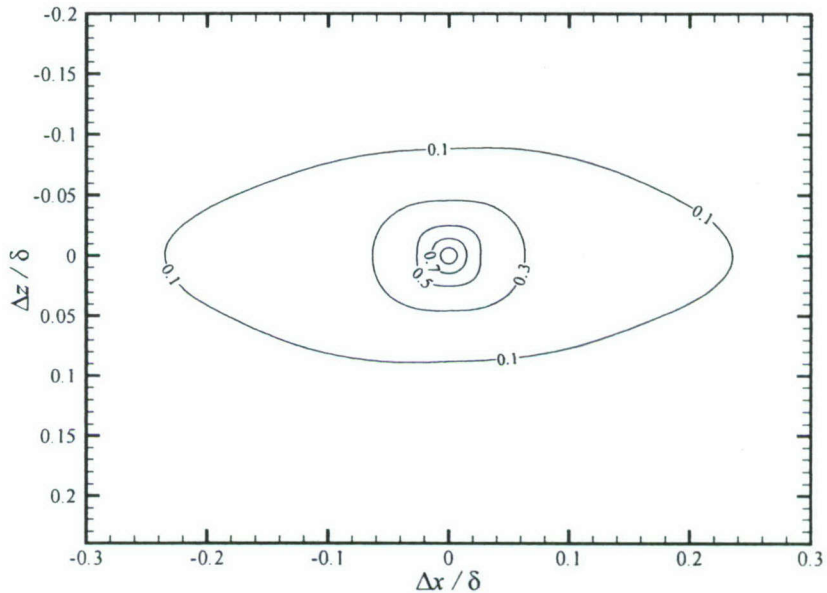
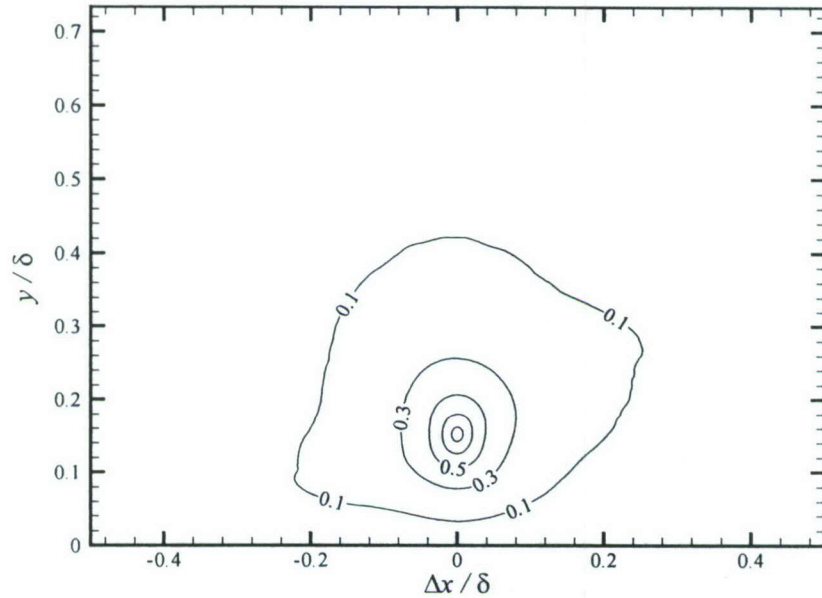


Figure 62: Wall-normal velocity correlation coefficients,  $\rho_{vv}$ , in the  $x - z$  plane at  $y = 0.15\delta$  for  $Re_\theta \approx 13000$ . (a) Smooth; (b) RF1. Contour levels are 0.1, 0.3, 0.5, 0.7 and 0.9.

(a)



(b)

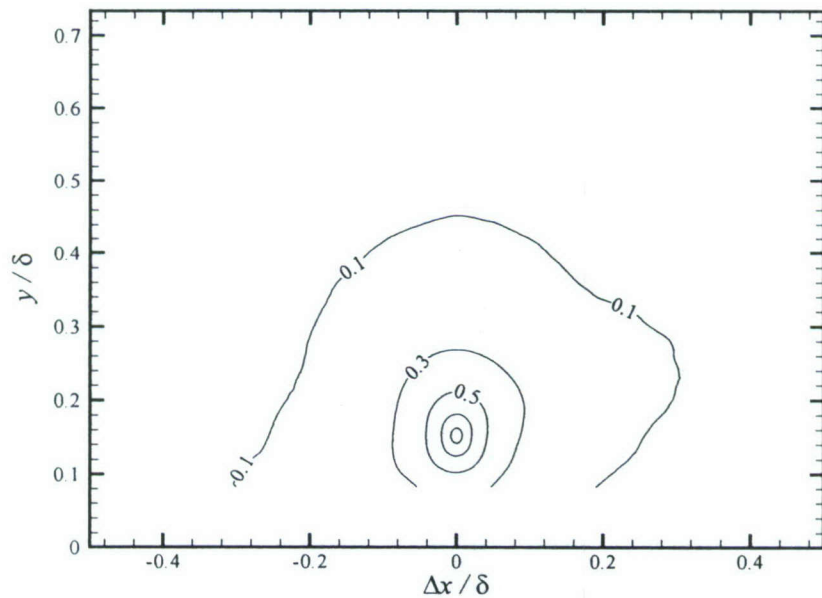


Figure 63: Wall-normal velocity correlation coefficients,  $\rho_{vv}$ , in the  $x - y$  plane at  $y = 0.15\delta$  for  $\text{Re}_\theta \approx 13000$ . (a) Smooth; (b) RF1. Contour levels are from 0.1 to 0.9 with interval of 0.1.

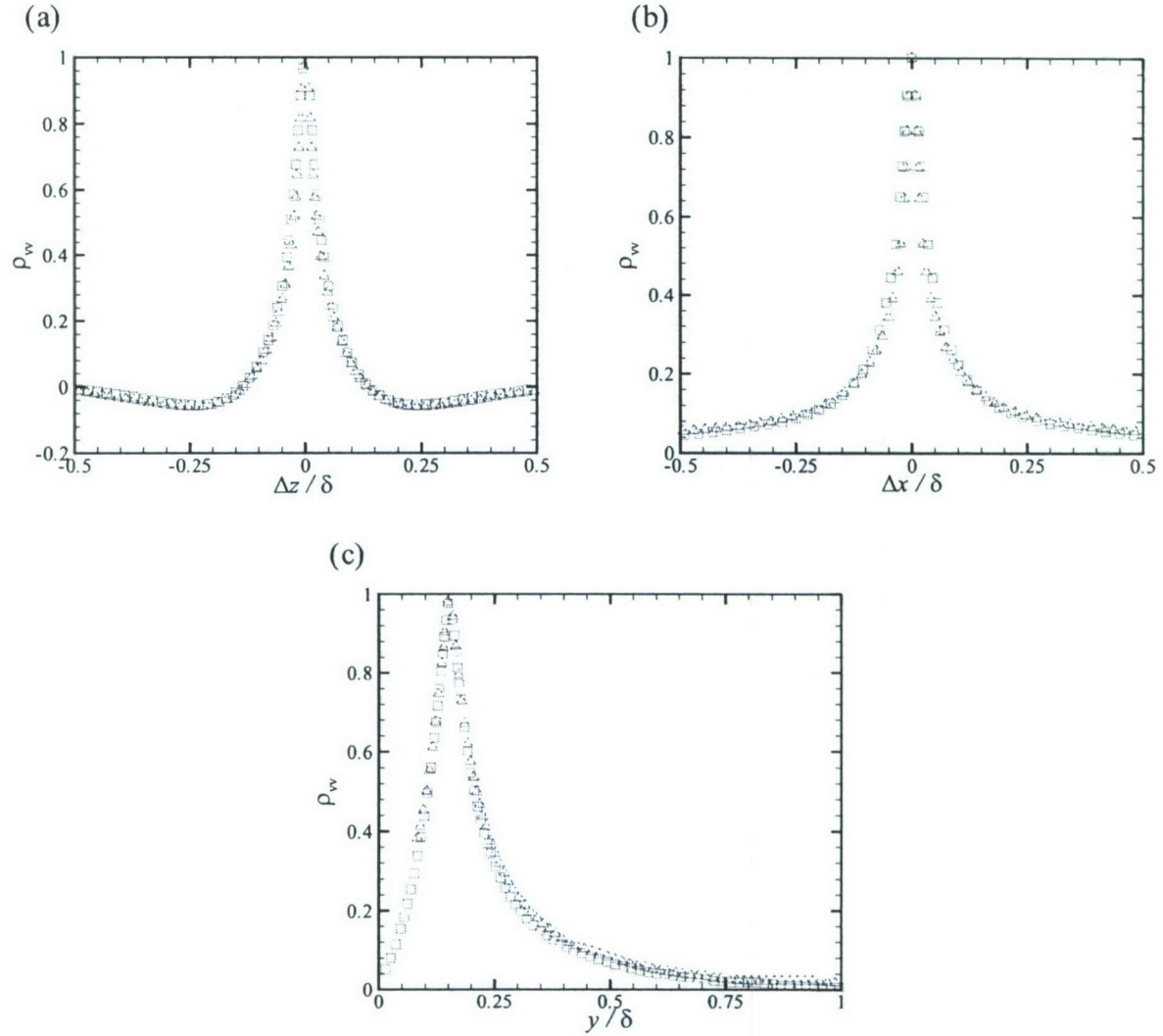


Figure 64: One-dimensional profiles of  $\rho_{vv}$  from figure 62 in the (a) spanwise ( $\Delta x = 0$ ), (b) streamwise ( $\Delta z = 0$ ) and (c) wall-normal ( $\Delta x = 0$ ) directions at  $y = 0.15\delta$  for  $Re_\theta \approx 13000$ .  $\square$ : Smooth;  $\triangle$ : RF1.

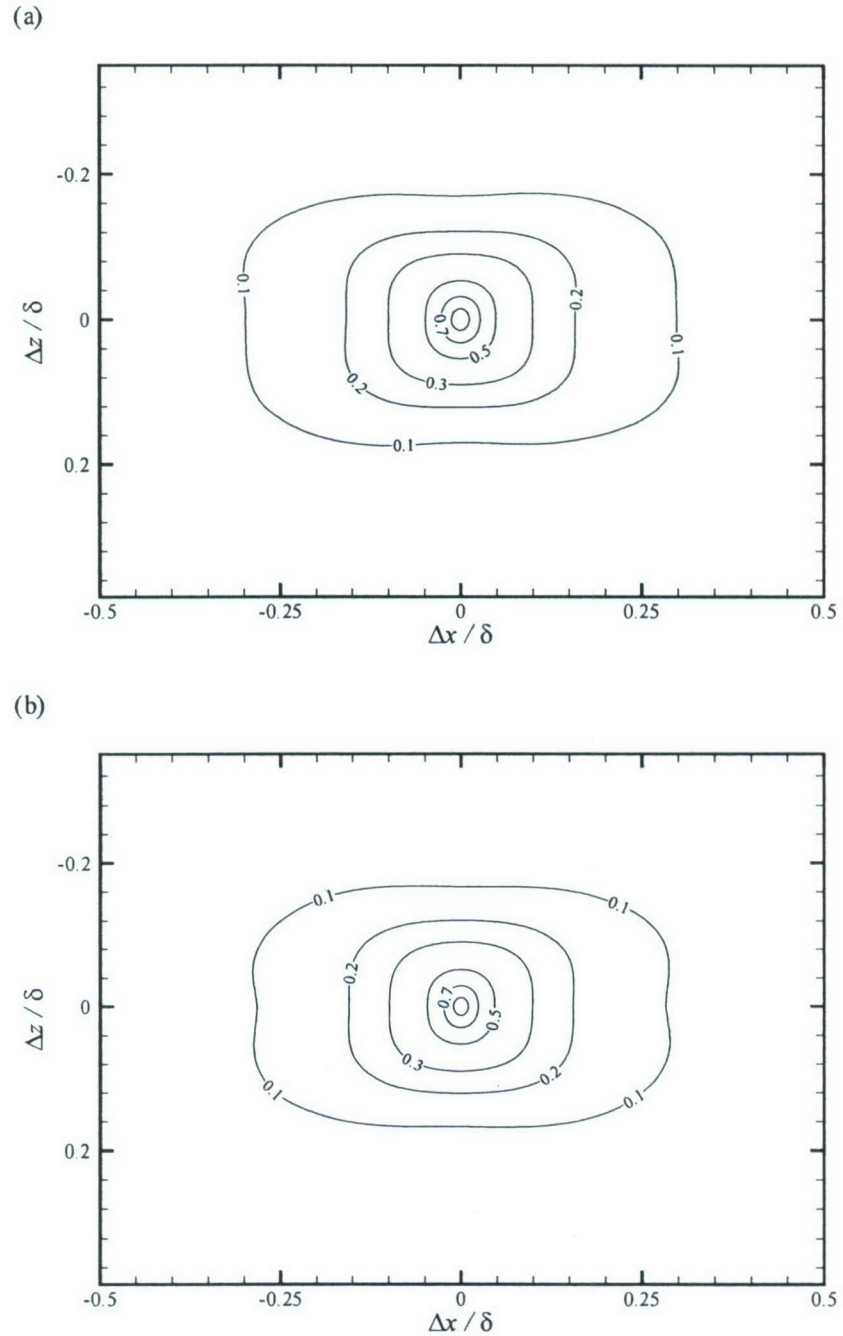


Figure 65: Spanwise velocity correlation coefficients,  $\rho_{ww}$ , in the  $x - z$  plane at  $y = 0.065\delta$  for  $Re_\theta \approx 13000$ . (a) Smooth; (b) RF1. Contour levels are 0.1, 0.2, 0.3, 0.5, 0.7 and 0.9.

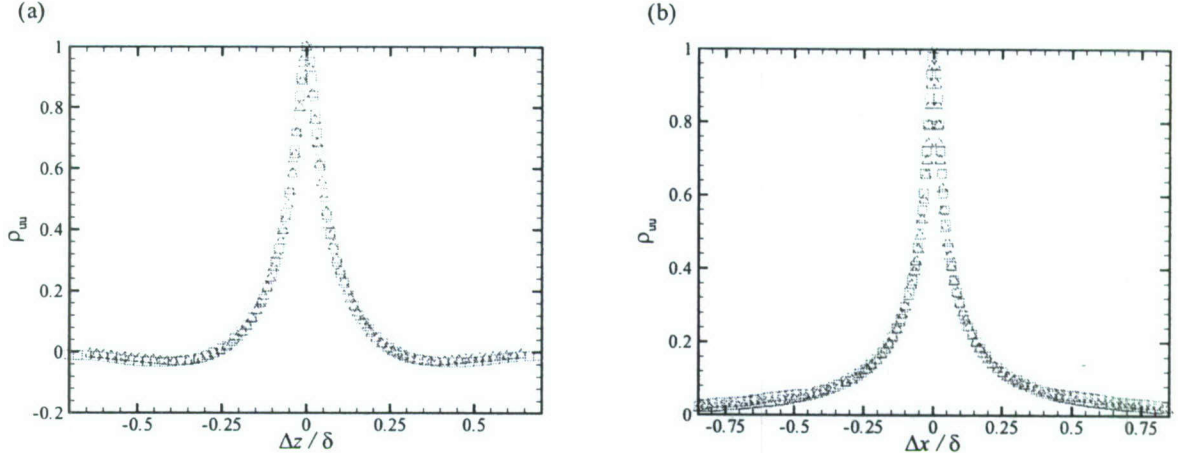


Figure 66: One-dimensional profiles of  $\rho_{ww}$  from figure 65 in the (a) spanwise ( $\Delta x = 0$ ) and (b) streamwise ( $\Delta z = 0$ ) directions at  $y = 0.065\delta$  for  $Re_\theta \approx 13000$ . □: Smooth; △: RF1.

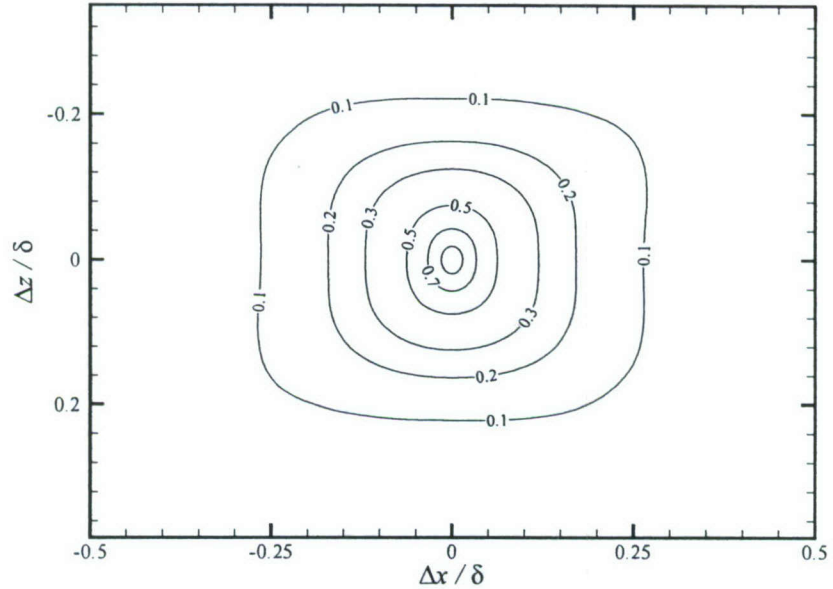
contours. This tendency toward an isotropic state with increasing wall-normal position is likely being driven by spanwise scale growth as the streamwise extent of  $\rho_{ww}$  at  $y = 0.15\delta$  is essentially then same as at  $y = 0.065\delta$  for both surface conditions. A direct comparison of one-dimensional profiles of  $\rho_{ww}$  in the spanwise and streamwise directions (figure 68) reveals excellent consistency between the smooth- and rough-wall flows. Finally, the two-dimensional PIV measurements in the streamwise–wall-normal plane only resolved the in-plane velocity components, so evaluation of  $\rho_{ww}$  in the  $x - y$  plane is not possible.

#### 6.3.4 Wall-normal vortex cores ( $\rho_{\lambda_{ci}\lambda_{ci}}$ )

As introduced earlier, swirling strength is a vortex identifier that is Galilean invariant and only identifies regions of rotation associated with vortex cores. However, since  $\lambda_{ci}$  is the imaginary portion of the complex-conjugate eigenvalues of the local velocity gradient tensor, it does not retain a sign that would discriminate rotational sense. Therefore, it has become customary to attach the sign of the local fluctuating in-plane vorticity to  $\lambda_{ci}$  as a means of discriminating between opposing rotation. Of particular interest here is the fact that  $\lambda_{ci}$  is far superior to even velocity-based correlations for studying the spatial characteristics of the smaller-scale wall-normal and spanwise vortices noted in the instantaneous velocity realizations of section 6.2.

Figure 69 presents two-point correlations of wall-normal swirling strength,  $\rho_{\lambda_{ci}\lambda_{ci}}$ , in the  $x - z$  plane at  $y = 0.065\delta$  for flow over the smooth and RF1 surfaces at  $Re_\theta \approx 13000$ . Recall that the wall-normal vortices identified in the  $x - z$  plane were conjectured to be slices through the legs/necks of hairpin-like structures as these vortices were found to occur outboard of the LMR's associated with hairpin packets. In this context, a wall-parallel slice through a roughly symmetric hairpin structure would yield opposing-sign wall-normal vortices separated in the spanwise direction outboard of the LMR's. Further, wall-normal vortices with the same rotational sense would be expected to align approximately in the streamwise direction due to the roughly streamwise-aligned vortices in a hairpin packet. Returning to figure 69,  $\rho_{\lambda_{ci}\lambda_{ci}}$  displays two distinct spatial characteristics: compact, roughly circular contours centered at  $\Delta x, \Delta z = (0, 0)$  and weaker contour levels elongated in the streamwise direction. The compact, circular contours can be interpreted as the imprint of the actual wall-normal vortex cores that populate the  $x - z$  plane at  $y = 0.065\delta$ . In contrast, the

(a)



(b)

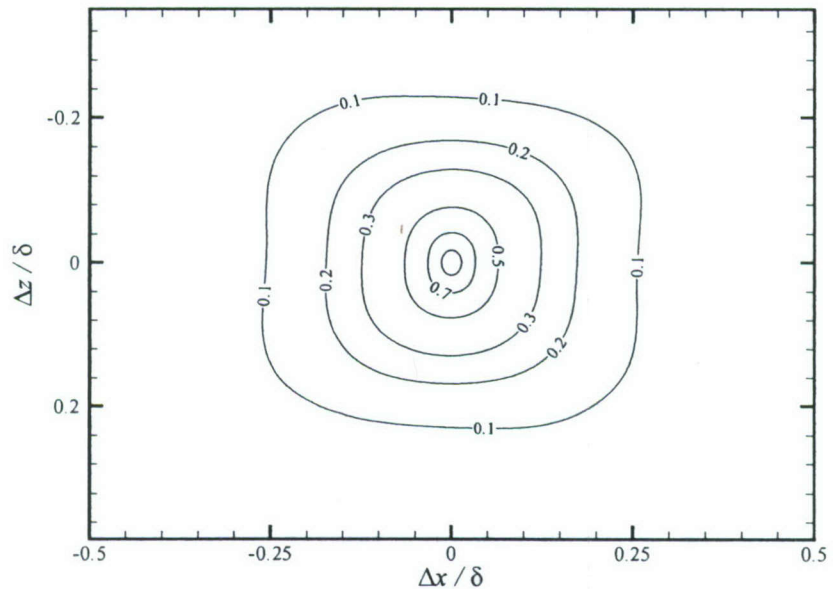


Figure 67: Spanwise velocity correlation coefficients,  $\rho_{ww}$ , in the  $x - z$  plane at  $y = 0.15\delta$  for  $Re_\theta \approx 13000$ . (a) Smooth; (b) RF1. Contour levels are 0.1, 0.2, 0.3, 0.5, 0.7 and 0.9.

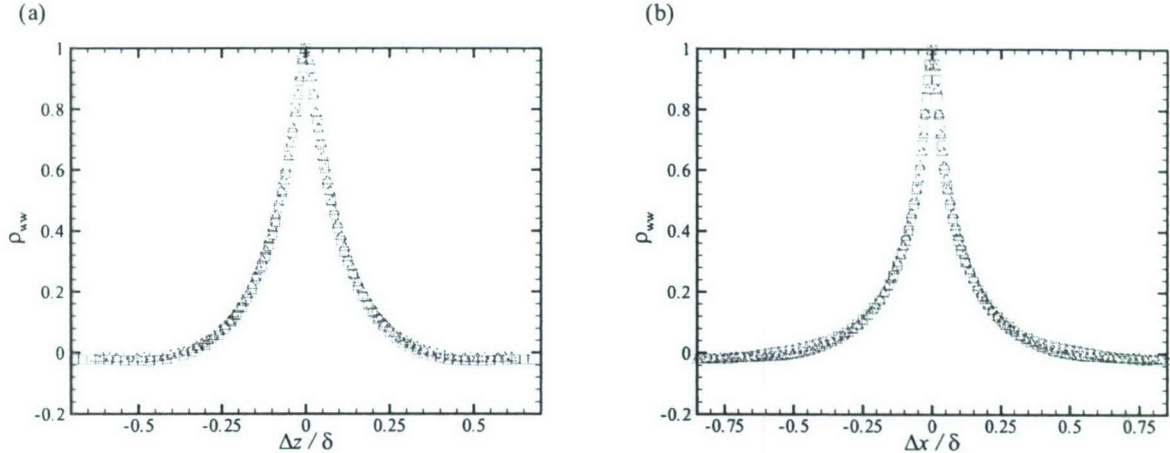


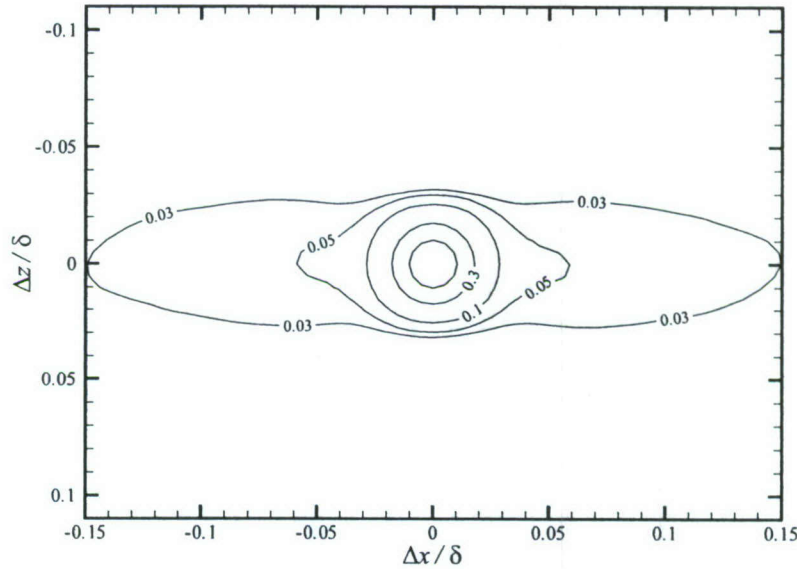
Figure 68: One-dimensional profiles of  $\rho_{ww}$  from figure 67 in the (a) spanwise ( $\Delta x = 0$ ) and (b) streamwise ( $\Delta z = 0$ ) directions at  $y = 0.15\delta$  for  $Re_\theta \approx 13000$ .  $\square$ : Smooth;  $\triangle$ : RF1.

streamwise-elongated contours in figure 69 are more consistent with correlation between consecutive, streamwise-aligned hairpin-like structures in outer-layer vortex organization. Interestingly, both the streamwise and spanwise extents of the compact, circular contours as well as the streamwise extent of the weaker, elongated contours appear reduced in the presence of roughness, most notably the latter.

To view these differences between the smooth- and rough-wall  $\rho_{\lambda_{ci}\lambda_{ci}}$  in the  $x - z$  plane at  $y = 0.065\delta$ , figure 70 presents one-dimensional profiles of  $\rho_{\lambda_{ci}\lambda_{ci}}$  in the spanwise and streamwise directions for  $Re_\theta \approx 13000$ . When the spatial separations are scaled in outer units [figures 70(a) and 70(b) for spanwise and streamwise directions, respectively], the reductions in the rough-wall spatial extents noted in the two-dimensional plots are readily apparent. However, when these one-dimensional profiles are plotted on spatial separations normalized in inner units, excellent collapse is noted in both the spanwise and streamwise directions (even for the longer streamwise tails of  $\rho_{\lambda_{ci}\lambda_{ci}}$ ). The collapse of  $\rho_{\lambda_{ci}\lambda_{ci}}$  for small spatial separations is in accordance with recent experimental evidence suggesting that the diameters of small-scale vortex cores in smooth-wall turbulence scale on the viscous length scale,  $y_*$  (Carlier & Stanislas, 2005; Wu & Christensen, 2006a). Evidently, this scaling also holds for the small-scale vortex cores present in the flow over the RF1 surface considered herein. Further, the observed collapse of  $\rho_{\lambda_{ci}\lambda_{ci}}$  on  $y_*$  for larger  $\Delta x$  indicates that the physics associated with this correlation tail is an inner-scale-dependent process. While no studies have conclusively assessed the exact streamwise spacing between consecutive vortices in outer-layer vortex organization nor the appropriate length scale of the flow that governs this process, the present results suggest that this spacing may be driven by inner rather than outer scales.

Figure 71 illustrates  $\rho_{\lambda_{ci}\lambda_{ci}}$  in the  $x - z$  plane further from the wall at  $y = 0.15\delta$  for flow over the smooth and RF1 surfaces at  $Re_\theta \approx 13000$ . The streamwise and spanwise extents of  $\rho_{\lambda_{ci}\lambda_{ci}}$  have clearly grown with increasing distance from the wall and both compact, circular contours as well as weaker, streamwise-elongated contours are evident for both surface conditions. Again, the streamwise and spanwise extents of  $\rho_{\lambda_{ci}\lambda_{ci}}$  appear reduced in the presence of roughness but this reduction is noted here with the spatial separations normalized in outer units. Nevertheless, this increase in vortex core diameter with wall-normal location is again consistent with recent studies of smooth-wall turbulence (Carlier & Stanislas, 2005, for example). Finally, although the collapse

(a)



(b)

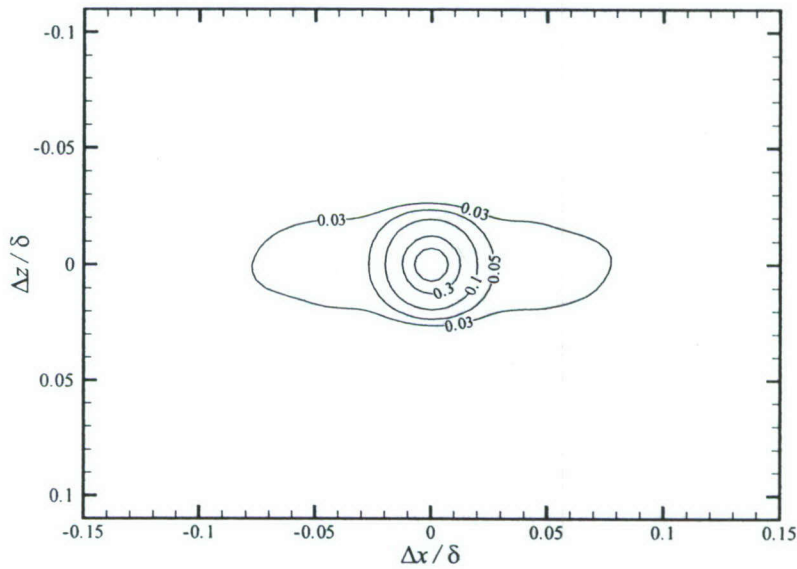


Figure 69: Wall-normal swirling strength correlation coefficients,  $\rho_{\lambda_{ci}\lambda_{ci}}$ , in the  $x - z$  plane at  $y = 0.065\delta$  for  $\text{Re}_\theta \approx 13000$ . (a) Smooth; (b) RF1. Contour levels are 0.03, 0.05, 0.1, 0.3 and 0.6.

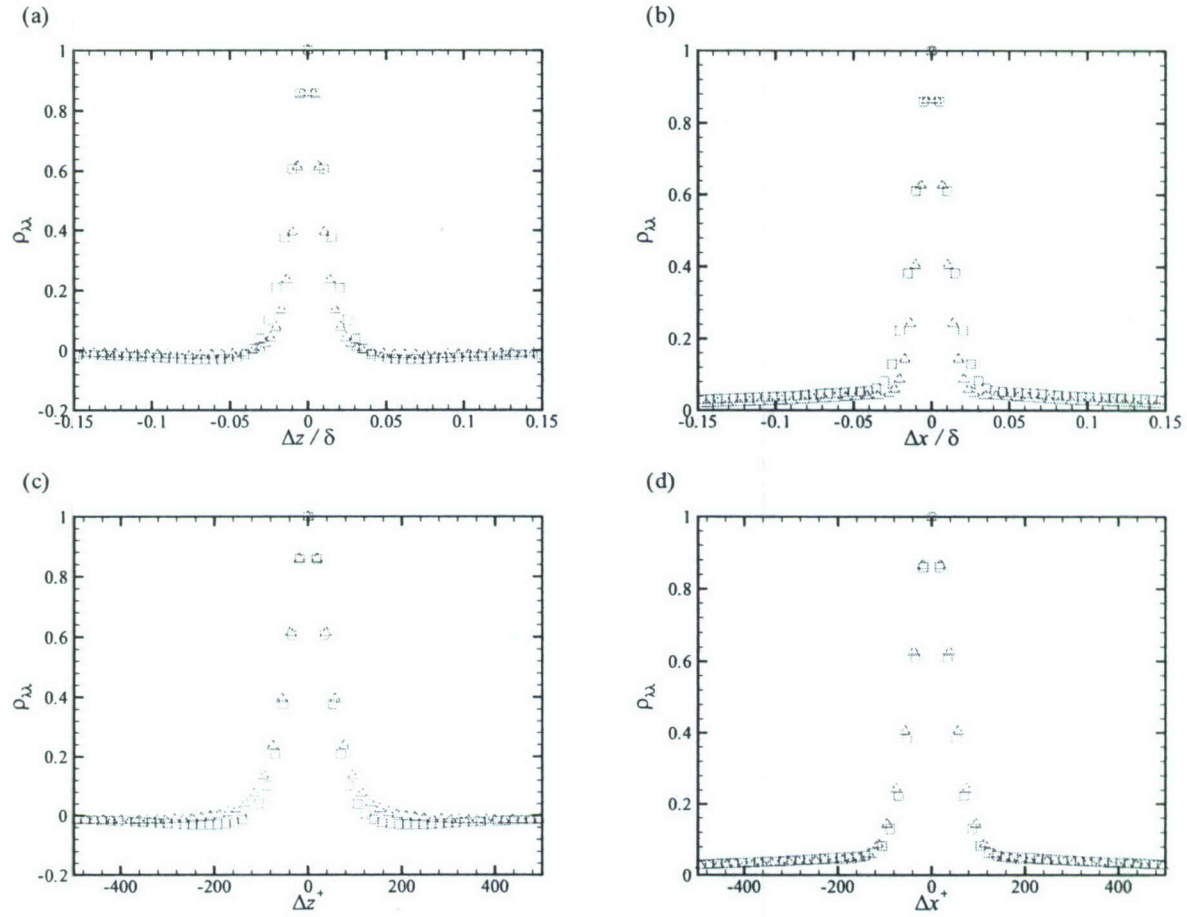


Figure 70: One-dimensional profiles of  $\rho_{\lambda_{ci}\lambda_{ci}}$  from figure 69 presented in (a, b) outer and (c, d) inner units in the spanwise ( $\Delta x = 0$ ) and streamwise ( $\Delta z = 0$ ) directions, respectively, at  $y = 0.065\delta$  for  $Re_\theta \approx 13000$ .  $\square$ : Smooth;  $\triangle$ : RF1.

on  $y_*$  is not quite as good at  $y = 0.15\delta$  as it is at  $y = 0.065\delta$ , the one-dimensional profiles of  $\rho_{\lambda_{ci}\lambda_{ci}}$  in the spanwise and streamwise directions presented in figure 72 still indicate that the diameters of wall-normal vortex cores and their streamwise spacing are dependent on inner scales.

### 6.3.5 Spanwise vortex cores ( $\rho_{\lambda_{ci}\lambda_{ci}}$ )

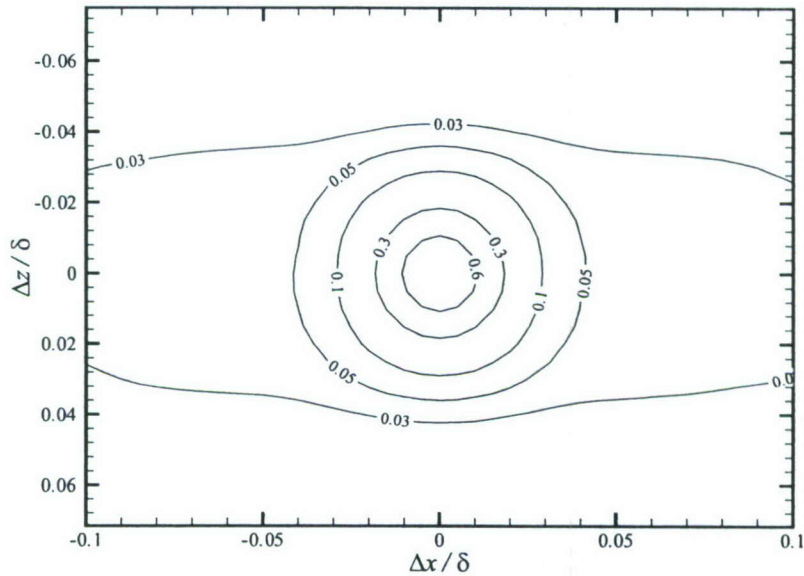
As noted in section 6.2, the majority of spanwise vortex cores with clockwise rotation (prograde) noted in the streamwise-wall-normal plane are interpreted to be slices through the heads of hairpin-like structures. Swirling strength can be computed in the  $x - y$  plane to reveal spanwise vortex cores and the sign of the fluctuating spanwise vorticity can be attached to  $\lambda_{ci}$  to distinguish between clockwise (prograde) and counterclockwise-rotating (retrograde) spanwise vortices. Figure 73 shows two-point correlations of spanwise swirling strength,  $\rho_{\lambda_{ci}\lambda_{ci}}$ , in the  $x - y$  plane at  $y = 0.15\delta$  for flow over the smooth and RF1 surfaces at  $Re_\theta \approx 13000$ . Both smooth- and rough-wall  $\rho_{\lambda_{ci}\lambda_{ci}}$  in the  $x - y$  plane display compact, circular contours as well as weaker, streamwise-elongated contours that are inclined slightly away from the wall. While the compact, circular contours are likely the imprint of the spanwise vortex cores themselves, the streamwise elongation and inclination away from the wall of the weaker correlation levels is entirely consistent with the spatial correlation of the heads of streamwise-aligned hairpin structures in outer-layer vortex organization. In fact, the smooth- and rough-wall inclination angles of  $\rho_{\lambda_{ci}\lambda_{ci}}$  are both approximately  $10^\circ$  which is quite consistent with the inclination angles noted for  $\rho_{uu}$  in the  $x - y$  plane (figures 57 and 59). Further, the smooth- and rough-wall  $\rho_{\lambda_{ci}\lambda_{ci}}$  both contain weak negative correlation levels downstream and above as well as upstream and below of the central correlation peak at  $(\Delta x, y) = (0, y_{ref} = 0.15\delta)$ . These negative correlation values indicate the occurrence of spatially-coincident prograde and retrograde spanwise vortices. Natrajan *et al.* (2007) first reported these negative correlation regions in  $\rho_{\lambda_{ci}\lambda_{ci}}$  within the  $x - y$  plane and postulated the latter arrangement to be a slice through the shoulder of an omega-shaped hairpin-like structure while the former arrangement may be due to ring-like vortices that have been observed in the outer-layer of smooth-wall turbulence (Falco, 1991, for example). Of interest is that these regions of negative correlation in  $\rho_{\lambda_{ci}\lambda_{ci}}$  become smaller and weaker in the rough-wall flow.

Finally, one-dimensional profiles of  $\rho_{\lambda_{ci}\lambda_{ci}}$  in the wall-normal and streamwise directions are shown in figure 74 scaled in both outer and inner units. Collapse with  $y_*$  is again consistent with recent studies that have reported inner-scale-dependence of the diameters of spanwise vortex cores (Carlier & Stanislas, 2005; Wu & Christensen, 2006a). This collapse on  $y_*$  is also consistent with the trends noted for  $\rho_{\lambda_{ci}\lambda_{ci}}$  in the  $x - z$  plane.

### 6.3.6 Impact of surface protrusions on spatial correlations in roughness sublayer

All of the aforementioned correlations in the streamwise-spanwise plane at  $y = 0.065\delta$  were computed assuming homogeneity in the streamwise and spanwise directions. While this assumption is certainly valid at  $y = 0.15\delta$  where the analysis in chapter 4 illustrated the lack of roughness-induced modifications at this wall-normal location, the correlations computed in the  $x - z$  plane at  $y = 0.065\delta$  assuming homogeneity may be slightly influenced by strong roughness protrusions (as was seen for single-point statistics in chapter 4). To assess this influence, two-point correlations in the  $x - z$  plane at  $y = 0.065\delta$  for flow over the RF1 surface at  $Re_\theta \approx 13000$  are computed at reference locations spatially-coincident with and just downstream of roughness protrusion F [see figure 32(b)]. This protrusion was observed to generate the strongest local heterogeneities in the single-point turbulence statistics presented in chapter 4. These correlations are computed assuming inhomogeneity in both the streamwise and spanwise directions, meaning they are based on a fixed reference point and are only averaged over the ensemble of realizations (in contrast to the homo-

(a)



(b)

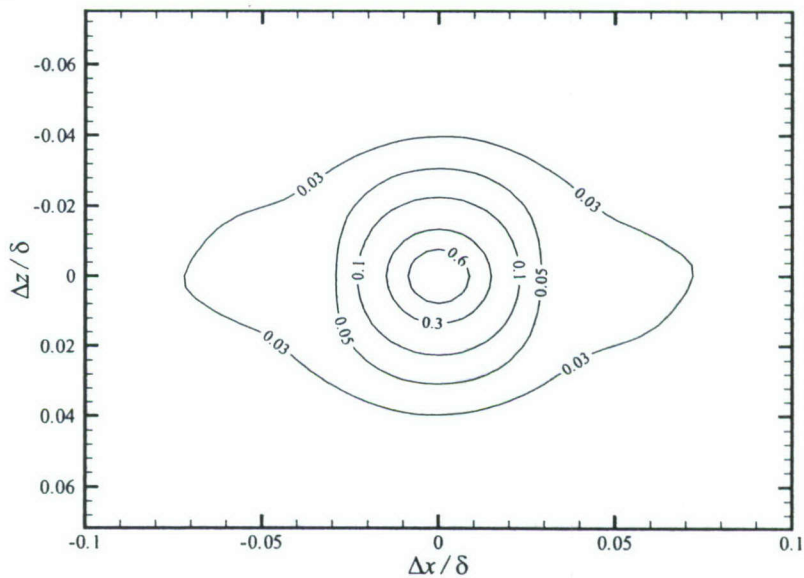


Figure 71: Wall-normal swirling strength correlation coefficients,  $\rho_{\lambda_{ci}\lambda_{ci}}$ , in the  $x - z$  plane at  $y = 0.15\delta$  for  $\text{Re}_\theta \approx 13000$ . (a) Smooth; (b) RF1. Contour levels are 0.03, 0.05, 0.1, 0.3 and 0.6.

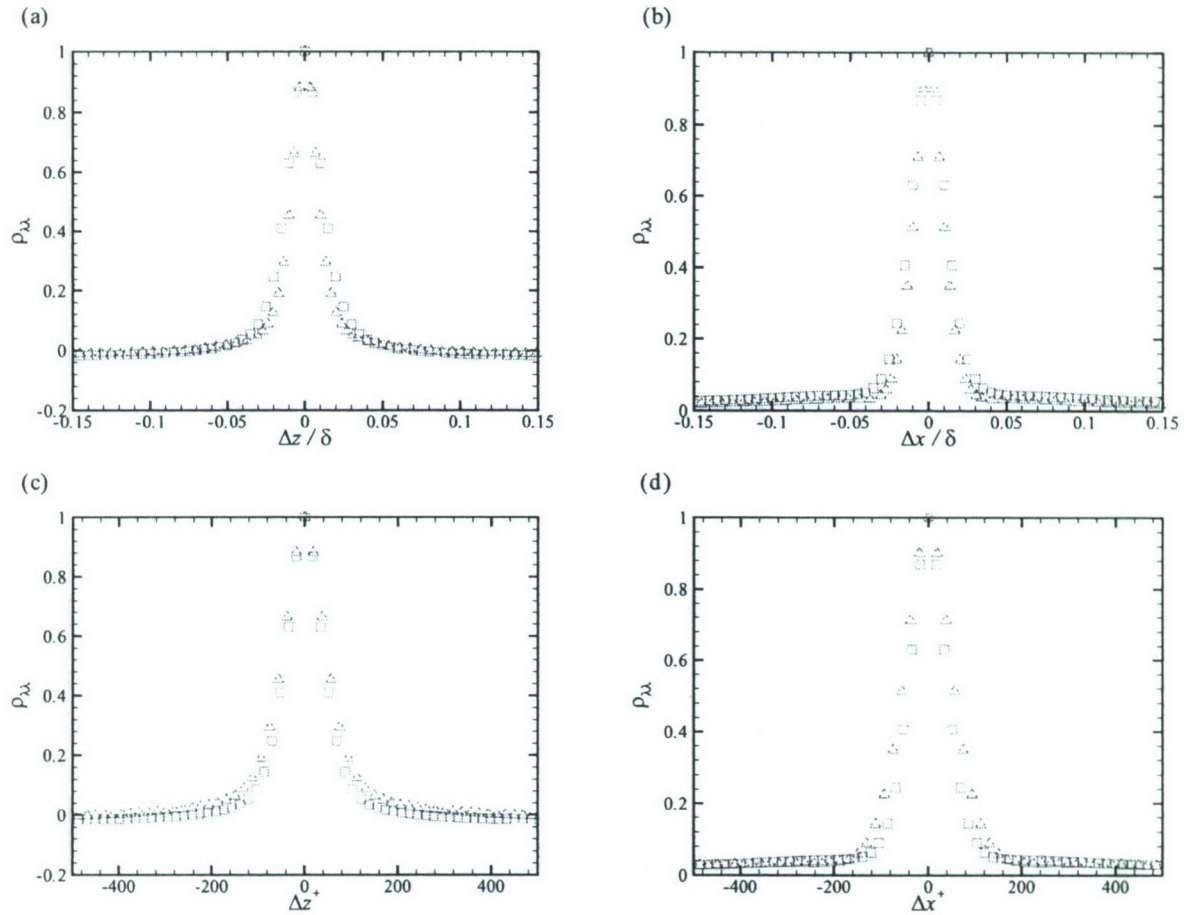
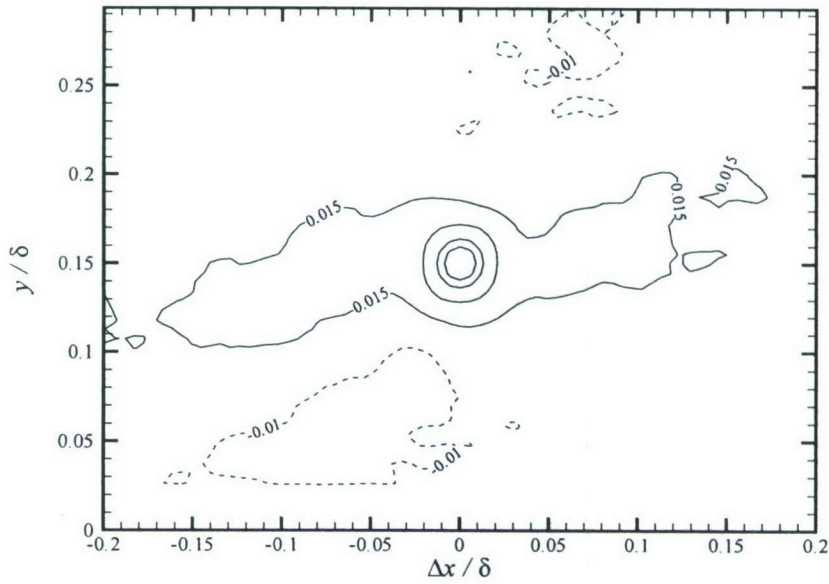


Figure 72: One-dimensional profiles of  $\rho_{\lambda_{ci}\lambda_{ci}}$  from figure 71 presented in (a, b) outer and (c, d) inner units in the spanwise ( $\Delta x = 0$ ) and streamwise ( $\Delta z = 0$ ) directions, respectively, at  $y = 0.15\delta$  for  $Re_\theta \approx 13000$ .  $\square$ : Smooth;  $\triangle$ : RF1.

(a)



(b)

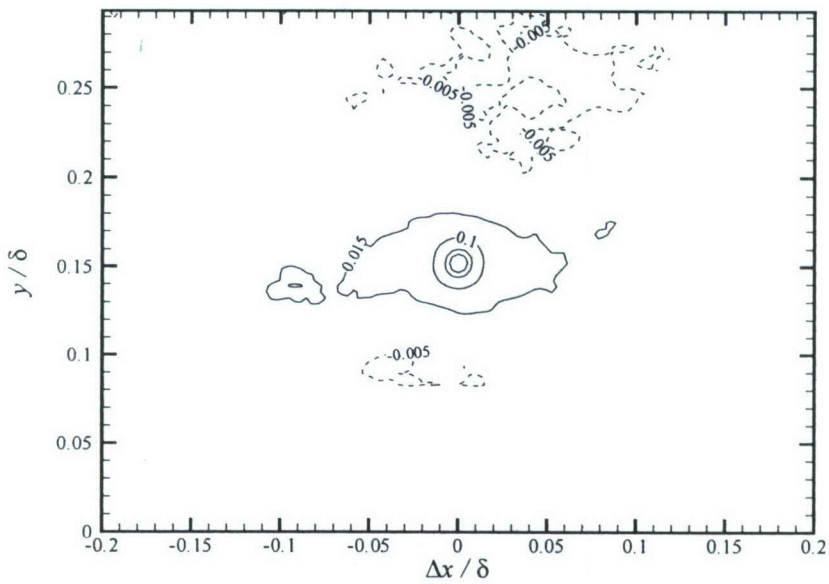


Figure 73: Spanwise swirling strength correlation coefficients,  $\rho_{\lambda_{ci}\lambda_{ci}}$ , in the  $x - y$  plane at  $y_{ref} = 0.15\delta$  for  $Re_\theta \approx 13000$ . (a) Smooth (Contour levels are -0.01, 0.015, 0.1, 0.3 and 0.5); (b) RF1 (Contour levels are -0.005, 0.015, 0.1, 0.3 and 0.5).

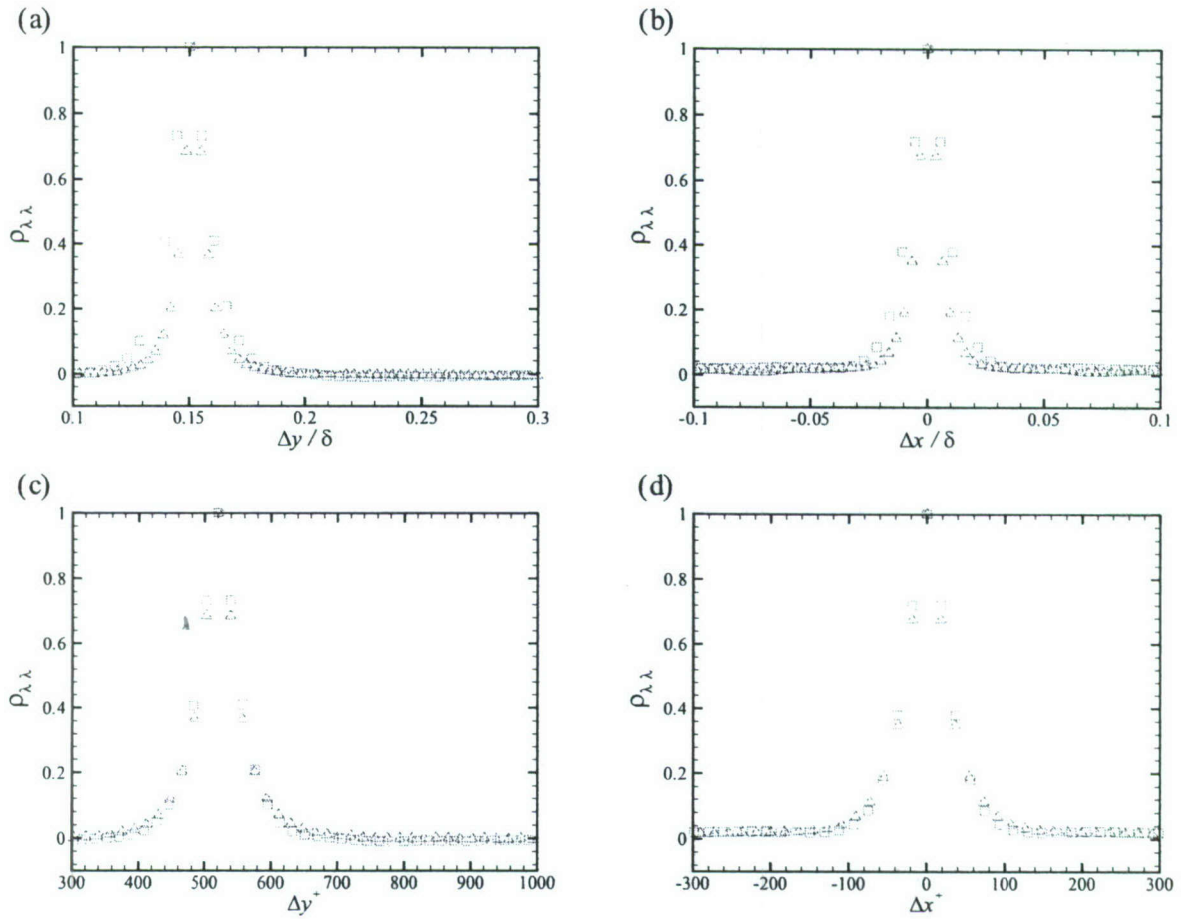


Figure 74: One-dimensional profiles of  $\rho_{\lambda_{ci}\lambda_{ci}}$  from figure 73 presented in (a, b) outer and (c, d) inner units in the wall-normal ( $\Delta x = 0$ ) and streamwise ( $y = y_{ref}$ ) directions, respectively, at  $y_{ref} = 0.15\delta$  for  $Re_\theta \approx 13000$ .  $\square$ : Smooth;  $\triangle$ : RF1.

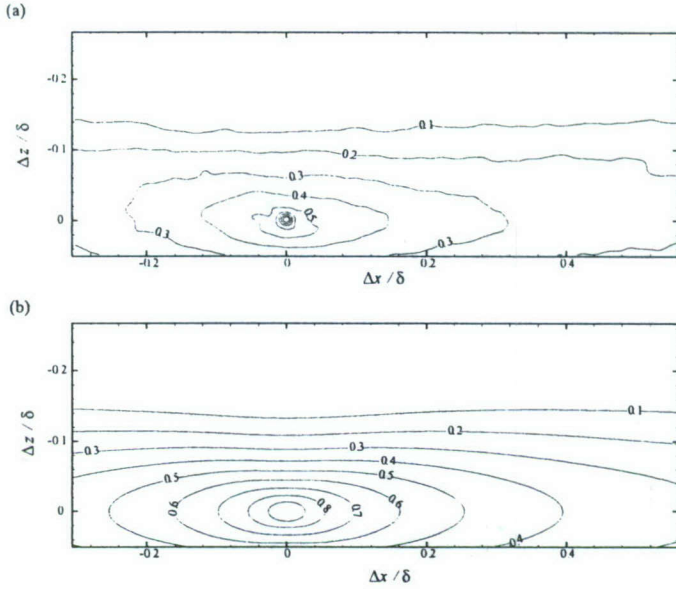


Figure 75: Streamwise velocity correlation coefficients,  $\rho_{uu}$ , in the  $x - z$  plane at  $y_{\text{ref}} = 0.065\delta$  for flow over the RF1 surface at  $\text{Re}_\theta \approx 13000$ . (a) Inhomogeneous correlation at a reference point directly above roughness protrusion F; (b) Homogeneous correlation. Contour levels are from 0.1 to 0.9 with interval of 0.1.

geneous correlations presented above wherein averaging is performed over the ensemble as well as in the streamwise and spanwise directions).

Figures 75(a)–77(a) present  $\rho_{uu}$ ,  $\rho_{vv}$  and  $\rho_{ww}$  in the  $x - z$  plane located at  $y = 0.065\delta$  for flow over the RF1 surface at  $\text{Re}_\theta \approx 13000$  computed with a reference point centered directly above roughness protrusion F. To facilitate comparison,  $\rho_{uu}$ ,  $\rho_{vv}$  and  $\rho_{ww}$  in this plane from the calculations assuming homogeneity [figures 54(b), 54(b) and 65(b)] are reproduced as figures 75(b)–77(b) with their centers shifted to allow direct comparison of length scales with the inhomogeneous correlations. Both  $\rho_{uu}$  and  $\rho_{vv}$  show a rather dramatic decrease in streamwise extent at both higher and lower correlation levels compared to their homogeneous counterparts (In the case of  $\rho_{uu}$ , the 0.1 and 0.2 contour levels appear unaffected by protrusion F). In contrast, the spanwise extent of  $\rho_{uu}$  appears relatively unaffected by protrusion F while the spanwise extent of  $\rho_{vv}$  is dramatically decreased. Interestingly, the spatial extents of  $\rho_{ww}$  in the streamwise and spanwise directions appear unaffected by protrusion F as the inhomogeneous correlation matches its homogeneous counterpart except for slight differences for small spatial separations (Note that the inhomogeneous correlations appear much noisier than their homogeneous counterparts because the number of samples averaged to generate inhomogeneous correlations is significantly reduced under this assumption). The relative insensitivity of the larger-scale features of  $\rho_{uu}$  and  $\rho_{ww}$  to roughness feature F is consistent with the observations of Djenidi *et al.* (1999) who reported that the outflows from square cavities did not appreciably affect the spatial characteristics of low-speed streaks in the near-wall region. They attributed this insensitivity to the substantial scale difference between the outflows generated by the roughness cavities and the large-scale streaks.

The inhomogeneous correlations computed for a reference location directly above roughness protrusion F indicate that these large-scale surface defects do indeed alter the character of the two-point correlations at  $y = 0.065\delta$ . However, these effects appear limited to small-to-intermediate

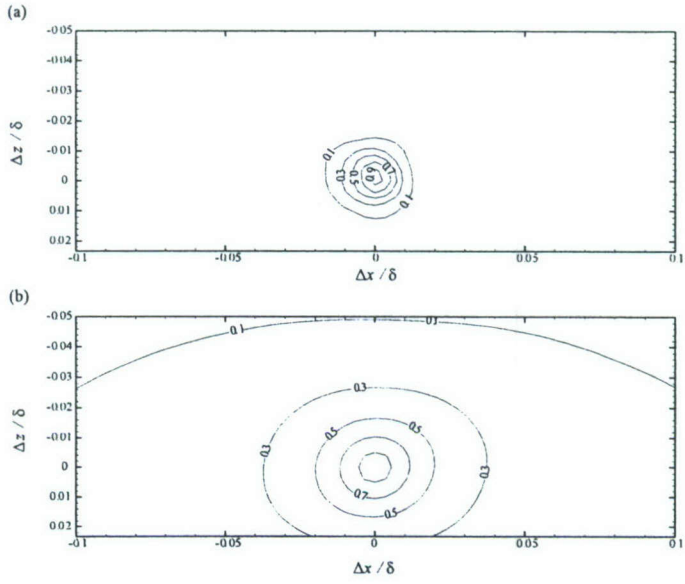


Figure 76: Wall-normal velocity correlation coefficients,  $\rho_{vv}$ , in the  $x - z$  plane at  $y_{\text{ref}} = 0.065\delta$  for flow over the RF1 surface at  $\text{Re}_\theta \approx 13000$ . (a) Inhomogeneous correlation at a reference point directly above roughness protrusion F; (b) Homogeneous correlation. Contour levels are from 0.1 to 0.9 with interval of 0.2.

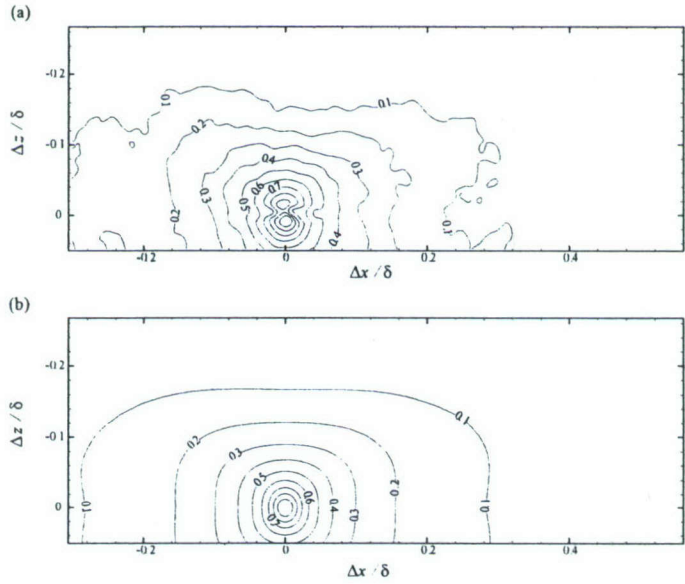


Figure 77: Spanwise velocity correlation coefficients,  $\rho_{ww}$ , in the  $x - z$  plane at  $y_{\text{ref}} = 0.065\delta$  for flow over the RF1 surface at  $\text{Re}_\theta \approx 13000$ . (a) Inhomogeneous correlation at a reference point directly above roughness protrusion F; (b) Homogeneous correlation. Contour levels are from 0.1 to 0.9 with interval of 0.1.

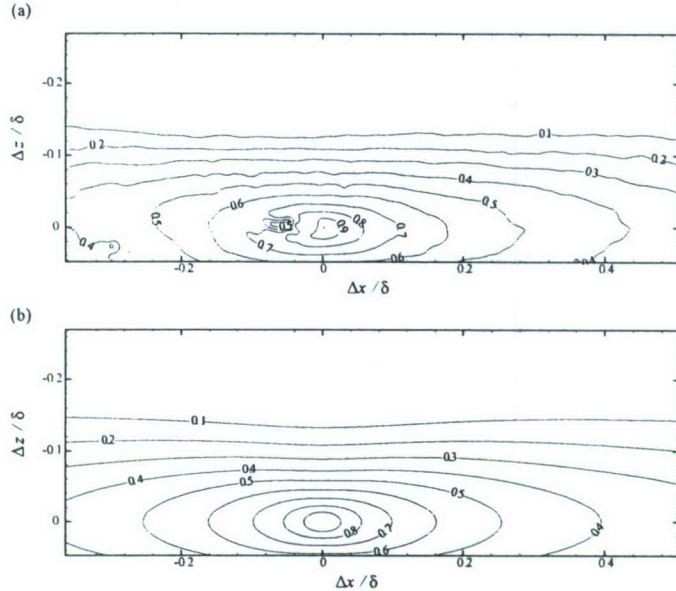


Figure 78: Streamwise velocity correlation coefficients,  $\rho_{uu}$ , in the  $x - z$  plane at  $y_{\text{ref}} = 0.065\delta$  for flow over the RF1 surface at  $\text{Re}_\theta \approx 13000$ . (a) Inhomogeneous correlation at a reference point  $0.055\delta$  downstream of roughness protrusion F; (b) Homogeneous correlation. Contour levels are from 0.1 to 0.9 with interval of 0.1.

spatial separations as the larger-scale characteristics of these inhomogeneous correlations mimic their homogeneous counterparts well, particularly for  $\rho_{uu}$  and  $\rho_{ww}$ . However, it is still not clear whether these modifications sustain themselves beyond the immediate vicinity of these surface defects. The evidence presented in chapter 4 overwhelming supports the contention that these roughness-induced modifications are relatively isolated to the immediate vicinity of the roughness protrusions and inhomogeneous correlations computed for a reference location  $0.055\delta$  downstream of protrusion F in the  $x - z$  plane at  $y = 0.065\delta$  [figures 78(a)–80(a) for  $\rho_{uu}$ ,  $\rho_{vv}$  and  $\rho_{ww}$ , respectively] indicate that this contention holds for the two-point correlations as well. The correlation  $\rho_{uu}$  recovers its large- and intermediate-scale characteristics that mark its homogenous version [figure 78(b)] although this correlation still retains a slight heterogeneity upstream of the reference location at a point spatially-coincident with protrusion F. Surprisingly,  $\rho_{vv}$  recovers the larger-scale coherent noted in its homogeneous version [figure 79(b)] even though the reference location is only 5% of  $\delta$  downstream of surface protrusion F. However,  $\rho_{vv}$  still retains some inhomogeneity upstream of the reference location where the impact of protrusion F is still observable. Finally,  $\rho_{ww}$  remains consistent between its inhomogeneous and homogeneous versions. Therefore, while the correlations for a reference location directly above F show strong roughness-induced modifications, these correlations appear to relax back toward their homogeneous characteristics quite quickly downstream as the inhomogeneous correlations 0.055 $\delta$  downstream of roughness feature F show increased consistency with their homogeneous counterparts.

Finally, figures 81(a)–83(a) present inhomogeneous versions of  $\rho_{uu}$ ,  $\rho_{vv}$  and  $\rho_{ww}$  in the  $x - z$  plane at  $y = 0.065\delta$  at a reference point located far from all dominant roughness protrusions to ascertain their consistency with their homogeneous counterparts. Interestingly, all three inhomogeneous velocity correlation coefficients show quite strong consistency with their homogeneous versions. This consistency indicates that the roughness-induced modifications observed in the immediate vicinity

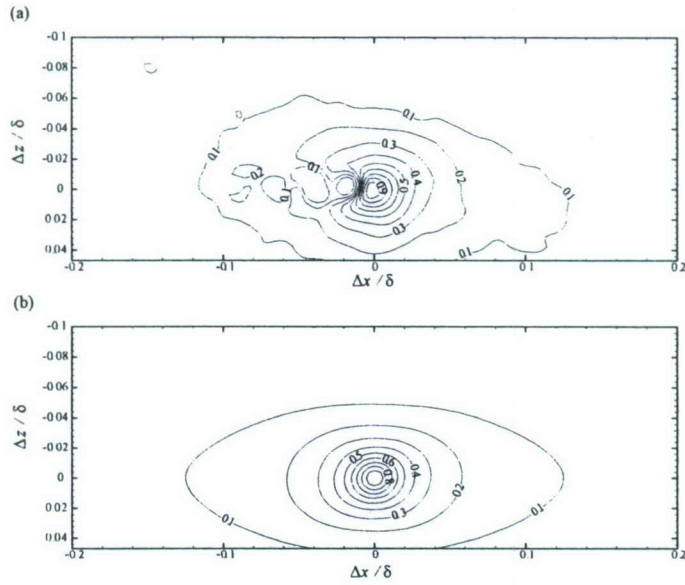


Figure 79: Wall-normal velocity correlation coefficients,  $\rho_{vv}$ , in the  $x - z$  plane at  $y_{\text{ref}} = 0.065\delta$  for flow over the RF1 surface at  $\text{Re}_\theta \approx 13000$ . (a) Inhomogeneous correlation at a reference point  $0.055\delta$  downstream of roughness protrusion F; (b) Homogeneous correlation. Contour levels are from 0.1 to 0.9 with interval of 0.2.

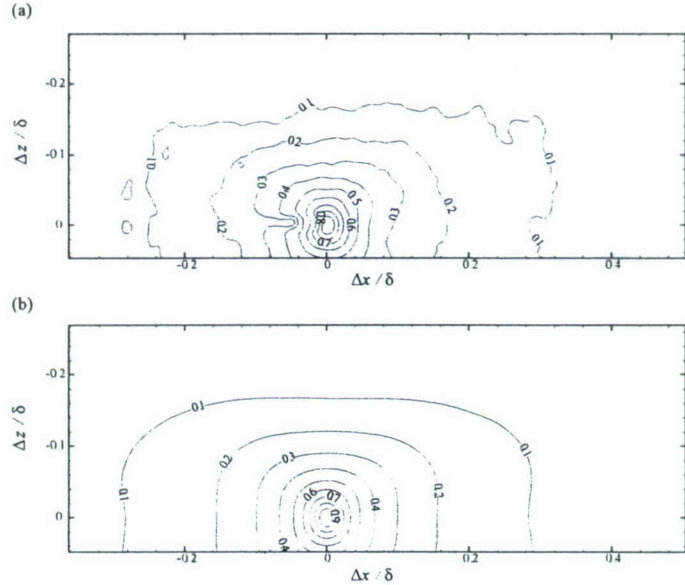


Figure 80: Spanwise velocity correlation coefficients,  $\rho_{ww}$ , in the  $x - z$  plane at  $y_{\text{ref}} = 0.065\delta$  for flow over the RF1 surface at  $\text{Re}_\theta \approx 13000$ . (a) Inhomogeneous correlation at a reference point  $0.055\delta$  downstream of roughness protrusion F; (b) Homogeneous correlation. Contour levels are from 0.1 to 0.9 with interval of 0.1.

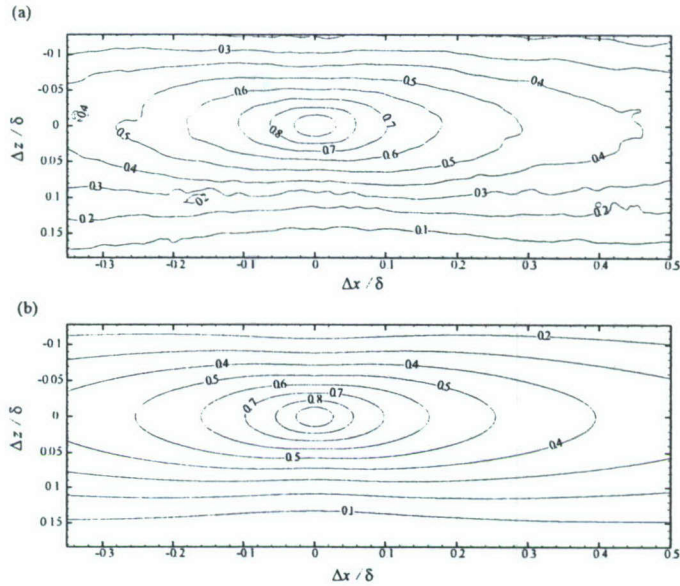


Figure 81: Streamwise velocity correlation coefficients,  $\rho_{uu}$ , in the  $x - z$  plane at  $y_{\text{ref}} = 0.065\delta$  for flow over the RF1 surface at  $\text{Re}_\theta \approx 13000$ . (a) Inhomogeneous correlation at a reference point away from all roughness protrusions; (b) Homogeneous correlation. Contour levels are from 0.1 to 0.9 with interval of 0.1.

of strong roughness protrusions affect the homogeneous correlations in a rather minimal manner. Very subtle differences can be seen at higher correlation levels where the streamwise and spanwise extents of these levels are only slightly larger in the inhomogeneous case (true for  $\rho_{uu}$  and  $\rho_{vv}$ ;  $\rho_{ww}$  shows no such effect). This difference is consistent with the fact that protrusion F significantly reduces the streamwise and spanwise extents of these higher correlation levels locally. As such, the homogeneous correlations at  $y = 0.065\delta$  discussed in detail above are indeed quite representative of the statistical character of this rough-wall flow, even at the  $y = 0.065\delta$  measurement location within the roughness sublayer, except in the immediate vicinity of intense roughness protrusions where modifications of their small-scale behavior can occur locally. However, these small-scale modifications seem to quickly disappear as the flow advects downstream, likely because they are rapidly engulfed by the surrounding turbulence.

#### 6.4 POD analysis

Proper orthogonal decomposition provides an efficient means for defining a suitable set of basis functions for an ensemble of data. Of particular interest in the present application of POD is to effectively separate large- and small-scale features of the flow in order to further document the impact of the RF1 surface on these spatial scales.

Following the description by Cazemier *et al.* (1998), the goal of POD analysis is to determine the best approximation of a given instantaneous turbulent velocity field,  $u(x, t)$ , in terms of  $N$  deterministic spatial POD modes  $\phi_i(x)$ ,  $i = 1, \dots, N$  and  $N$  random temporal functions  $a_i(t)$ ,  $i = 1, \dots, N$ . Mathematically, this problem can be expressed as

$$\min \int_{\Omega} \int_T \left\{ u(x, t) - \sum_{i=1}^N a_i(t) \phi_i(x) \right\}^2 dt dx, \quad (43)$$

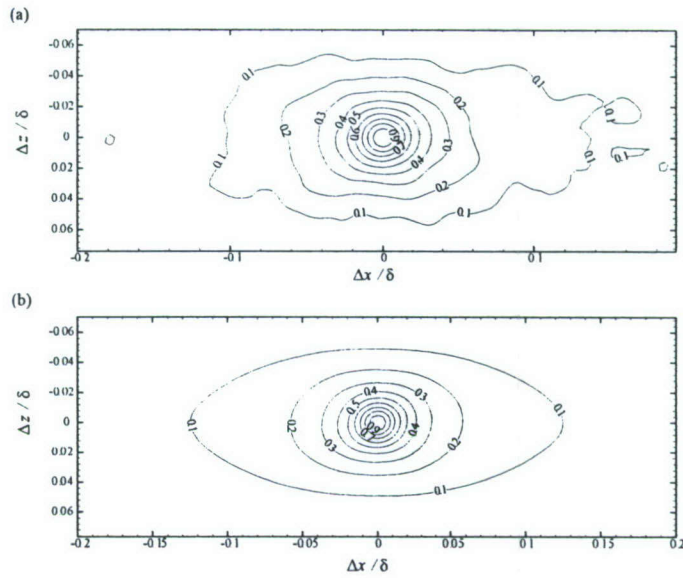


Figure 82: Wall-normal velocity correlation coefficients,  $\rho_{vv}$ , in the  $x - z$  plane at  $y_{\text{ref}} = 0.065\delta$  for flow over the RF1 surface at  $\text{Re}_\theta \approx 13000$ . (a) Inhomogeneous correlation at a reference point away from all roughness protrusions; (b) Homogeneous correlation. Contour levels are from 0.1 to 0.9 with interval of 0.2.

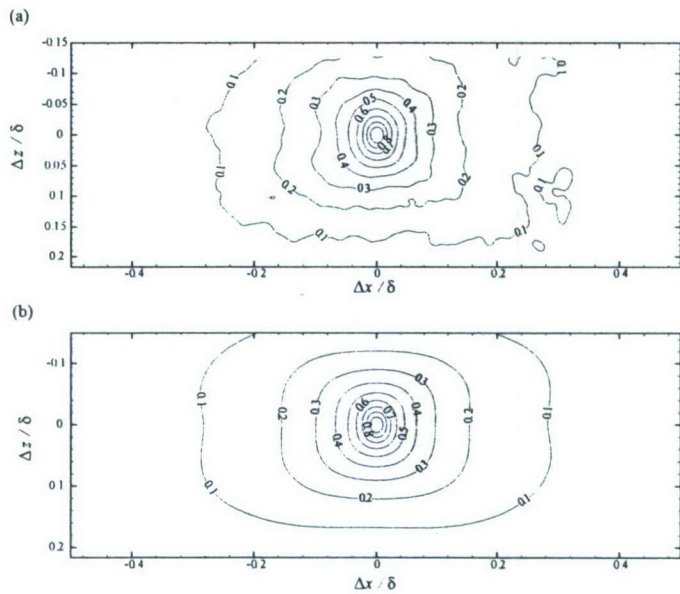


Figure 83: velocity correlation coefficients,  $\rho_{ww}$ , in the  $x - z$  plane at  $y_{\text{ref}} = 0.065\delta$  for flow over the RF1 surface at  $\text{Re}_\theta \approx 13000$ . (a) Inhomogeneous correlation at a reference point away from all roughness protrusions; (b) Homogeneous correlation. Contour levels are from 0.1 to 0.9 with interval of 0.1.

where the integrations are over the spatial domain,  $\Omega$ , and a time interval,  $T$ . Arbitrary variations of the unknowns  $\phi_i(x)$  and  $a_i(t)$  lead to

$$\int_T \left( u - \sum_j a_j \phi_j \right) a_i dt = 0 = \int_{\Omega} \left( u - \sum_j a_j \phi_j \right) \phi_i dx. \quad (44)$$

Assuming orthogonality of  $\phi(x)$  and  $a(t)$  in POD analysis ( $\int_{\Omega} \phi_i \phi_j dx = 0 = \int_T a_i a_j dt$  for  $i \neq j$ ), Eq. (44) can be simplified as

$$\phi_i(x) = \frac{\int_T u a_i dt}{\int_T a_i^2 dt} \quad (45)$$

and

$$a_i(t) = \frac{\int_{\Omega} u \phi_i dx}{\int_{\Omega} \phi_i^2 dx}. \quad (46)$$

Substituting Eq. (45) into Eq. (46) and Eq. (46) into Eq. (45) yields two eigenvalue problems with positive definite Hermitian kernels of the form

$$\lambda_i \phi_i(x) = \int_{\Omega} \left( \int_T u(x, t) u(x', t) dt \right) \phi_i(x') dx' \quad (47)$$

and

$$\lambda_i a_i(t) = \int_T \left( \int_{\Omega} u(x, t) u(x, t') dx \right) a_i(t') dt'. \quad (48)$$

Equation (47) shows that the spatial POD modes,  $\phi_i(x)$ , represent the eigenfunctions of the integral operator with the temporal auto-correlation of  $u(x, t)$  as a kernel. Similarly, Eq. (48) shows that the temporal coefficients,  $a_i(t)$ , are the eigenfunctions of the integral operator with the spatial auto-correlation of  $u(x, t)$  as a kernel. Both equations are equivalent for solving for the POD modes  $\phi_i(x)$  and coefficients  $a_i(t)$ . Classical POD originally introduced by Lumley utilizes Eq. (47) while snapshot POD, first suggested by Sirovich (1987), employs Eq. (48).

The above eigenvalue problems are Fredholm integral equations of the second type whose properties are given by the Hilbert–Schmidt theorem (Mikhlin, 1957, for example). This theorem states that the eigenfunctions are orthogonal which verifies the assumption of orthogonality of  $\phi(x)$  and  $a(t)$  and thus the eigenfunctions are solutions of Eq. (43). In addition, the Hilbert–Schmidt theorem states that the eigenvalues  $\lambda_i$  are real and positive and form a decreasing and convergent series. The instantaneous velocity field  $u(x, t)$  can therefore be fully reconstructed from the eigenfunctions when  $N \rightarrow \infty$ . It should be noted that the eigenfunctions are usually normalized such that spatial POD modes are ortho-normal ( $\int_{\Omega} \phi_i^2 dx = 1$ ) and the coefficients  $a_i$  are square roots of the eigenvalues ( $\int_T a_i^2 dt = \lambda_i$ ). Further, POD analysis is usually performed on the fluctuating velocity fields, meaning that the  $i^{th}$  eigenvalue,  $\lambda_i$ , represents the turbulent kinetic energy contribution of the  $i^{th}$  POD mode,  $\phi_i$ , and the fractional contribution of  $i^{th}$  POD mode to the total turbulent kinetic energy,  $E_i$ , can be expressed as

$$E_i = \frac{\lambda_i}{E}, \quad (49)$$

where  $E = \sum_{i=1}^N \lambda_i$  is twice the total turbulent kinetic energy of the flow. Further, it can be shown that POD eigenfunctions are optimal in the sense that, for a given number of modes  $N$ , the projection on the subspace spanned by the  $N$  leading POD eigenfunctions contains the largest kinetic energy on average compared to any other set of basis functions (Cordier & Bergmann, 2002). Finally, a reconstruction of any given instantaneous fluctuating field at  $t_n$  using the leading  $K$  POD modes can be realized by

$$u(x, t_n) \approx u_L(x, t_n) = \sum_{k=1}^K a_k(t_n) \phi_k(x). \quad (50)$$

Particle image velocimetry provides velocity fields  $u^{n,m}$  at discrete grid points  $x^n$  and at time intervals  $t^m$ . Let  $N_g$  be the total number of grid points within a velocity field and  $M$  be the total number of velocity fields in a given ensemble. Because of the discrete nature of the spatial velocity fields as well as their acquisition the POD analysis described above must be discretized, meaning that the spatial and temporal integrations must become summations over  $n$  and  $m$ . As a result, the discretized versions of the eigen-problems in Eqs. (45) and (46) become eigenvalue problems of matrices. For two-component velocity vector fields  $(u, v)$  [as is the case for the streamwise–wall normal PIV measurements presented herein, for example], the spatial POD modes are also vectors given by  $(\phi_u, \phi_v)$  and the discretized version of Eq. (47) can be expressed in matrix form as

$$\lambda_i \begin{bmatrix} \phi_{u,i}^1 \\ \dots \\ \phi_{u,i}^{N_g} \\ \phi_{v,i}^1 \\ \dots \\ \phi_{v,i}^{N_g} \end{bmatrix} = C \begin{bmatrix} \phi_{u,i}^1 \\ \dots \\ \phi_{u,i}^{N_g} \\ \phi_{v,i}^1 \\ \dots \\ \phi_{v,i}^{N_g} \end{bmatrix}, \quad (51)$$

where

$$C = \begin{bmatrix} R_{uu}^{n,n'} & R_{uv}^{n,n'} \\ R_{vu}^{n,n'} & R_{vv}^{n,n'} \end{bmatrix}, \quad (52)$$

and

$$R_{\alpha,\beta}^{n,n'} = \sum_{m=1}^M \begin{bmatrix} \alpha^{1,m} \beta^{1,m} & \dots & \alpha^{1,m} \beta^{N_g,m} \\ \dots & \dots & \dots \\ \alpha^{N_g,m} \beta^{1,m} & \dots & \alpha^{N_g,m} \beta^{N_g,m} \end{bmatrix}. \quad (53)$$

Thus, the POD modes and eigenvalues are the eigenvectors and eigenvalues of the symmetric positive definite matrix  $C$ . Similarly, Eq. (48) can be discretized as

$$\lambda_i \begin{bmatrix} a_i^1 \\ \dots \\ a_i^M \end{bmatrix} = S \begin{bmatrix} a_i^1 \\ \dots \\ a_i^M \end{bmatrix}, \quad (54)$$

where

$$S = \begin{bmatrix} q^1 q^1 & \dots & q^1 q^M \\ \dots & \dots & \dots \\ q^M q^1 & \dots & q^M q^M \end{bmatrix}, \quad (55)$$

and

$$q^\gamma = \sum_{n=1}^{N_g} ((u^{n,\gamma})^2 + (v^{n,\gamma})^2). \quad (56)$$

In this context, the coefficients  $a_i^m$  and eigenvalues are determined from the diagonalization of the symmetric positive definite matrix  $S$ . Note that the coefficients  $a_i$  computed in this manner are often ortho-normal. From this analysis, the POD modes at grid point  $x^n$  are computed from Eq. (45) as

$$\phi_{u,i}^n = \frac{\sum_{m=1}^M (u^{n,m} a_i^m)}{\sqrt{\lambda_i}}, \quad \phi_{v,i}^n = \frac{\sum_{m=1}^M (v^{n,m} a_i^m)}{\sqrt{\lambda_i}}. \quad (57)$$

Finally, it is readily apparent that the dimension of the matrix  $C$  in classical POD is equal to the number of grid points ( $\sim 10^5$  in the current experiments). In contrast, the dimension of the matrix  $S$  in snapshot POD is equal to the number of time intervals (or snapshots) in an ensemble

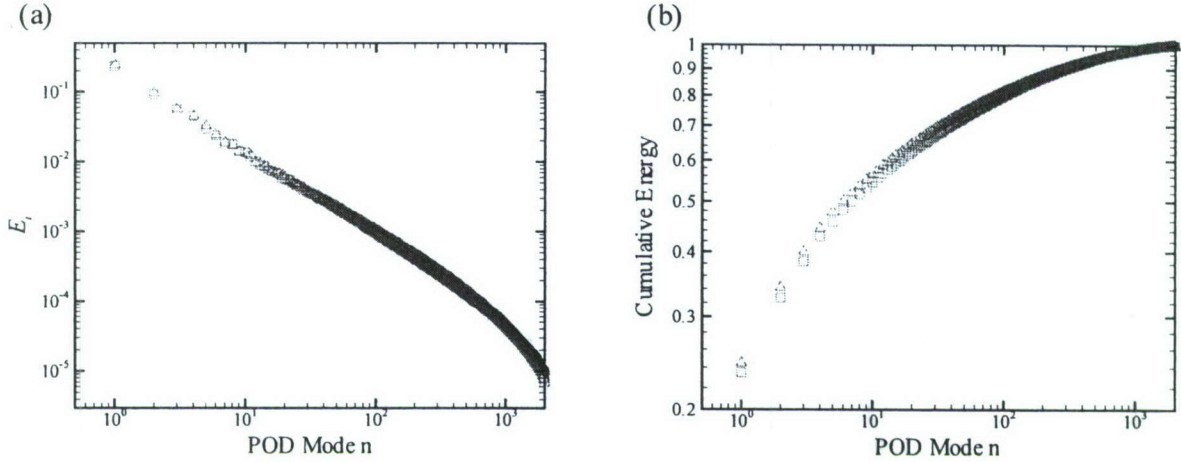


Figure 84: POD energy distributions in the  $x - y$  plane for flow over the smooth and RF1 surfaces at  $Re_\theta \approx 13000$ . (a) Fractional contribution of each POD mode to the total energy,  $E_i$ ; (b) Cumulative energy distribution.  $\square$ : Smooth;  $\triangle$ : RF1.

( $\sim 10^3$  for the present study). Therefore, it is clearly more efficient to employ the snapshot POD method to analyze the PIV ensembles in the present study since the computational effort will be reduced compared to classical POD. The use of snapshot POD to analyze PIV ensembles is not new as many recent PIV studies of various flows have employed this method to study the character of the most energetic flow scales (Druault *et al.*, 2005; Kostas *et al.*, 2005; Geers *et al.*, 2005; Gurka *et al.*, 2006; Pedersen & Meyer, 2002; Bernero & Fiedler, 2000, among others). In the present effort, snapshot POD is employed to study the characteristics of the larger and smaller scales of the flows over the smooth and RF1 surfaces at  $Re_\theta \approx 13000$  using both the two-dimensional PIV fields in the  $x - y$  plane and as well as the stereo PIV measurements in the  $x - z$  planes at  $y = 0.065\delta$  and  $0.15\delta$ .

#### 6.4.1 Streamwise–wall-normal plane

Snapshot POD analysis is first performed on the streamwise and wall-normal fluctuating velocity components ( $u', v'$ ) from the two-dimensional PIV ensembles in the  $x - y$  plane for flow over the smooth and RF1 surfaces at  $Re_\theta \approx 13000$ . This analysis is performed over the wall-normal domain  $y \leq 0.5\delta$  using 2000 instantaneous velocity fields (snapshots) per flow condition. Only 50% of the boundary-layer thickness was selected for analysis in order to reduce the computational cost of this analysis and also because the physics in the outer 50% of the boundary layer is of little interest in the present context since the flow over the RF1 surface behaves similarly to the smooth-wall flow far from the surface. In addition, the full ensemble sizes (i.e., number of snapshots) were not employed in the POD analysis to again reduce the computational cost of this analysis.

Figure 84(a) presents the fractional contributions of individual POD modes to the total turbulent kinetic energy,  $E_i$ , for flow over the smooth and RF1 surfaces at  $Re_\theta \approx 13000$ . Lower-order POD modes are representative of larger-scale, energy-containing features of the flow while higher-order POD modes correspond to smaller-scale and less energetic turbulent events. The smooth- and rough-wall energy distributions are extremely similar as collapse is noted throughout the range of POD modes from the most- to least-energetic. The fractional energy contributions of the first ten POD modes for flow over the smooth and RF1 surfaces are tabulated in table 7 and the differences

Table 7: The fractional energy contribution of the first ten POD modes for flow over the smooth and RF1 surfaces in  $x - y$  plane at  $\text{Re}_\theta \approx 13000$ .

Fractional Energy		
	Smooth	RF1
POD Mode	1	0.235
	2	0.0922
	3	0.0565
	4	0.0447
	5	0.0293
	n	0.0237
	7	0.0181
	8	0.0177
	9	0.0142
	10	0.0136

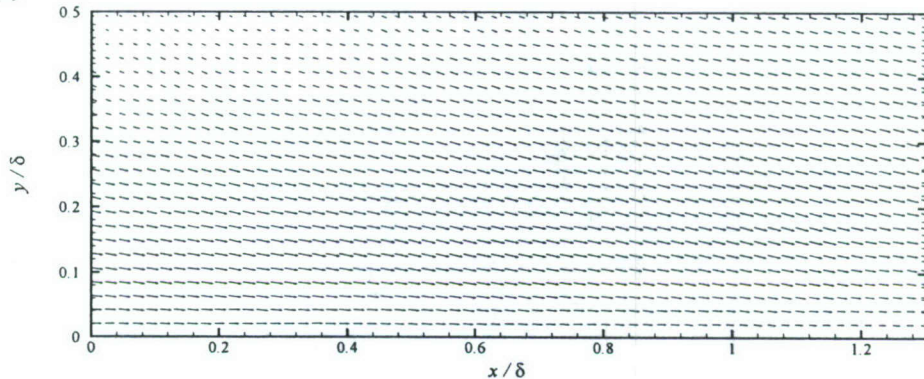
between the smooth- and rough-wall cases for fixed mode number are less than 1%. Figure 84(b) presents the distribution of cumulative energy defined as

$$\text{Cumulative energy contained in modes 1 to } m = \sum_1^m E_i, \quad (58)$$

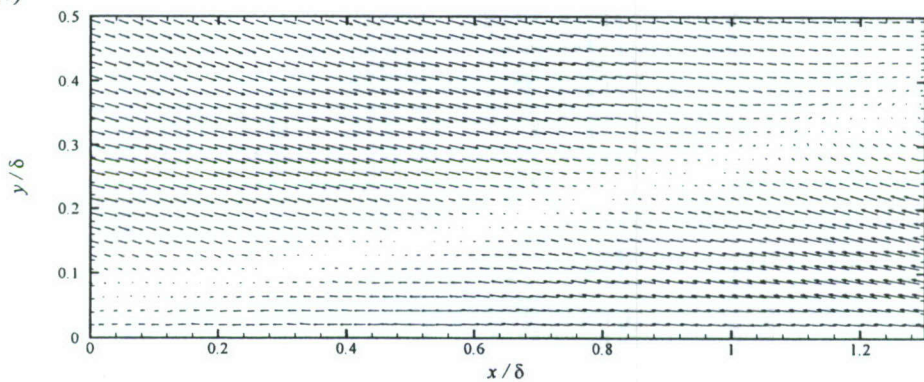
computed from the energy spectra presented in figure 84(a). As with the energy spectra, the cumulative POD energy profiles collapse well between the smooth- and rough-wall flows. Finally, the complexity of a given flow can be assessed by determining the number of POD modes required to capture 95% of the total energy. For the present smooth- and rough-wall cases, more than 400 modes are needed to capture 95% of the kinetic energy ( $u'^2 + v'^2$ ) from the  $x - y$  plane PIV measurements. As a comparison, Sen *et al.* (2007) recently reported snapshot POD results for a low-Re turbulent channel flow ( $\text{Re}_\tau = 180$ ) for which only 20–30 modes are required to capture 95% of the energy. Thus, the present flows are quite complex owing to the wide range of dynamically-important spatial scales present at the relatively high Reynolds number of  $\text{Re}_\theta \approx 13000$ .

The POD eigenfunctions corresponding to the first three most energetic modes in the  $x - y$  plane for flow over the smooth and RF1 surfaces at  $\text{Re}_\theta \approx 13000$  are presented in figures 85 and 86, respectively. It is immediately evident that the spatial character of the first three eigenfunctions is qualitatively consistent between the smooth- and rough-wall flows. The first mode, which contributes about a quarter of the total energy, displays a relatively uniform flow field. The second POD mode, which accounts for approximately 10% of the energy, is characterized by a long shear layer inclined away from the wall at approximately  $45^\circ$  beneath which exists a large-scale Q2 event opposed by a large-scale Q4 event above the inclined shear layer. This pattern is quite consistent with observations of inclined shear layers in instantaneous velocity fields at a characteristic angle of  $45^\circ$  often noted just upstream of hairpin vortex heads beneath which exists strong ejections of low-speed fluid away from the wall and above which often exists intense sweeps of high-speed fluid toward the wall. It is the interaction of these two Reynolds-stress-producing events that is responsible for the generation of these inclined shear layers. The third mode, which contributes

(a)



(b)



(c)

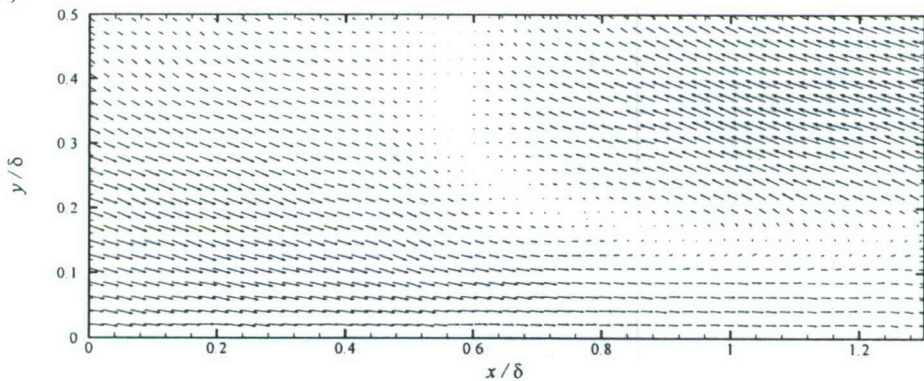
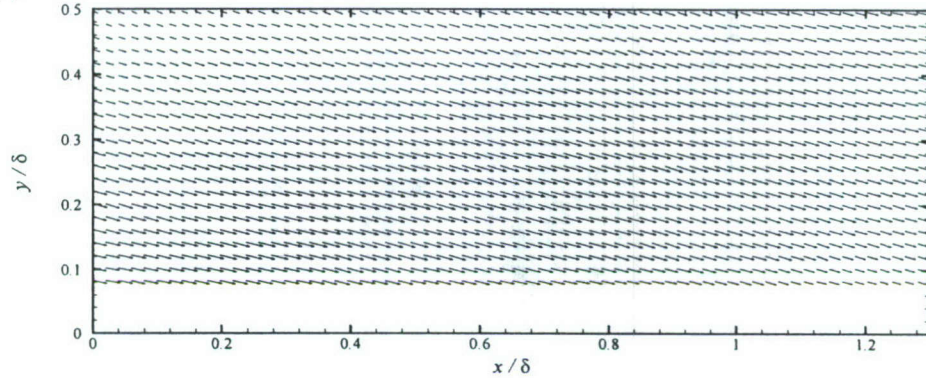
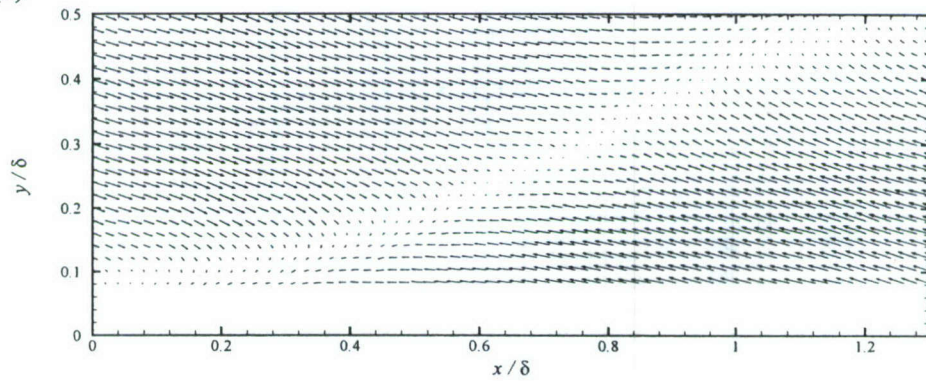


Figure 85: POD eigenfunctions in the  $x - y$  plane for flow over the smooth wall at  $\text{Re}_\theta = 11943$ .  
 (a) Mode 1; (b) Mode 2; (c) Mode 3. Not every vector is shown for clarity.

(a)



(b)



(c)

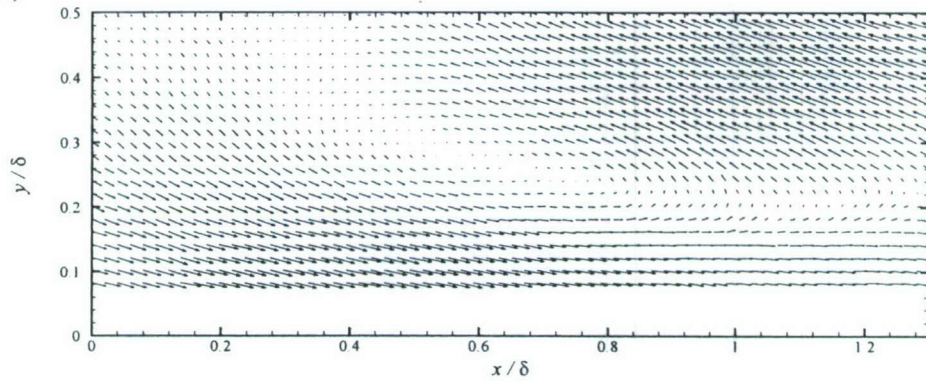


Figure 86: POD eigenfunctions in the  $x - y$  plane for flow over the RF1 surface at  $\text{Re}_\theta = 11943$ .  
 (a) Mode 1; (b) Mode 2; (c) Mode 3. Not every vector is shown for clarity.

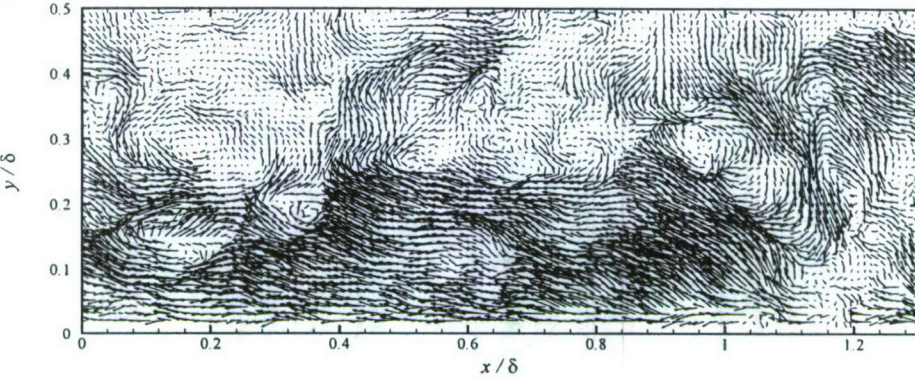
about 6% of the energy, is marked by a long shear layer that separates large-scale  $Q_1$  and  $Q_3$  events. Of particular interest, these vector plots of the leading three POD eigenfunctions illustrate that the most energetic large-scale turbulent events generate significant Reynolds shear stress. In particular, the turbulent events that contribute negatively to the Reynolds shear stress ( $Q_2$  and  $Q_4$  events in mode 2) contain more kinetic energy than the events that contribute positively to the Reynolds shear stress ( $Q_1$  and  $Q_3$  events in mode 3). This trend is entirely consistent with the fact that  $\langle u'v' \rangle < 0$ . Finally, while the smooth- and rough-wall modes show strong qualitative consistency, some subtle differences can be observed. For example, the shear layer in mode two has a slightly larger inclination angle in the RF1 case compared to the smooth-wall result. In contrast, the upstream portion of the shear layer in the third mode is inclined slightly closer to the wall for the rough-wall case.

As noted earlier, one of the most beneficial uses of the POD basis functions is to low-pass filter instantaneous velocity realizations in order to study the physics of the larger- and smaller-scale features of the flow. In the present effort, this decomposition enables the study of roughness-induced modifications of the larger and smaller spatial scales. Each individual fluctuating velocity field (or snapshot) is reconstructed using Eq. (50) from a subset of the leading (most energetic) POD modes. In the present analysis, the number of modes employed in this reconstruction is chosen to be the minimum number required to capture 50% of the total energy ( $u'^2 + v'^2$ ). As such, the leading five (5) POD modes are employed in the reconstruction for the smooth-wall flow while the first six (6) modes are used for reconstruction of the rough-wall flow. The resulting reconstructed velocity fields,  $\mathbf{u}'_L(\mathbf{x})$ , represent low-order (larger-scale) representations of the original fluctuating velocity fields while the difference between a given original fluctuating velocity field and its associated low-order field yields a residual (smaller-scale) field,  $\mathbf{u}'_R(\mathbf{x})$ . In this context, an ensemble of residual velocity fields for a given flow condition contains the remaining 50% of the kinetic energy generated by smaller-scale flow events.

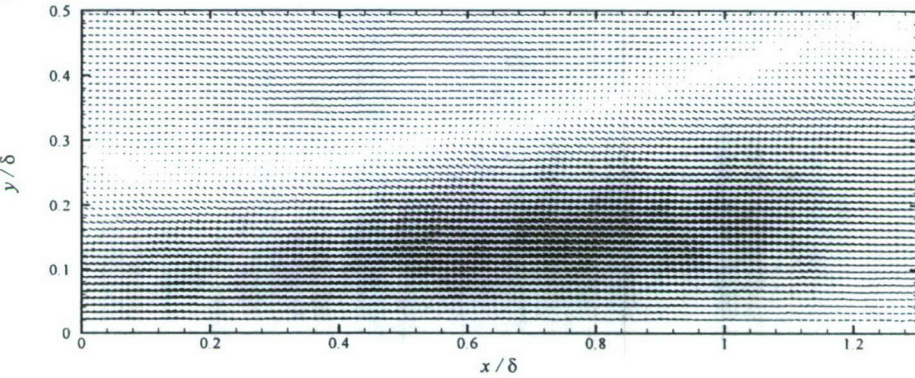
Figure 87(a) presents a representative instantaneous fluctuating velocity field in the  $x - y$  plane for flow over the smooth wall at  $Re_\theta \approx 13000$  and is the same realization as that presented in figure 43(a). Several clockwise-rotating (prograde) spanwise vortices are aligned in the streamwise direction forming an inclined interface. Beneath this interface exists a large-scale region of low-momentum fluid collectively induced by this packet of vortices. The low-order (large-scale) velocity field associated with this realization is presented in figure 87(b) and the inclined interface, along with the large-scale region of streamwise momentum deficit, are captured quite accurately in this low-order representation. In contrast, the associated residual velocity field contains the clusters of small-scale swirling motions together with intermittent strong sweeps and ejections [figure 87(c)]. Similar spatial features are apparent in a representative instantaneous fluctuating velocity field from the rough-wall flow presented in figure 88(a) along with its associated low-order and residual velocity fields [figures 88(b) and 88(c), respectively].

While visualization of the instantaneous low-order and residual velocity fields provides a glimpse of the large- and small-scale features of the smooth- and rough-wall flows, it does not provide quantitative measures of the influence of roughness on these spatial scales. However, since this decomposition generates ensembles of large- and small-scale velocity fields for each flow condition, one can compute the contributions of the larger and smaller spatial scales of the flow to the Reynolds normal and shear stresses. These calculations are accomplished by simply ensemble-averaging and line-averaging the low-order and residual ensembles separately for each flow condition. This process generates profiles of Reynolds normal and shear stresses attributable to the larger and smaller spatial scales, respectively, and comparison of these profiles to the total profiles reported in chapter 3 provides a measure of the importance of these spatial scales to the overall turbulent stresses for both smooth- and rough-wall flow.

(a)



(b)



(c)

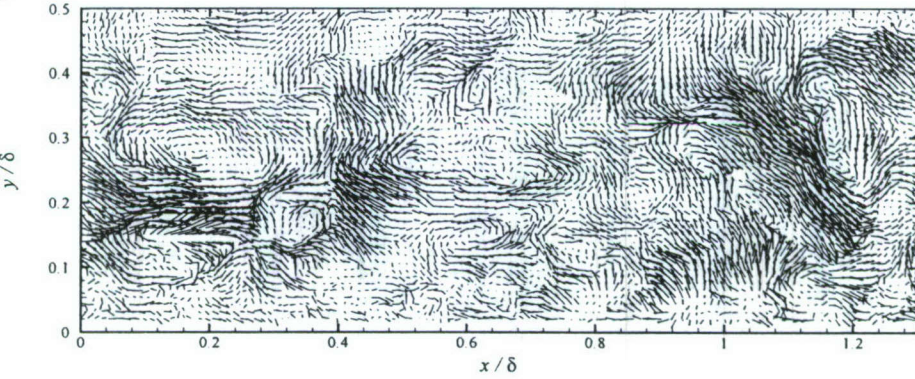


Figure 87: (a) A representative fluctuating velocity field in the  $x - y$  plane for flow over the smooth wall at  $\text{Re}_\delta = 11943$  [same field as figure 43(a)]. (b) Low-order (large-scale) representation of the velocity field in (a) generated by projecting this field onto the first five POD modes. (c) Residual (small-scale) velocity field. Not every vector is shown for clarity.

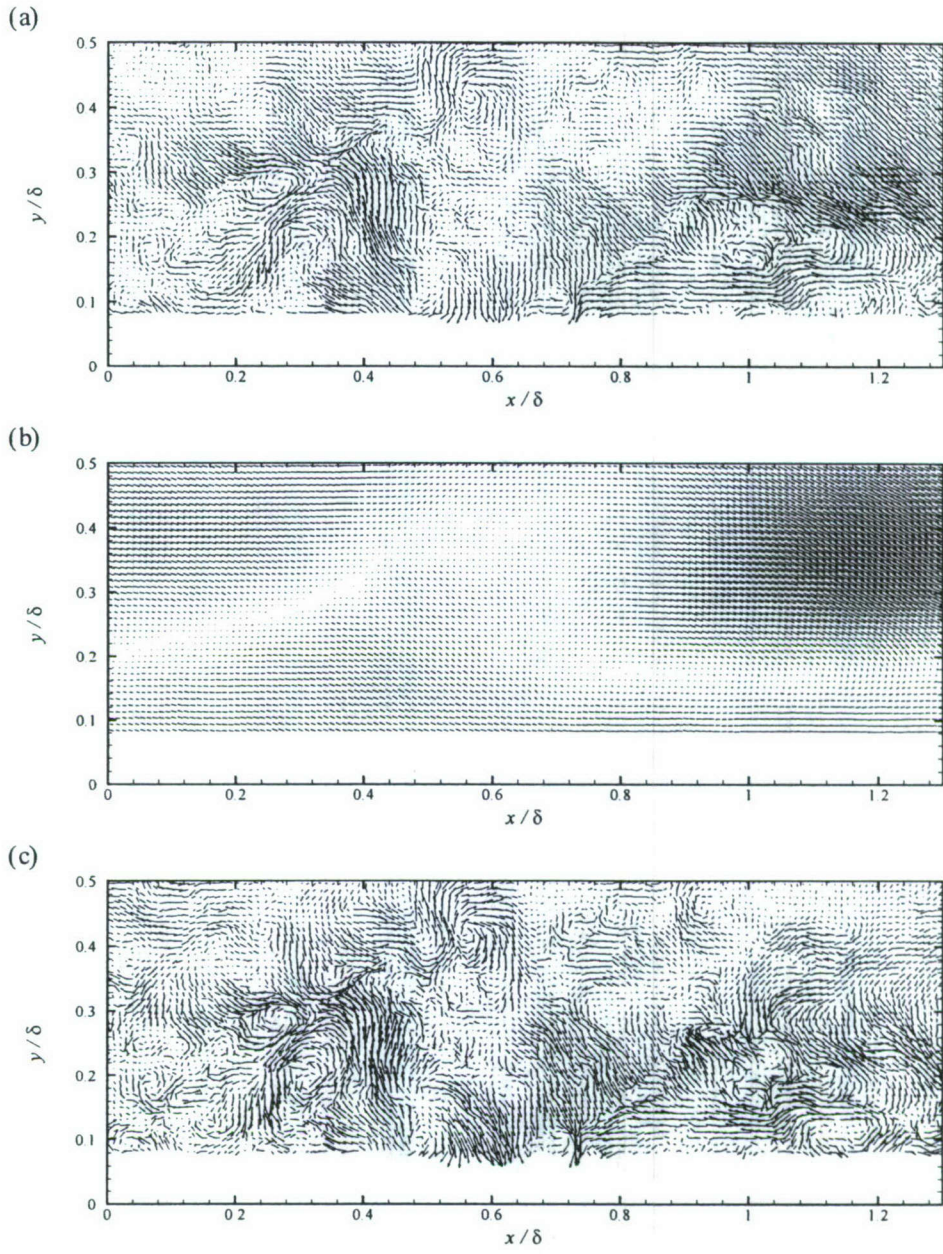


Figure 88: (a) A representative fluctuating velocity field in the  $x - y$  plane for flow over the RF1 surface at  $Re_\theta = 14781$  [same field as figure 44(a)]. (b) Low-order (large-scale) representation of the velocity field in (a) generated by projecting this field onto the first six POD modes. (c) Residual (small-scale) velocity field. Not every vector is shown for clarity.

Figure 89(a) presents profiles of  $\langle u'^2 \rangle$  computed from the original fluctuating velocity fields (referred to as the “total” profiles) as well as from the low-order and residual ensembles for smooth- and rough-wall flow. As was discussed in chapter 3, the total profiles of  $\langle u'^2 \rangle$  for flow over the smooth and RF1 surfaces display similarity in the outer region in accordance with Townsend’s wall similarity hypothesis. Interestingly, the low-order and residual contributions to  $\langle u'^2 \rangle$  also show this similarity as the smooth- and rough-wall results collapse reasonably well in the outer layer. In addition, it is clear that larger-scale features of the flow generate a vast majority of  $\langle u'^2 \rangle$  everywhere except very close to the wall. In contrast, the smaller scales of the flow dominate  $\langle v'^2 \rangle$  [figure 89(b)] in both the smooth- and rough-wall cases with only a small fraction of  $\langle v'^2 \rangle$  carried by the larger spatial scales of both flows. As with  $\langle u'^2 \rangle$ , the smooth- and rough-wall contributions to  $\langle v'^2 \rangle$  from large and small scales collapse in the outer layer in accordance with the notion of outer-layer similarity. Finally, the contributions of larger and smaller spatial scales to the Reynolds shear stress,  $\langle u'v' \rangle$ , along with the total profiles of  $\langle u'v' \rangle$  are presented in figure 89(c). For  $y > 0.1\delta$ , the large-scale spatial structures embody a significant fraction (70–80%) of  $\langle u'v' \rangle$  which is roughly three times the amount of turbulent shear stress embodied in the smaller scales. This trend is consistent with the large-scale contributions to  $\langle u'^2 \rangle$  in the outer layer. As with the Reynolds normal stresses, the large- and small-scale contributions to  $\langle u'v' \rangle$  collapse in the outer layer irrespective of surface condition.

Two-point correlations can also be computed from the low-order (larger scale) and residual (smaller scale) velocity ensembles for flow over the smooth and RF1 surfaces at  $Re_\theta \approx 13000$  in order to study the similarities and differences between the characteristic spatial signatures and scales of the dominant larger and smaller spatial scales of the flow. These correlations are particularly useful in further interpreting the trends noted in the previous section for spatial correlations of the full velocity fields. Figures 90 and 91 present two-point streamwise velocity correlation coefficients in the  $x - y$  plane at  $y_{ref} = 0.15\delta$  for  $Re_\theta \approx 13000$  computed from the low-order ( $\rho_{u_L u_L}$ ) and residual ( $\rho_{u_R u_R}$ ) velocity ensembles for flow over the smooth and RF1 surfaces, respectively. The correlation  $\rho_{u_L u_L}$  is elongated in the streamwise direction and inclined slightly away from the wall for both smooth- and rough-wall flow. These characteristics are entirely consistent with the large-scale spatial characteristics of  $\rho_{uu}$  presented in figure 57 for smooth- and rough-wall flow. On the other hand,  $\rho_{u_R u_R}$  is marked by spatially compact positive correlation contours centered at the reference location for both smooth- and rough-wall flow attributable to smaller spatial scales. Of particular interest, these spatially-compact positive correlation levels are bounded upstream and downstream as well as above and below by regions of weak negative correlation. The smaller regions of weak negative correlation directly above and below the reference location are consistent with the swirling motion of spanwise vortex cores, likely the heads of hairpin-like vortices (a region of negative correlation beneath the reference location in the rough-wall case is not observed due to a lack of data close to the rough surface). In contrast, the larger regions of weak negative correlation upstream and downstream of the reference location are likely due to turbulent events induced by adjacent hairpin-like structures in outer-layer vortex organization.

Figure 92 presents one-dimensional profiles of  $\rho_{u_L u_L}$  and  $\rho_{u_R u_R}$  at  $y_{ref} = 0.15\delta$  for flow over the smooth and RF1 surfaces at  $Re_\theta \approx 13000$ . The rough-wall  $\rho_{u_L u_L}$  profiles display reduced spatial extents in both the wall-normal and streamwise directions compared to the smooth-wall result. This difference is most notable in the streamwise direction where the streamwise extent of the large-scale features is dramatically reduced by roughness at this wall-normal location. This reduction is consistent, though more dramatic, than the reduction in the streamwise extent of  $\rho_{uu}$  observed in figure 58 which includes contributions from all spatial scales. Interestingly, the streamwise extent of  $\rho_{u_R u_R}$  is much more consistent between smooth- and rough-wall flow, although a slight reduction in the presence of roughness is still apparent. A reduction in the wall-normal extent of  $\rho_{u_L u_L}$  is

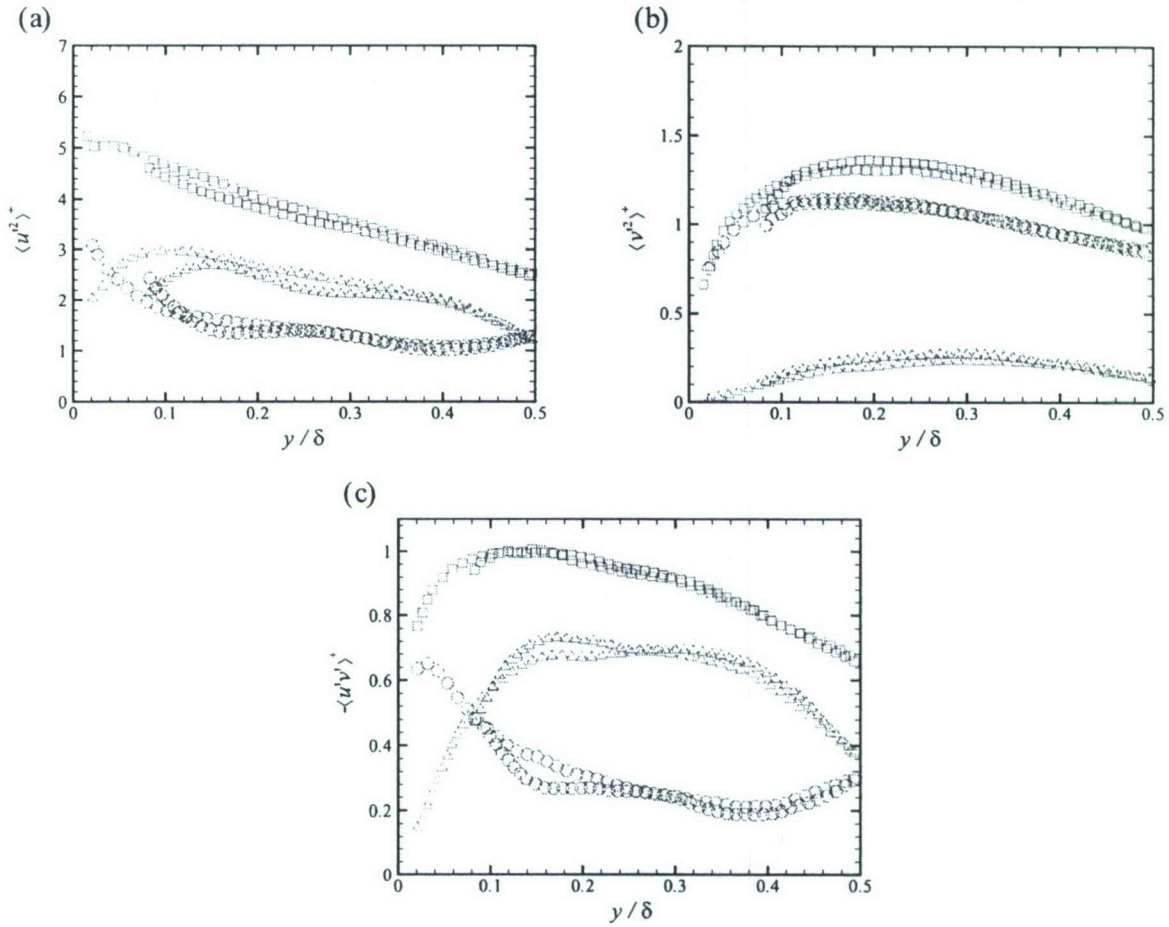


Figure 89: Comparison of Reynolds-stress contributions from low-order and residual velocity fields for flow over the smooth and RF1 surfaces at  $\text{Re}_\theta \approx 13000$ . (a)  $\langle u'^2 \rangle$ ; (b)  $\langle v'^2 \rangle$ ; (c)  $-\langle u'v' \rangle$ .  $\square$ : Original velocity fields;  $\triangle$ : Low-order velocity fields;  $\circ$ : Residual velocity fields. Red symbols represent results for the smooth-wall flow and blue symbols represent results for the RF1 flow. Not every data point is shown for clarity.

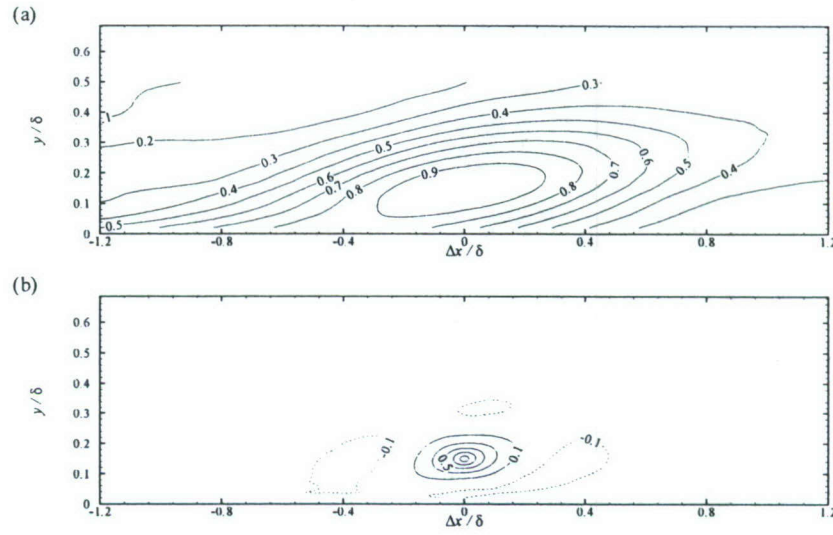


Figure 90: Streamwise velocity correlation coefficients in the  $x - y$  plane at  $y = 0.15\delta$  for flow over the smooth wall at  $Re_\theta = 11943$ . (a)  $\rho_{u_L u_L}$  (contour levels from 0.1 to 0.9 with an interval of 0.1); (b)  $\rho_{u_R u_R}$  (contour levels from -0.1 to 0.9 with an interval of 0.2).

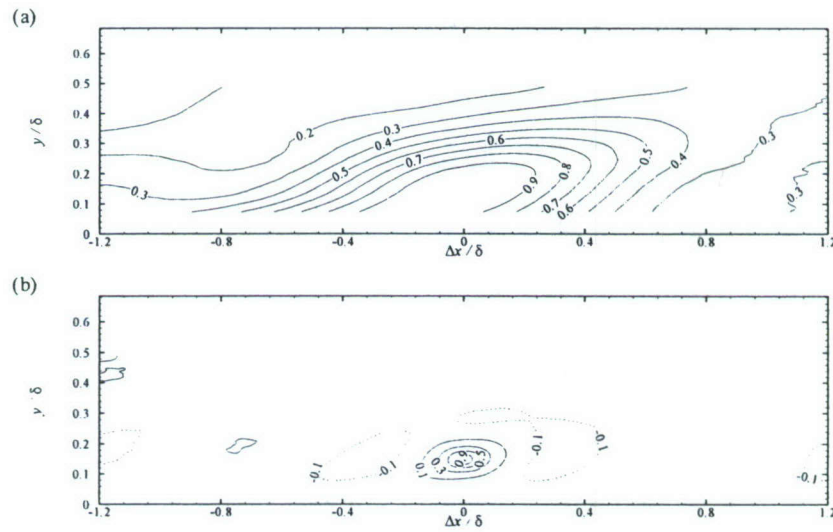


Figure 91: Streamwise velocity correlation coefficients in the  $x - y$  plane at  $y = 0.15\delta$  for flow over the RF1 surface at  $Re_\theta = 14781$ . (a)  $\rho_{u_L u_L}$  (contour levels from 0.1 to 0.9 with an interval of 0.1); (b)  $\rho_{u_R u_R}$  (contour levels from -0.1 to 0.9 with an interval of 0.2).

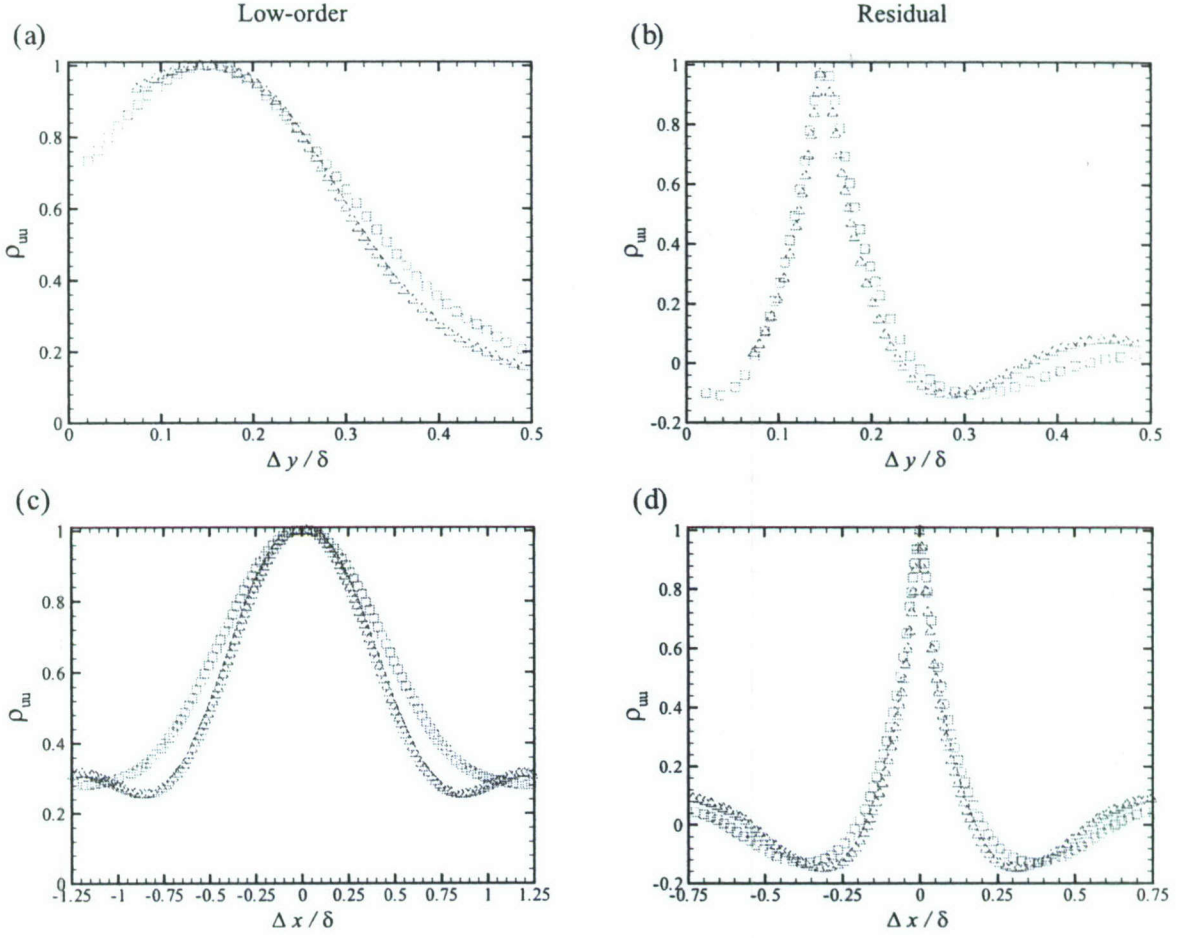


Figure 92: One-dimensional profiles of  $\rho_{u_L u_L}$  and  $\rho_{u_R u_R}$  in the (a, b) wall-normal and (c, d) streamwise directions at  $y_{\text{ref}} = 0.15\delta$  for flow over the smooth and RF1 surfaces at  $\text{Re}_\theta \approx 13000$ .  $\square$ : Smooth;  $\triangle$ : RF1.

also noted, although this reduction is much less dramatic than that observed in the streamwise direction. Finally,  $\rho_{u_R u_R}$  displays better consistency between smooth- and rough-wall flows than its large-scale counterpart.

Two-point correlations of wall-normal velocity are also computed for the low-order ( $\rho_{v_L v_L}$ ) and residual ( $\rho_{v_R v_R}$ ) velocity ensembles at  $y = 0.15\delta$  for flow over the smooth and RF1 surfaces (figures 93 and 94). As with  $\rho_{u_L u_L}$  and  $\rho_{u_R u_R}$ , the spatial characteristics of  $\rho_{v_L v_L}$  and  $\rho_{v_R v_R}$  are similar between smooth- and rough-wall flow. The correlation  $\rho_{v_L v_L}$  is, as one would expect, marked by large spatial scales in both the streamwise and wall-normal directions likely due to large-scale regions of ejections and sweeps noted in the instantaneous low-order velocity fields shown in figures 87(b) and 88(b). In particular, hairpin vortex packets likely contribute to this large-scale  $\rho_{vv}$  via the collectively-induced motions beneath the inclined interface of these large-scale structures. On the other hand,  $\rho_{v_R v_R}$  is characterized by spatially-compact correlation contours that are quite consistent with the characteristics of  $\rho_{vv}$  obtained from the original velocity fields (figure 63). This consistency is not surprising given that the smaller scales of the flow dominate  $\langle v'^2 \rangle$  [figure 89(b)]. The spatial scales of  $\rho_{v_L v_L}$  and  $\rho_{v_R v_R}$  for flow over the smooth and RF1

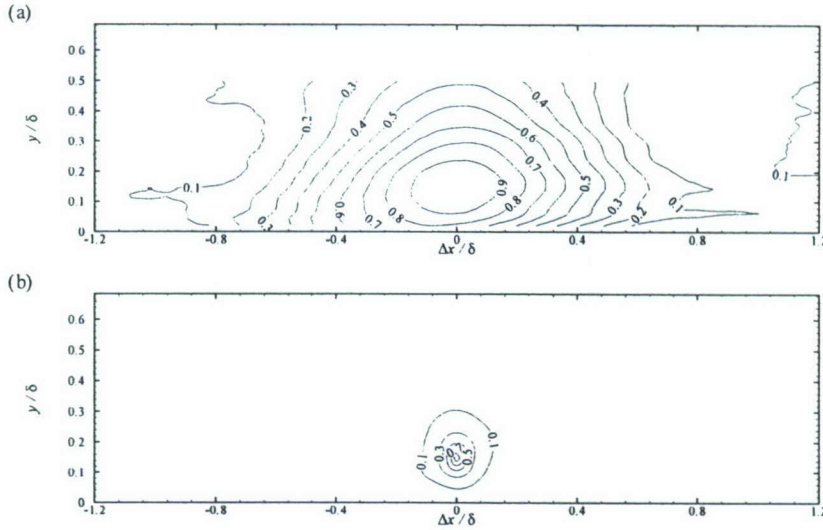


Figure 93: Wall-normal velocity correlation coefficients in the  $x - y$  plane at  $y = 0.15\delta$  for flow over the smooth wall at  $\text{Re}_\theta = 11943$ . (a)  $\rho_{vLvL}$  (contour levels from 0.1 to 0.9 with an interval of 0.1); (b)  $\rho_{vRvR}$  (contour levels from 0.1 to 0.9 with an interval of 0.2).

surfaces are compared in figure 95 which presents one-dimensional profiles of these correlations in the wall-normal and streamwise directions. The wall-normal extent of  $\rho_{vLvL}$  is quite consistent between smooth- and rough-wall flow while its streamwise extent is slightly reduced for flow over the RF1 surface compared to the smooth-wall case. This reduction is far less dramatic than that observed for  $\rho_{uLuL}$ , but is nevertheless indicative of a fundamental reduction in the coherence of the larger spatial scales of the flow in the presence of roughness. In contrast, both the wall-normal and streamwise extents of  $\rho_{vRvR}$  are quite consistent between smooth- and rough-wall flow. This consistency, coupled with the consistency noted in  $\rho_{uRuR}$ , indicates that the smaller spatial scales of the flow are relatively immune to roughness effects.

#### 6.4.2 Streamwise–spanwise plane

Proper orthogonal decomposition is also applied to the PIV ensembles in the  $x - z$  plane at both  $y = 0.065\delta$  and  $y = 0.15\delta$  using 1600 snapshots per flow condition. Since these ensembles were acquired using stereo PIV, POD is applied to all three velocity components within the wall-parallel planes. The POD energy distributions in the streamwise–spanwise plane for flow over the smooth and RF1 surfaces at  $y = 0.065\delta$  and  $y = 0.15\delta$  are presented in figures 96 and 97, respectively, for  $\text{Re}_\theta \approx 13000$ . The fractional energy contributions as well as the cumulative POD energy distributions are similar between the smooth- and rough-wall flows at both wall-normal locations. The fractional energy contributed by the ten most energetic POD modes at both  $y = 0.065\delta$  and  $y = 0.15\delta$  for the smooth- and rough-wall flows are tabulated in table 8. The energy content of each mode is similar between the smooth and rough cases, although slightly better agreement is noted further from the wall at  $y = 0.15\delta$ . This trend is not surprising since  $y = 0.065\delta$  is well within the roughness sublayer for the RF1 case. Further, the kinetic energy within these streamwise–spanwise planes is distributed amongst a broad range of spatial scales as evidenced by the relatively gradual convergence of the cumulative POD energy distributions. In this regard, more than 700 POD modes are needed at  $y = 0.065\delta$  to capture 95% of the energy while more than 600 modes are required at

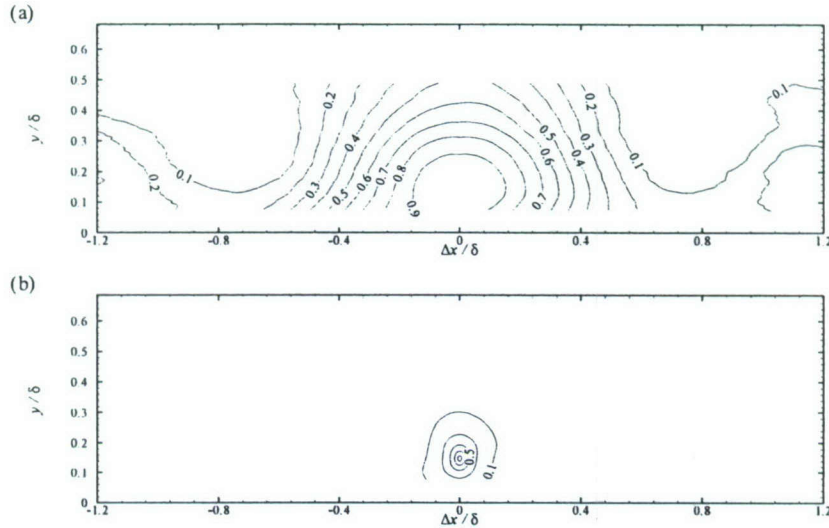


Figure 94: Wall-normal velocity correlation coefficients,  $\rho_{vv}$ , in the  $x - y$  plane at  $y = 0.15\delta$  for flow over the RF1 surface at  $Re_\theta = 14781$ . (a)  $\rho_{v_L v_L}$  (contour levels from 0.1 to 0.9 with an interval of 0.1); (b)  $\rho_{v_R v_R}$  (contour levels from 0.1 to 0.9 with an interval of 0.2).

$$y = 0.15\delta.$$

As was done in the POD analysis of the streamwise-wall normal plane velocity ensembles, the POD eigenfunctions in the  $x - z$  planes at  $y = 0.065\delta$  and  $0.15\delta$  are used to generate ensembles of low-order and residual velocity fields for each flow case by projecting the instantaneous fluctuating velocity fields of a given ensemble onto the minimum number of leading POD modes required to capture 50% of the turbulent kinetic energy for that ensemble. As such, the first 20 POD modes are used in the reconstruction for the smooth-wall flow at  $y = 0.065\delta$ , the first 22 modes are used for flow over the RF1 surface at  $y = 0.065\delta$ , the first 15 modes are employed for the smooth-wall flow at  $y = 0.15\delta$  and the first 16 modes are necessary for flow over the RF1 surface at  $y = 0.15\delta$ . Examples of instantaneous low-order and residual velocity fields in the streamwise-spanwise plane of both smooth- and rough-wall flows at  $y = 0.065\delta$  and  $y = 0.15\delta$  are presented in figures 98–101 for  $Re_\theta \approx 13000$ . It is seen that the low-order velocity fields consistently display large-scale LMR's and HMR's coincident with elongated regions of ejections and sweeps, respectively, for both the smooth and rough cases. These LMR's and HMR's have long streamwise extents (greater than the streamwise field of view of these fields) and they appear to meander in the spanwise direction. These characteristics are entirely consistent with the large-scale characteristics of hairpin vortex packets sliced by streamwise-spanwise measurement planes. In contrast, the residual velocity fields are each characterized by intense small-scale wall-normal vortex cores as well as intermittent, yet intense, sweeps and ejections. Therefore, while the large-scale LMR's and HMR's generated by hairpin vortex packets reside in the low-order fields, the wall-normal vortices thought to be slices through the legs/necks of the individual hairpins within a packet as well as the intense ejections and sweeps generated locally by these structures reside in the residual (smaller scale) fields. Despite these qualitative consistencies between the smooth and rough cases, there exist subtle differences, particularly in the residual fields at  $y = 0.065\delta$ . Comparing the representative instantaneous smooth-wall residual field in figure 98(b) to the instantaneous rough-wall residual field in figure 99(b) reveals the presence of strong  $v'$  events in the rough-wall case, particularly spatially-coincident with strong roughness protrusions as discussed in chapter 4. These differences

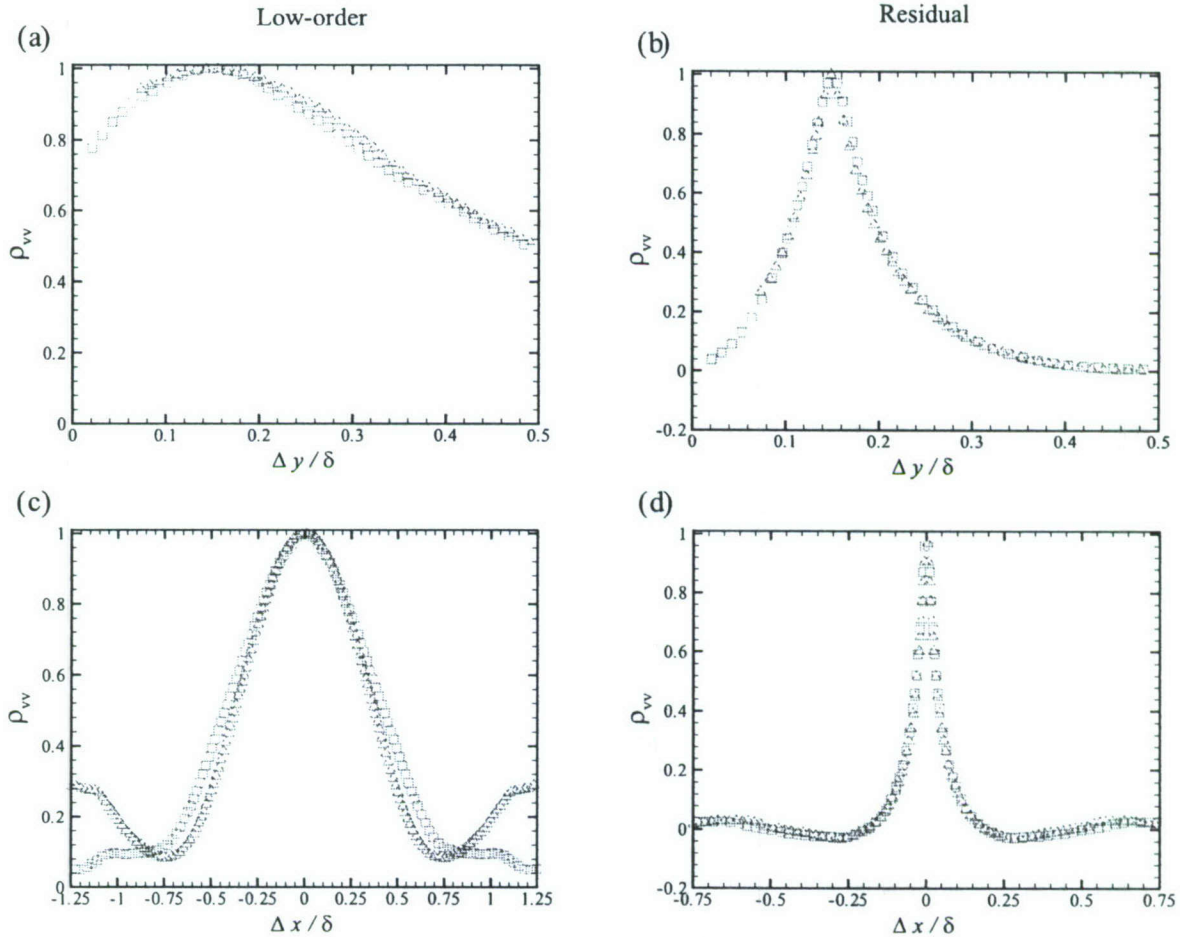


Figure 95: One-dimensional profiles of  $\rho_{v_L v_L}$  and  $\rho_{v_R v_R}$  in the (a, b) wall-normal and (c, d) streamwise directions at  $y_{\text{ref}} = 0.15\delta$  for flow over the smooth and RF1 surfaces at  $\text{Re}_\theta \approx 13000$ .  $\square$ : Smooth;  $\triangle$ : RF1.

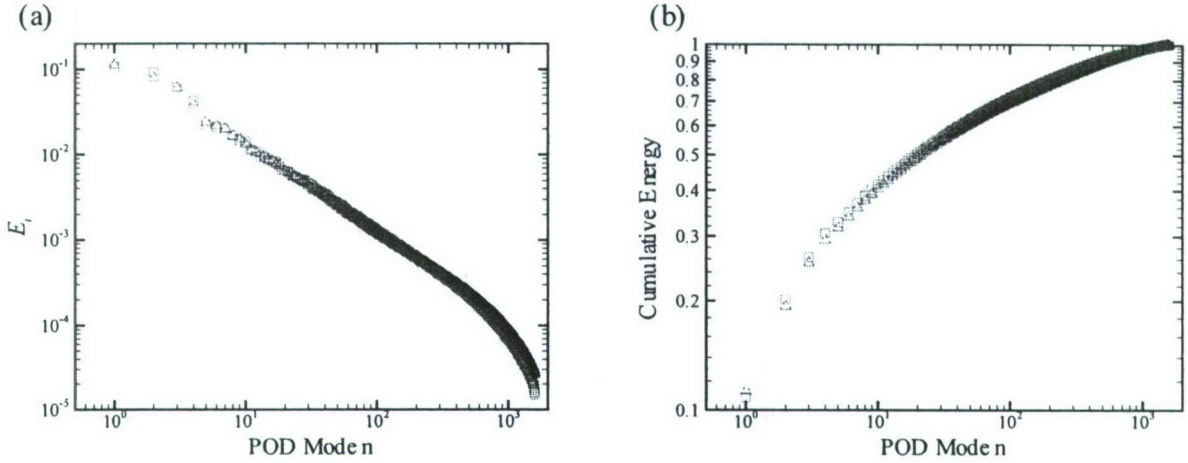


Figure 96: POD energy distributions in the  $x - z$  plane at  $y = 0.065\delta$  for flow over the smooth and RF1 surfaces at  $Re_\theta \approx 13000$ . (a) Fractional contribution of each POD mode to the total energy,  $E_i$ ; (b) Cumulative energy distribution.  $\square$ : Smooth;  $\triangle$ : RF1.

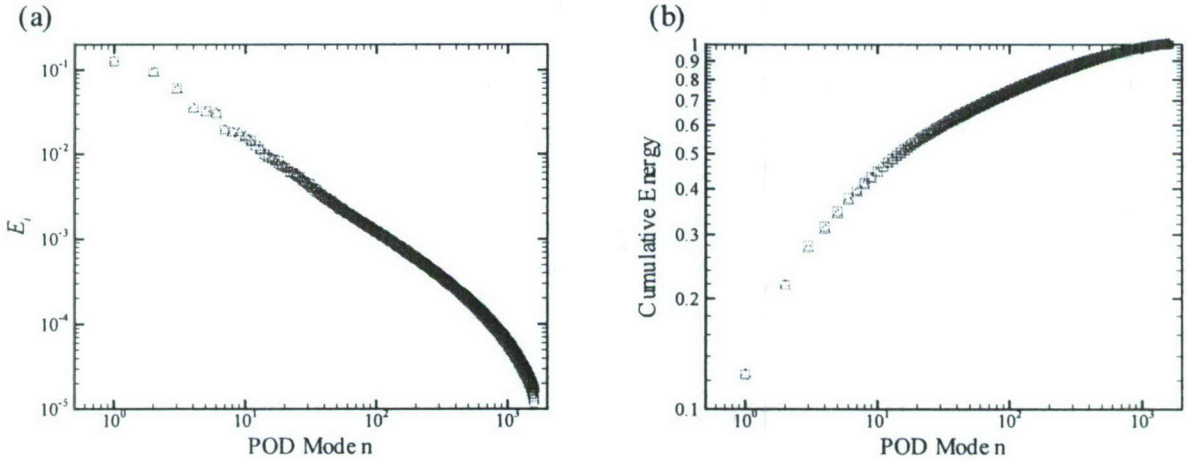


Figure 97: POD energy distributions in the  $x - z$  plane at  $y = 0.15\delta$  for flow over the smooth and RF1 surfaces at  $Re_\theta \approx 13000$ . (a) Fractional contribution of each POD mode to the total energy,  $E_i$ ; (b) Cumulative energy distribution.  $\square$ : Smooth;  $\triangle$ : RF1.

Table 8: The fractional energy contribution of the first ten POD modes in  $x - z$  planes at  $y = 0.065\delta$  and  $0.15\delta$  for flow over the smooth and RF1 surfaces at  $\text{Re}_\theta \approx 13000$ .

POD Mode n	Fractional Energy at $y = 0.065\delta$		POD Mode n	Fractional Energy at $y = 0.15\delta$	
	Smooth	RF1		Smooth	RF1
1	0.108	0.113	1	0.124	0.124
2	0.0933	0.0805	2	0.0947	0.0932
3	0.062	0.0601	3	0.0612	0.0574
4	0.0428	0.0387	4	0.0353	0.0345
5	0.0224	0.0241	5	0.0327	0.0312
6	0.0211	0.0221	6	0.0299	0.0305
7	0.0168	0.0202	7	0.0194	0.0193
8	0.0148	0.0167	8	0.0182	0.018
9	0.0143	0.0154	9	0.016	0.0179
10	0.0109	0.0133	10	0.0153	0.0161

diminish considerably with increasing distance from the wall as the instantaneous smooth- and rough-wall fields at  $y = 0.15\delta$  show stronger quantitative consistency.

The contributions of the low-order and residual velocity fields to the mean Reynolds normal and shear stresses at  $y = 0.065\delta$  and  $y = 0.15\delta$  for flow over both the smooth and RF1 surfaces are tabulated in table 9 for  $\text{Re}_\theta \approx 13000$ . Large-scale flow features are found to embody a significant fraction of the streamwise Reynolds normal stress at both wall-normal locations, consistent with the POD analysis in the streamwise–wall-normal plane. In contrast, a majority of the wall-normal and spanwise Reynolds normal stresses is attributable to the smaller spatial scales, most significantly in the case of  $\langle v'^2 \rangle$ . With regard to the Reynolds shear stress, large and small scales are found to contribute relatively equally at  $y = 0.065\delta$  for both smooth- and rough-wall flow while the larger scales become the dominant contributor in both flows to  $\langle u'v' \rangle^+$  further away from the wall at  $y = 0.15\delta$ . This latter trend is again consistent with the smooth- and rough-wall POD analysis performed in the streamwise–wall-normal plane.

The average spatial characteristics embodied in the low-order and residual velocity ensembles are assessed via spatial correlations of velocity. Figures 102 and 103 present  $\rho_{uu}$  computed from the low-order and residual velocity ensembles in the  $x - z$  plane at  $y = 0.065\delta$  for flow over the smooth and RF1 surfaces, respectively, at  $\text{Re}_\theta \approx 13000$ . As should be expected,  $\rho_{u_L u_L}$  embodies statistical imprints consistent with the streamwise-elongated, spanwise-alternating LMR’s and HMR’s noted in the instantaneous low-order velocity fields presented in figures 98(a) and Figure 99(a). In particular, it is the alternating occurrence of LMR’s and HMR’s in the spanwise direction that is responsible for the weaker, yet streamwise-elongated negative correlation regions in  $\rho_{u_L u_L}$ . These spatial characteristics are quite consistent with the large-scale characteristics of  $\rho_{uu}$  computed from the original velocity fields at  $y = 0.065\delta$  (figure 54). In contrast,  $\rho_{u_R u_R}$  is quite compact in both streamwise and spanwise directions and regions of negative correlation surround the positive correlation peak. This arrangement is consistent with the spatial characteristics of small-scale wall-normal vortex cores in the  $x - z$  plane as well as intermittent Reynolds-stress-producing events with opposing streamwise velocities. Similar spatial characteristics are noted in

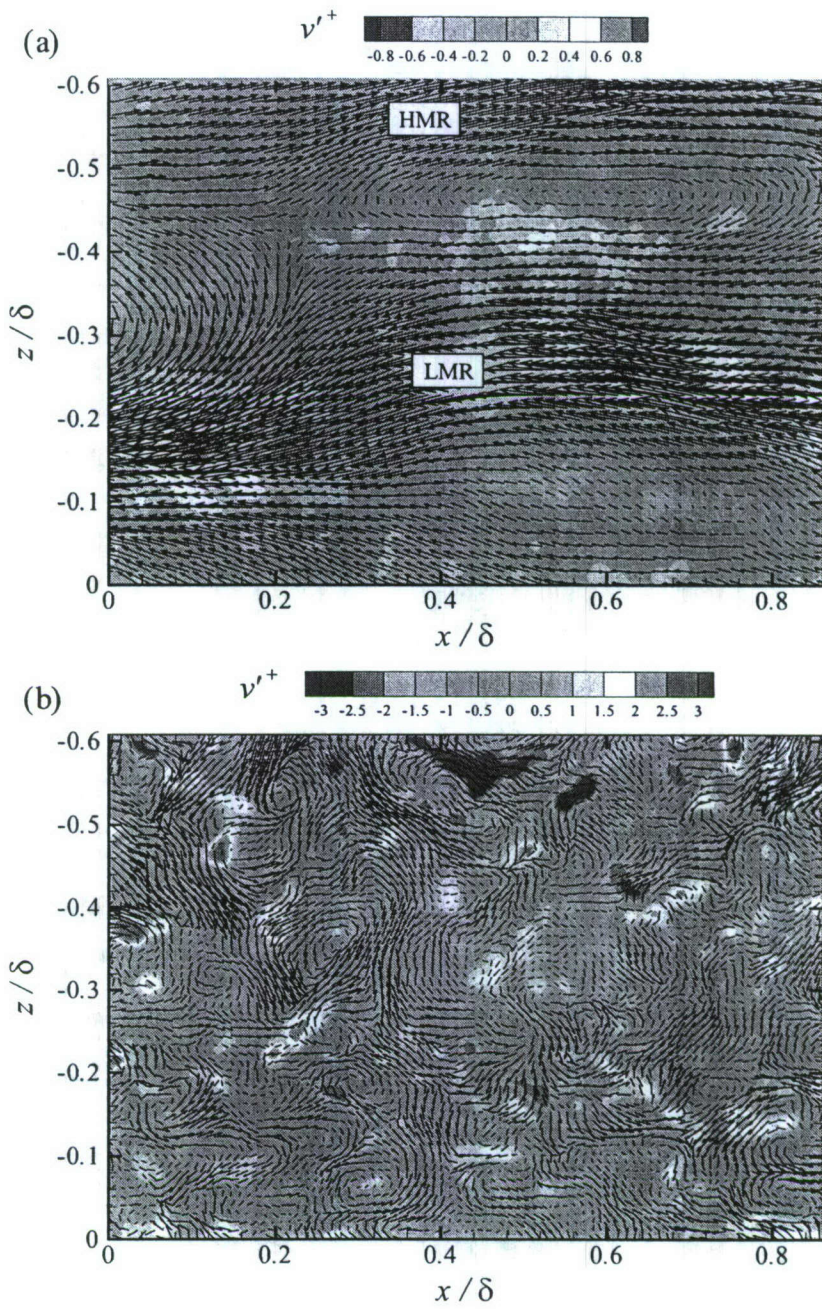


Figure 98: Representative instantaneous (a) low-order and (b) residual velocity fields in the  $x - z$  plane at  $y = 0.065\delta$  for flow over the smooth wall at  $Re_\theta = 11943$  generated by projecting the instantaneous fluctuating velocity field in figure 45(a) onto the first 20 POD modes. The in-plane velocity components ( $u'^+$ ,  $w'^+$ ) are presented as vectors while the out-of-plane velocity component  $v'^+$  is presented as background contours. Not every vector is shown for clarity.

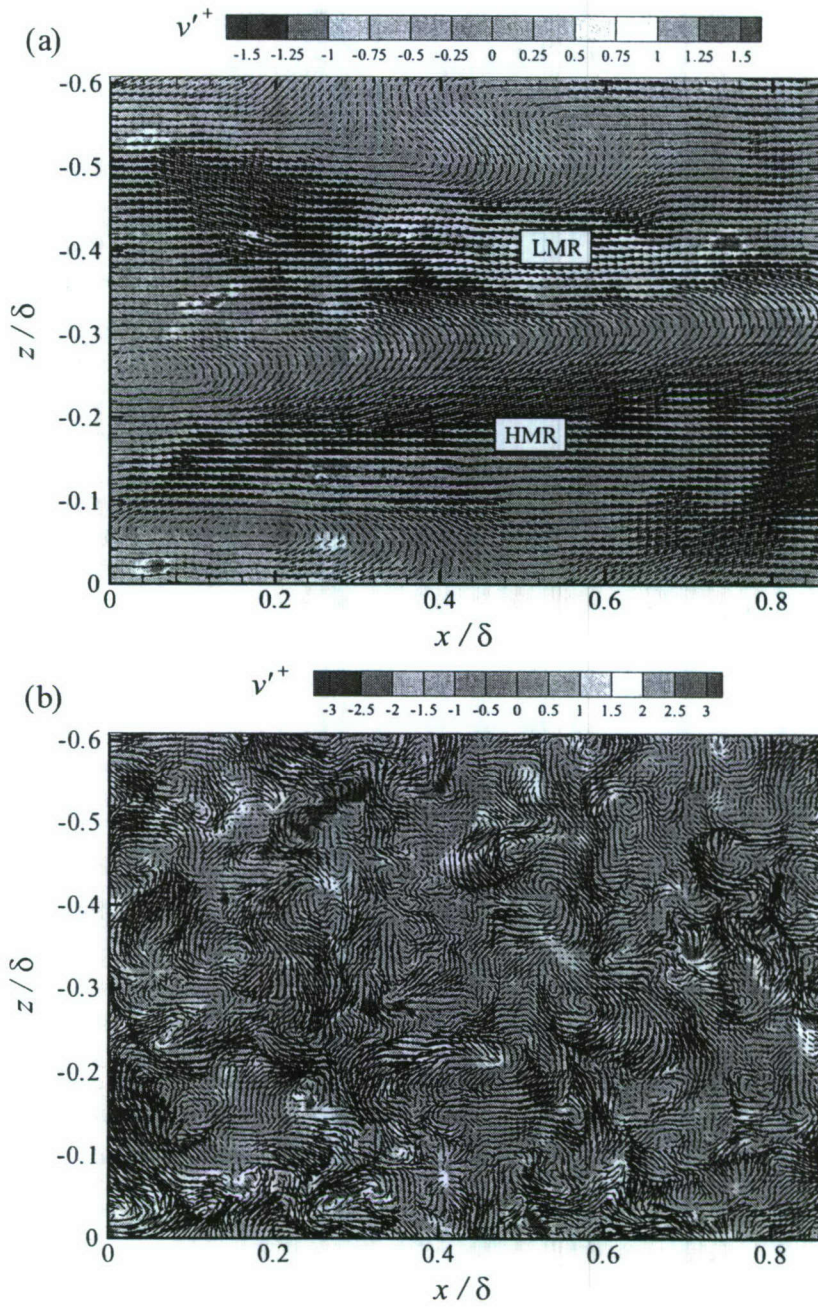


Figure 99: Representative instantaneous (a) low-order and (b) residual velocity fields in the  $x - z$  plane at  $y = 0.065\delta$  for flow over the RF1 surface at  $Re_\theta = 14781$  generated by projecting the instantaneous fluctuating velocity field in figure 47(a) onto the first 22 POD modes. The in-plane velocity components ( $u'^+$ ,  $w'^+$ ) are presented as vectors while the out-of-plane velocity component  $v'^+$  is presented as background contours. Not every vector is shown for clarity.

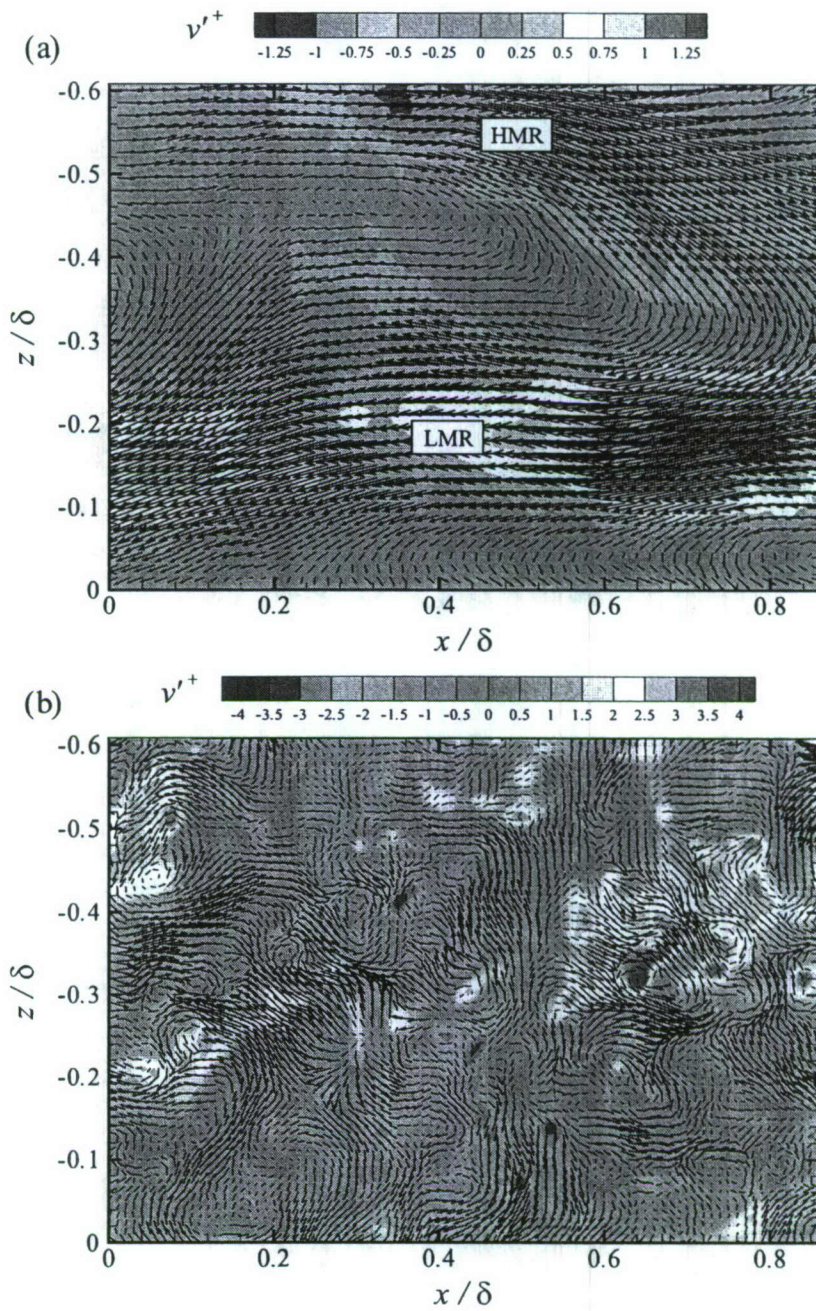


Figure 100: Representative instantaneous (a) low-order and (b) residual velocity fields in the  $x - z$  plane at  $y = 0.15\delta$  for flow over the smooth wall at  $Re_\theta = 11943$  generated by projecting the instantaneous fluctuating velocity field in figure 49(a) onto the first 15 POD modes. The in-plane velocity components ( $u'^+$ ,  $w'^+$ ) are presented as vectors while the out-of-plane velocity component  $v'^+$  is presented as background contours. Not every vector is shown for clarity.

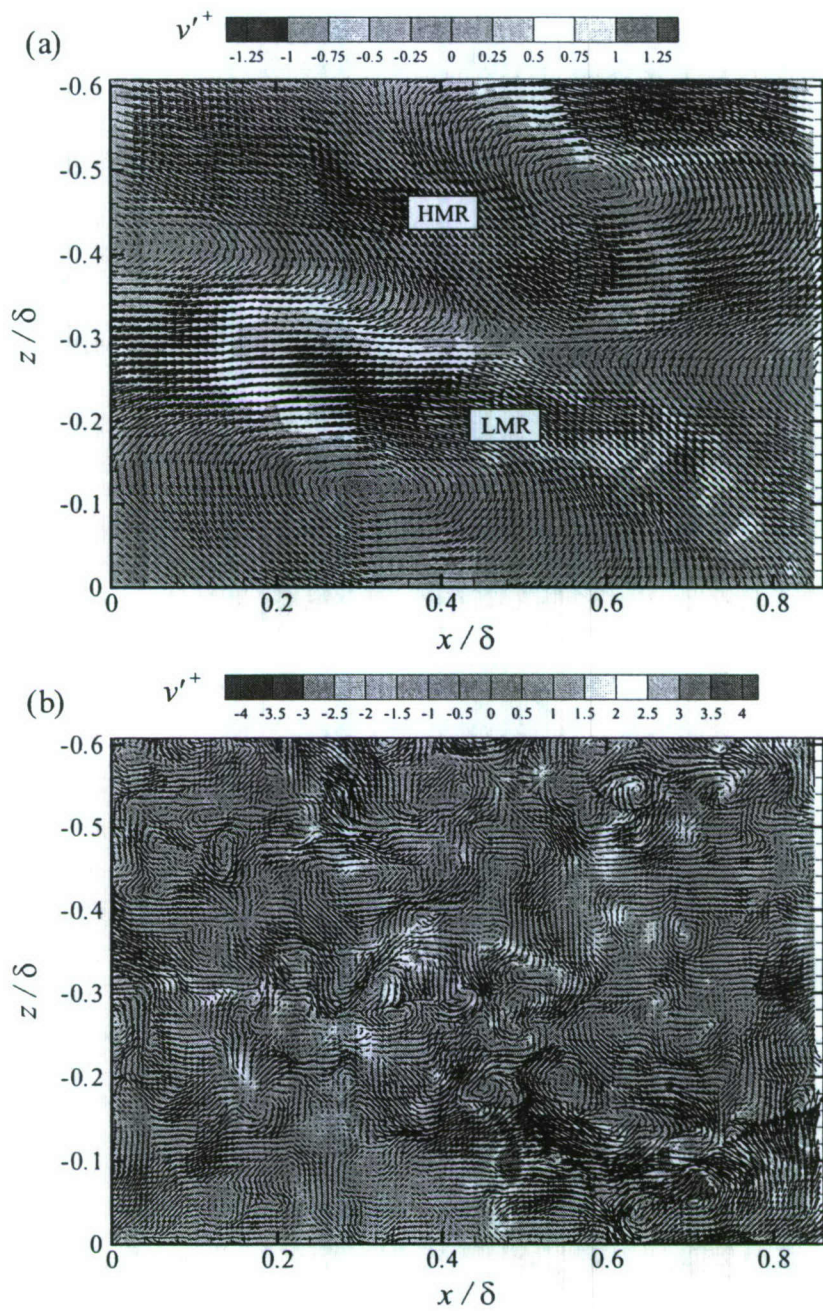
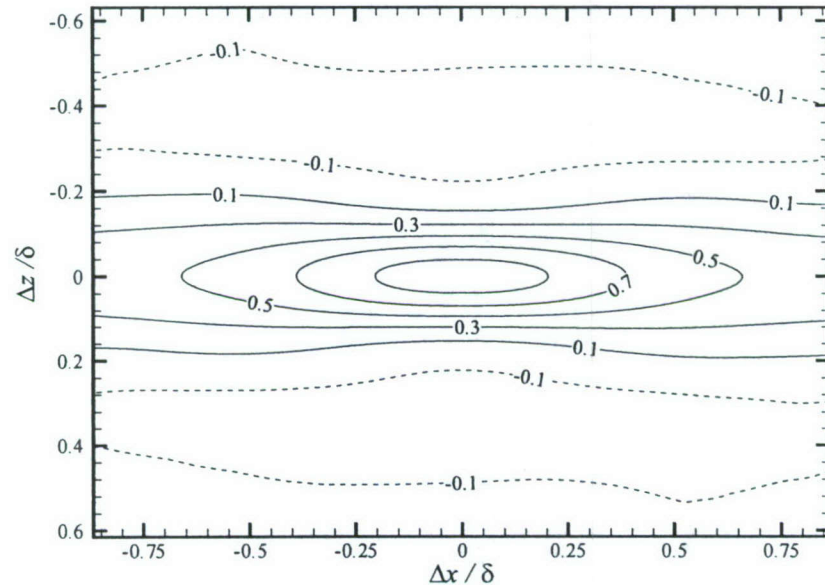


Figure 101: Representative instantaneous (a) low-order and (b) residual velocity fields in the  $x - z$  plane at  $y = 0.15\delta$  for flow over the RF1 surface at  $Re_\theta = 14781$  generated by projecting the instantaneous fluctuating velocity field in figure 51(a) onto the first 16 POD modes. The in-plane velocity components ( $u'^+$ ,  $w'^+$ ) are presented as vectors while the out-of-plane velocity component  $v'^+$  is presented as background contours. Not every vector is shown for clarity.

(a)



(b)

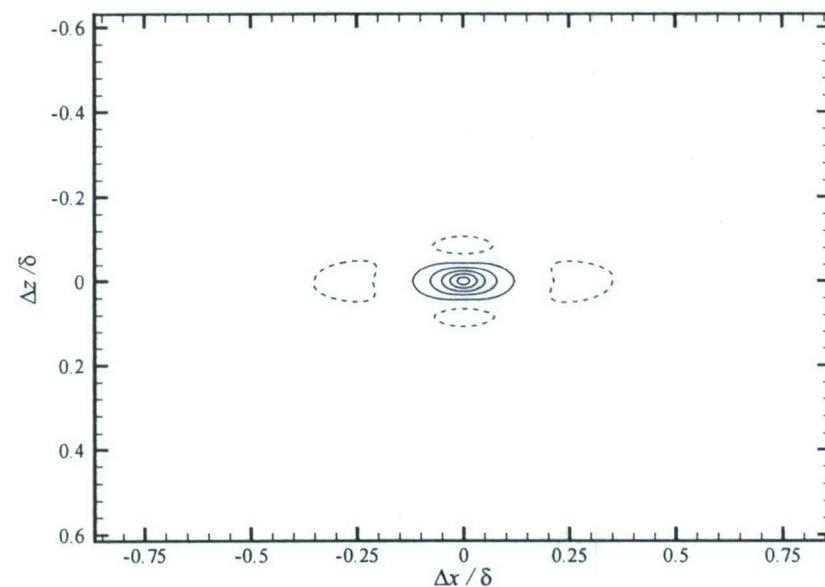


Figure 102: Streamwise velocity correlation coefficients in the  $x - z$  plane at  $y = 0.065\delta$  for flow over the smooth wall at  $Re_\theta \approx 13000$ . (a)  $\rho_{u_L u_L}$ ; (b)  $\rho_{u_R u_R}$ . Contour levels from -0.1 to 0.9 with an interval of 0.2.

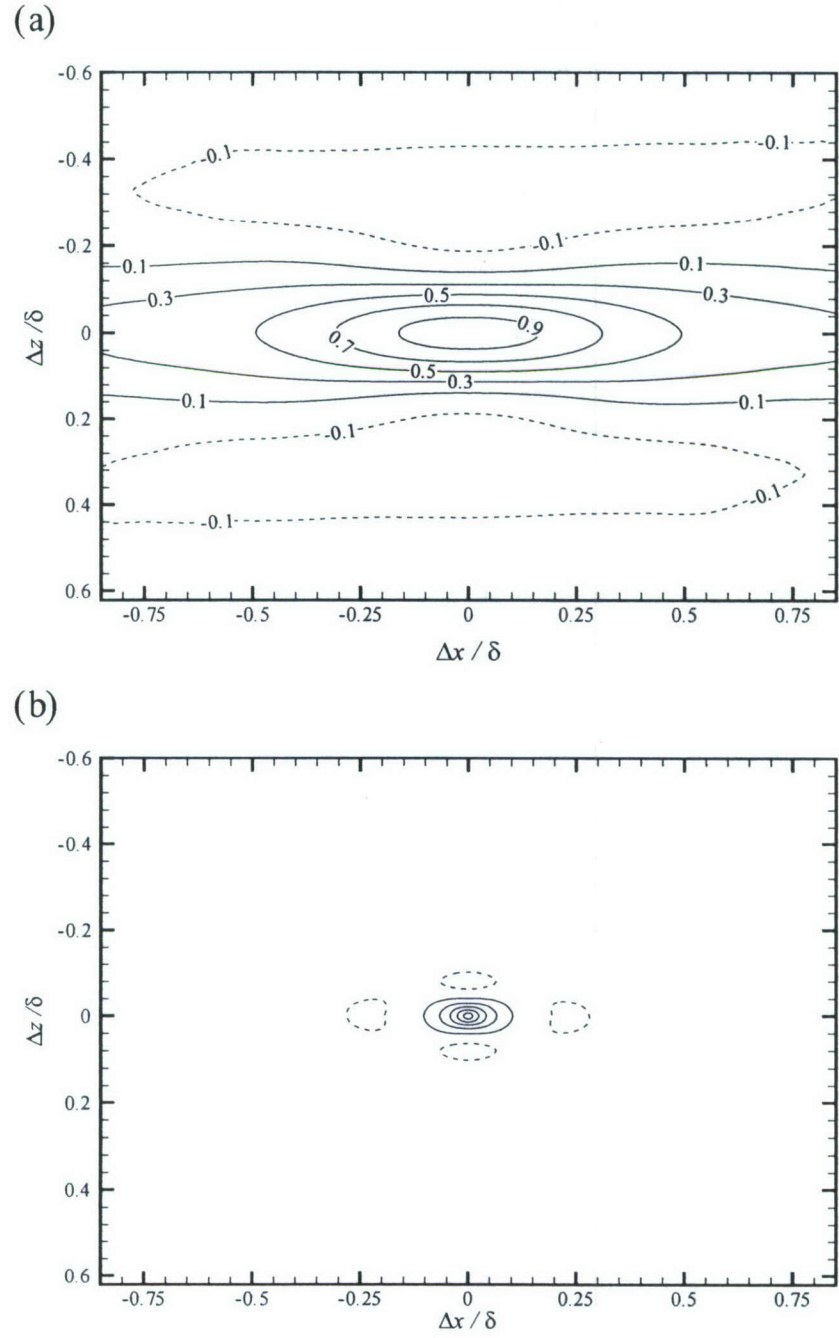


Figure 103: Streamwise velocity correlation coefficients in the  $x - z$  plane at  $y = 0.065\delta$  for flow over the RF1 surface at  $\text{Re}_\theta \approx 13000$ . (a)  $\rho_{u_L u_L}$ ; (b)  $\rho_{u_R u_R}$ . Contour levels from -0.1 to 0.9 with an interval of 0.2.

Table 9: Contributions to the Reynolds normal and shear stresses computed from the low-order and residual velocity ensembles for flow over the smooth and RF1 surfaces at  $y = 0.065\delta$  and  $y = 0.15\delta$  for  $\text{Re}_\theta \approx 13000$ .

Reynolds stress	Surface	$y = 0.065\delta$		$y = 0.15\delta$	
		Low-Model	Residual	Low-Model	Residual
$\langle u'^2 \rangle^+$	Smooth	3.43	1.65	3.08	1.38
	RF1	2.76	1.3	2.64	1.13
$\langle v'^2 \rangle^+$	Smooth	0.12	1.05	0.17	1.15
	RF1	0.13	1.04	0.21	1.28
$\langle w'^2 \rangle^+$	Smooth	0.51	1.38	0.59	1.29
	RF1	0.53	1.11	0.61	1.03
$\langle -u'v' \rangle^+$	Smooth	0.48	0.48	0.63	0.35
	RF1	0.47	0.35	0.65	0.26

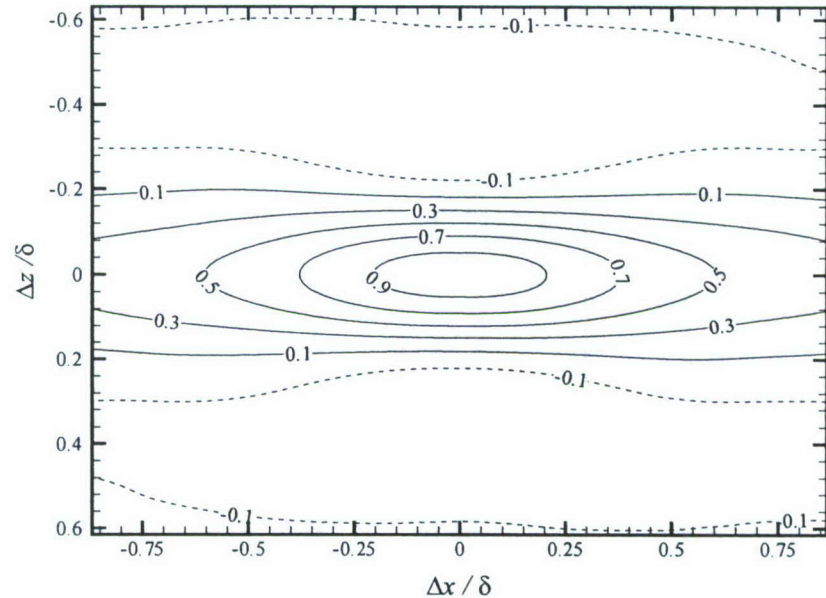
$\rho_{u_L u_L}$  and  $\rho_{u_R u_R}$  in the  $x - z$  plane at  $y = 0.15\delta$  (figures 104 and 105), although their spanwise extents increase slightly compared to their counterparts at  $y = 0.065\delta$ . This spanwise scale growth with increasing wall-normal position is well documented in wall-bounded turbulent flows (Tomkins & Adrian, 2003).

Figure 106 presents one-dimensional profiles of  $\rho_{u_L u_L}$  and  $\rho_{u_R u_R}$  in the streamwise and spanwise directions at  $y = 0.065\delta$ , facilitating comparison of the spatial extents of these correlations for the smooth and RF1 cases at  $\text{Re}_\theta \approx 13000$ . The spanwise extents of  $\rho_{u_L u_L}$  and  $\rho_{u_R u_R}$  are quite consistent between the smooth and rough cases. This insensitivity is consistent with the similarity in spanwise extents of  $\rho_{uu}$  computed from the original velocity fields for smooth- and rough-wall flow (figure 55). However, the streamwise extent of  $\rho_{u_L u_L}$  is reduced considerably in the presence of roughness while the streamwise extent of  $\rho_{u_R u_R}$  shows little sensitivity to roughness. Similar trends are noted in the one-dimensional profiles of  $\rho_{u_L u_L}$  and  $\rho_{u_R u_R}$  at  $y = 0.15\delta$  (figure 107), though the reduction in streamwise extent of  $\rho_{u_L u_L}$  in the rough-wall case is weaker at this wall-normal location indicating a decreased influence of roughness away from the surface.

Wall-normal velocity correlation coefficients  $\rho_{v_L v_L}$  and  $\rho_{v_R v_R}$  for flow over the smooth and RF1 surfaces at  $\text{Re}_\theta \approx 13000$  at  $y = 0.065\delta$  and  $y = 0.15\delta$  are presented in figures 108–111. All  $\rho_{v_L v_L}$  cases are elongated in the streamwise direction and flanked by weaker negative correlation regions in the spanwise direction. These patterns are entirely consistent with the spanwise-alternating large-scale regions of ejections and sweeps noted in the instantaneous low-order velocity fields in the  $x - z$  plane at both wall-normal locations. In contrast,  $\rho_{v_R v_R}$  is quite compact spatially, indicative of the strong influence of small-scale flow features on the wall-normal velocity fluctuations. The spatial extents of  $\rho_{v_L v_L}$  and  $\rho_{v_R v_R}$  are compared via one-dimensional profiles in figures 112 and 113 at  $y = 0.065\delta$  and  $0.15\delta$ , respectively. Consistent with  $\rho_{u_L u_L}$  and  $\rho_{u_R u_R}$  at  $y = 0.065\delta$ , the spanwise extents of  $\rho_{v_L v_L}$  and  $\rho_{v_R v_R}$  are insensitive to roughness as the smooth and rough cases collapse well. Similar collapse of  $\rho_{v_L v_L}$  and  $\rho_{v_R v_R}$  in the spanwise direction is noted at  $y = 0.15\delta$ . However, the streamwise extent of  $\rho_{v_L v_L}$  is reduced significantly in the presence of roughness at  $y = 0.065\delta$  while the streamwise extent of  $\rho_{v_R v_R}$  shows little sensitivity to roughness. Further from the wall at  $y = 0.15\delta$ , both  $\rho_{v_L v_L}$  and  $\rho_{v_R v_R}$  appear insensitive to roughness effects as the smooth- and rough-wall profiles collapse in all cases.

Finally, spanwise velocity correlation coefficients  $\rho_{w_L w_L}$  and  $\rho_{w_R w_R}$  at  $y = 0.065\delta$  are presented

(a)



(b)

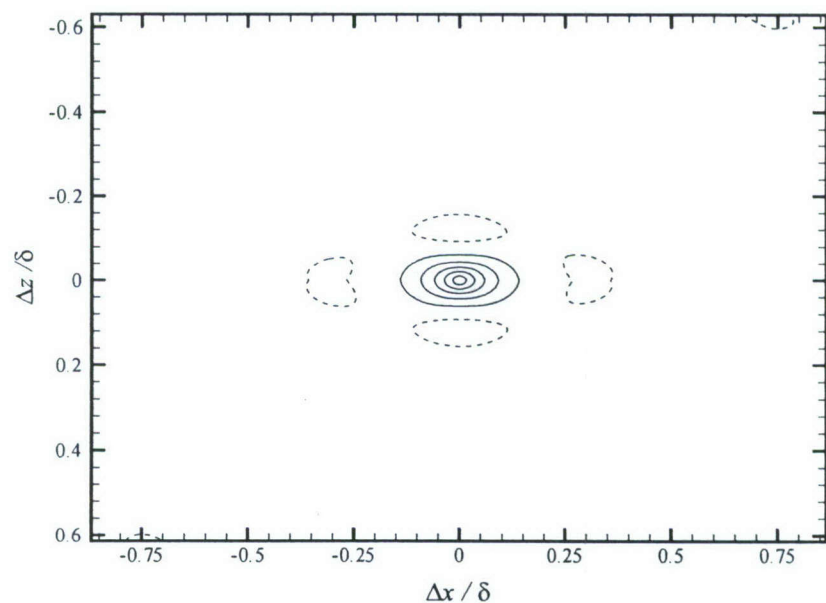
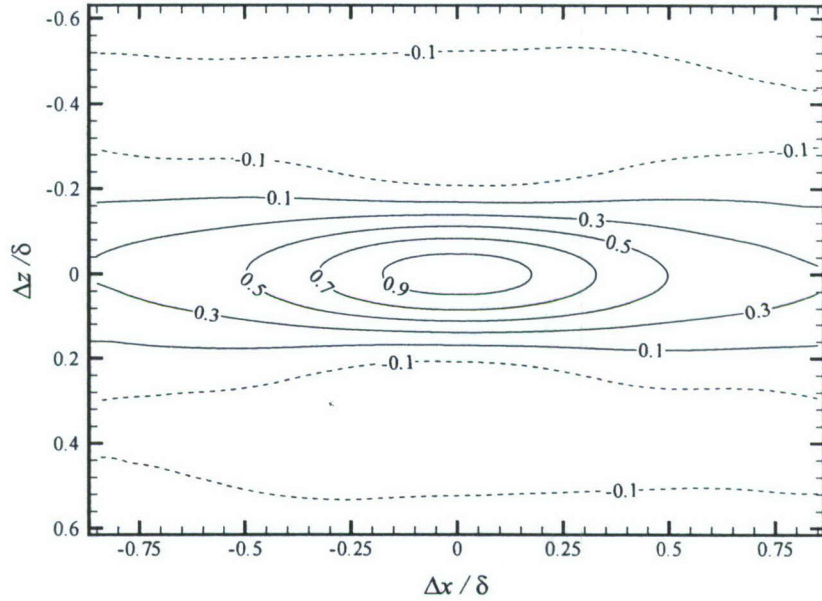


Figure 104: Streamwise velocity correlation coefficients in the  $x - z$  plane at  $y = 0.15\delta$  for flow over the smooth wall at  $\text{Re}_\theta \approx 13000$ . (a)  $\rho_{u_L u_L}$ ; (b)  $\rho_{u_R u_R}$ . Contour levels from -0.1 to 0.9 with an interval of 0.2.

(a)



(b)

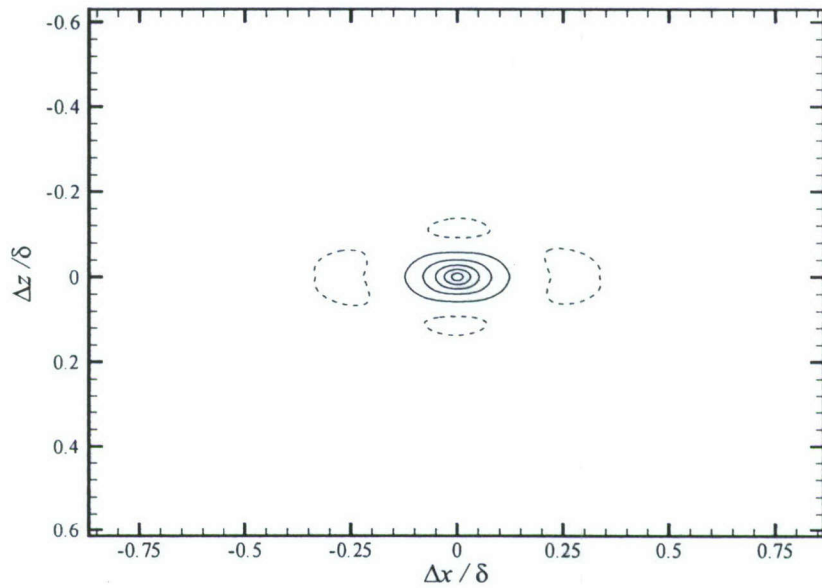


Figure 105: Streamwise velocity correlation coefficients in the  $x - z$  plane at  $y = 0.15\delta$  for flow over the RF1 surface at  $\text{Re}_\theta \approx 13000$ . (a)  $\rho_{u_L u_L}$ ; (b)  $\rho_{u_R u_R}$ . Contour levels from -0.1 to 0.9 with an interval of 0.2.

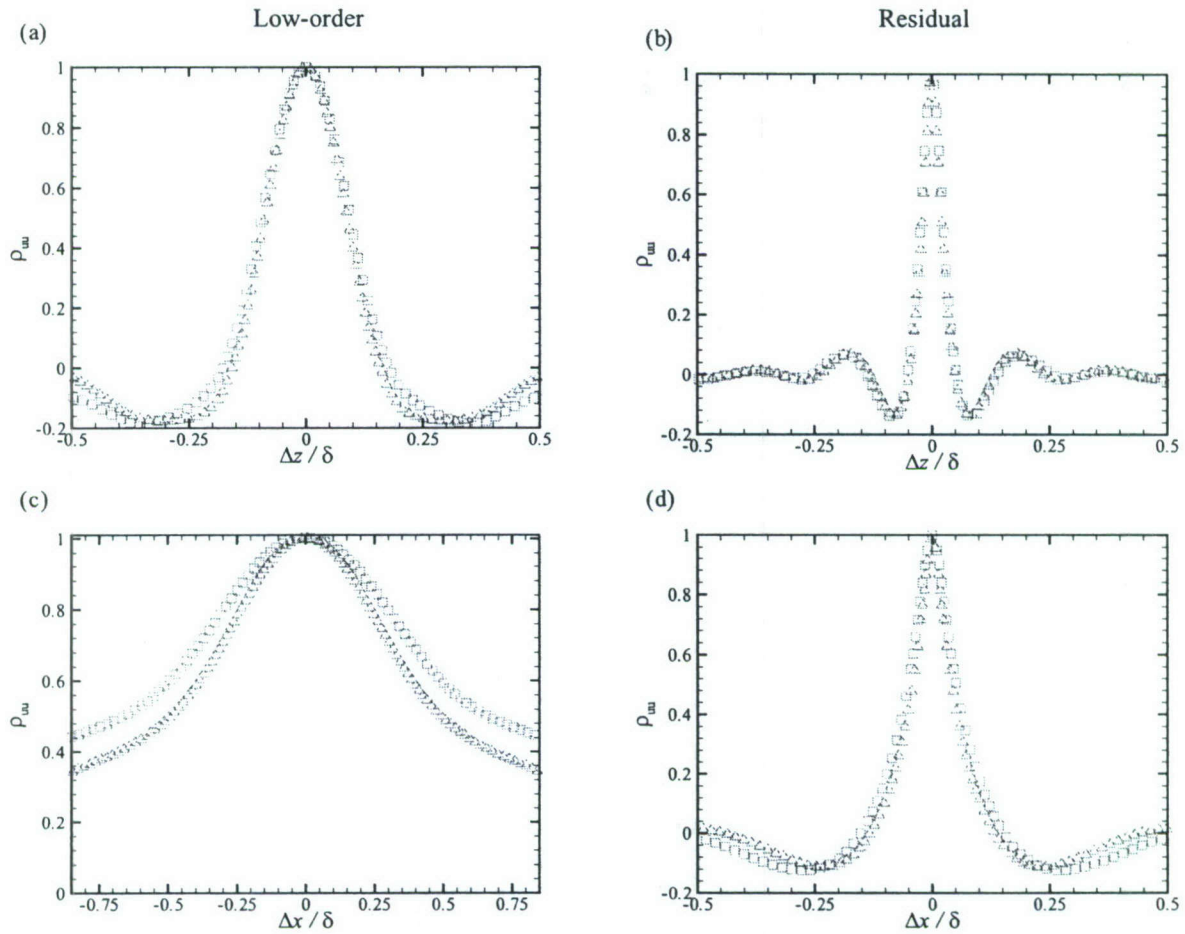


Figure 106: One-dimensional profiles of  $\rho_{u_L u_L}$  and  $\rho_{u_R u_R}$  in the (a, b) spanwise and (c, d) streamwise directions at  $y = 0.065\delta$  for flow over the smooth and RF1 surfaces at  $Re_\theta \approx 13000$ .  $\square$ : Smooth;  $\triangle$ : RF1.

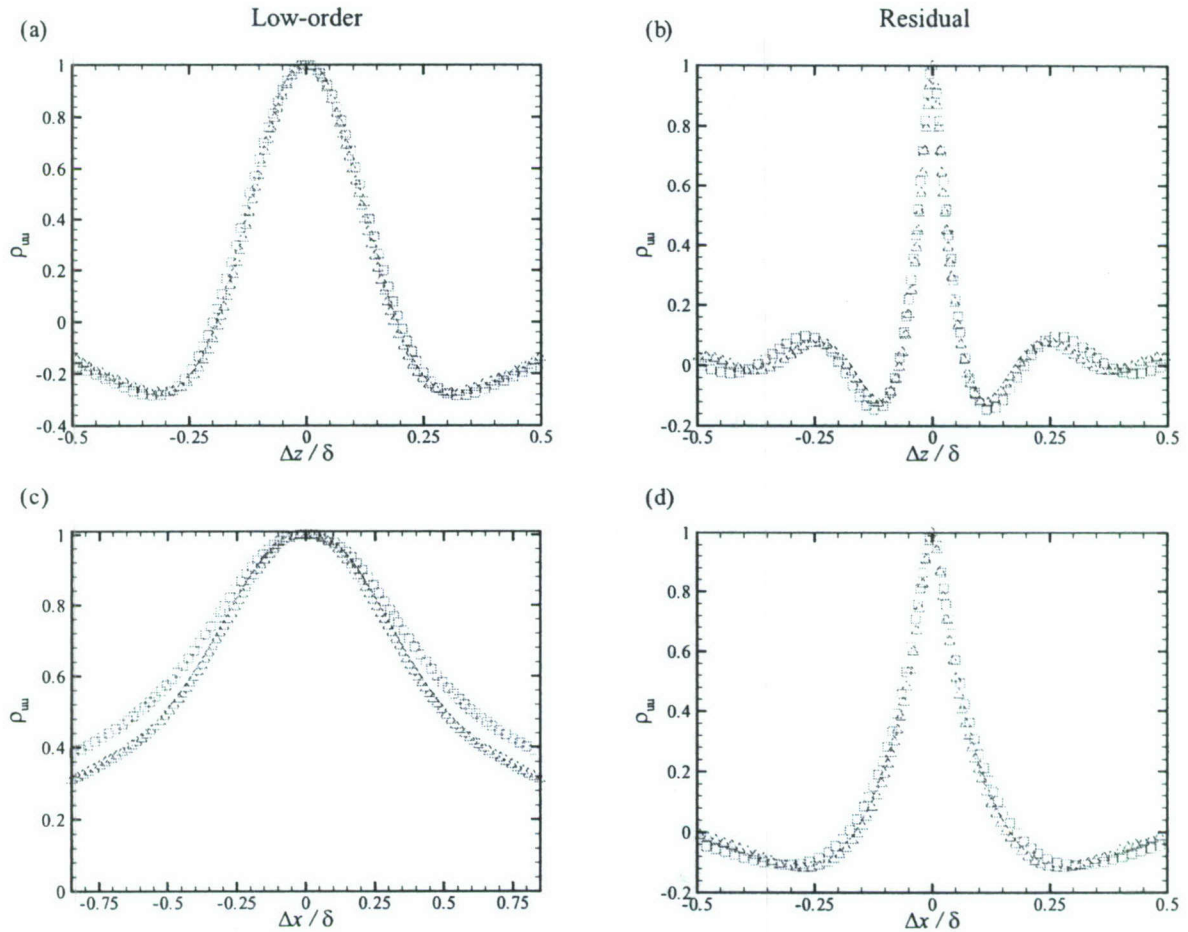


Figure 107: One-dimensional profiles of  $\rho_{u_L u_L}$  and  $\rho_{u_R u_R}$  in the (a, b) spanwise and (c, d) streamwise directions at  $y = 0.15\delta$  for flow over the smooth and RF1 surfaces at  $Re_\theta \approx 13000$ .  $\square$ : Smooth;  $\triangle$ : RF1.

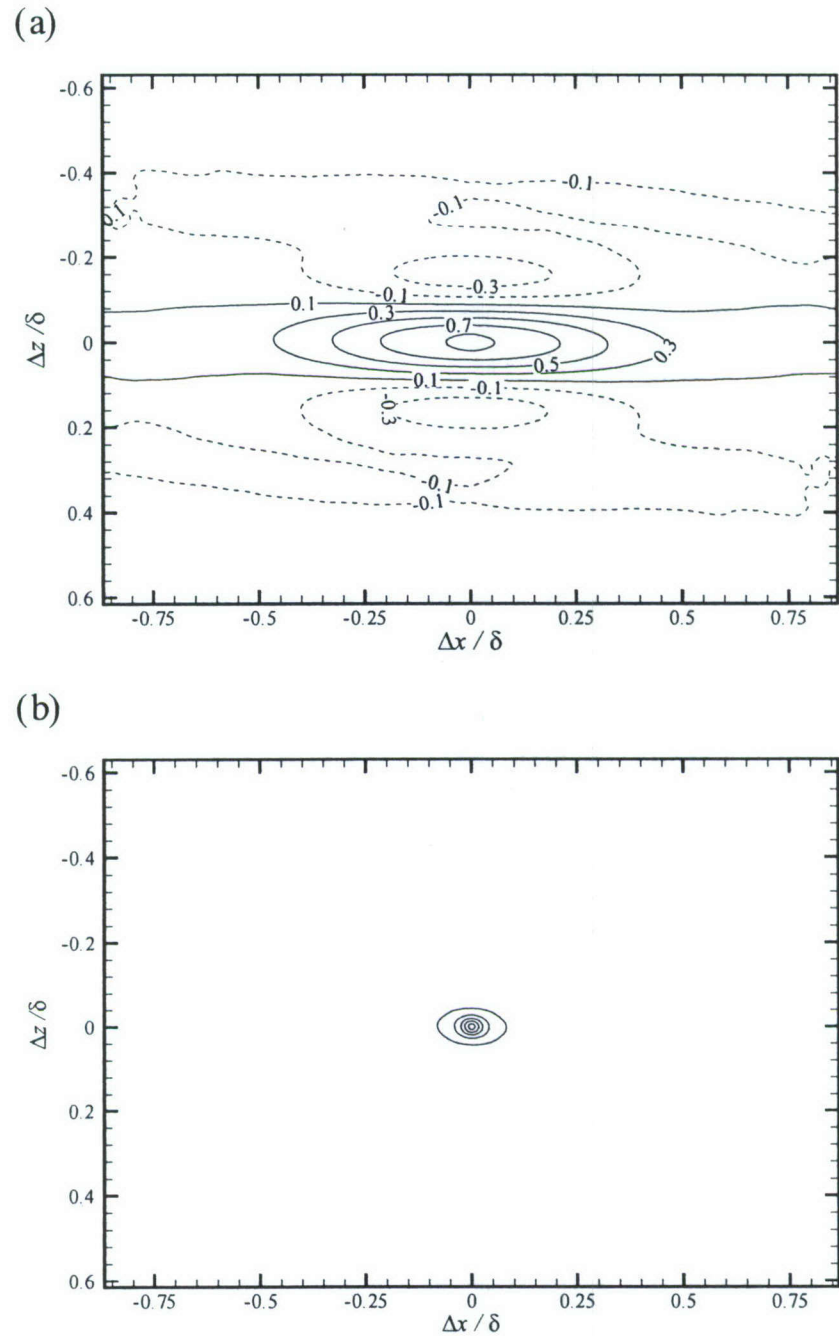
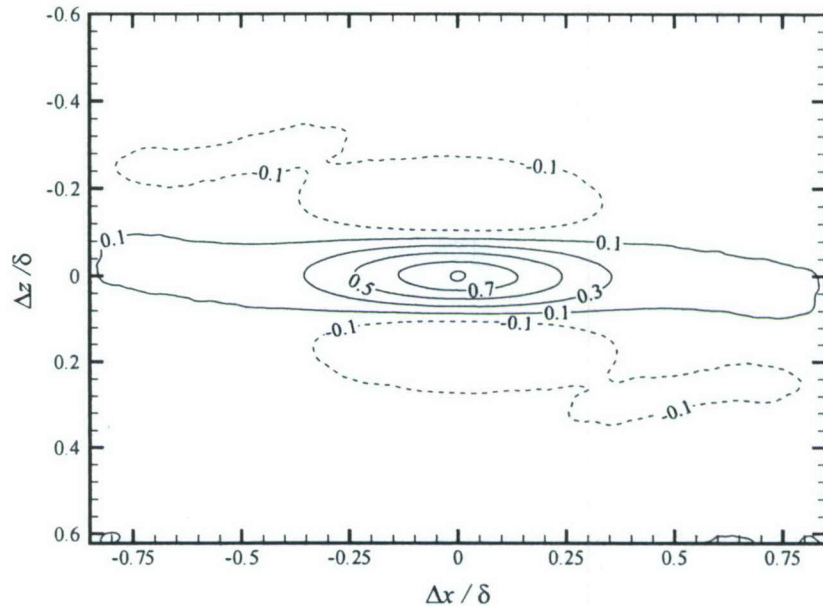


Figure 108: Wall-normal velocity correlation coefficients in the  $x - z$  plane at  $y = 0.065\delta$  for flow over the smooth wall at  $\text{Re}_\theta \approx 13000$ . (a)  $\rho_{v_L} v_L$ ; (b)  $\rho_{v_R} v_R$ . Contour levels from -0.3 to 0.9 with an interval of 0.2 in (a) and from 0.1 to 0.9 with an interval of 0.2 in (b).

(a)



(b)

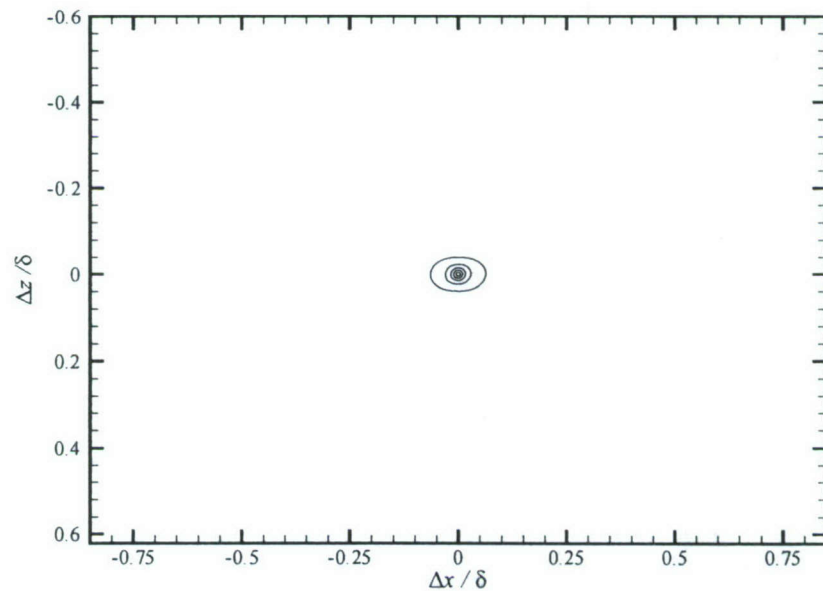
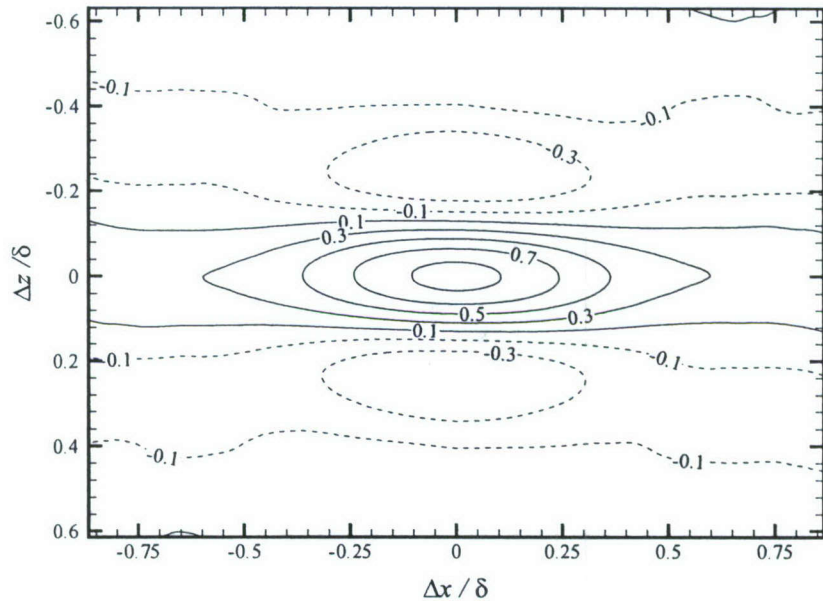


Figure 109: Wall-normal velocity correlation coefficients in the  $x - z$  plane at  $y = 0.065\delta$  for flow over the RF1 surface at  $Re_\theta \approx 13000$ . (a)  $\rho_{v_L v_L}$ ; (b)  $\rho_{v_R v_R}$ . Contour levels from -0.3 to 0.9 with an interval of 0.2 in (a) and from 0.1 to 0.9 with an interval of 0.2 in (b).

(a)



(b)

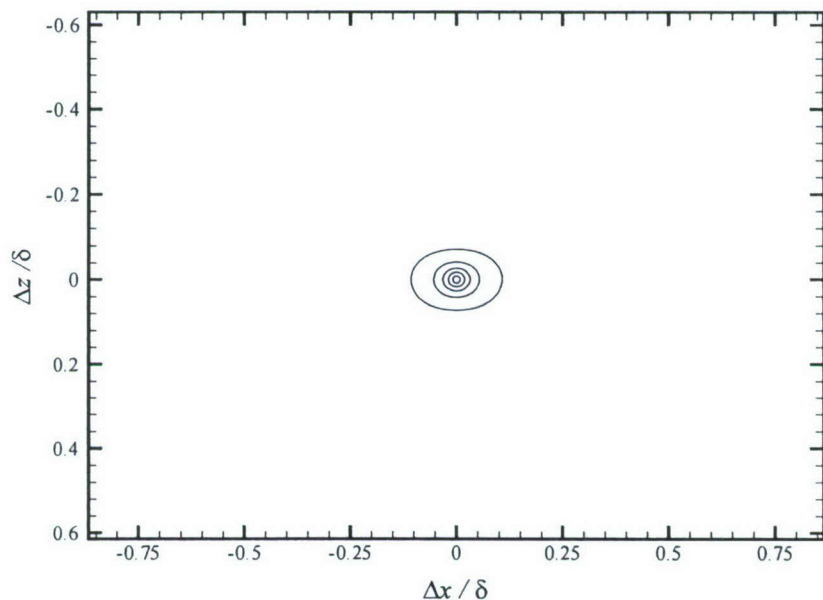
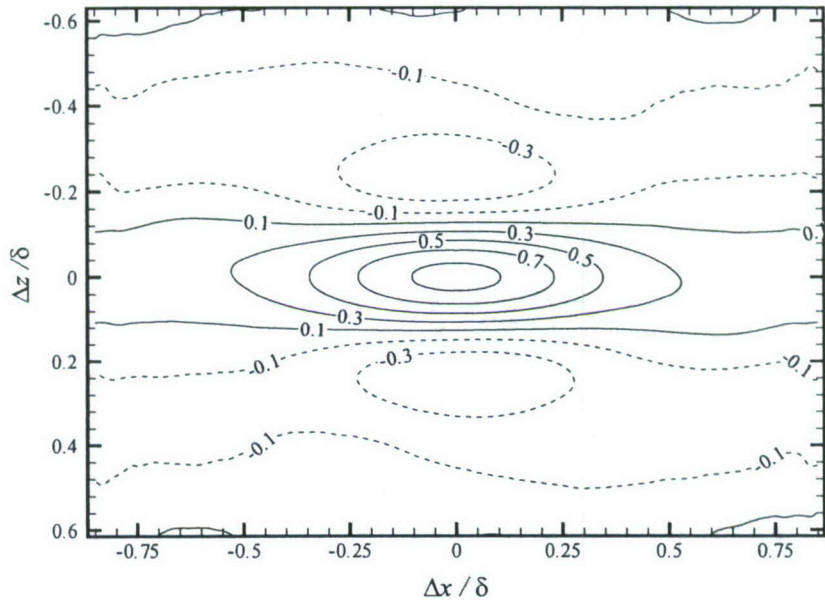


Figure 110: Wall-normal velocity correlation coefficients in the  $x - z$  plane at  $y = 0.15\delta$  for flow over the smooth wall at  $Re_\theta \approx 13000$ . (a)  $\rho_{v_L v_L}$ ; (b)  $\rho_{v_R v_R}$ . Contour levels from -0.3 to 0.9 with an interval of 0.2 in (a) and from 0.1 to 0.9 with an interval of 0.2 in (b).

(a)



(b)

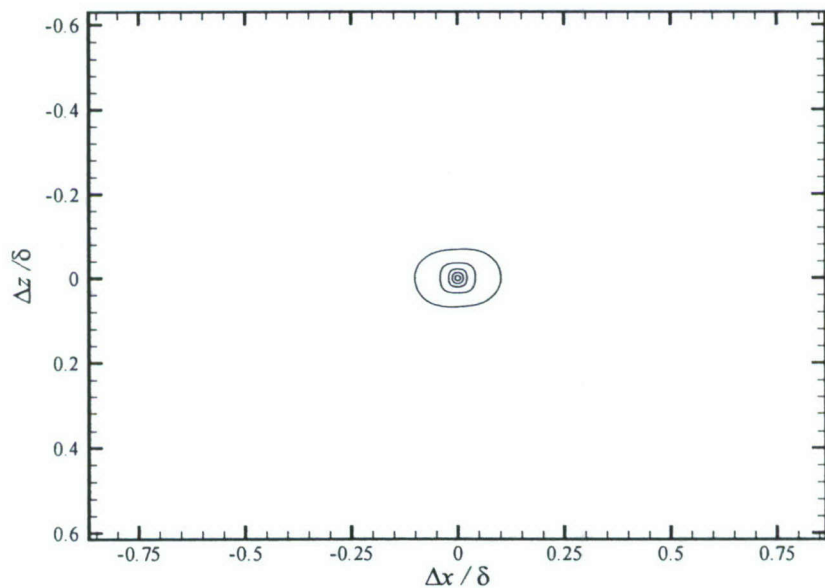


Figure 111: Wall-normal velocity correlation coefficients in the  $x - z$  plane at  $y = 0.15\delta$  for flow over the RF1 surface at  $\text{Re}_\theta \approx 13000$ . (a)  $\rho_{v_L v_L}$ ; (b)  $\rho_{v_R v_R}$ . Contour levels from -0.3 to 0.9 with an interval of 0.2 in (a) and from 0.1 to 0.9 with an interval of 0.2 in (b).

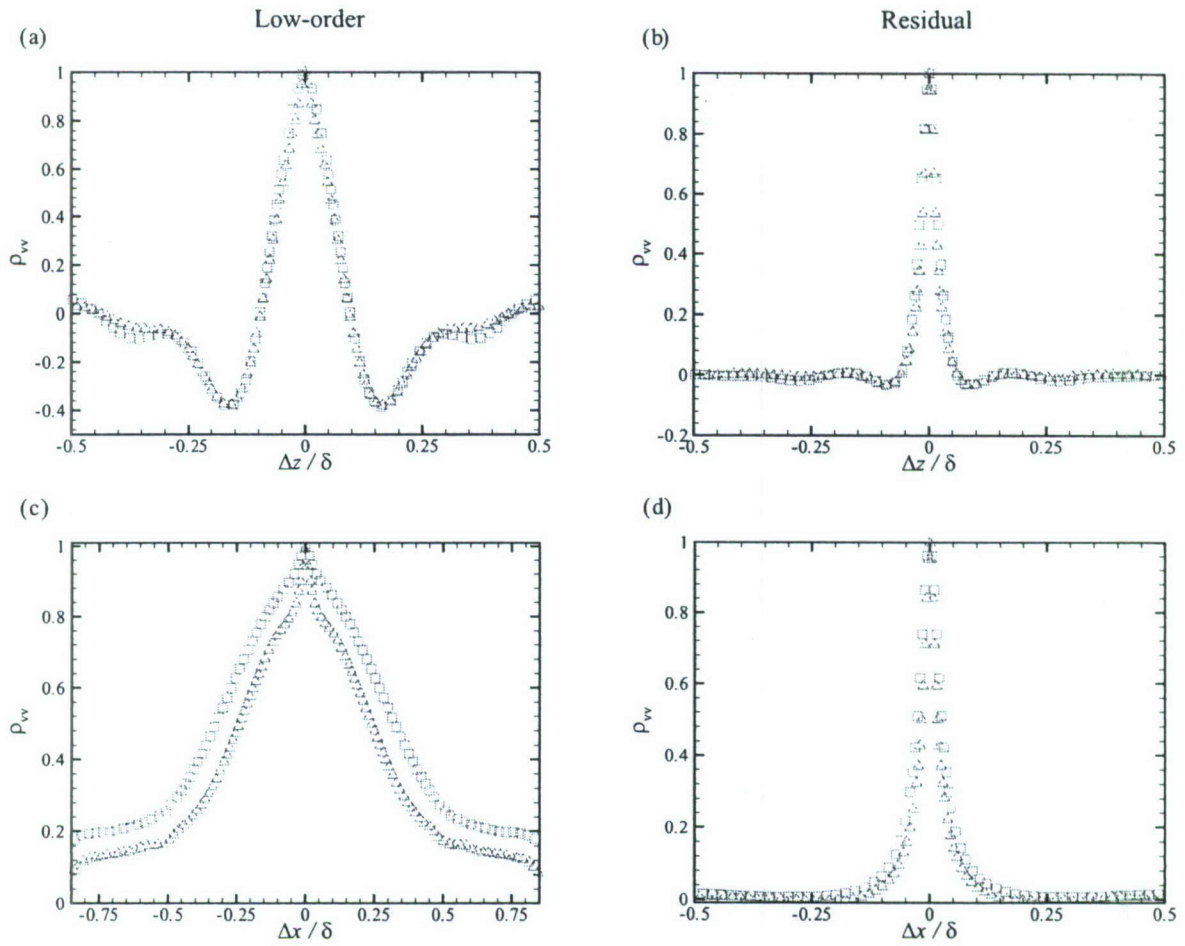


Figure 112: One-dimensional profiles of  $\rho_{v_L v_L}$  and  $\rho_{v_R v_R}$  in the (a, b) spanwise and (c, d) streamwise directions at  $y = 0.065\delta$  for flow over the smooth and RF1 surfaces at  $Re_\theta \approx 13000$ .  $\square$ : Smooth;  $\triangle$ : RF1.

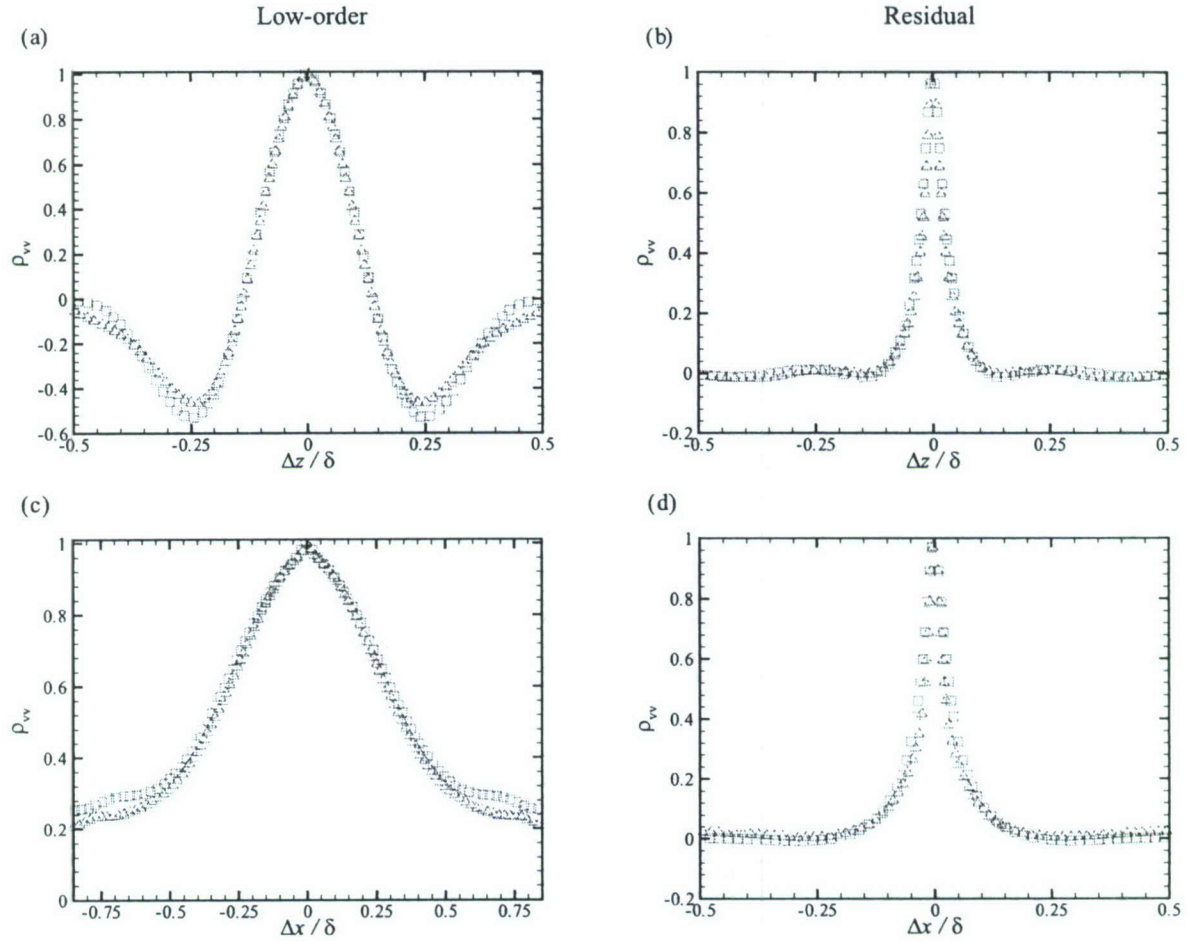


Figure 113: One-dimensional profiles of  $\rho_{v_L v_L}$  and  $\rho_{v_R v_R}$  in the (a, b) spanwise and (c, d) streamwise directions at  $y = 0.15\delta$  for flow over the smooth and RF1 surfaces at  $Re_\theta \approx 13000$ .  $\square$ : Smooth;  $\triangle$ : RF1.

in figures 114 and 115 for flow over the smooth and RF1 surfaces, respectively, at  $\text{Re}_\theta \approx 13000$ . The correlation  $\rho_{w_L w_L}$  is slightly elongated in the streamwise direction for both smooth- and rough-wall flow, particularly closer to the wall at  $y = 0.065\delta$ . In addition, a tendency toward isotropy is noted in  $\rho_{w_L w_L}$  for both smooth- and rough-wall flow at  $y = 0.15\delta$ . On the other hand,  $\rho_{w_R w_R}$  is quite compact and relatively isotropic in spatial character at both wall-normal locations. As presented in Figure 118, one-dimensional profiles of  $\rho_{w_L w_L}$  and  $\rho_{w_R w_R}$  in the spanwise direction show little sensitivity to roughness at both wall-normal locations as the smooth- and rough-wall profiles collapse well. In contrast, the streamwise extent of  $\rho_{w_L w_L}$  is reduced in the presence of roughness, consistent with the reductions in streamwise extent of  $\rho_{u_L u_L}$  and  $\rho_{v_L v_L}$ . Consistent with the streamwise extents of  $\rho_{u_R u_R}$  and  $\rho_{v_R v_R}$ , the streamwise extents of  $\rho_{w_R w_R}$  appear relatively insensitive to roughness at both wall-normal locations. Finally, the rough-wall  $\rho_{w_L w_L}$  in the streamwise direction at  $y = 0.15\delta$  falls below zero and then rises above zero to achieve a secondary positive correlation peak. This pattern is consistent with the imprint of spanwise meandering of the large-scale motions in the logarithmic region of the flow. The absence of this behavior in the smooth-wall case may be indicative of an enhanced spanwise meandering of these large-scale motions in the presence of the RF1 surface.

## 6.5 Conditional averaging

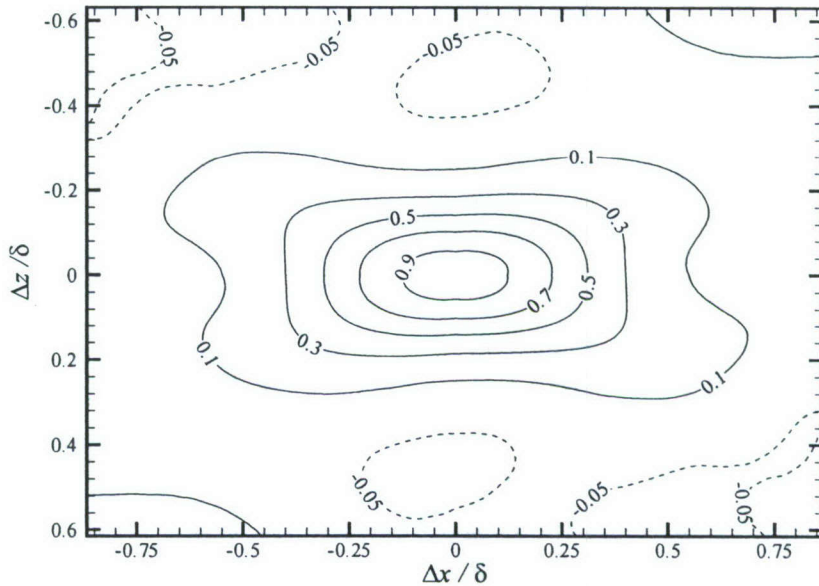
Conditional averaging is a powerful analysis technique in turbulence because it allows one to extract specific features of the flow given a certain event of interest. For example, one can specify a threshold on the magnitude of a  $Q2$  event and assess the average velocity field or swirling strength field associated with this event. In this regard, conditional averaging represents a robust methodology for reducing the complexity of turbulent flows as a means of identifying the most influential features of the flow.

As was seen in the instantaneous velocity realizations presented in figures 45–52, vortical structures bounding LMR’s and HMR’s play a pivotal role in the generation of turbulent stresses, particularly Reynolds shear stress which is intimately tied to the production of turbulence via a coupling between the mean and turbulent kinetic energy equations. Conditional averaging is therefore employed herein to study the average characteristics of velocity and swirling strength events that dominate the generation of Reynolds shear stress via  $Q2$  ( $u' < 0, v' > 0$ ; ejection) and  $Q4$  ( $u' > 0, v' < 0$ ; sweep) motions. Of particular interest is documenting any modifications of these processes in the presence of the RF1 surface.

Conditional averaging is performed both in the streamwise–spanwise planes at  $y = 0.065\delta$  and  $y = 0.15\delta$  as well as the streamwise–wall-normal for flow over the smooth and RF1 surfaces at  $\text{Re}_\theta \approx 13000$ . The analysis presented herein is limited to studying the strongest  $Q2$  and  $Q4$  events, so a threshold of  $|u'(x, y, z)v'(x, y, z)|_Q \geq 4\sigma_u(y)\sigma_v(y)$  is imposed where  $Q$  distinguishes between  $Q2$  and  $Q4$  events based on the signs of  $u'$  and  $v'$  ( $u' < 0, v' > 0$  for  $Q2$  events and  $u' > 0, v' < 0$  for  $Q4$  events). Note that  $\sigma_u$  and  $\sigma_v$  are computed by ensemble-averaging as well as area-averaging each velocity ensemble in the  $x - z$  planes. For analysis in the  $x - y$  plane, these RMS velocities are computed by ensemble- and line-averaging the fields within each ensemble.

With respect to conditional averaging in  $x - z$  planes, each instantaneous velocity realization within an ensemble for a given flow condition is searched for the strongest  $Q2$  and  $Q4$  events that satisfy the threshold. The spatial location where an event satisfying the threshold occurs is referred to as the *event location*. A subregion of the quantity of interest,  $\alpha$  (velocity or swirling strength), centered about the event location is then extracted and this region in the instantaneous field is subsequently masked. Masking ensures that this region will not be searched again so that all samples to the conditional average will be statistically independent. This process continues until no further  $Q2$  or  $Q4$  events larger than the threshold are detected in an ensemble. This procedure

(a)



(b)

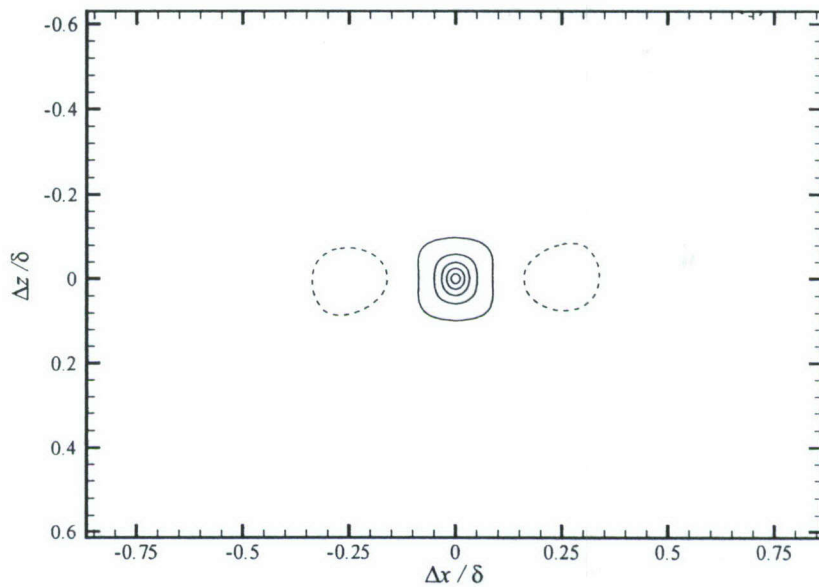


Figure 114: Spanwise velocity correlation coefficients in the  $x - z$  plane at  $y = 0.065\delta$  for flow over the smooth wall at  $\text{Re}_\theta \approx 13000$ . (a)  $\rho_{w_L w_L}$ ; (b)  $\rho_{w_R w_R}$ . Contour levels are -0.05, 0.1, 0.3, 0.5, 0.7, 0.9.

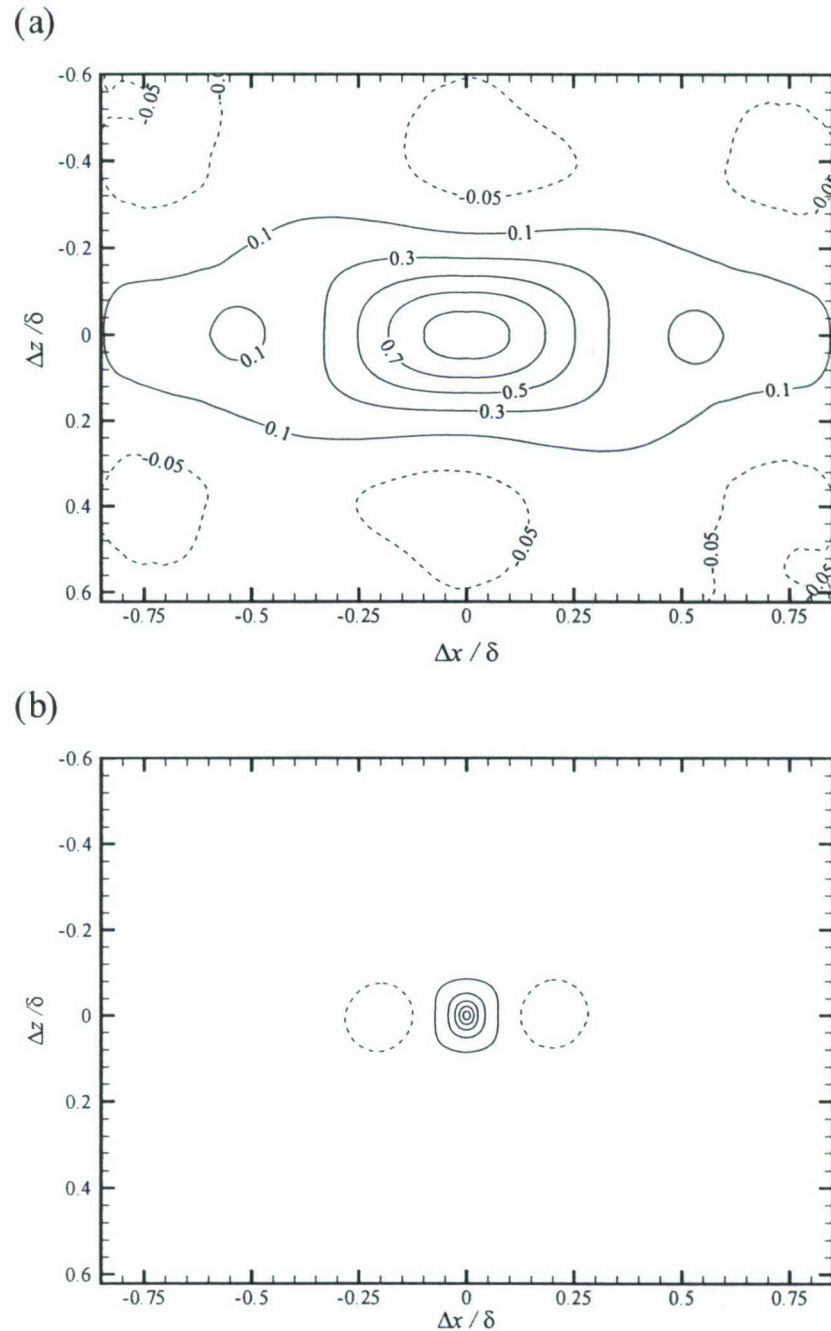


Figure 115: Spanwise velocity correlation coefficients in the  $x - z$  plane at  $y = 0.065\delta$  for flow over the RF1 surface at  $\text{Re}_\theta \approx 13000$ . (a)  $\rho_{w_L w_L}$ ; (b)  $\rho_{w_R w_R}$ . Contour levels are -0.05, 0.1, 0.3, 0.5, 0.7, 0.9.

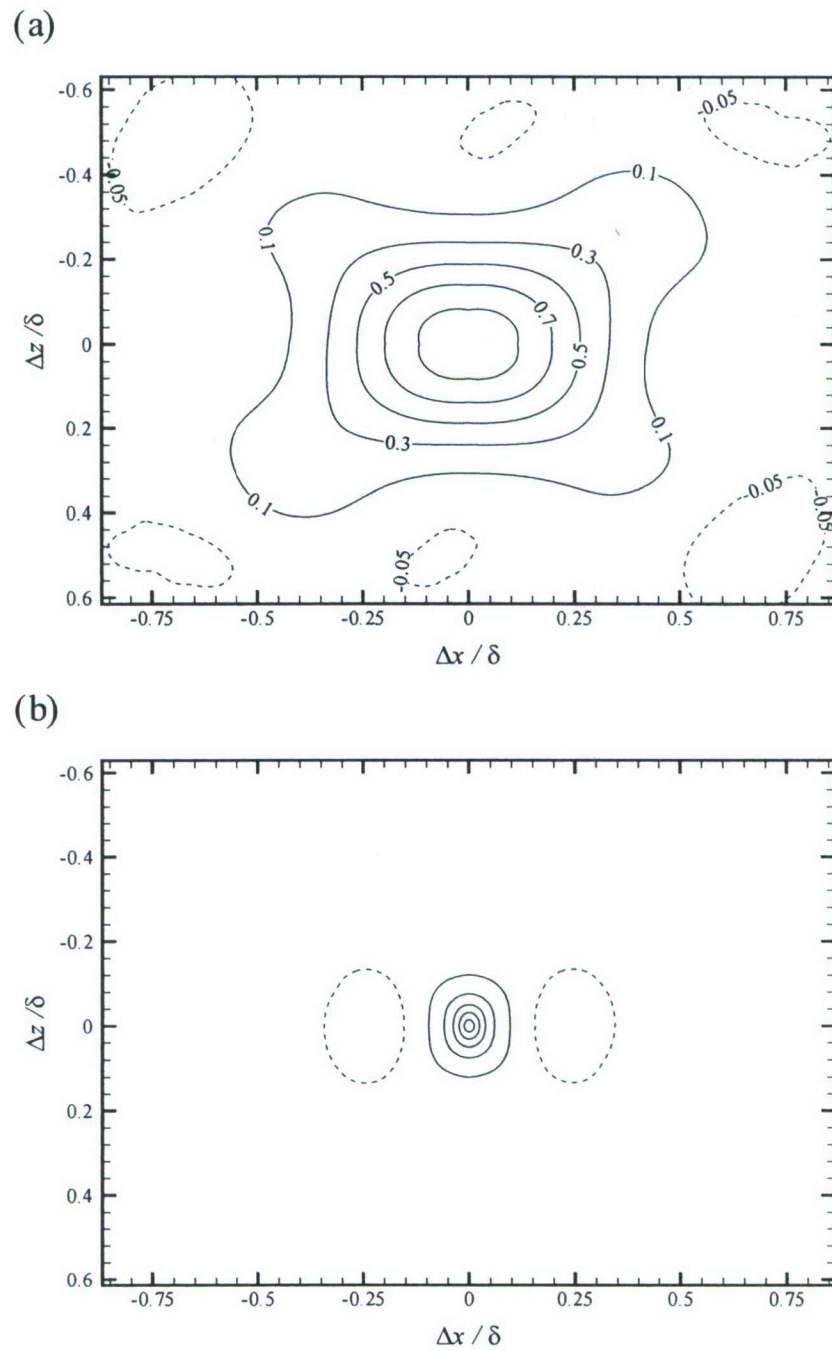


Figure 116: Spanwise velocity correlation coefficients in the  $x - z$  plane at  $y = 0.15\delta$  for flow over the smooth wall at  $\text{Re}_\theta \approx 13000$ . (a)  $\rho_{w_L w_L}$ ; (b)  $\rho_{w_R w_R}$ . Contour levels are -0.05, 0.1, 0.3, 0.5, 0.7, 0.9.

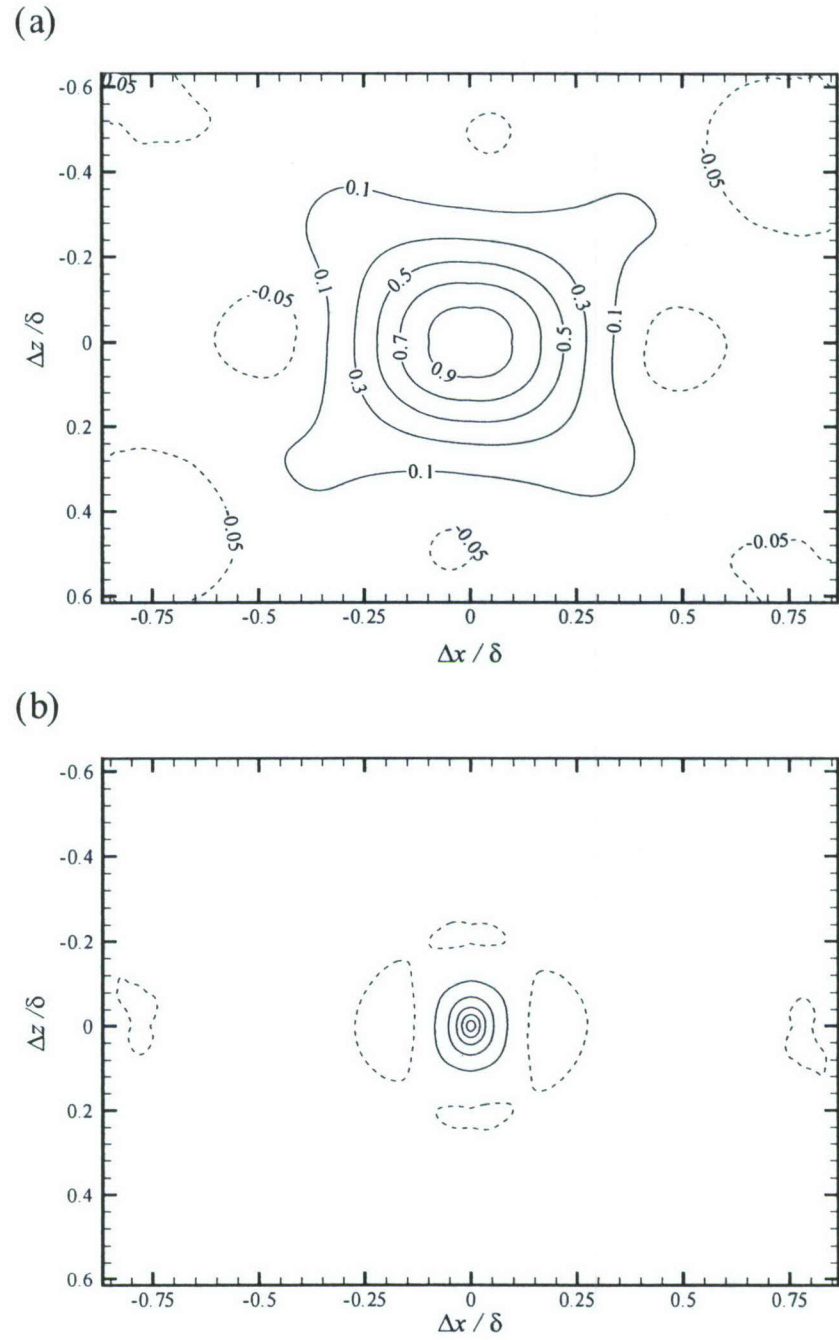


Figure 117: Spanwise velocity correlation coefficients in the  $x - z$  plane at  $y = 0.15\delta$  for flow over the RF1 surface at  $\text{Re}_\theta \approx 13000$ . (a)  $\rho_{w_L w_L}$ ; (b)  $\rho_{w_R w_R}$ . Contour levels are -0.05, 0.1, 0.3, 0.5, 0.7, 0.9.

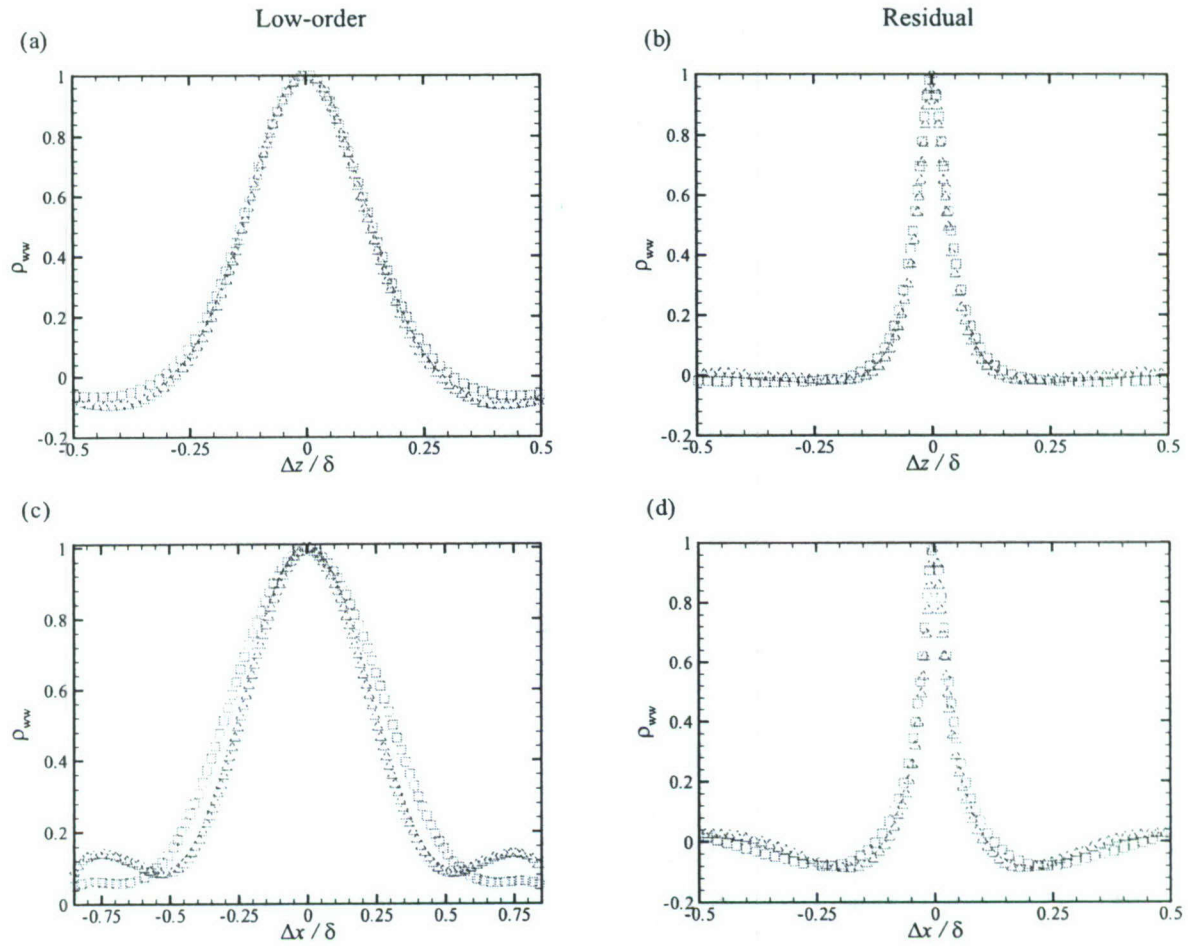


Figure 118: One-dimensional profiles of  $\rho_{w_L w_L}$  and  $\rho_{w_R w_R}$  in the (a, b) spanwise and (c, d) streamwise directions at  $y = 0.065\delta$  for flow over the smooth and RF1 surfaces at  $Re_\theta \approx 13000$ . ■: Smooth; △: RF1.

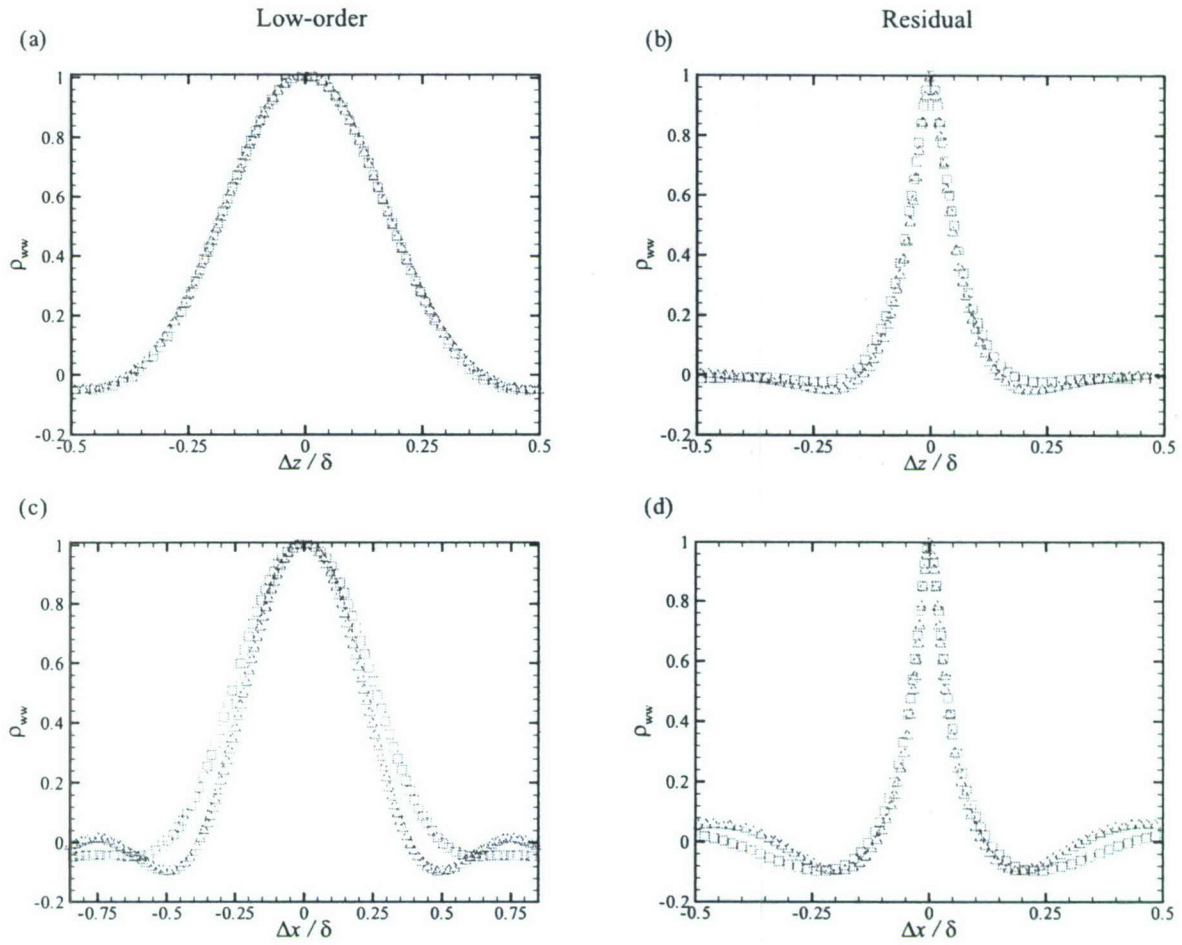


Figure 119: One-dimensional profiles of  $\rho_{w_L w_L}$  and  $\rho_{w_R w_R}$  in the (a, b) spanwise and (c, d) streamwise directions at  $y = 0.15\delta$  for flow over the smooth and RF1 surfaces at  $Re_\theta \approx 13000$ .  $\square$ : Smooth;  $\triangle$ : RF1.

generates  $N$  samples for inclusion in the conditional average which can be expressed as

$$\left\langle \alpha \left| u'(x, z; y) v'(x, z; y) \right|_Q \geq 4\sigma_u(y)\sigma_v(y) \right\rangle (\Delta x, \Delta z; y) = \frac{1}{N} \sum_{j=1}^N \alpha_j(\Delta x + x_o, \Delta z + z_o; y), \quad (59)$$

where  $\Delta x$  and  $\Delta z$  are spatial separations in the streamwise and spanwise directions relative to the event location  $(x_o, z_o; y)$  at which the threshold is met and  $\alpha_j$  is the quantity of interest over a subregion associated with the  $j^{th}$  identified event location. In a similar manner, the conditional average of a quantity of interest,  $\alpha$  can be expressed as

$$\left\langle \alpha \left| u'(x, y_{\text{ref}}) v'(x, y_{\text{ref}}) \right|_Q \geq 4\sigma_u(y_{\text{ref}})\sigma_v(y_{\text{ref}}) \right\rangle (\Delta x, \Delta y; y_{\text{ref}}) = \frac{1}{N} \sum_{j=1}^N \alpha_j(\Delta x + x_o, \Delta y + y_{\text{ref}}; y_{\text{ref}}), \quad (60)$$

where  $y_{\text{ref}}$  represents the wall-normal location of the identified events and  $\Delta y$  is the wall-normal distance relative to the event location  $(x_o, y_{\text{ref}})$ .

### 6.5.1 Q2 events

Figure 120 presents the conditionally-averaged fluctuating velocity fields associated with intense Q2 events (ejections of low-speed fluid away from the wall) for flow over the smooth and RF1 surfaces in the  $x - z$  planes at  $y = 0.065\delta$  and  $y = 0.15\delta$  for  $\text{Re}_\theta \approx 13000$ . Instantaneous evidence (figures 45–52) indicates that intense ejections occur within streamwise-elongated LMR's in the  $x - z$  plane at both  $y = 0.065\delta$  and  $0.15\delta$  for smooth- and rough-wall flows. These conditionally-averaged fluctuating velocity fields confirm this inference as they are marked by intense regions of streamwise momentum deficit (spatial imprints of LMR's). Strong positive wall-normal velocity fluctuations are also observed locally around the event location and spatially-coincident with the LMR footprint. It is the combined effect of  $u' < 0$  and  $v' > 0$  at the event location that is responsible for the intense Q2 event identified by the detection procedure. Interestingly, these conditionally-averaged velocity fields both within and at the outer edge of the roughness sublayer show strong qualitative consistency between the smooth- and rough-wall flows. Further, these fields support the notion that the intermittency of occurrence of intense Q2 events is attributable to the small-scale, intermittent character of the wall-normal velocity fluctuations (supported by the spatially-compact character of  $\rho_{vv}$ ). However, it should be noted that the contours of  $v'$  in figure 120 indicate a larger-scale, albeit weaker, region of  $v'$  spatially-coincident with the LMR. This weaker, larger-scale feature in  $v'$  is interpreted as the collectively-induced ejections of multiple vortices in hairpin vortex packets while the intense, smaller-scale region of  $v'$  centered at the event location is more likely attributable to the intense ejection generated locally around the individual vortices. Further, the spanwise extent of these Q2 events increases slightly with wall-normal position in both smooth- and rough-wall flow.

Line contours are included in each plot within figure 120 illustrating the conditionally-averaged swirling-strength field associated with an intense Q2 event. These swirling-strength fields indicate that intense Q2 events are bounded in the spanwise direction by counter-rotating wall-normal vortex cores in both smooth- and rough-wall flow at  $y = 0.065\delta$  and  $0.15\delta$ . This pattern is quite consistent with the notion that hairpin-like structures are primarily responsible for the generation of these intense, intermittent ejections of low-speed fluid away from the wall. Interestingly, the fluctuating velocity fields do not display swirling motions spatially-coincident with the  $\lambda_{ci}$  contours. However, the absence of these swirling patterns in the velocity fields is directly attributable to the fact that these wall-normal vortices do not advect with the mean velocity at this wall-normal location. Removal of an alternate (slower) advection velocity from these velocity fields (not shown for brevity) does indeed reveal counter-rotating swirling patterns in the velocity fields that are

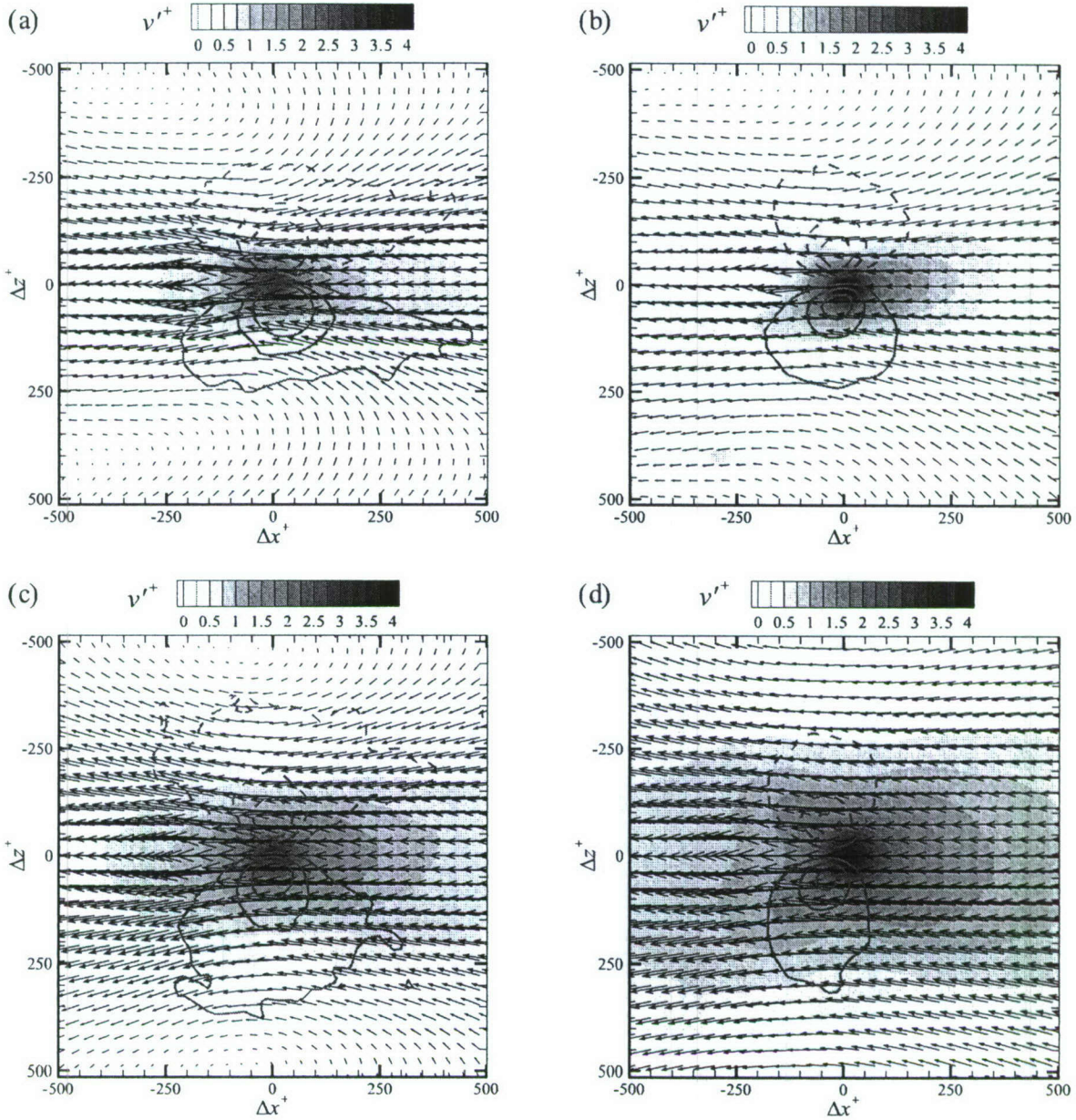


Figure 120: Conditionally-averaged fluctuating velocity fields given an intense  $Q2$  event in the  $x - z$  plane at (a, b)  $y = 0.065\delta$  and (c, d)  $y = 0.15\delta$  at  $Re_\theta \approx 13000$  for flow over the smooth and RF1 surfaces, respectively. The streamwise and spanwise velocity components,  $u$  and  $w$ , are shown as vectors and the wall-normal velocity component,  $v$ , is shown by gray-scale contours. Line contours are also overlaid illustrating the associated conditionally-averaged swirling strength field given an intense  $Q2$  event (dashed lines represent negative contour levels).

spatially-coincident with the patches of  $\lambda_{ci}$ . Finally, while the conditionally-averaged  $\lambda_{ci}$  fields indicate the presence of equal strength, counter-rotating pairs bounding the  $Q2$  events in the spanwise direction (a pattern consistent with slicing through symmetric hairpin structures), this arrangement is simply an artifact of the averaging process utilized to achieve these conditional fields. In reality, as noted earlier, most wall-normal vortices bounding LMR's and HMR's occur in isolation rather than in counter-rotating pairs (Tomkins & Adrian, 2003; Ganapathisubramani *et al.*, 2003), indicating that asymmetric hairpin-like structures are likely to occur more frequently than idealized symmetric vortices (This example serves as an excellent lesson as to the care that must be taken when interpreting patterns observed in conditionally-averaged fields in the context of instantaneous behavior!). Nevertheless, these  $x - z$ -plane fields illustrate strong consistency between the smooth- and rough-wall flows with regard to the structural attributes responsible for the generation of intense  $Q2$  events at  $y = 0.065\delta$  and  $0.15\delta$ .

Conditional averages of the fluctuating velocity field and swirling-strength field based on an intense  $Q2$  event are also computed in the  $x - y$  plane at  $y_{ref} = 0.15\delta$  for flow over the smooth and RF1 surfaces at  $Re_\theta \approx 13000$  ( $x - y$  plane velocity data is not available at  $y = 0.065\delta$  for the RF1 case so conditional averages in this plane are not presented for this wall-normal location). A threshold of  $|u'(x, y_{ref})v'(x, y_{ref})|_Q \geq 4\sigma_u(y_{ref})\sigma_v(y_{ref})$  is employed, consistent with that used in the  $x - z$  plane analysis. The results of this analysis are presented in figure 121 where, as expected, intense ejections of low-speed fluid away from the wall are noted near the event location. The associated conditionally-averaged  $\lambda_{ci}$  fields are overlaid on the conditionally-averaged fluctuating velocity fields and a strong negative region of  $\lambda_{ci}$  is observed downstream and above the  $Q2$  event location. This region of prograde  $\lambda_{ci}$  is interpreted as the imprint of a hairpin vortex head which, coupled with the neck and leg(s) of the hairpin, induces the strong  $Q2$  event at the event location. This pattern is noted in both the smooth- and rough-wall conditional averages at  $y = 0.15\delta$  and, coupled with the patterns noted in the  $x - z$  plane at  $y = 0.15\delta$ , provide strong support for the proposition that hairpin-like structures drive the generation of  $Q2$  events in the smooth- and rough-wall flows under consideration herein.

### 6.5.2 $Q4$ events

Figure 122 presents the conditionally-averaged fluctuating velocity fields given an intense  $Q4$  event in the  $x - z$  plane at  $y = 0.065\delta$  and  $y = 0.15\delta$  for flow over the smooth and RF1 surfaces at  $Re_\theta \approx 13000$ . A streamwise-elongated region of high-momentum fluid is noted and interpreted as the spatial imprint of HMR's. An intense, yet compact region of negative  $v'$  is noted at the event location which, coupled with the HMR behavior, is responsible for the intense  $Q4$  event at the event location. Consistent with the conditionally-averaged fluctuating velocity fields given an intense  $Q2$  event, these fields display a weak, but large-scale region of non-zero (negative here)  $v'$  interpreted as collectively-induced, large-scale sweep motions outboard of hairpin vortex packets. Overlaid on these velocity fields are the associated conditionally-averaged  $\lambda_{ci}$  fields given an intense  $Q4$  event and counter-rotating wall-normal vortex cores are found to bound the  $Q4$  event in the spanwise direction. As noted earlier, this symmetry is simply an artifact of the averaging performed to generate these fields. Nevertheless, these patterns indicate that intense sweep motions likely occur outboard of individual hairpin-like vortices, consistent with the rotational sense of the hairpin legs/neck.

Finally, figure 123 presents the conditionally-averaged fluctuating velocity fields and swirling-strength fields in the  $x - y$  plane given an intense  $Q4$  event at  $y_{ref} = 0.15\delta$  for flow over the smooth and RF1 surfaces at  $Re_\theta \approx 13000$ . As expected, intense sweeps of high-speed fluid toward the wall are noted in the velocity fields for both smooth- and rough-wall flow. The conditionally-averaged  $\lambda_{ci}$  fields indicate the presence of prograde  $\lambda_{ci}$  upstream and below the imposed  $Q4$  event and this

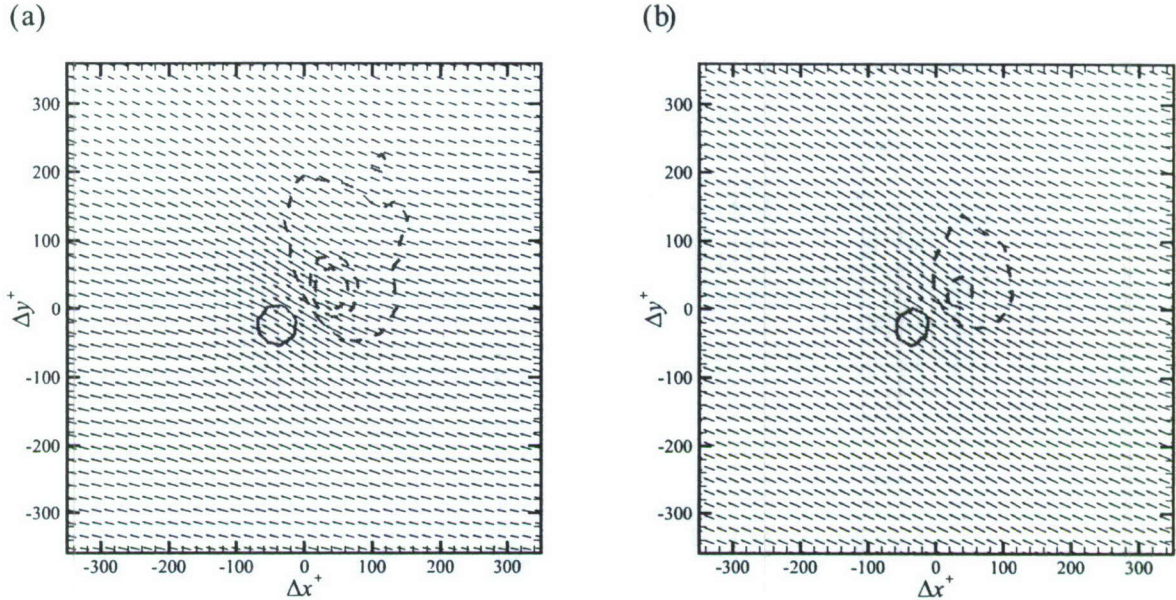


Figure 121: Conditionally-averaged fluctuating velocity fields given an intense  $Q2$  event in the  $x - y$  plane at  $Re_\theta \approx 13000$  for flow over the (a) smooth and (b) RF1 surfaces at  $y = 0.15\delta$ . Line contours are overlaid in each plot illustrating the associated conditionally-averaged swirling strength field given an intense  $Q2$  event (dashed lines represent negative contour levels).

pattern is interpreted as a slice through the head of a hairpin vortex whose induction generates an intense  $Q4$  event downstream and above its core. This behavior is entirely consistent with the clockwise rotation of prograde spanwise vortices and, coupled with the evidence presented in the  $x - z$  plane at  $y = 0.15\delta$ , supports the contention that hairpin-like structures are the primary generator of Reynolds shear stress via  $Q4$  (sweep) events.

## 6.6 Summary

The results presented in this chapter highlight both strong similarities and important differences between the spatial structure of flow over the smooth and RF1 surfaces at  $Re_\theta \approx 13000$ . Instantaneous velocity realizations in both the  $x - y$  and  $x - z$  planes for smooth- and rough-wall flow indicate that large-scale LMR's and HMR's exist in both flows and that these large-scale features generate a vast majority of the turbulent shear stress. In addition, both of these large-scale features are interpreted to be the by-product of hairpin vortex packets, indicating that such structures exist in both the smooth- and rough-wall flows.

Despite the qualitative consistencies noted in the instantaneous realizations of smooth- and rough-wall flow, spatial correlations of velocity in the  $x - y$  and  $x - z$  planes highlight quantitative differences in the spatial character of these flows. In particular, the large-scale streamwise extent of two-point streamwise velocity correlation coefficients,  $\rho_{uu}$ , is reduced in the presence of the RF1 surface, most notably at  $y = 0.065\delta$  which is well within the roughness sublayer. In contrast, the streamwise extents of  $\rho_{vv}$  and  $\rho_{ww}$  appear relatively unaffected by roughness as are the spanwise extents of all three velocity correlation coefficients. Previous studies have highlighted the imprints of hairpin vortex packets on the two-point velocity correlations, particularly the consistency between the long streamwise extent of  $\rho_{uu}$  and the streamwise length scales of hairpin packets. As such, the

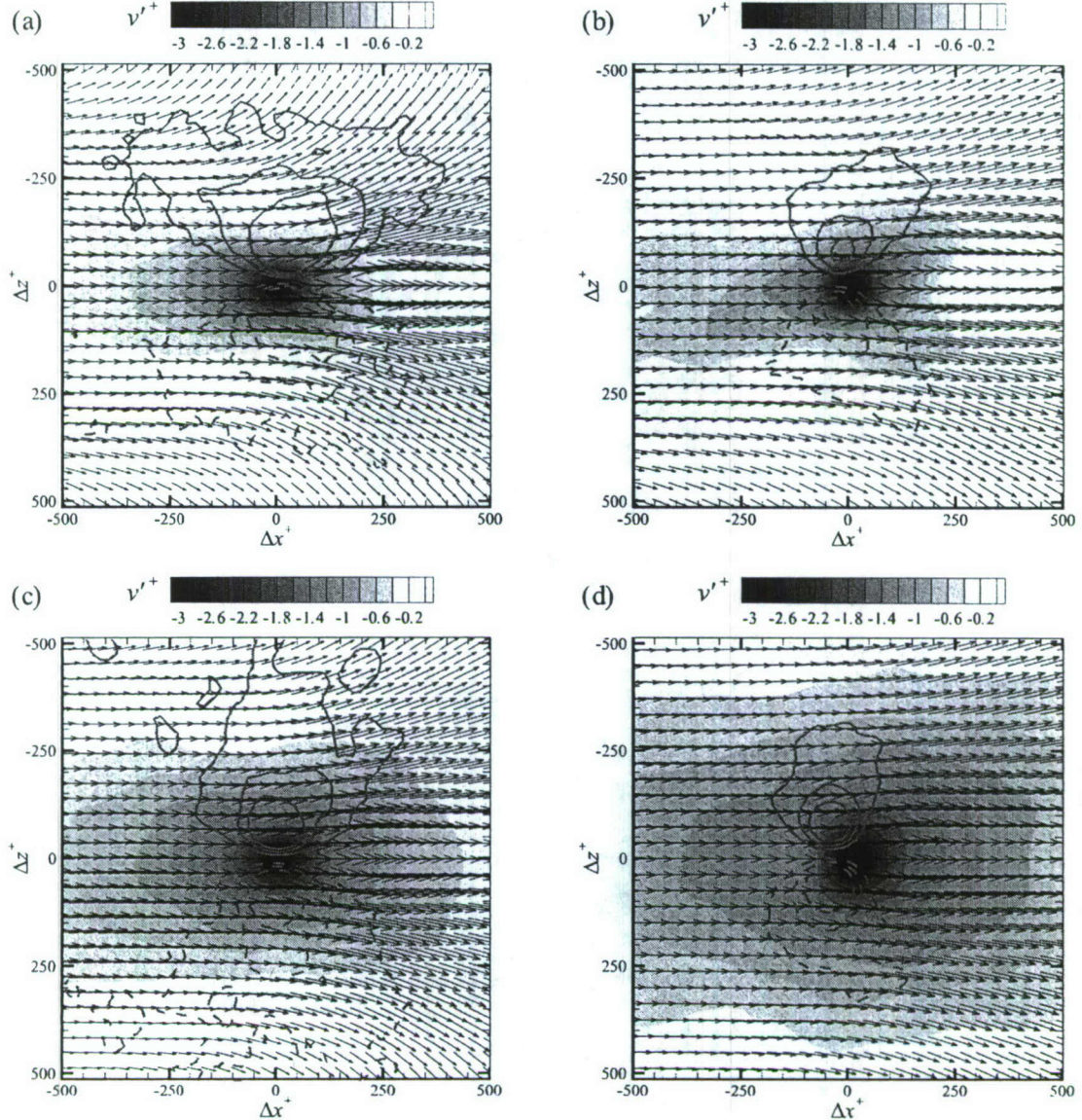


Figure 122: Conditionally-averaged fluctuating velocity fields given an intense  $Q4$  event in the  $x - z$  plane at (a, b)  $y = 0.065\delta$  and (c, d)  $y = 0.15\delta$  at  $Re_\theta \approx 13000$  for flow over the smooth and RF1 surfaces, respectively. The streamwise and spanwise velocity components,  $u$  and  $w$ , are shown as vectors and the wall-normal velocity component,  $v$ , is shown by gray-scale contours. Line contours are also overlaid illustrating the conditionally-averaged swirling strength field given an intense  $Q4$  event (dashed lines represent negative contour levels).

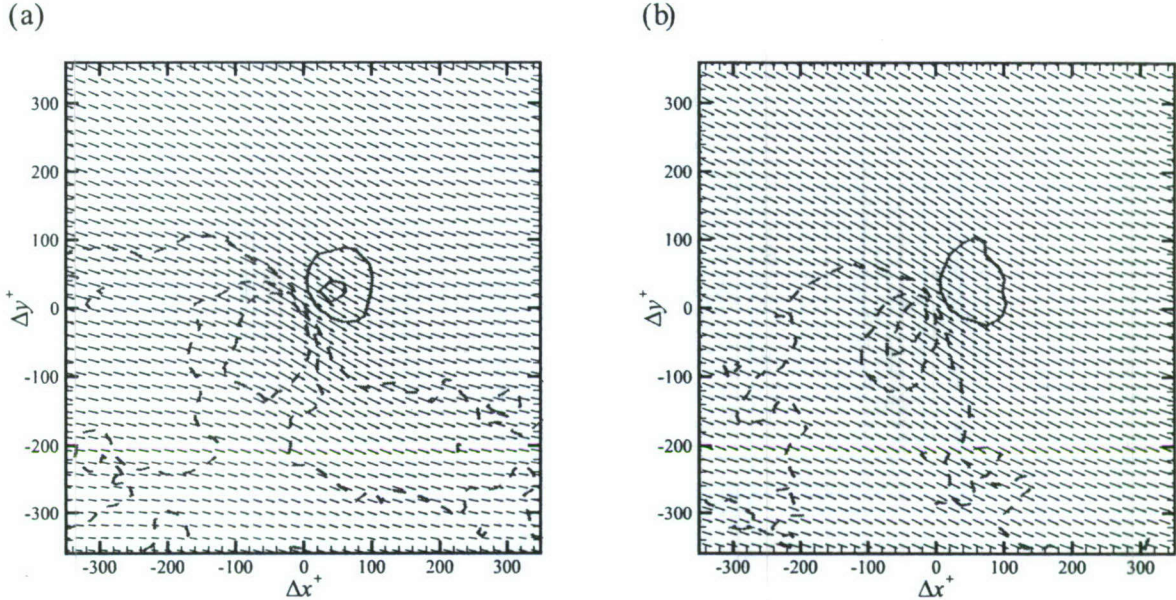


Figure 123: Conditionally-averaged fluctuating velocity fields given an intense  $Q4$  event in the  $x - y$  plane at  $Re_\theta \approx 13000$  for flow over the (a) smooth and (b) RF1 surfaces at  $y = 0.15\delta$ . Line contours are overlaid in each plot illustrating the associated conditionally-averaged swirling strength field given an intense  $Q4$  event (dashed lines represent negative contour levels).

reduction in the streamwise extent of  $\rho_{uu}$  in the presence of the RF1 surface may be indicative of a roughness-induced modification of the streamwise extent of hairpin packets. Such a modification may manifest itself as a reduction in the streamwise spacing of consecutive vortices in a packet, a suppression of the vortex regeneration mechanism thought to be the impetus behind outer-layer vortex organization and/or an alteration of the spanwise meandering of the large-scale motions in the log layer. Interestingly, while the streamwise extent of  $\rho_{uu}$  is altered by roughness, its inclination angle is not.

Decomposition of the velocity ensembles into large- and small-scale ensembles via POD reveals that the largest spatial scales tend to be most sensitive to roughness effects. Indeed, two-point correlation coefficients of the large-scale velocity fields indicate that the large-scale features of all three velocity components are reduced in streamwise extent in the presence of the RF1 surface. In contrast, the spanwise extents of these large-scale correlations are unchanged in the presence of roughness. Further, similar correlations of the small-scale velocity fields indicate strong insensitivity to rough-wall effects. Nevertheless, the contributions of the large- and small-scale features of the flow to the turbulent stresses are found to be similar irrespective of surface condition.

Finally, conditional averages of swirling strength and fluctuating velocity fields in the  $x - z$  and  $x - y$  planes given strong  $Q2$  and  $Q4$  events reveal spatial signatures consistent with hairpin-like structures in both smooth- and rough-wall flow. This evidence indicates that hairpin vortices, and their organization into larger-scale packets, represent the primary generation mechanism for  $Q2$  and  $Q4$  events for flow over the smooth and RF1 surface considered herein.

## 7 Summary

### 7.1 Principal conclusions

The present research centered on experimentally investigating the turbulent flow over highly irregular roughness replicated from a turbine blade damaged by deposition of foreign materials. Of particular interest was understanding how the flow over this surface might behave compared to many past studies of flow over more idealized roughness topographies. Understanding these similarities and differences is important since most roughness topographies encountered in practical flows of interest are non-ideal and more akin to the highly-irregular roughness considered herein.

The present results provide detailed evidence that the outer-layer flow over the turbine-blade roughness considered herein is similar to that of smooth-wall flow when the turbulence statistics are scaled appropriately by the friction velocity. This similarity is entirely in accordance with Townsend's wall-similarity hypothesis which presumes that roughness sets the wall shear stress and the boundary layer thickness and the outer-layer turbulence adjusts itself to these conditions in a universal manner. The similarity noted in this study extends from the mean velocity profiles in deficit scaling, to the single-point turbulence statistics (including pdf's and quadrant analysis of the instantaneous Reynolds-stress-producing events) as well as to two-point correlations of velocity far from the rough surface. This latter similarity between smooth- and rough-wall flow is important because it hints at similarity in the spatial structure of smooth- and rough-wall flow. *Finally, this similarity is quite crucial from a turbulence modeling and control standpoint, since the development of models and control strategies rely heavily on testing and simulations in smooth-wall turbulence. As such, this similarity indicates that such methods developed in smooth-wall test-beds may be appropriate for use in more practical flow systems affected by (highly irregular) roughness.*

Measurements were also performed in streamwise–spanwise planes located at  $y = 0.065\delta$  and  $y = 0.15\delta$  in flows over the smooth and RF1 surfaces. For the rough-wall cases, the first wall-parallel measurement plane is well within the roughness sublayer while the second resides at the outer edge of the roughness sublayer. The measurements at  $y = 0.065\delta$  show that strong roughness protrusions into the flow generate strong heterogeneities in the turbulence, although these effects only exist locally around these surface defects. In particular, no discernable wake signatures are noted downstream of these roughness protrusions, further supporting the notion that they do not significantly impact the global character of the flow. However, analysis of the  $y = 0.15\delta$  data reveals that these turbulence heterogeneities do not extend far from the wall as the turbulence appears relatively homogeneous at this wall-normal location. Measurements at lower Re indicate that these turbulence heterogeneities are more intense at higher Re, supporting the notion that the wall-normal extent of the roughness sublayer is Reynolds-number dependent. *Further, these results suggest that since the turbulence is generally only modified in the immediate vicinity of the roughness, these modifications likely only play a pivotal role in terms of contributing the local skin friction.*

Finally, significant effort was spent on understanding the similarities and differences in the spatial structure of the smooth- and rough-wall flows considered herein. Instantaneous velocity realizations in both the  $x - y$  and  $x - z$  planes for smooth- and rough-wall flow indicate that large-scale low- and high-momentum regions (LMR's and HMR's) exist in both flows and that these large-scale features generate a vast majority of the turbulent shear stress. In addition, both of these large-scale features are interpreted to be the by-product of hairpin vortex packets, indicating that such structures exist in both the smooth- and rough-wall flows. However, despite the qualitative consistencies noted in these instantaneous realizations, spatial correlations of velocity highlight quantitative differences in the spatial character of the smooth- and rough-wall flows. In particular, the large-scale streamwise extent of two-point streamwise velocity correlation coefficients,  $\rho_{uu}$ , is

reduced in the presence of the RF1 surface, most notably at  $y = 0.065\delta$  which is well within the roughness sublayer. In contrast, the streamwise extents of  $\rho_{vv}$  and  $\rho_{ww}$  appear relatively unaffected by roughness as are the spanwise extents of all three velocity correlation coefficients. Previous studies have highlighted the imprints of hairpin vortex packets on the two-point velocity correlations, particularly the consistency between the long streamwise extent of  $\rho_{uu}$  and the streamwise length scales of hairpin packets. As such, the reduction in the streamwise extent of  $\rho_{uu}$  in the presence of the RF1 surface may be indicative of a roughness-induced modification of the streamwise extent of hairpin packets. Interestingly, while the streamwise extent of  $\rho_{uu}$  is altered by roughness, its inclination angle is not.

Decomposition of the velocity ensembles into large- and small-scale ensembles via POD reveals that the largest spatial scales tend to be most sensitive to roughness effects. Indeed, two-point correlation coefficients of the large-scale velocity fields indicate that the large-scale features of all three velocity components are reduced in streamwise extent in the presence of the RF1 surface. In contrast, the spanwise extents of these large-scale correlations are unchanged in the presence of roughness. Further, similar correlations of the small-scale velocity fields indicate strong insensitivity to rough-wall effects. Nevertheless, the contributions of the large- and small-scale features of the flow to the turbulent stresses are found to be similar irrespective of surface condition. *From a modeling standpoint, similarity in smaller-scale structure may provide an indication that smooth-wall LES models could be sufficient for capturing small-scale contributions in rough-wall flows.* Finally, conditional averages of swirling strength and fluctuating velocity fields in the  $x - z$  and  $x - y$  planes given strong  $Q2$  and  $Q4$  events reveal spatial signatures consistent with hairpin-like structures in both smooth- and rough-wall flow. This evidence indicates that hairpin vortices, and their organization into larger-scale packets, represent the primary generation mechanism for  $Q2$  and  $Q4$  events for flow over the smooth and RF1 surface considered herein.

## 7.2 Next steps

With respect to the flow in the immediate vicinity of the roughness, our results indicate that the large-scale roughness elements play an important role in enhancing turbulence in the roughness sublayer which in turn contributes to an enhancement of the drag. In this regard, the implication for rough-wall turbulence modeling and control is that the smaller-scale roughness features in an irregular topography only contribute in a secondary fashion. Therefore, it may be possible to develop low-order models of highly irregular roughness that only retain the large-scale surface defects but still generate the same turbulence modifications within and outside the roughness sublayer (In the latter case, shortening of the streamwise length scales of the larger-scale structures, for example). Such low-order models would make large-scale computations over these types of surfaces possible by removing the requirement of complex gridding near surfaces with both large- and small-scale topographical characteristics. The development of such models is the focus of an AFOSR YIP award made to the PI in 2007 and this effort is well underway in the PI's lab.

Another issue not tackled in the present effort is the impact of roughness on the longest scales of motion. Previous studies have shown scales with streamwise extents on the order of  $5 - 15\delta$  to exist in smooth-wall turbulent flows, including pipes (Kim & Adrian, 1999; Guala *et al.*, 2006), channels (Balakumar & Adrian, 2007) and boundary layers (Balakumar & Adrian, 2007; Hutchins & Marusic, 2007). These studies indicate that such motions consist of streamwise-elongated low-momentum regions that meander in the spanwise direction. Kim & Adrian (1999) was the first to propose the possibility that individual hairpin vortex packets may align coherently in some manner to form these very-large-scale motions (VLSM's) that are most prevalent in the near-wall and logarithmic regions of the flow. One possibility in the present context is that roughness may alter the characteristics of these VLSM's, including their streamwise extent as well as the degree to which they meander in the

spanwise direction. Both of these possible modifications of VLSM's could contribute to the streamwise shortening of the large-scale motions observed in section 6, although a fundamental alteration of the vortex regeneration cycle thought to facilitate packet organization could also account for this shortening. We have performed preliminary measurements in a streamwise–spanwise measurement plane over the RF1 surface at  $y = 0.065\delta$  for  $Re_\theta \approx 13000$  using time-resolved 2D PIV with an acquisition rate of 1 kHz. This system was graciously loaned to us by TSI, Inc. for evaluation purposes. While the aforementioned studies regarding VLSM's employed hot-wire anemometry to study very large spatial scales from single-point velocity measurements (and in some cases multiple (10) points simultaneously with multiple hot-wire probes), time-resolved PIV allows one to measure velocities at many points in the 2D measurement plane ( $\sim 5000 - 10000$ ) instantaneously but at a high repetition rate. The long scales in the streamwise direction can then be reconstructed using Taylor's hypothesis (just as with hot wires) but at many spatial locations simultaneously. One would have to employ  $O(100)$  or more hot-wire probes simultaneously to achieve the data yield we have achieved by employing Taylor's hypothesis in concert with time-resolved PIV velocity fields (the latter is also devoid of the significant cost associated with calibrating this many hot-wire probes). Our preliminary data reveals the existence of extremely long low-momentum regions for flow over the RF1 surface that extend beyond  $8\delta$  in the streamwise direction. Interestingly, these VLSM's meander quite appreciably in the spanwise direction, consistent with the work of Hutchins & Marusic (2007) who observed similar low-momentum features in smooth-wall turbulence from velocity data acquired with a rake of 10 hot-wire sensors spaced in the spanwise direction at  $0.1\delta$  in conjunction with reconstruction of streamwise spatial scales via Taylor's hypothesis. For reference, our time-resolved PIV results have a velocity grid spacing in the streamwise and spanwise directions of  $0.02\delta$  compared to the  $0.1\delta$  resolution of Hutchins & Marusic (2007). As such, this comparison serves as an excellent example of the obvious advantages of this unique application of time-resolved PIV compared to conventional high-frequency single-point probes (or rakes of single-point probes). In any case, the existence of these VLSM's in the presence of the RF1 surface indicates that such motions are an important characteristic of rough-wall flows as well. We are presently analyzing this data further to determine whether roughness alters the spanwise meandering of these motions. It should be noted that the use of time-resolved PIV is key to facilitating the study of spatial motions of this scale as they are certainly not accessible with standard PIV techniques.

Finally, given the wide parameter space associated with rough-wall turbulence, including element size, geometry, aspect ratio, distribution, roughness Reynolds number, and the ratio of boundary layer thickness to roughness height, further studies are needed to develop more quantitative and accurate thresholds for the validity of wall similarity. It is certainly advantageous to hypothesize that the turbulence in rough-wall flow is similar to the smooth-wall case outside of a thin layer where the specific details of the rough surface exert their influence (as was observed for the practical surface considered herein). The wide-spread applicability of such a hypothesis for rough-wall flows that satisfy certain quantifiable characteristics would greatly simplify modeling and control of outer-layer physics which becomes increasingly dominant with  $Re$ . The trouble is that these certain quantifiable characteristics have still yet to be sufficiently characterized. As noted earlier, there is still debate as to whether the geometric scale of the roughness ( $k$ ) is more/less important in this regard that the equivalent sand grain height ( $k_s$ ). Measurements over practical roughness topographies garnered from other applications beyond turbine blades would be instructive in this regard. In addition, revisiting some of the seminal experiments of Schlichting (1979) in which he carefully considered the impact of different geometries and spatial patterns of discrete roughness elements in the skin friction would be quite instructive as well. The substantially better experimental facilities and methods we have at our disposal nowadays would allow our community to revisit such effects with greater accuracy and detail in the context of outer-layer similarity as well

as the dependence of the detailed physics in the roughness sublayer on these roughness parameters.

## 8 Publications and presentations associated with this funding

### 8.1 Journal articles

- Wu, Y. and Christensen, K. T. 2008. Structural Characteristics of Flow over a Practical Rough-Wall Topography. *J. Fluid Mech.*, to be submitted.
- Wu, Y. and Christensen, K. T. 2008. Turbulence Modifications in the Roughness Sublayer of Flow over Irregular Roughness. *AIAA J.*, to be submitted.
- Bons, J. and Christensen, K. T. 2008. A Comparison of Drag and Heat Transfer for Real vs. Simulated Surface Roughness Characterizations. *AIAA J. Prop. Power*, submitted.
- Wu, Y. and Christensen, K. T. 2007. Outer-Layer Similarity in the Presence of a Practical Rough-Wall Topography. *Phys. Fluids* **19** (8), 085108.
- Natrajan, V. K., Wu, Y. and Christensen, K. T. 2007. Spatial Signatures of Retrograde Spanwise Vortices in Wall Turbulence. *J. Fluid Mech.* **574**, 155-167.
- Wu, Y. and Christensen, K. T. 2006. Reynolds-Stress Enhancement Associated with a Short Fetch of Roughness in Wall Turbulence. *AIAA J.* **44** (12), 3098-3106.
- Wu, Y. and Christensen, K. T. 2006. Population Trends of Spanwise Vortices in Wall Turbulence. *J. Fluid Mech.* **568**, 55-76.

### 8.2 Conference proceedings

- Wu, Y. and Christensen, K. T. 2008. Structural Characteristics of Flow Over a Highly-Irregular Surface Topography. *46th AIAA Aerospace Sciences Meeting*, AIAA Paper 2008-0648.
- Wu, Y. and Christensen, K. T. 2007. Turbulence Modifications in the Roughness Sublayer of Flow over a Highly-Irregular Surface Topology. *37th AIAA Fluid Dynamics Conference*, AIAA Paper 2007-3995.
- Bons, J. and Christensen, K. T. 2007. Review of Surface Roughness Characterizations: Real versus Simulated Roughness Models. *37th AIAA Fluid Dynamics Conference*, AIAA Paper 2007-3997 (invited).
- Wu, Y. and Christensen, K. T. 2007. The Validity of Outer-Layer Similarity in the Presence of Highly-Irregular Surface Roughness. *45th AIAA Aerospace Sciences Meeting*, AIAA Paper 2007-0528.
- Wu, Y., Natrajan, V. K. and Christensen, K. T. 2006. Reynolds-Stress Enhancement Associated with a Short Fetch of Roughness in Wall Turbulence. *44th AIAA Aerospace Sciences Meeting*, AIAA Paper 2006-1117.

### 8.3 Invited presentations

- "Measurements of Flow over Irregular Roughness," *5th International Workshop on Wall-Bounded Turbulent Flows*, Baltimore, 2008.

- “Educing Coherent Structures and Their Impact from Planar Velocimetry Measurements in Laboratory Boundary Layers,” *American Geophysical Union (AGU) Fall Meeting*, San Francisco, CA, 2007.
- “The Character of Turbulence over Smooth and Highly-Irregular Rough Walls,” *Department of Aerospace Engineering and Mechanics, University of Minnesota*, 2007.
- “Statistical and Structural Features of Turbulence in the Presence of Smooth and Highly-Irregular Rough Walls,” *Department of Mechanical, Materials and Aerospace Engineering, Illinois Institute of Technology*, 2006.
- “Statistical and Structural Features of Turbulence in the Presence of Smooth and Highly-Irregular Rough Walls,” *Department of Mechanical and Aerospace Engineering, Arizona State University*, 2006.
- “Population Trends of Spanwise Vortices in Wall Turbulence,” *3rd International Workshop on Wall-Bounded Turbulent Flows*, Chicago, 2005.

## 9 Honors and awards attained during funding period

### 9.1 PI

- Promoted to Associate Professor with indefinite tenure (Aug. 2007)
- NSF CAREER Award (2007)
- AFOSR Young Investigator Award (2006)
- Invited participant: Symposium on Fluid Science and Turbulence (2008)
- Invited participant: 3rd, 4th and 5th International Workshops on Wall-Bounded Turbulent Flows (2005, 2006, 2008)
- Invited Member: Scientific Advisory Committee, International Symposium on Applications of Laser Techniques to Fluid Mechanics (2007-date)
- Member: AIAA Fluid Dynamics Technical Committee (2007-date)
- Invited Member: AIAA Roughness Study Group (2006-date)

### 9.2 Graduate student

- Appointed Assistant Professor in Mechanical Engineering Dept., Wright State University (beginning Aug. 2008)
- Numerous travel grants from Graduate College, UIUC (2005-2008)

## References

- ACARLAR, M. S. & SMITH, C. R. 1987a A study of hairpin vortices in a laminar boundary layer. *J. Fluid Mech.* **175** (Part 1.), 1–41.
- ACHARYA, M., BORNSTEIN, J. & ESCUDIER, M. P. 1986 Turbulent boundary layers on rough surfaces. *Exp. Fluids* **4**, 33–47.
- ADRIAN, R. J. 1995 Limiting resolution of particle image velocimetry for turbulent flow. In *Advances in Turbulence Research*.
- ADRIAN, R. J., MEINHART, C. D. & TOMKINS, C. D. 2000 Vortex organization in the outer region of the turbulent boundary layer. *J. Fluid Mech.* **422**, 1–54.
- ALLEN, J. J., SHOCKLING, M. A., KUNKEL, G. J. & SMITS, A. J. 2007 Turbulent flow in smooth and rough pipes. *Phil. Trans. R. Soc. A* **365**, 699–714.
- ALTENHOFEN, R. E. 1952 Rectification. In *Manual of Photogrammetry*. (ed. D. American Society of Photogrammetry, Washington), p. 457.
- ANDREOPoulos, J. & WOOD, D. H. 1982 The response of a turbulent boundary layer to a short length of surface roughness. *J. Fluid Mech.* **118**, 143–164.
- ANTONIA, R. A. & LUXTON, R. E. 1971 The response of a turbulent boundary layer to a step change in surface roughness. part 1. smooth to rough. *J. Fluid Mech.* **48**, 721–761.
- ASHRAFIAN, A., ANDERSSON, H. I. & MANHART, M. 2004 DNS of turbulent flow in a rod-roughened channel. *International Journal of Heat and Fluid Flow* **25**, 373–383.
- BAKE, S., MEYER, G. W. & RIST, U. 2002 Turbulence mechanism in klebanoff transition: A quantitative comparison of experiment and direct numerical simulation. *J. Fluid Mech.* **459**, 217–243.
- BAKEWELL, H. P. & LUMLEY, J. L. 1967 Viscous sublayer and adjacent wall region in turbulent pipe flow. *Phys. Fluids* **10**, 1880–1889.
- BAKKEN, O. M., FROGSTAD, P. A., ASHRAFIAN, A. & ANDERSSON, H. I. 2005 Reynolds number effects in the outer layer of the turbulent flow in a channel with rough walls. *Phys. Fluids* **17** (065101).
- BALAKUMAR, B. J. & ADRIAN, R. J. 2007 Large- and very-large-scale motions in channel and boundary-layer flows. *Phil. Trans. Royal Soc. A* **365**, 665–681.
- BALL, K., SIROVICH, L. & KEEFE, L. 1991 Dynamical eigenfunction decompositon of turbulent channel flow. *International Journal for Numerical Methods in Fluids* **12**, 585–604.
- BANDYOPADHYAY, P. R. & WATSON, R. D. 1988 Structure of rough-wall turbulent boundary layers. *Phys. Fluids* **31**, 1877–1883.
- BERKOOZ, G., HOLMES, P. & LUMLEY, J. 1993 The proper orthogonal decomposition in the analysis of turbulent flows. *Annu. Rev. Fluid Mech.* **25**, 539–75.
- BERNERO, S. & FIEDLER, H. 2000 Application of particle image velocimetry and proper orthogonal decomposition to the study of a jet in a counterflow. *Experiments in Fluids* pp. S274–S281.

- BESSM, J. M. & STEVENS, L. J. 1984 Cross-correlation measurements in a turbulent boundary layer above a rough wall. *Phys. Fluids* **27**, 2365–2366.
- BHAGANAGAR, K., KIM, J. & COLEMAN, G. 2004 Effect of roughness on wall-bounded turbulence. *Flow, Turbulence and Combustion* **72**, 463–492.
- BIJILLON, F., NINO, Y. & GARCIA, M. H. 2006 Measurements of turbulence characteristics in an open-channel flow over a transitionally-rough bed using particle-image velocimetry. *Exp. Fluids* **41**, 857.
- BONS, J. P. 2002 St and cf augmentation for real turbine roughness with elevated freestream turbulence. *J. Turbomach.* **124**, 632–644.
- BONS, J. P., TAYLOR, R. P., MCCLAIN, S. T. & RIVIR., R. B. 2001 The many faces of turbine surface roughness. *J. Turbomach.* **123**, 739–748.
- BRADSHAW, P. 2000 A note on "critical roughness" height and "transitional roughness". *Phys. Fluids* **6**, 1611–14.
- BROOKE, J. W. & HANRATTY, T. J. 1992 Origin of turbulence-producing eddies in a channel flow. *Phys. Fluids A* **5** (4), 1011–1022.
- BROWN, G. L. & THOMAS, A. S. W. 1977 Large structure in a turbulent boundary layer. *Phys. Fluids* **20**, S243–S252.
- CARLIER, J. & STANISLAS, M. 2005 Experimental study of eddy structures in a turbulent boundary layer using particle image velocimetry. *J. Fluid Mech.* **535**, 143–188.
- CASTRO, I. P. & ROBINS, A. G. 1977 The flow around a surface-mounted cube in uniform and turbulent streams. *J. Fluid Mech.* **79**, 307–335.
- CAZEMIER, W., VERSTAPPEN, R. W. C. P. & VELDMAN, A. E. P. 1998 Proper orthogonal decomposition and low-dimensional models for driven cavity flows. *Phys. Fluids* **10** (7), 1685–1699.
- CHRISTENSEN, K. T. 2001 Experimental investigation of acceleration and velocity fields in turbulent channel flow. PhD thesis, Department of Theoretical and Applied Mechanics, UIUC.
- CHRISTENSEN, K. T. 2004 The influence of peak-locking errors on turbulence statistics computed from piv ensembles. *Experiments in Fluids* **36** (3), 484–497.
- CHRISTENSEN, K. T. & ADRIAN, R. J. 2001 Statistical evidence of hairpin vortex packets in wall turbulence. *J. Fluid Mech.* **431**, 433–443.
- CHRISTENSEN, K. T. & ADRIAN, R. J. 2002 Measurement of instantaneous eulerian acceleration fields by particle-image accelerometry: Method and accuracy. *Experiments in Fluids* **33** (6), 759–769.
- CHRISTENSEN, K. T. & WU, Y. 2005 Characteristics of vortex organization in the outer layer of wll turbulence. In *4th International Symposium on Turbulence and Shear Flow Phenomena..*
- CHRISTENSEN, K. T., WU, Y., ADRIAN, R. J. & LAI, W. 2004 Statistical imprints of structure in wall turbulence. In *AIAA Paper 2004-1116*.

- COLEBROOK, C. F. 1939 Turbulent flow in pipes with particular reference to the transition region between the smooth- and rough-pipe laws. *J. Inst. Civil Eng.* **11**, 133–56.
- CONNELLY, J. S., SCHULTZ, M. P. & FLACK, K. A. 2006 Velocity-defect scaling for turbulent boundary layers with a range of relative roughness. *Exp. in Fluids* **40**, 188–195.
- CORDIER, L. & BERGMANN, M. 2002 Proper orthogonal decomposition: an over view, von karman institute for fluid dynamics. In *Lecture Series 2002-04 on Post-Processing of Experimental and Numerical Data..*
- CUI, J., PATEL, V. C. & LIN, C.-L. 2003 Large-eddy simulation of turbulent flow in a channel with rib roughness. *International Journal of Heat and Fluid Flow* **24**, 372–388.
- DELO, C. J., KELSO, R. M. & SMITS, A. J. 2004 Three-dimensional structure of a low-reynolds-number turbulent boundary layer. *J. Fluid Mech.* **512**, 47–83.
- DEMARE, S., LABRAGA, L. & TOURNIER, C. 1999 Comparison and scaling of the bursting period in rough and smooth walls channel flows. *Journal of Fluids Engineering* **121**, 735–745.
- DJENIDI, L., ELAVARASAN, R. & ANTONIA, R. A. 1994 Lda measurements in a turbulent boundary layer over a *d*-type rough wall. *Exp. Fluids* **16**, 323–29.
- DJENIDI, L., ELAVARASAN, R. & ANTONIA, R. A. 1999 The turbulent boundary layer over transverse square cavities. *J. Fluid Mech.* **395**, 271–294.
- DRUAULT, P., GUIBERT, P. & ALIZON, F. 2005 Use of proper orthogonal decomposition for time interpolation from piv data. *Experiments in Fluids* **39**, 1009–1023.
- FALCO, R. E. 1977 Coherent motions in the outer region of turbulent boundary layers. *Phys. Fluids* **20** (10), S124–S132.
- FALCO, R. E. 1983 New results, a review and synthesis of the mechanism of turbulence production in boundary layers and its modification. *AIAA Paper* pp. 83–0377.
- FALCO, R. E. 1991 A coherent structure model of the turbulent boundary layer and its ability to predict reynolds number dependence. *Phil. Trans. R. Soc. Lond. A* **336**, 103–129.
- FLACK, K. A., SCHULTZ, M. P. & SHAPIRO, T. A. 2005 Experimental support for townsend's reynolds number similarity hypothesis on rough walls. *Phys. Fluids* **17**, 035102.
- FLORES, O., JIMENEZ, J. & DEL ALAMO, J. C. 2007 Vorticity organization in the outer layer of turbulent channels with disturbed walls. *J. Fluid Mech.* **591**, 145–154.
- GANAPATHISUBRAMANI, B., HUTCHINS, N., HAMBLETON, W. T., LONGMIRE, E. K. & MARUSIC, I. 2005 Investigation of large-scale coherence in a turublent boundary layer using two-point correlations. *J. Fluid Mech.* **524**, 57–80.
- GANAPATHISUBRAMANI, B., LONGMIRE, E. K. & MARUSIC, I. 2002 Investigation of three dimensionality in the near field of a round jet using stereo piv. *J. Turbulence* **3** (016).
- GANAPATHISUBRAMANI, B., LONGMIRE, E. K. & MARUSIC, I. 2003 Characteristics of vortex packets in turbulent boundary layers. *J. Fluid Mech.* **478**, 35–46.
- GEERS, L., TUMMERS, M. & HANJALIC, K. 2005 Particle imaging velocimetry-based identification of coherent structures in normally impinging multiple jets. *Phys. Fluids* **17**, 055105.

- GRASS, A. J. 1971 Structural features of turbulent flow over smooth and rough boundaries. *J. Fluid Mech.* **50**, 233–255.
- GRASS, A. J., STUART, R. J. & MANSOUR-TEHRANI, M. 1993 Common vortical structure of turbulent flows over smooth and rough boundaries. *AIAA Journal* **31** (5), 837–47.
- GUALA, M., HOMMEMA, S. E. & ADRIAN, R. J. 2006 Large-scale and very-large-scale motions in turbulent pipe flow. *J. Fluid Mech.* **554**, 521–542.
- GUNTHER, A. & VON ROHR, P. R. 2003 Large-scale structures in a developed flow over a wavy wall. *J. Fluid Mech.* **478**, 257–285.
- GURKA, R., LIBERZON, A. & HETSRONI, G. 2006 Pod of vorticity fields: A method for spatial characterization of coherent structures. *International Journal of Heat and Fluid Flow* **27**, 416–423.
- HAMA, F. R. 1954 Boundary layer characteristics for smooth and rough surfaces. *Soc. Nav. Archit. Mar. Eng., Trans.* **62**, 333–358.
- HEAD, M. R. & BANDYOPADHYAY, P. 1981 New aspects of turbulent boundary-layer structure. *J. Fluid Mech.* pp. 297–338.
- HOLMES, P., LUMLEY, J. & BERKOOZ, G. 1996 *Turbulence, Coherent Structures, Dynamical Systems and Symmetry*. Cambridge University Press, Cambridge.
- HUTCHINS, N. & MARUSIC, I. 2007 Evidence of very long meandering features in the logarithmic region of turbulent boundary layers. *J. Fluid Mech.* **579**, 1–28.
- JIMENEZ, J. 2004 Turbulent flow over rough wall. *Annu. Rev. Fluid Mech.* **36**, 173.
- KARLSSON, R. I. 1980 Studies of skin friction in turbulent boundary layers on smooth and rough walls. PhD thesis, Department of Allied Thero and Fluid Dynamics, Chalmers University of Technology, Göteborg, Sweden.
- KEANE, R. D. & ADRIAN, R. J. 1992 Theory of cross-correlation analysis of piv images. *Applied Scientific Research* **49**, 191–215.
- KEIRSBULK, L., LABRAGA, L., MAZOUZ, A. & TOURNIER, C. 2002 Surface roughness effects on turbulent boundary layer structures. *J. Fluids Eng.* **124**, 127–135.
- KIM, K. C. & ADRIAN, R. J. 1999 Very large-scale motion in the outer layer. *Phys. Fluids* **11**, 417–422.
- KLEWICKI, J. C. & HIRSCHI, C. R. 2004 Flow field properties local to near-wall shear layers in a low reynolds number turbulent boundary layer. *Phys. Fluids* **16**, 4163–4176.
- KLINE, S. J., REYNOLDS, W. C., SCHRAUB, F. A. & RUNSTADLER, P. W. 1967 The structure of turbulent boundary layers. *J. Fluid Mech.* **30**, 741–773.
- KOSTAS, J., SORIA, J. & CHONG, M. 2005 A comparison between snapshot pod analysis of piv velocity and vorticity data. *Experiments in Fluids* **38**, 146–160.
- KOVASZNAY, L. S. G., KIBENS, V. & BLACKWELDER, R. F. 1970 Large-scale motion in the intermittent region of a turbulent boundary layer. *J. Fluid Mech.* **41**, 283–326.

- KROGSTAD, P. A., ANDERSSON, H. I., BAKKEN, O. M. & ASHRAFIAN, A. 2005 An experimental and numerical study of channel flow with rough walls. *J. Fluid Mech.* **530**, 327–352.
- KROGSTAD, P. A. & ANTONIA, R. A. 1994 Structure of turbulent boundary layers on smooth and rough walls. *J. Fluid Mech.* **277**, 1–21.
- KROGSTAD, P. A. & ANTONIA, R. A. 1999 Surface roughness effects in turbulent boundary layers. *Exp. Fluids* **27**, 450–460.
- KROGSTAD, P. A., ANTONIA, R. A. & BROWNE, L. W. B. 1992 Comparison between rough and smooth-wall turbulent boundary layers. *J. Fluid Mech.* **245**, 599–617.
- KRUSE, N., GUNTHER, A. & VON ROHR, P. R. 2003 Dynamics of large-scale structures in turbulent flow over a wavy wall. *J. Fluid Mech.* **485**, 87–96.
- LAWSON, N. J. & WU, J. 1997 Three-dimensional particle image velocimetry: error analysis of stereoscopic techniques. *Meas. Sci. Technol.* **8**, 894–900.
- LIBERZON, A., GURKA, R., TISELJ, I. & HETSRONI, G. 2005 Spatial characterization of the numerically simulated vorticity fields of a flow in a flume. *Theoret. Comput. Fluid Dynamics* **19**, 115–125.
- LIGRANI, P. M., HARRISON, J. L., MAHMMOD, G. I. & HILL, M. L. 2001 Flow structure due to dimple depressions on a channel surface. *Phys. Fluids* **13** (11), 3442–51.
- LIGRANI, P. M. & MOFFAT, R. J. 1986 Structure of transitionally rough and fully rough turbulent boundary layers. *J. Fluid Mech.* **162**, 69–98.
- LOIU, T.-M., CHANG, Y. & HWANG, D.-W. 1990 Experimental and computational study of turbulent flows in a channel with two pairs of turbulence promoters in tandem. *J. Fluid Eng.* **112**, 302–10.
- LIU, Z., ADRIAN, R. & HANRATTY, T. 2001 Large-scale modes of turbulent channel flow: transport and structure. *J. Fluid Mech.* **448**, 53–80.
- LIU, Z.-C., ADRIAN, R. & HANRATTY, T. 1994 Reynolds number similarity of orthogonal decomposition of the outer layer of turbulent wall flow. *Phys. Fluids* **6** (8), 2815–2819.
- LU, S. S. & WILLMARSH, W. W. 1973 Measurements of the structure of the reynolds stress in a turbulent boundary layer. *J. Fluid Mech.* **60**, 481–511.
- LUMLEY, J. L. 1967 The structures of inhomogeneous turbulent flow. In *Proceedings of the international colloquium on the fine scale structure of the atmosphere and its influence on radio wave propagation* (ed. A. M. Yaglom & V. I. Tararsky), pp. 166–178. Nauka, Moscow.
- MARTINUZZI, R. & TROPEA, C. 1993 The flow around surface-mounted, prismatic obstacles placed in a fully developed channel flow. *J. Fluids Eng.* **115**, 85–92.
- MEINHART, C. D. 1994 Investigation of turbulent boundary-layer structure using particle-image velocimetry. PhD thesis, Department of Theoretical and Applied Mechanics, University of Illinois at Urbana-Champaign.
- MEINHART, C. D. & ADRIAN, R. J. 1995 On the existence of uniform momentum zones in a turbulent boundary layer. *Phys. Fluids* **7**, 694–696.

- MIKHLIN, S. G. 1957 *Integral Equations, and their Applications to Certain Problems in Mechanics, Mathematical Physics and Technology..* Pergamon, Oxford.
- MOIN, P., LEONARD, A. & KIM, J. 1986 Evolution of a curved vortex filament into a vortex ring. *Phys. Fluids* **29**, 955–963.
- MOIN, P. & MOSER, R. D. 1989 Characteristic-eddy decomposition of turbulence in a channel. *J. Fluid Mech.* **200**, 471–509.
- MORRIS, S. C., STOLPA, S. R., SLABOCH, P. E. & KLEWICKI, J. C. 2007 Near-surface particle image velocimetry measurements in a transitionally rough-wall atmospheric boundary layer. *J. Fluid Mech.* **580**, 319–338.
- MULHEARN, P. J. & FINNIGAN, J. J. 1978 Turbulent flow over a very rough, random surface. *Boundary-Layer Meteorol.* **15**, 109–132.
- NAKAGAWA, S. & HANRATTY, T. J. 2001 Particle image velocimetry measurements of flow over a wavy wall. *Phys. Fluids* **13** (11), 3504–3507.
- NAKAGAWA, S. & HANRATTY, T. J. 2003 Influence of a wavy boundary on turbulence. ii. intermediate roughened and hydraulically smooth surfaces. *Exp. Fluids* **35**, 437–447.
- NATRAJAN, V. K., WU, Y. & CHRISTENSEN, K. T. 2007 Spatial signatures of retrograde spanwise vortices in wall turbulence. *J. Fluid Mech.* **574**, 155–167.
- NIKURADSE, J. 1933 Laws of flow in rough pipes. *NACA Technical Memorandum* (1292).
- ORLANDI, P., LEONARDI, S., TUZI, R. & ANTONIA, R. A. 2003 Direct numerical simulation of turbulent channel flow with wall velocity disturbances. *Phys. Fluids* **15** (12), 3587–3601.
- PEARSON, B. R., ELAVARASAN, E. & ANTONIA, R. A. 1998 Effect of a short roughness strip on a turbulent boundary layer. *Applied Science Research* **59**, 61–75.
- PEDERSEN, J. & MEYER, K. 2002 Pod analysis of flow structures in a scale model of a ventilated room. *Experiments in Fluids* **33**, 940–949.
- PERRY, A. E. & CHONG, M. S. 1982 On the mechanism of wall turbulence. *J. Fluid Mech.* **119**, 173–217.
- PERRY, A. E. & LI, J. D. 1990 Experimental support for the attached-eddy hypothesis in zero-pressure-gradient turbulent boundary layers. *J. Fluid Mech.* **218**, 405–438.
- PERRY, A. E., SCHOFIELD, W. H. & JOUBERT, P. N. 1969 Rough wall turbulent boundary layers. *J. Fluid Mech.* **37** (2), 383–413.
- POGGI, D., PORPORATO, A. & RIDOLFI, L. 2003 Analysis of the small-scale structure of turbulence on smooth and rough walls. *Phys. Fluids* **15** (1), 35–46.
- PRASAD, A. K. 2000 Stereoscopic particle image velocimetry. *Exp. Fluids* **29**, 103–116.
- PRASAD, A. K., ADRIAN, R. J., LANDRETH, C. C. & OFFUTT, P. W. 1992 Effect of resolution on the speed and accuracy of particle image velocimetry interrogation. *Experiments in Fluids* **13**, 105–116.

- RAUPACH, M. R. 1981 Conditional statistics of reynolds stress in rough-wall and smooth-wall turbulent boundary layers. *J. Fluid Mech.* **108**, 363–382.
- RAUPACH, M. R., ANTONIA, R. A. & RAJAGOPALAN, S. 1991 Rough-wall turbulent boundary layers. *Appl. Mech. Rev.* **44**, 1–25.
- RAUPACH, M. R., COPPIN, P. A. & LEGG, B. J. 1986 Experiments on scalar dispersion within a model plant canopy. part i: The turbulence structure. *Boundary-Layer Meteorol.* **35**, 21–52.
- RAUPACH, M. R., THOM, A. S. & EDWARDS, I. 1980 A wind-tunnel study of turbulent flow close to regularly arrayed rough surfaces. *Boundary-Layer Meteorol.* **18**, 373–397.
- SABOT, J. & COMTE-BELLOT, G. 1976 Intermittency of coherent structures in the core region of fully developed turbulent pipe flow. *J. Fluid Mech.* **74**, 767–796.
- SABOT, J., SALEH, I. & COMTE-BELLOT, G. 1977 Effects of roughness on the intermittent maintenance of reynolds shear stress in pipe flow. *Phys. Fluids* **20**, Pt II (10), S150–S155.
- SAVORY, E. & TOY, N. 1986 The flow regime in the turbulent near wake of a hemisphere. *Exp. Fluids* **4** (4), 181–188.
- SCHLICHTING, H. 1979 *Boundary-Layer Theory*. McGraw-Hill, New York.
- SCHOFIELD, W. H. & LOGAN, E. 1990 Turbulent shear flow over surface mounted obstacles. *J. Fluids Eng.* **112**, 376–385.
- SCHOPPA, W. & HUSSAIN, F. 2000 Coherent structure dynamics in near-wall turbulence. *Fluid Dyn Res* **26**, 119–139.
- SCHULTZ, M. P. & FLACK, K. A. 2003 Turbulent boundary layers over surfaces smoothed by sanding. *J. Fluids Eng.* **125**, 863–870.
- SCHULTZ, M. P. & FLACK, K. A. 2005 Outer layer similarity in fully rough turbulent boundary layers. *Exp. Fluids* **38**, 328.
- SEN, M., BHAGANAGAR, K. & JUTTIJUDATA, V. 2007 Application of proper orthogonal decomposition (pod) to investigate a turbulent boundary layer in a channel with rough walls. *Journal of Turbulence* **8** (41).
- SHAFI, H. S. & ANTONIA, R. A. 1997 Small-scale characteristics of a turbulent boundary layer over a rough wall. *J. Fluid Mech.* **342**, 263–293.
- SIROVICH, L. 1987 Turbulence and the dynamics of coherent structures. part 1. coherent structures. *Q. Appl. Math.* **45**, 561.
- SIROVICH, L., BALL, K. & HANDLER, R. 1991 Propagating structures in wall-bounded turbulent flows. *Theoretical and Computational Fluid Dynamics* **2**, 307–317.
- SMALLEY, R. J., ANTONIA, R. A. & DJENIDI, L. 2001 Self-preservation of rough-wall turbulent boundary layers. *Eur. J. Mech. B-Fluids* **20**, 591–602.
- SMITH, C. R. 1984 A synthesized model of the near-wall behavior in turbulent boundary layers. In *Proc. 8th Symp. on Turbulence* (ed. J. Z. . G. Patterson), pp. 333–364. University of Missouri-Rolla.

- SMITH, C. R., WALKER, J. D. A., HAIDARI, A. H. & SOBRUN, U. 1991 On the dynamics of near-wall turbulence. *Phil. Trans. R. Soc. Lond. A* **336**, 131–175.
- SMITS, A. J. & WOOD, D. H. 1985 The response of turbulent boundary layers to sudden perturbations. *Ann. Rev. Fluid Mech.* **17**, 321–58.
- SOLOFF, S. M. 1998 An investigation of the small-scale structure in a turbulent pipe flow using high resolution particle image velocimetry. Master's thesis, Department of Theoretical and Applied Mechanics, University of Illinois at Urbana-Champaign, Urbana, Ill.
- SOLOFF, S. M., ADRIAN, R. J. & LIU, Z.-C. 1997 Distortion compensation for generalized stereoscopic particle image velocimetry. *Meas. Sci. Technol.* **8** (1441–1454).
- SUBRAMANIAN, C. S., KING, P. I., REEDER, M. F., OU, S. & RIVER, R. B. 2004 Effects of strong irregular roughness on the turbulent boundary layer. *Flow, Turbulence and Combustion* **72**, 349–368.
- TACHIE, M. F., BERGSTROM, D. J. & BALACHANDAR, R. 2000 Rough wall turbulent boundary layers in shallow open channel flow. *J. Fluids Eng.* **122**, 533–541.
- TACHIE, M. F., BERGSTROM, D. J. & BALACHANDAR, R. 2003 Roughness effects in low- $re_\theta$ . *Exp. in Fluids* **35**, 338–346.
- TEITEL, R. & ANTONIA, R. A. 1990 The interaction region of a turbulent duct flow. *Phys. Fluids A* **2**, 808–813.
- THEODORSEN, T. 1952 Mechanism of turbulence. In *Proc. 2nd Midwestern Conf. on Fluid Mechanics*, pp. 1–19. Ohio State University, Columbus.
- TOMKINS, C. D. 2001 The structure of turbulence over smooth and rough walls. PhD thesis, University of Illinois at Urbana-Champaign.
- TOMKINS, C. D. & ADRIAN, R. J. 2003 Spanwise structure and scale growth in turbulent boundary layers. *J. Fluid Mech.* **490**, 37–74.
- TOWNSEND, A. A. 1976 *The structure of turbulent shear flow.*, 2nd edn. Cambridge University Press.
- VOLINO, R. J., SCHULTZ, M. P. & FLACK, K. A. 2007 Turbulence structure in rough- and smooth-wall boundary layers. *J. Fluid Mech.* **592**, 263–293.
- WALLACE, J. M. & BRODKEY, R. S. 1977 Reynolds stress and joint probability density distributions in the u-v plane of a turbulent channel flow. *Phys. Fluids* **20**, 351–355.
- WALLACE, J. M., ECKELMANN, H. & BRODKEY, R. S. 1972 The wall region in turbulent shear flow. *J. Fluid Mech.* **54**, 39–48.
- WEBER, R. O. 1999 Remarks on the definition and estimation of friction velocity. *Boundary-Layer Meteorol.* **93**, 197–209.
- WESTERWEEL, J. 1997 Fundamentals of digital particle image velocimetry. *Measurement Science and Technology* **8**, 1379–1392.
- WIENEKE, B. 2005 Stereo-piv using self-calibration on particle images. *Exp. Fluids* **39**, 267–280.

- WU, Y. 2008 Experimental investigation of highly irregular roughness effects in wall turbulence. PhD thesis, Department of Mechanical Science and Engineering, UIUC.
- WU, Y. & CHRISTENSEN, K. T. 2006a Population trends of spanwise vortices in wall turbulence. *J. Fluid Mech.* **568**, 55–76.
- WU, Y. & CHRISTENSEN, K. T. 2006b Reynolds-stress enhancement associated with a short fetch of roughness in wall turbulence. *AIAA J.* **44**, 3098.
- ZANG, W. & PRASAD, A. K. 1997 Performance evaluation of a scheimpflug stereocamera for stereoscopic particle image velocimetry. *App. Opt.* **36**, 8738–8744.
- ZHOU, J., ADRIAN, R. J. & BALACHANDAR, S. 1996 Autogeneration of near-wall vortical structures in channel flow. *Phys. Fluids* **8**, 288–290.
- ZHOU, J., ADRIAN, R. J., BALACHANDAR, S. & KENDALL, T. M. 1999 Mechanisms for generating coherent packets of hairpin vortices in channel flow. *J. Fluid Mech.* pp. 353–396.
- ZHOU, J., MEINHART, C. D., BALACHANDAR, S. & ADRIAN, R. 1997 Formation of coherent hairpin packets in wall turbulence. In *Self-Sustaining Mechanisms of Wall Turbulence* (ed. R. L. Panton), pp. 109–134. Southampton, UK: Computational Mechanics.